Characterising the properties and evolution of surface spots on young stellar objects with citizen science photometry

Carys Herbert

School of Astronomy and Astrophysics
University of Kent
Canterbury, UK

June 2024

A thesis submitted to University of Kent for the degree of
Doctor of Philosophy

Abstract

Young stellar objects (YSOs) display variability on the timescale of the rotational period due to surface spots rotating in and out of the observer's line of sight. The fast rotation of young stars results in photometric variability on the order of days.

In this thesis, a methodology has been developed that uses the peak-to-peak amplitude of variation in multi filter broad band photometry to characterise surface spots on YSOs. This methodology was then applied to data obtained through the Hunting Outbursting Young Stars citizen science project. Firstly, to YSOs in IC 5070 with high cadence data, and then to long duration light curves in the same field. Finally, all YSOs in HOYS fields were searched for periodicity and spot properties were established for all suitable sections of light curves.

Across all YSO samples, two thirds of spot-induced variability is due to cold spots, and one third is due to warm/hot spots. The majority of all spots detected have surface coverage values below 30 percent. Most cold spots are 300 – 1500 K below the stellar temperature. The threshold of detection is around 300 K above or below the stellar temperature, dependent on coverage. A significant distribution of large, low temperature contrast warm spots (300 – 2500 K above stellar temperature) has been observed, alongside a small population of high temperature ($>$2500 K above stellar temperature), low coverage hot spots attributed to accretion.

Spot properties have been related to stellar properties, particularly inner disc excess. Cold spots appear on objects with no preference to inner disc excess, while warm/hot spots have been observed as more or equally common on objects without an inner disc excess depending on the sample. The observed warm spots are hence either related to accretion as low-density accretion structures, or plages as have been observed on non-accreting YSOs.

Declarations

The content of this thesis was composed by the author, and has not been submitted for the purposes of a qualification at any other institution or for any other degree.

All work is the authors own, unless explicitly stated otherwise. All instances where use has been made of other work has been cited.

The content of Chapters 3 and 4 has been published in Herbert et al. (2023). The content of Chapters 5 and 6 has been published in Herbert et al. (2024).

Acknowledgements

Firstly, I would like to thank my supervisor *Dirk Froebrich*, who helped guide me through this project and has always supported my development as an astronomer. I am also grateful to *James Urquhart*, my second supervisor, who always made sure I was keeping my head above water. Thanks also to *Tim Kinnear* who is endlessly generous, both with his time and his goodwill.

Additionally, I would like to thank the astronomers that contribute data to the Hunting Outbursting Young Stars citizen science project. *Siegfried Vanaverbeke* for his assistance identifying periodic variables with the GLS method. *Aleks Scholz* for providing helpful comments on my published papers and the theory section of this thesis. I also acknowledge the financial support of the *Science and Technology Facilities Council*.

This achievement would not have happened without the support of my family and friends. I wish all the best to all of my PhD companions, those who have finished and left, and those who are still going. To name a few: *Aishling Dignam*, *Aashini Patel*, *Allie Corrigan*, *Ivana Grozdanova*, *Matthew Dickers*, *Ethan Finch*, *Holly Stokes-Geddes*.

To the *IAYC*, you formed me as an astronomer and as a person. When I first attended the IAYC at 17 years old, I never thought I would end up here; completing a PhD and running the IAYC as the president of the International Workshop for Astronomy. The *IAYC leaders* are endlessly inspiring and brilliant, and some of the silliest people I know. I love you all.

My thanks go to *kayaking* for keeping me humble and proving that sometimes what you need isn't natural talent but tenacity. To *archery*, for giving me a sense of achievement and something to aim for (pun intended). To *jiu-jitsu*, you taught me to always get back up. To *all the friends I made through those activities*, thank you for all the great times.

Daniela Hardikerova, knowing you has changed me for the better. *Miles Pitt*, you always knew when the duck needed turning. *Dan Bard*, you are kind and compassionate, and I know you are always in my corner. *Nikki Miller*, you've been one step ahead of me since we met. If you could do it, so could I. *Jasmine Calladine*, we have weathered many storms together and I know wherever we end up we will continue to do so. *Duncan and Elizabeth Dwinell*, you supported me with patience and kindness, and I don't believe I would have made it to university (let alone to a PhD) without you. *Poppy* was the best, most empathetic cat. I owe a lot to brother, *Owen*, who is funny and charismatic, and my constant desire to emulate him made me who I am today.

And finally, to my parents, *Sharon and Phil*, I know that I am never out in the world alone because you are always behind me.

Contents

List of Figures

List of Tables

1

Introduction

Here, a brief context for this thesis is provided, alongside the aims and outline for this thesis.

1.1 Spots on young stellar objects

Variability is a key feature in young stellar objects (YSOs). One main reason why YSOs are more variable than main-sequence stars is that they are hosting strong magnetic fields, causing cool spots in interaction with the stellar photosphere and hot spots in interaction with the accretion flow from the disk. The presence of these spots, combined with the fast rotation of young stars, then induces periodic photometric variability on timescales of days (see reviews by Herbst et al. (2007) and Bouvier et al. (2014)).

Photometric light curves, taken quasi-simultaneously in multiple bands have been an important tool to study the properties of spots for over 30 years (see e.g. Bouvier et al., 1993, 1995; Carpenter et al., 2001). While light curves do not provide resolved pictures of the stellar surface like Doppler Imaging or related techniques (e.g. Strassmeier, 2002; Strassmeier et al., 2003; Skelly et al., 2009; Donati & Landstreet, 2009), they can convey a measurement of the temperature contrast between spots and stellar photosphere (thus allowing to distinguish between hot and cool spots), as well as the coverage, the fraction of the surface covered by spots (Strassmeier, 1992; Bouvier et al., 1995; Scholz et al., 2009, 2012). In addition, multi-filter light curves can be obtained for large numbers of objects, helping to establish statistical trends.

Cold spots are regions on the photosphere, analogous to sun spots, that are hundreds of degrees cooler than the stellar temperature. These cause flux variations of generally less than ten percent (e.g. Strassmeier, 2009). Cold spots are expected to be present during all stages of the pre-main sequence evolution of stars, whereas hot spots are thought to be exclusive to accreting classical T Tauri (Stage 2) stars with full or transition discs (Herbst et al., 1994).

Hot spots are considered to be footprints of accretion with temperatures that are several thousand degrees above the stellar temperature and coverage less than a few percent of the stellar surface (Hartmann et al., 2016; Muzerolle et al., 1998). Emission lines as an indicator of accretion require these high temperatures. However, recent surveys present a more diverse picture with low temperature contrast, high coverage regions (Scholz et al., 2009, 2012; Bozhinova et al., 2016).

1.2 Thesis aims and structure

This thesis aims to develop a methodology that uses multi filter photometry to identify YSOs with surface features, distinguish between hot and cold spots, and characterise the spot temperature and surface coverage. This methodology will then be applied to light curves of YSOs obtained through the Hunting Outbursting Young Stars (HOYS) citizen science project. The aim of this is characterise typical spot temperature and coverage distributions, and relate spot properties with their YSOs.

In order to develop a methodology to determine spot properties from multi filter photometry and characterise surface spots on YSOs, the thesis aims and structure are as follows. Chapter 2 outlines relevant theory surrounding YSOs. This chapter also introduces the HOYS citizen science project, and details the data obtained through the project that is the basis of this thesis. Chapter 3 outlines a methodology to fit spot properties to the peak-to-peak amplitudes of periodic light curves, alongside details of statistical and systematic uncertainties. In Chapter 4 the spot fitting methodology is applied to a sample of periodic YSOs in IC 5070, identified over an 80 days in 2018 in Froebrich et al. (2021). In this chapter, the methodology is reflected upon to inform next steps. Chapter 5 identifies a sample of periodic YSOs in IC 5070 which have long duration light curves, and the procedure for determining peak-to-peak amplitudes over time is established. Chapter 6 details the amplitude and phase evolution of periodic YSOs in IC 5070 and analyses the spot property results of long term light curves. A number of individually interesting objects are identified and discussed. Chapter 7 applies the previously established methodologies to search for periodic YSOs across all HOYS target regions and determine spot properties, providing a large sample of spot properties. In Chapter 8 a detailed summary and the conclusions of this work are provided. Future work is also outlined.

2

Young stellar objects: theory and data

2.1 Young stellar object overview

Young stellar objects (YSOs) are pre-main sequence stars. Before stars reach sufficient temperatures to initiate the fusion of hydrogen, the temperature and hence the luminosity for these objects is caused by gravitational collapse and contraction. The star formation process is fundamentally different for low and intermediate mass stars ($M < 8\ M_{\odot}$) when compared to massive stars ($M > 8\ M_{\odot}$) (Tan et al., 2014). This work will focus on low and intermediate mass stars.

Low and intermediate mass stars are formed by the collapse of cool molecular clouds (Shu et al., 1987). Inside clouds, dense cores form and collapse inwards. The inner regions are optically thick to their own radiation, which causes the temperature of the core to increase. Interior to this, a denser hydrostatic core forms surrounded by an envelope, which is a protostar. The dusty envelope infalls into a circumstellar accretion disc, and the central object becomes optically visible from the

majority of viewing angles. While the object is surrounded by material a significant portion of the emission arises from the circumstellar disc, especially in the infrared.

The spectral energy distribution (SED) of YSOs has been used to characterise the relation of star to disc emission, and therefore the evolutionary stage of the object. Lada (1987) defines three classes (1-3) of YSOs using SEDs in wavelengths $2 < \lambda < 25$ μm using an infrared spectral index α_{SED}, defined in Equation 2.1. A sketch depicting these classes is shown in Fig. 2.1.

$$\alpha_{SED} = \frac{d\log(\lambda F_\lambda)}{d\log\lambda} \tag{2.1}$$

Class 1 objects ($\alpha_{SED} > 0$) are protostars generally optically obscured by their envelope. The majority of a Class 1 object's luminosity is emitted in the far infrared ($25 < \lambda < 100$ μm), and extends beyond into longer wavelengths. The material in the envelope settles into an accretion disc due to the conservation of angular momentum in the collapsing cloud, this takes ~ 0.5 Myr (Evans et al., 2009).

Class 2 sources ($-2 < \alpha_{SED} < 0$) have cleared their envelope. This leaves the star optically visible. The accretion disc contributes an infrared excess to the SED. Stars in this class are actively accreting and spectroscopic observations display many associated emission line features. Class 2 objects with masses below 2 $M_\odot$ are known as classical T-Tauri stars (CTTS) named after the brightest star in the Taurus-Aur region, which became the prototype for this type star (Joy, 1945). Stars in this class with masses 2 – 8 $M_\odot$ are known as Herbig Ae/Be objects (Herbig, 1960).

Class 3 objects have very little remaining infrared excess. The majority of the disc has either been accreted or dissipated by alternative means such as planet formation or photoevaporation. The timescale for the evolution from Class 2 to Class 3 is < 10 Myr, although we will examine this more closely in Section 2.2.1. The remaining disc is optically thin. Class 3 objects have significantly reduced or ceased accretion and therefore do not show strong emission line features. Hence, they are also known as weak-line T Tauri stars (WTTS). This separation was initially defined as the equivalent width (EW) of the H_α line being less than $10\mathring{A}$, as H_α is strongly correlated with the mass accretion rate (e.g. Muzerolle et al., 2001).

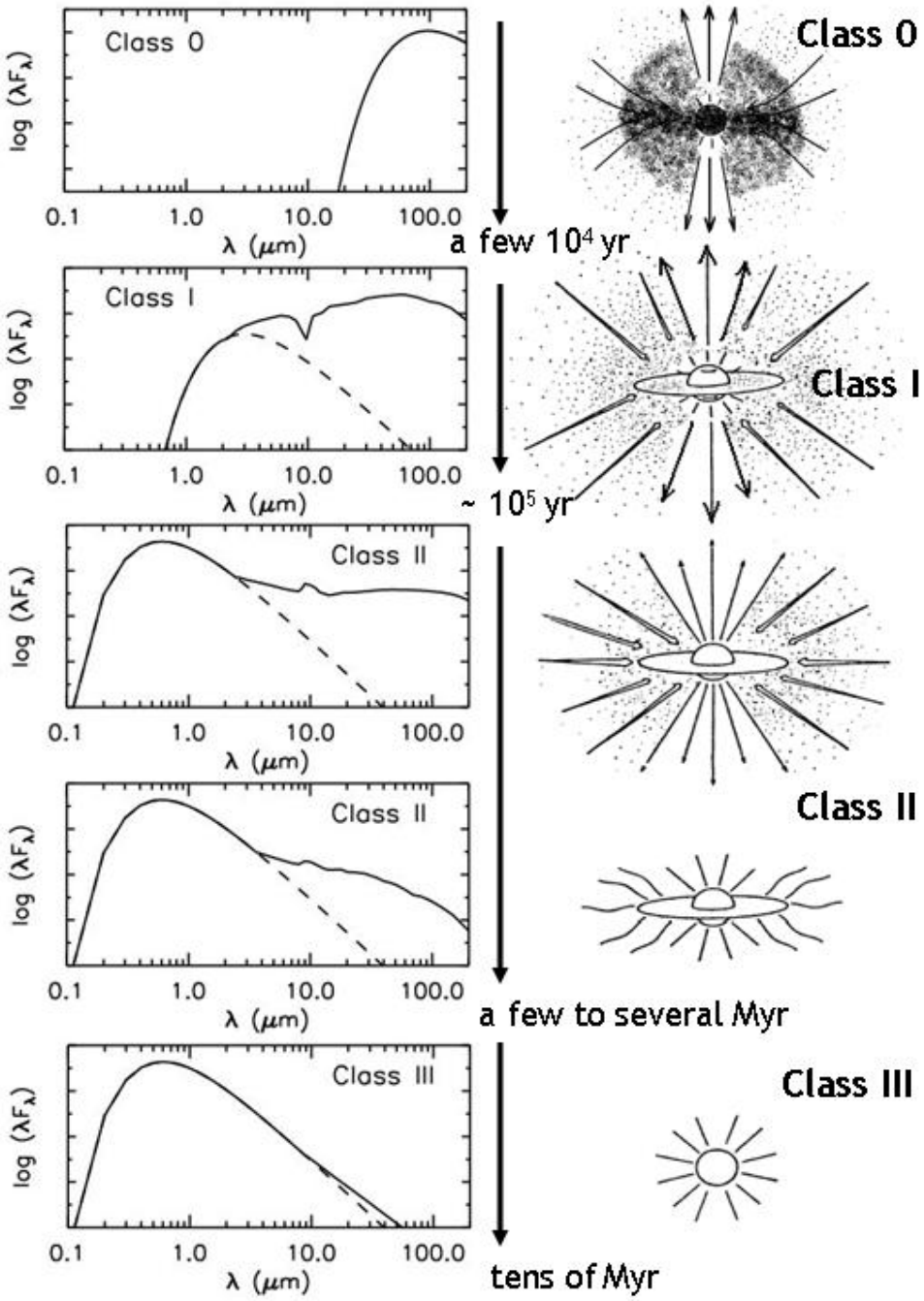

Figure 2.1: Sketch of class system definitions for YSOs, showing the circumstellar envelopes and discs alongside their SEDs. Adapted from Wilking (1989) by Elise Furlan (https://www.elisefurlan.com/Research.html).

The class definitions of prestellar cores were extended by Andre et al. (1993) to include a precursory stage to Class 1, i.e. Class 0. Class 0 objects are undetectable at $\lambda < 10\mu$m as the majority of the material remains in the envelope rather than distributed across a disc. This protostellar stage is very short, $\sim 10^4$ yr, (Hueso & Guillot, 2005). Greene et al. (1994) further refined the separation between Class 1 and 2 by introducing an intermediate 'flat-spectrum' sources with $0.3 > \alpha_{SED} \geq -0.3$. Greene et al. (1994) additionally revises the boundary between Class 2 and Class 3, with Class 3 for sources $\alpha_{SED} < -1.6$. These values are listed in Table 2.1, and will be the adopted classification system throughout the analysis in this work.

Lada (1987) defines these as classes, and are often taken as being synonymous to evolutionary stage. The caveat here is that the infrared spectral index may not always align with the evolutionary stage. For example, a Class 2 system viewed at an angle through disc material will have a higher spectral index than its stage. Resolved images, and observations in multiple wavelengths are required to be precise about evolutionary stage.

All objects in this work are either low, or intermediate mass stars which follow this regime. Massive stars are separated from this regime because above 8 $M_\odot$ hydrogen fusion is initiated while the star is actively accreting and appear from their natal clouds on the main sequence. Massive stars do not feature in this work, and so their formation is not discussed here, see Tan et al. (2014) for an overview of massive star formation.

Table 2.1: Class definitions for YSOs using α_{SED} values from Greene et al. (1994).

Class	α_{SED}
Class 1	$\alpha_{SED} > 0.3$
Flat Spectrum	$-0.3 \leq \alpha_{SED} \leq 0.3$
Class 2	$-1.6 < \alpha_{SED} < -0.3$
Class 3	$\alpha_{SED} \leq -1.6$

2.2 Discs

2.2.1 Stage 2 discs

This work examines the star disc system, and so an understanding of circumstellar discs is crucial to inform our discussion. Beyond the protostellar stages the envelope has fallen into a circumstellar disc. The disc is comprised of gas and dust orbiting the core. At formation, the composition of the disc is approximately that of the interstellar medium (ISM). The ISM has a dust-to-gas ratio of 100, i.e. gas account for 99 percent of the total mass. Observations of gas are more challenging as gas emits at specific wavelengths and is obscured by dust, therefore direct measurement requires spectroscopic observations. Dust on the other hand, is easy to observe either due to long-wavelength emission or optical thickness.

Disc mass tends to be lower around low mass stars $\frac{M_d}{M_\star} \sim 0.01$, and for Class 2 objects is typically ~ 0.005 $M_\odot$ (Williams & Cieza, 2011). Defining the outer edge of a disc is challenging as it is placing a boundary on a diffuse structure. Vicente & Alves (2005) used the visible ionisation front to estimate the disc radii for a sample of 125 YSOs in a young ($\sim$ 1 Myr) cluster in Orion. They inferred a median radius of 75 AU, and extrapolate that over the full sample of YSOs with infrared excesses 75 percent are likely to have a radius ≤ 75 AU. Two objects in this sample were identified with radii of 338 AU and 621 AU from their silhouettes in HST images, demonstrating the wide variety of disc sizes.

The disc scale height perpendicular to the plane of the disc increases with radius, this is known as disc flaring. Disc flaring was identified in Kenyon & Hartmann (1987) as emission from the central star is scattered by the material in a flared disc in such a way that would not be possible with a geometrically flat disc. Figure 2.2 is Fig. 2 from Duchêne et al. (2024), which observed the edge-on disc system of 2MASS J04202144+2813491, a 0.4 $M_\odot$ YSO in Taurus chosen for its large disc ($r_{disc} \approx 1000$ AU, one of the largest identified discs in the region). This object is therefore an excellent example to examine disc structure. The dark, dusty midplane of the disc is optically thick and the flaring is clearly visible. The scattered light creates the 'bowl' shape above and below the

disc.

Dust behaves very differently in the disc depending on the size of the dust grains. The typical grain size distribution for dust in the ISM, and therefore the initial distribution for the dust in the disc, approximately follows a power law of $N(a) \propto a^{-3.5}$ where $a \sim 0.001 - 0.25\,\mu$m (Pei, 1992). Grains that are $\leq 10\,\mu$m are completely coupled to the gas in the disc and are fully mixed vertically. Duchêne et al. (2024), in order to mimic the HST-JWST observations, conclude that turbulence in the disc is strong enough to completely bring the small dust particles to the disc surface. Larger dust grains on the $100\,\mu$m scale are completely decoupled, and settle in the midplane of the disc. The intermediate regime on the scale of tens of μm, is currently the subject of many studies as this understanding is crucial for pebble and eventually planet formation, with no definitive conclusions thus far.

Observations from the Atacama Large Millimeter/submillimeter Array (ALMA) have revolutionised the observations of protoplanetary discs as millimeter/submillimeter observations are able to observe through dust which obscures optical observations. HL Tau is an object aged 1-2 Myr evolving from Class 1 to 2, with a high disc mass of 0.03 – 0.14 $M_\odot$. The object has a highly collimated outflow traced to 100 AU from the disc which extends to $\sim 10^4$ AU. Crucially, it is orientated 40° from face-on which allows for direct observations of the disc.

ALMA observations in 2014 revealed several bright rings separated by dark rings with resolutions on the scale of a few AU (ALMA Partnership et al., 2015). Observations at three wavelengths are displayed in Fig. 2.3. The interior 10 AU of the system is bright, and optically thick even at 2.9 mm (the longest wavelength of the observations). Bright rings contain concentrations of dust, the optical thickness is not solely due to increased depth but also requires an increase in grain size. The dark regions contain ten times less dust (Pinte et al., 2016) but also show evidence of dust-grain growth. The removal of dust in these dark regions is attributed to planet formation. The height of the dusty millimeter continuum emitting region is of the order of 1 AU at 100 AU (Pinte et al., 2016), clearly showing the settling of the dust in the disc to be geometrically thin, especially when compared to the structure. The gas-to-dust ratio in these rings is around 5, a dramatic

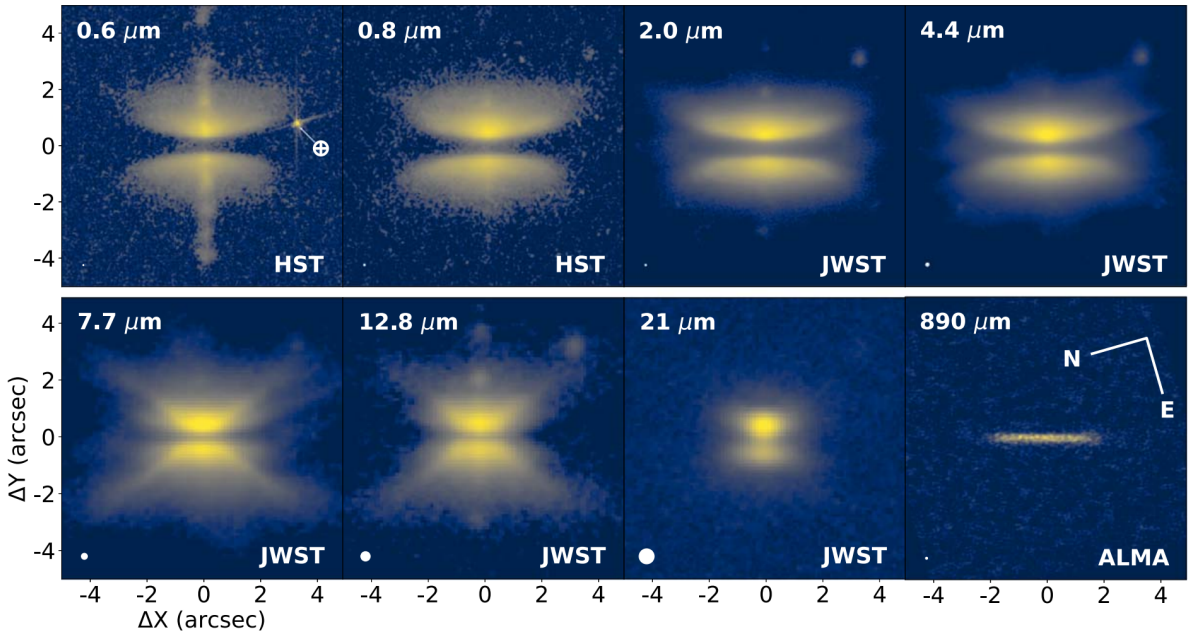

Figure 2.2: Figure 2 from Duchêne et al. (2024). Hubble Space Telescope, the JWST, and ALMA observations of 2MASS J04202144+2813491.

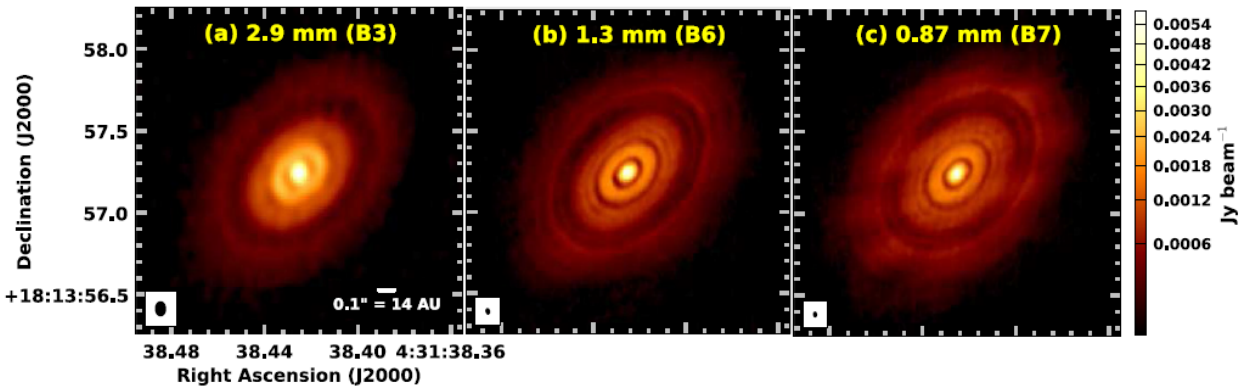

Figure 2.3: Three panels from Fig. 2 in ALMA Partnership et al. (2015), reformatted. Showing ALMA observations of HL Tau at three wavelengths.

difference from the 100 typical in the ISM.

We have now covered the large scale disc structure but crucial to our understanding is the inner disc. Dust cannot exist too close to the central star due to the increase in temperatures. At ~ 0.1 AU there is an inner wall as the temperatures overtake the dust destruction limit of 1400 K (Pollack et al., 1994). Optically thick dust exists in the disc up to this radius (Muzerolle et al., 2003), which is heated and produces emission in the near infrared (NIR, 2 – 5μm) and the mid infrared (MIR, 5 – 20μm) (Espaillat et al., 2010). Interior to the dust destruction radius or due to dust clearing (which we will examine in the following section, Section 2.2.2) emission from the warm gas in the inner disc can be observed. Despite a potentially high density of gas in the inner disc, with the absence of dust, the region is optically thin. Spectroscopy is required to probe the region with the temperatures of the inner disc reaching molecular excitation temperature. The specifics of spectroscopic observations are not relevant here, see Najita et al. (2007a) for a review.

2.2.2 Disc evolution

Transition and pre-transition discs

First identified in Strom et al. (1989), some YSOs display clear MIR and far infrared excesses with little to no NIR emission. Therefore, it was concluded that this was an intermediary stage of the disc's evolution. These are now referred to as transitional discs, i.e. transitioning between Class 2 and 3 (Espaillat et al., 2014). The region interior to a radius R_{hole} is optically thin and has been cleared of dust. The dust wall that on a full disc would be very close to the star, is now some way removed and this part of the SED is missing. The SED returns to a typical CTTS SED at longer wavelengths. An example of this is presented in Fig. 2.4 (right). An additional scenario exists where the 'normal' inner dust wall remains, but a gap has been cleared in the disc over a radius R_{gap} and this has removed a portion of the SED. These are referred to as pre-transitional discs (Espaillat et al., 2014), shown in the middle panel of Fig. 2.4. The capacity to detect these gaps depends on the instrument, the width of the gap (and hence how much of the SED is removed), and the portion of the SED that R_{gap} corresponds to. Millimeter and submillimeter observations show

that rings with dust-poor gaps are common, and hence the term transition disc may be a misnomer. Studies that rely on resolving the disc are limited to gaps larger than the angular resolution. Gaps in discs are frequently beyond the IR SED with $R_{gap} \sim 15 - 75$ AU (e.g. Andrews et al., 2011). Inner disc holes are easier to detect as more than 80 percent of the emission at $\leq 10\,\mu$m originates within 1 AU of the central star (D'Alessio et al., 2006).

There are two broad mechanisms by which the inner disc is cleared of dust; planet formation and photoevaporation. Planet formation is an umbrella term for several distinct processes. In Strom et al. (1989) the mechanism proposed for the clearing of the inner disc was the formation of rocky planetary cores effectively sweeping up the dust in the inner disc. This process leaves the gas relatively unaffected, and so the inner disc remains gas rich. This has been observed in the CI Tau system with VLTI/GRAVITY (Gravity Collaboration et al., 2023). Planets that are massive to cause significant gaps in the disc (Jupiter-mass and above) are then likely to dramatically influence the accretion of the object (Najita et al., 2007b). The disc will no longer be able to bypass the gap in order to sustain the inner disc edge, and so once the inner disc has been accreted accretion onto to object will cease. We will examine the accretion of transition disc objects in more detail in Section 2.3.2.

The final process that causes inner disc dissipation, and indeed can continue on to affect the wider disc, is internal photoevaporation. Internal photoevaporation is energetic emission from the central star in UV and X-ray heating the disc surface. At $\sim 7 - 10$ AU the thermal velocity overtakes the escape velocity, and a flow carries material out of the disc. There comes a point where the disc is being depleted by photoevaporation more quickly than the disc can resupply, and the inner and outer disc become decoupled. The inner disc is then accreted but is not resupplied, rapidly leaving behind an inner hole. This process is called the 'UV-switch' model (Carpenter et al., 2001). The switch is 'flipped' when the accretion rate reduces to below a critical value.

Evolved and debris discs

Whether evolved discs ought to be included as a category of transition disc is a subject of debate. Evolved discs show global reductions in their SED, as opposed to regional reductions. Evolved

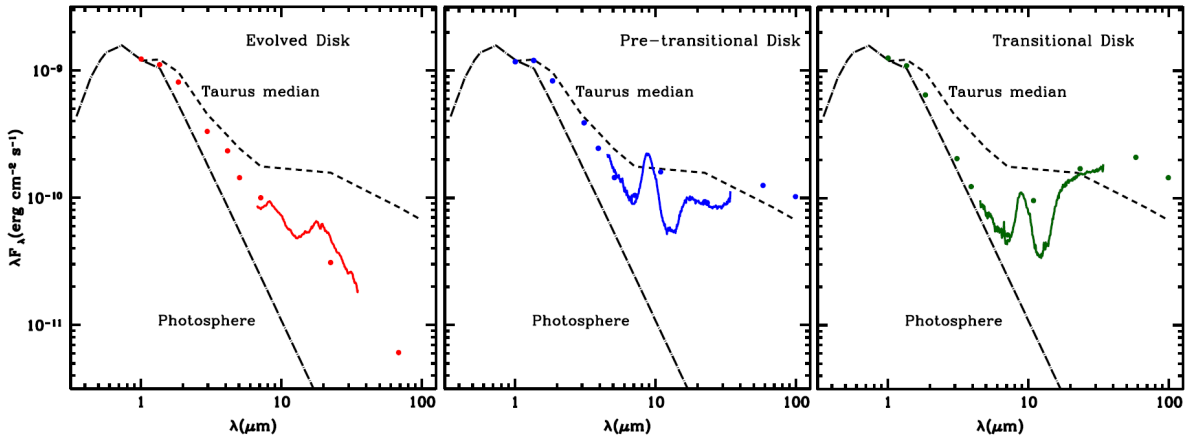

Figure 2.4: SEDs of an evolved disc (RECX 11, Ingleby et al. (2011)), a pre-transitional disc (LkCa 15, Espaillat et al. (2007)), and a transitional disc (GM Aur, Calvet et al. (2005). The Taurus median D'Alessio et al. (1999). Figure 1 from Espaillat et al. (2014).

discs are composed of gas and dust which can be fit with an SED (Sicilia-Aguilar et al., 2011), and display little IR excess above the photosphere which indicates that the disc has undergone a significant reduction in disc flaring. The left panel of Fig. 2.4 shows the SED of an evolved disc. Although the SED is significantly reduced compared to the Taurus median in the ranges 2 – 10 μm, the SED is above the transition disc object. This implies diminished dust globally but not the total depletion as in the transition disc example. The Taurus median has commonly been used as a proxy for typical disc properties, but this may not be applicable to all regions due to differences in the stellar environment (Fang et al., 2013).

The SEDs of evolved discs display little IR excess above the photosphere, especially at longer wavelengths which indicates that the disc has undergone a significant reduction in disc flaring. As we have seen larger dust grains settle towards the midplane, and so evolved discs contain a higher proportion of large, optically thin dust grains. Barenfeld et al. (2016) survey of the Upper Scorpius OB association ($\sim$10 Myr), shows the debris/evolved discs showed no remaining CO. Although, the loss of gas is not true for all evolved discs (Ingleby et al., 2011).

In the studies of young clusters evolved discs are often conflated with debris discs as they are indistinguishable from IR excess. At the point where a star reaches the main sequence it has either completely lost its disc or has an optically thin debris disc. Approximately 20 percent

of solar type main sequence stars have some kind of debris disc (Hughes et al., 2018). Debris discs are not residual remains of protoplanetary discs that are established and remain undisturbed. Debris discs are comprised of large dust grains and planetesimals in ring-like structures extending hundred of AU around the central star. The dust in debris discs requires constant feeding in with the creation of new dust through the grinding down of larger planetesimals to submillimeter sizes through a process known as collisional cascade (Wyatt et al., 2015; Matthews et al., 2014). It is for this reason that debris discs are also sometimes referred to as discs of 'second-generation' dust. Throughout this work, primordial dust discs will be referred to as evolved rather than debris discs.

Lifetimes of discs

Disc dispersal is studied by comparing the proportions of discs in the stellar populations of different star forming regions. Half of all stars have lost their NIR excess by 3 Myr and by 10 Myr the fraction remaining is practically zero (e.g. Haisch et al., 2001; Hernández et al., 2007).

The disc dispersal age is mass dependent, with low-mass stars holding onto their discs for longer. The Upper Scorpius OB association (~ 10 Myr) contains a large population of young stars with masses ~ 0.01 – 20 $M_\odot$. In the region 20 percent of very low mass < 0.2 $M_\odot$ retain their discs, when mass increases to M< 1.3 $M_\odot$ this value is 14 percent. Stars with masses 1.3 – 1.5 $M_\odot$ have 5 percent, and above 1.5 $M_\odot$ less than 1 percent retain an inner disc, and 4 – 20 percent retain some outer disc (Carpenter et al., 2006; Luhman & Mamajek, 2012; Luhman & Esplin, 2020).

This mass dependence does not seem to hold for very low mass objects (< 0.2 $M_\odot$) and brown dwarfs in the young (~ 1 Myr) Coronet cluster (Sicilia-Aguilar et al., 2008, 2011). The region has an overall disc fraction of 50 – 65 percent, and 50 percent of these show inner disc holes. The disc bearing stars that are not transition disc objects show an SED more consistent with evolved discs with reduced disc flaring. The region contains only a few intermediate mass stars, and no massive stars influencing the environment. It is therefore unlikely that external photoevaporation is prematurely dispersing the discs. For these low-mass objects it appears that discs evolve more rapidly than expected but spend longer at the transition disc stage than the typical UV-switch model suggests. This region is compared with the less populated, older (4 Myr) region Tr 37 in Sicilia-

Aguilar et al. (2013), which shows complex disc evolution on M-type stars. It is indicated that the higher stellar density leads to smaller discs forming.

Once disc evolution is initiated, dispersal occurs rapidly. The 'UV-switch' model theorises that depletion takes place over 10^5 yr. The σ Ori cluster ($\sim$ 3 Myr) has a 30 – 35 percent disc fraction, with 15 percent showing reduced NIR and MIR excess consistent with transition discs (Hernández et al., 2007). This fraction implies that the process of clearing the inner disc of dust takes ≤ 0.5 Myr.

The timescale of the transition disc stage depends on the disc dispersal mechanism. A large sample of 401 TTS in NGC 2264 ($\sim$ 3 Myr) observed with *Spitzer* and MegaCam (Canada-France-Hawaii-Telescope, CHFT) revealed that 209 were identified to have full discs, 28 were transition disc, and 164 evolved disc objects (Sousa et al., 2019). The transition discs in this sample displayed weak dust emission in the inner disc, implying a depleted though not completely cleared inner disc. The mean of R_{hole} was found to be 10.4 $\pm$ 2.8 AU, with a minimum 0.09 AU and maximum 78 AU. The wide range of hole size corresponds the formation mechanism, small holes less than 10 AU make up correspond to internal photoevaporation whereas larger holes are likely to be caused by planet formation. In this young sample, 18 percent of objects align with the photoevaporation model which further implies that at young ages the cause of transition disc is more likely planet formation while photoevaporation dominates at later stages. Najita et al. (2007b) concludes that young transition disc objects with higher disc masses (> 0.01 $M_\odot$) are more likely to have Jupiter-mass planets causing the inner disc clearing, as the accretion rate is likely to be above the critical value for the 'UV-switch'.

Internal factors are not the only contributing factors to disc dispersal timescale. Monsch et al. (2023) determined from modelling disc-locking (the slowing of the rotation of the star due to star-disc interactions, to be examined in Section 2.4) a disc fraction of 65 percent in the 1 – 2 Myr regions of the Orion Nebula Cluster (ONC) and Taurus. The authors concluded that this disc fraction, combined with the low age implied that internal photoevaporation was not sufficient to disperse the discs on this timescale, and that external photoevaporation likely plays a significant

role in disc dispersal. This is especially the case in the high-density ONC where there are several massive stars nearby which dramatically alter their environment. Alternatively, Taurus has considerably lower stellar density and contains no massive stars.

2.3 Accretion onto young stellar objects

2.3.1 Magnetospheric accretion

As YSOs approach the main sequence they accrete or otherwise disperse their circumstellar material. The majority of the final mass of the star is accreted in short bursts of high-rate accretion in the protostellar stages (0,1). These are known as episodic accretion events, and are required to solve the so-called 'luminosity problem'. The problem is that to generate a 1 $M_\odot$ star in the 10^5 yr protostellar stage a mass accretion rate of 10^{-5} $M_\odot yr^{-1}$ is required. The predicted resultant luminosity of this accretion is far above the luminosity observed for the majority of protostars (Kenyon et al., 1990). Therefore, we assume that a significant proportion of the stellar mass is accreted in very short, high rate accretion events. Evans et al. (2009) concluded that half of a star's final mass is accreted in just 7 percent of its 0.5 Myr Class 1 lifetime. These accretion events produce bright outbursts, which we will examine in Section 2.5.1.

CTTS undergo magnetospheric accretion which channels material from the inner disc ($\sim$1 AU) onto the star at typical rates of $\sim 10^{-8}$ $M_\odot yr^{-1}$ for 1 – 2 Myr (Hartmann, 1998). The magnetic field truncates the disc at a few stellar radii and the material flows along magnetic field lines in accretion columns. In the accretion flow the gas is heated to $\sim$8000 K, which produces broad emission lines. The accretion column hits the star at free fall speeds (300 km s^{-1}) and just above the photosphere creates an accretion shock with temperatures of the order of 10^6 K, which produces far ultraviolet (FUV) and soft X-ray emission irradiating the surrounding material (Ingleby et al., 2014, 2013). This energy is reabsorbed by the accretion column above and below the shock region. Calvet & Gullbring (1998) modelled the reprocessing of this energy. The photosphere absorbs $\sim \frac{3}{4}$ of the energy of the accretion shock. The emitted energy is therefore, $\frac{1}{4}$ travelling away from the star heating the preshock region to temperatures of $\sim 10^4$ K and $\sim \frac{3}{4}$ towards the star heating the

photosphere to 8000 – 10000 K. The preshock region is optically thin, and adds emission in the FUV and in the Balmer series (dominated by H_α leading to the classification of CTTS of EW in H_α with EW > 10 $\mathring{A}$, and WTTS EW$< 10\mathring{A}$), alongside emission lines such as Si IV, C IV, N V and He II. The strength of the emission corresponds to the accretion rate, and therefore the study of the emission lines provides important insight to the accretion of these objects. It is also observed that the accretion column density corresponds to the strength of the UV emission, with high density accretion columns creating more UV emission.

The heating of the photosphere at the base of the accretion column absorbs the majority of the energy from the accretion column. The base of the accretion column covers $f \approx 0.001 - 0.01$. This photospheric hot spot dominates the photometry in the optical, we will examine variability in more detail in Section 2.5.

Figure 2.5 shows a sketch from Hartmann et al. (2016) showing the idealised structure of the accretion columns. This assumes a dipolar magnetic field aligned with the rotation. However, analysis of the magnetic fields of CTTSs with Zeeman-Doppler Imaging (ZDI) has shown that CTTS can host stable higher order magnetic fields such as TW Hya which is dominated by octupole components (Donati et al., 2011b,a) or highly complex fields such as V2247 Oph (Gregory & Donati, 2011). As a PMS star develops a radiative core the dipole becomes weaker and the field becomes more complex (Gregory et al., 2012; Donati et al., 2011b). Tognelli et al. (2015) demonstrated that the timescale of developing a radiative core depends on the mass ranging from 0.5 Myr (for 2 $M_\odot$) to 9.3 Myr (for 0.5 $M_\odot$).

Presented in Fig. 2.6 are the extrapolated accretion supporting magnetic field lines for AA Tau, TW Hya (2010), and V2247 Oph from Zeeman Dopler Imaging (ZDI) (Johnstone et al., 2014). The footprints of the accretion for strong bipolar flows are located at high latitudes. Higher order fields force the accretion footprints to mid latitudes, and complex fields cause the footprints to present a mixture of mid-to-low latitudes (Johnstone et al., 2014). It is also clear that the higher order, and complex fields extend less distance away from the central star. In the case of AA Tau, the strong dipole induces a warp in the inner disc which we will examine in Section 2.5.2. We will

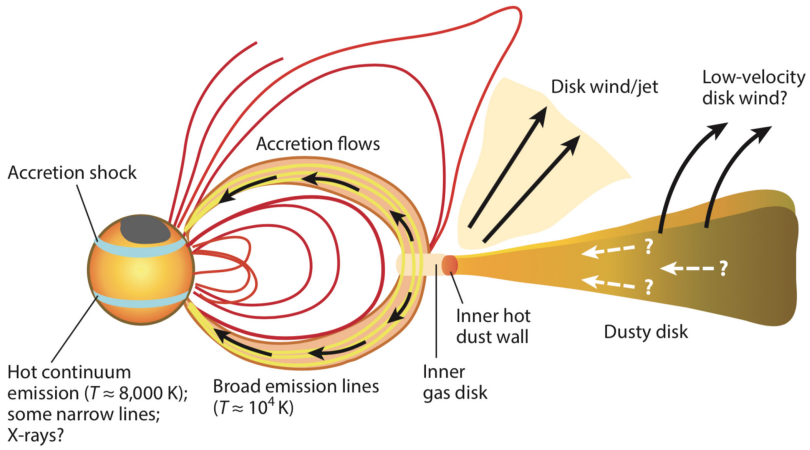

Figure 2.5: Schematic of magnetospheric accretion on a YSO. Taken from Hartmann et al. (2016).

examine the effect of the positioning of these footprints on the photometry in Section 2.5.

2.3.2 Accretion and disc evolution

We have touched upon the relation between disc evolution and accretion rate. There are two key factors involved, firstly the proportion of objects at various stages of disc evolution that are accreting and secondly the accretion rate. The majority of transition disc objects are accretors, with typical proportions of 70 – 80 percent (Kim et al., 2009; Cieza et al., 2010; Merín et al., 2010). Transition discs that are dust depleted may still be gas-rich towards the inner edge, allowing for accretion to continue (Manara et al., 2014).

In an NGC 2264 sample ($1 - 5$ Myr) (Sousa et al., 2019), 28 transition disc objects were iden-

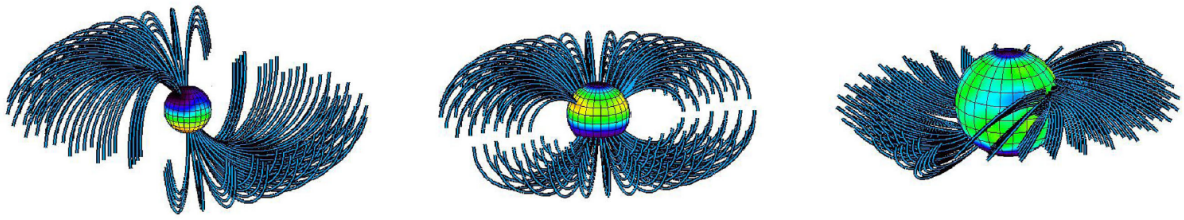

Figure 2.6: Accretion supporting magnetic field line extrapolations for three objects representing three typical accretion geometries. AA Tau (left) representing a strong bipolar field, TW Hya (middle) has an octuple field, and V2247 Oph (right) has a complex field. Adapted from Fig. 11 in Johnstone et al. (2014).

tified with 82 percent of transition disc objects still accreting. From these, 18 percent of transition disc candidates had low accretion rates ($< 10^{-9}$ $M_{\odot}yr^{-1}$). A further study of 58 members of NGC 2264 measured the accretion rate using the H_{α} emission line width (Shapiro et al., 2016). The accretion rate for transition disc objects was half the rate of the full disc objects. The accretion rate of the discless stars was an order of magnitude lower, below the rate observable by UV photometry. When measuring accretion using the UV excess for an NGC 2264 sample in Venuti et al. (2014), the mean accretion rates for the transition disc and full disc objects were within 10^{-10} $M_{\odot}yr^{-1}$, but the transition disc objects had a larger deviation.

The accretion rates for transition discs in Taurus ($1 - \sim 2$ Myr) and Ophiuchus ($< 1 - 2$ Myr) were compared with CTTS in the same regions. In the Najita et al. (2007b) study of Taurus, typical accretion rates were ten times lower for the transition disc objects when adjusted for disc mass. The transition disc objects were also found to have discs four times larger. In this sample transition disc defined as objects with SEDs less than the Taurus median, therefore globally evolved objects are likely included in the analysis. The sample was expanded in Najita et al. (2015) and also tended to have lower accretion rates for disc masses and higher disc masses. As we have seen, in young regions the primary cause of transition disc formation is expected to be Jupiter mass planet formation. Considering the high disc masses of the Taurus and Ophiuchus regions the authors excluded photoevaporation as the cause of the transition discs, as the accretion rate far exceeds the photoevaporation rate. Instead, the formation of Jupiter-mass planets is more likely to have dramatically altered the disc structure and the accretion rate.

The order of magnitude of difference between the accretion rate of transition disc objects and full disc objects is not observed in older regions. A half-order of magnitude difference is observed in 15 transition discs in NGC 2068 (~ 2 Myr) and IC 348 (~ 3 Myr) (Espaillat et al., 2012). In this study transition disc was defined as inner disc holes, and distinguished between transition discs and pre-transition discs with inner disc gaps. The accretion rate of pre-transition discs was measured at an order of magnitude above transition discs. As previously mentioned, it is observationally challenging to distinguish between transition and pre-transition discs depending on the position of

the inner disc gap and therefore portion of the SED affected.

In the region of Tr 37 (4 Myr), the transition disc fraction is identified at around 10 percent (Sicilia-Aguilar et al., 2006). This is a slightly higher proportion than typical studies due to measurements at 24 μm and high resolution spectra allowing for better characterisation of the outer disc. The discs in the Tr 37 region show less disc flaring and settling of dust consistent with disc evolution. Half of the transition disc objects showed no signs of accretion, and the remaining half were almost all below the threshold detection by UV photometry (10^{-9} $M_{\odot}yr^{-1}$). While there are no transition disc objects with a high accretion rate ($> 10^{-8}$ $M_{\odot}yr^{-1}$), there is little difference between the accretion rates of transition disc and full disc objects (Sicilia-Aguilar et al., 2010).

Evolved discs are also capable of accretion. Evolved discs have diminished gas and dust such as RECX-11 (left panel of Fig. 2.4) in η Chamaeleontis (97 pc, 5 – 9 Myr). Ingleby et al. (2011) demonstrated that it was still undergoing accretion at the low rate of 3×10^{-10} $M_{\odot}yr^{-1}$. The SED is reduced which implies the presence of dust and H_2 emission was used to demonstrate that gas is still present in the inner disc, and so accretion is able to continue at a reduced rate. Disc-bearing WTTS across 11 clusters aged 2 – 16 Myr were found to have a 20 – 30 percent proportion of accretors, all at a low rate (Thanathibodee et al., 2022). Unsurprisingly, out of these stars those in younger regions were more likely to be accreting.

2.4 Rotation of young stellar objects

2.4.1 Regulating angular momentum

When stars appear on the zero age main sequence (ZAMS), they have angular momentum that is 5 – 6 orders of magnitude below the angular momentum of the clouds that collapse to form them. The initial rotation rate of YSOs comes from the angular momentum of the cloud. The observed initial rotation rates of stars up to 1 $M_{\odot}$ emerging from the protostellar stage cover a range of $P \sim 1 - 10$ d. The angular momentum dispersal mechanism within the cloud has been simulated in various studies with no definitive conclusions (e.g. Gallet & Bouvier, 2012).

In the first ~ 5 Myr of the stars evolution the rotation rate remains largely stable, despite the

angular momentum delivered to the central star with accretion. After this period of stability, as the star contracts towards the ZAMS the stars 'spin-up' with lower limits for the rotation rate of 0.2 d, and then spin down on the early main sequence to their final rotation rates (e.g. Bouvier et al., 2014). The dominant method for controlling the stellar angular momentum on long timescales is magnetised stellar winds (e.g. Matt et al., 2012).

We are generally interested in the first 10 Myr, and so we focus on the time during which these objects have relatively stable rotation, and the end of that stability. In this period, there must be a counteracting torque or angular momentum dispersal mechanism acting upon the star. If the star were free to contract and increase in angular momentum with accretion, the star would reach break up speed within 10^5 yr (Pudritz & Matt, 2014).

A star-disc interaction, known as disc-braking that regulates the rotation was proposed by Koenigl (1991). In disc-braking, or disc-locking, the spin-up torque is counteracted by the accreting magnetic field lines that intersect with the disc at or beyond the corotation radius. An additional aspect of star-disc interaction that influences the stellar rotation rate is proposed in the X-wind model, where the magnetic field of the star interacts with the disc close to the corotation radius. This causes an exchange of mass and angular momentum, triggering an outward wind. This model was first proposed with a dipolar field (Ostriker & Shu, 1995), but has since been observed on objects with complex magnetic fields (Mohanty & Shu, 2008).

Accretion may also assist in the arresting the momentum of the star by losing a proportion of the angular momentum through accretion driven stellar winds. In Matt & Pudritz (2008), it was determined that for the outflow spin-down torque to balance with the accretion spin-up torque, the outflow must contain ten percent of the mass accretion rate. This proportion is generally considered unlikely, and therefore alternative systems are expected to assist in the dispersal of angular momentum, such as magnetospheric ejections.

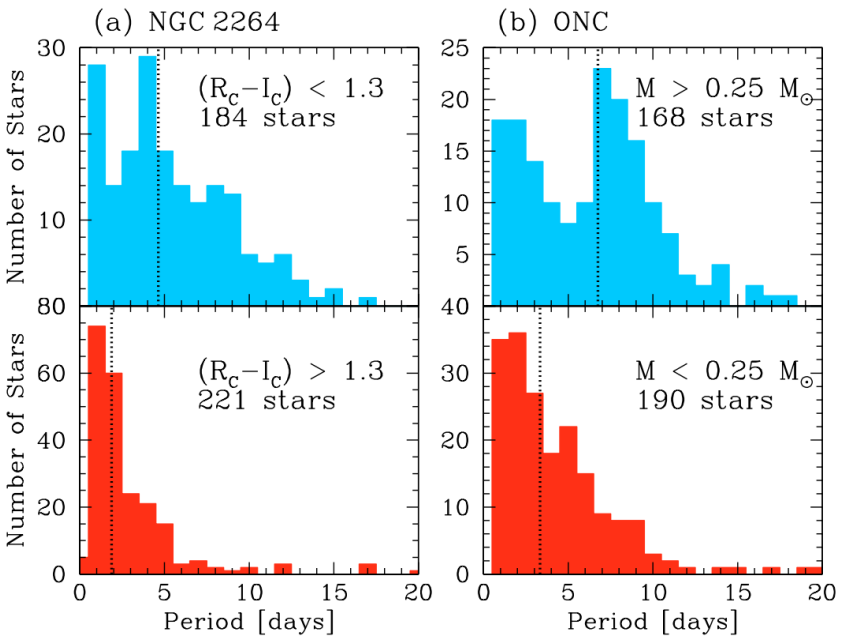

Figure 2.7: The rotation period distribution in NGC 2264 identified in Lamm et al. (2005) and the ONC identified in Herbst et al. (2001, 2002). Vertical lines indicate the median in each sample. Figure 3 taken from Lamm et al. (2005).

2.4.2 Rotation period distribution in young clusters

In the context of this thesis, we are interested in the inner disc environment and therefore star-disc interactions. The most significant evidence for disc-braking arresting the stellar momentum is the rotation period distribution in young clusters. A bimodal distribution of periods in young clusters has been well established in numerous studies (e.g. Edwards et al., 1993; Herbst et al., 2001; Lamm et al., 2005). A selection of stellar populations are discussed in this section, focusing on young (< 10 Myr) clusters. The period distributions of stars in NGC 2264 and the ONC are presented in Fig. 2.7. A bimodal distribution split into fast and slow rotators can be explained by disc-braking slowing the rotation rate, and then once the star-disc connection is released the star spins up to a fast rotation rate. There are very few objects with a moderate rotation rate, which indicates that the spin-up process occurs over a short timescale. In NGC 2264 the fast and slow distributions are separated at $P \sim 2$ d (Lamm et al., 2005), while for the younger ONC the separation is at $P \sim 5$ d (Herbst et al., 2001, 2002).

It is clear that objects with discs in general have slower rotation rates that stars without discs. However, rarely it is possible for disc-bearing objects to be released from disc braking and begin to spin up. Rebull et al. (2006) related IRAC colour excess at [3.6μm] - [8μm] as a disc indicator to rotation rates in the ONC, although these wavelengths are less than 10 μm this could be described as an inner disc indicator. The region showed a clear bimodal distribution for the periods separating populations of fast and slow rotators at $P \sim 1.8$ d. Slow rotators preferentially showed disc excess, especially for objects over 0.25$M_{\odot}$. The rotation periods of very low mass objects (as shown in the bottom two panels of Fig. 2.7) is the subject of its own study, see Section 4.2 in Hernández et al. (2007) for a review.

According to disc-braking theory during the accretion phase of the YSO's life, it will have a stable rotation rate. However, simulations have shown that the model for disc-braking is overly simplistic. In order to effectively arrest the rotation rate the magnetic field must be dipolar with strength in the order of kG (Gallet et al., 2019), leading to a positive correlation between the dipolar component and rotation rate (e.g. Johnstone et al., 2014). As discussed in Section 2.3.1, a YSO will form a radiative core which weakens the dipolar component of the magnetic field. The timescale is dependent on mass, with a 2 $M_{\odot}$ object taking around around 0.5 Myr to devlop a radiative core while a 0.5 $M_{\odot}$ object takes nearly 10 Myr. An object that has formed a radiative core, will have more complex magnetic fields and the dipole component will not be sufficient to slow the rotation rate. In this way, a star can be accreting via complex magnetic field lines but not be slowed by disc-braking. It has also been observed that the region of the disc that is magnetically linked to the star is likely very small, largely limited to the corotation radius (Zanni & Ferreira, 2013).

As we have seen, many CTTS have complex magnetic fields that are supporting accretion. An example is TW Hya, which has been observed to be in the process of spinning up as the dipole weakens (Donati et al., 2011b). In the 2 – 4 Myr σ Ori cluster accreting objects are almost exclusively slow rotators which aligns with expectations for disc-braking. Non-accretors cover a wide range of rotational periods (Scholz & Eislöffel, 2004). However, in the 4 Myr Tr 37 region, there were no statistically significant changes between the rotational distribution of accreting and

non-accreting objects (Sicilia-Aguilar et al., 2006). It is therefore not so clear-cut that accreting objects have slowed rotation rates, and non-accreting stars do not.

Finally, it is generally assumed that CTTS are fully convective and rotate as a solid body, and therefore will not show any differential rotation. Once a radiative core develops and the internal structure becomes layered, the rotation causes shearing between the core and envelope. This core-envelope decoupling has been observed in older, open clusters such as Praesepe (~ 630 Myr) (Cao et al., 2023) but has also been assumed to contribute to the rotation period distribution in older clusters, such as ~ 13 Myr cluster h Per (Moraux et al., 2013).

2.5 Photometric variability

YSOs were first identified due to their variability (Joy, 1945). The strong magnetic fields and highly variable accretion patterns present variability over a wide range of timescales and amplitudes. Figure 2.8, taken from Fischer et al. (2023), presents an overview of various "flavours" of YSO variability. In blue are accretion related events, red refers to extinction related events, and yellow refers to stellar phenomena. We will explore these categories in this section.

2.5.1 Accretion variability

Accretion related events cause some of the most extreme variability on the order of several magnitudes. An FU Ori outburst is an accretion event during which up to 0.01 $M_{\odot}$is accreted in a 100 yr timescale (Audard et al., 2014). The prototypical FU Ori outburst occurred in 1936-37, during which its B-band luminosity increased by 6 mag (e.g. McLaughlin, 1945; Herbig, 1977). FU Ori outbursts increase luminosity by 5 – 6 mag over > 1 yr and decrease over 10 – 100 yr. During an FU Ori event, the normal magnetospheric accretion of the star completely collapses. The majority of the luminosity of the outburst arises from the disc (Hartmann & Kenyon, 1996). EXpr (named from the star EX Lup) events are another kind of episodic accretion. These outbursts of 3 – 5 mag last for months, and sometimes reoccur periodically or quasi-periodically every few years. During an EXor event, the spectra show features similar to T Tauri stars with unusually high magnetospheric accretion (e.g. Lorenzetti et al., 2009). Recently, it has been demonstrated that not

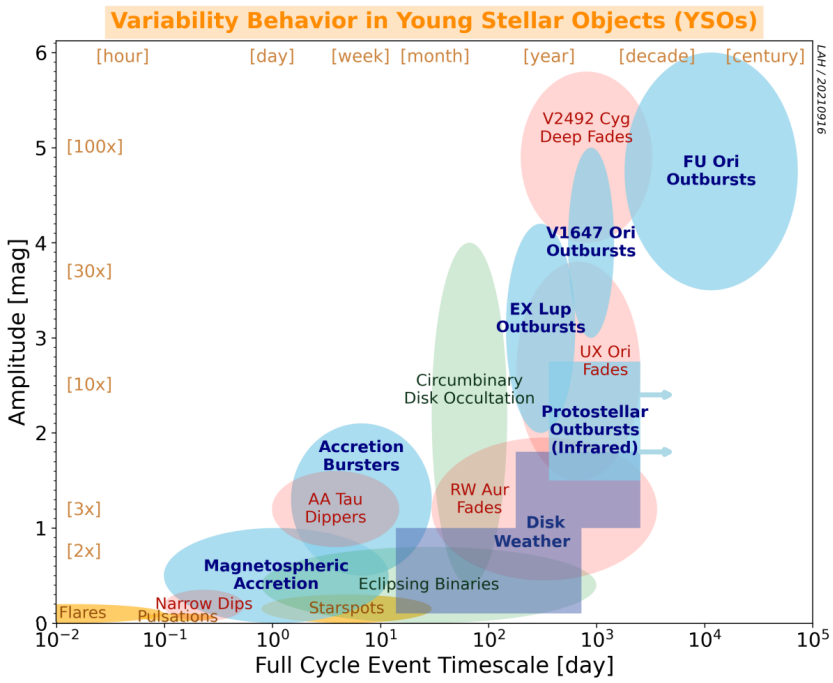

Figure 2.8: Amplitude versus timescale for various kinds of YSO variability. Taken from Fischer et al. (2023)

.

all apparent FU Ori or EXor type outbursts show their prototypical spectroscopic signatures. An intermediate stage of V1647 Ori outburst is named to define outbursts which have characteristics between EXor and FU Ori type outbursts (Audard et al., 2014).

In order to address the luminosity problem, YSOs must undergo some kind of episodic accretion (Kenyon et al., 1990). However, it is an open question whether these episodic accretion events are distinct or form a continuum. Additionally, small scale bursts due to variable accretion with durations of less than a year and less than a few magnitudes are also observed on accreting YSOs (Stauffer et al., 2014).

2.5.2 Circumstellar extinction

When we generally consider extinction, we consider interstellar reddening and obscuration by interstellar clouds, however YSOs are surrounded by dust in their discs which can cause extinction. From Section 2.2.1 the circumstellar disc that surrounds TTS is comprised of mixed dust and gas

in a flared shape. Warps or prominences in the disc may rotate in-front of and occult the star. These prominences can occur periodically or aperiodically. In the case of the periodic occultations, the radius of the warp determines the period. Assuming Keplerian rotation, the radius of rotating material is given by Equation 2.2.

$$r_c = \left(\frac{P_{kep}}{2\pi}\right)^{\frac{2}{3}} (GM_\star)^{\frac{1}{3}} . \tag{2.2}$$

Inner disc warps, or prominences close to the corotation radius cause occultations with a period near the rotation period. The prototypical object for this kind of behaviour is AA Tau (Bouvier et al., 1999). AA Tau has periodic dimming of ≈1.4 mag in the B-, V-, R-, and I-bands caused by a warped inner disc, which periodically rotates into the line of sight of the star. The dimming is approximately achromatic, implying that the dust grains causing the extinction are over 1 μm in size. As we have discussed in Section 2.2.1, dust grains that are less than 10 μm are coupled with the gas in the disc with larger grains settling towards the midplane.

Several AA Tau type objects have since been observed presenting high amplitude (1 – 2 mag), periodic dimming events e.g. Rodriguez et al. (2015); McGinnis et al. (2015); Evitts et al. (2020).

2.5.3 Stellar phenomena

YSOs are active, rapidly rotating stars with strong magnetic fields which have intrinsic variability. This thesis will examine rotational modulation due to spots on the surface of YSOs. We will examine the causes and our current understanding of spots in Section 2.6. Here, we focus on the photometric variability. YSOs with surface spots that are either warmer or cooler than the photosphere cause periodic brightness changes on the timescale of the rotation period, assuming the spot rotates in and out of the observer's line of sight. This rotational modulation has been used extensively as a direct measure of the rotation period (e.g. Rydgren & Vrba, 1983; Bouvier et al., 1986). The amplitude of variation depends on the nature of the spot, but is typically 0.1 – 0.8 mag (e.g. Strassmeier, 2009).

Rotational modulation relies on spots rotating in and out of the line of sight. In this way, polar

spots do not cause the flux to modulate. The flux is modulated by asymmetries in the surface spots with respect to the axis of rotation. Figure 2.9, taken from Luger et al. (2021) demonstrates that for a series of stars (orientated at 60° inclination; the geometric median), identical flux modulation in a single filter can be produced by 1 – 6 spots on a stellar surface. Luger et al. (2021) also demonstrates that the rotational modulation caused by an single equatorial spot is identical to the rotational modulation of a star with both an equatorial spot and a polar spot with half the temperature contrast. This degeneracy effectively highlights the need for multi filter observations to establish any spot properties from photometry.

While spots are the focus of this work, it is worth mentioning briefly that YSOs also display other forms of intrinsic variability. High cadence observations with TESS have allowed for detections of high frequency pulsations in young stars. Young δ Scuti stars (1.5 – 3.5 $M_{\odot}$) have been observed with pulsations of ~ 0.01 mag with $P \approx 0.05$ d (e.g. Bedding et al., 2020; Kirmizitas et al., 2022). Additionally, flares last on the order of hours to a few days, and mainly produce X-ray variability as a consequence of the temperatures on the order of 10^7 K (e.g. Vargas-González et al., 2023).

2.6 Surface spots

2.6.1 Cold spots

Cold surface star spots are generally considered analogous to sunspots. They are caused by magnetic fields looping out of the surface of the star, causing a local cooling. This cool region appears dark on the photosphere. While not strictly analogous, sunspots provide a detailed, well studied example.

The number of sunspots on the surface of the Sun follows an 11-year cycle. In Hale et al. (1919), George Ellery Hale used observations of sunspots to demonstrate the Sun's bipolar magnetic field. Around 60 percent of sunspots appear in pairs, with the two spots of opposing polarity. The polarity of the leading spot is the same across all spot-pairs in the hemisphere, and is opposite to the leading spots of the other hemisphere. The magnetic field reverses direction between

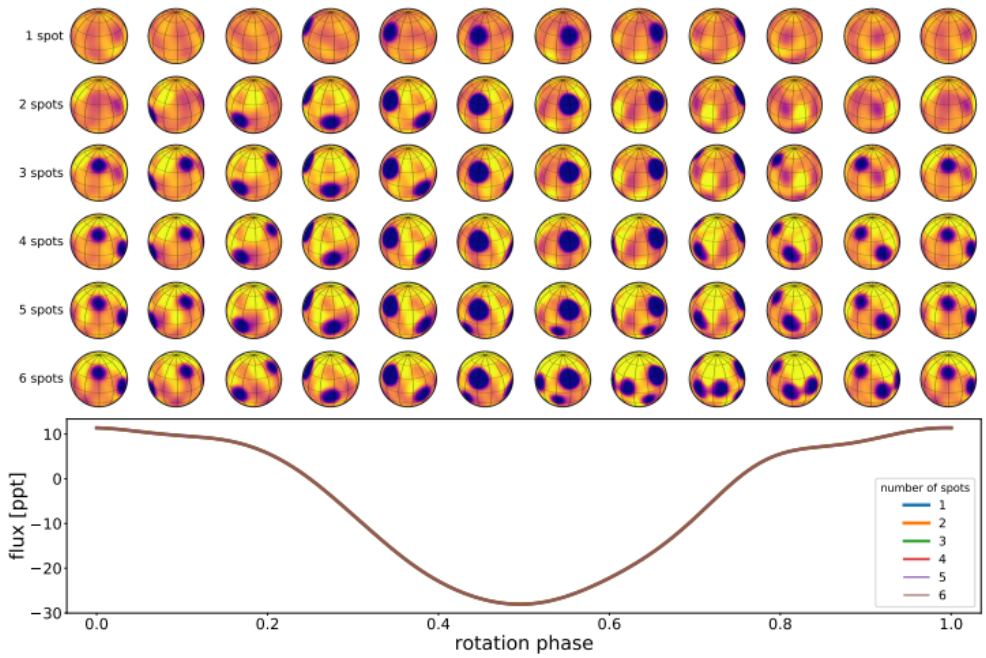

Figure 2.9: Constructed light curve from a stellar surface with 1 – 6 spots. All at inclination 60°, and using the same colour scale. Taken from Luger et al. (2021).

solar cycles, and so the leading spot takes the opposite polarity in the following cycle. Although we now understand that not all sunspots follow this pattern, approximately 8 percent of spots are 'anti-Hale' (Li, 2018).

At solar minimum, spots preferentially appear at higher latitudes (30 – 45°) while at solar maximum they appear at lower latitudes ($\sim$15°) and migrate towards the equator as the cycle approaches solar maximum. The lifetime of sunspots is proportional to their size, with larger sunspots surviving on the order of months. Sunspots are not uniform dark regions, as seen in Fig. 2.10. The central umbra is typically 1000 – 1900 K cooler than the photosphere, this is surrounded by the preumbra which is 250 – 400 K below the photosphere (Solanki, 2003). A review of archival data determined that the penumbra to umbra ratio oscillated between 5 – 8 between 1900 and 1976 (Hathaway, 2013).

Small sunspots are more common than large spots, with spot size as a fraction of the solar hemisphere ranging from a few 10^{-6} to 10^{-3} (Baumann & Solanki, 2005). At solar maximum, the sunspot number increases and total coverage is 0.002 – 0.005 (Penza et al., 2021). The luminosity

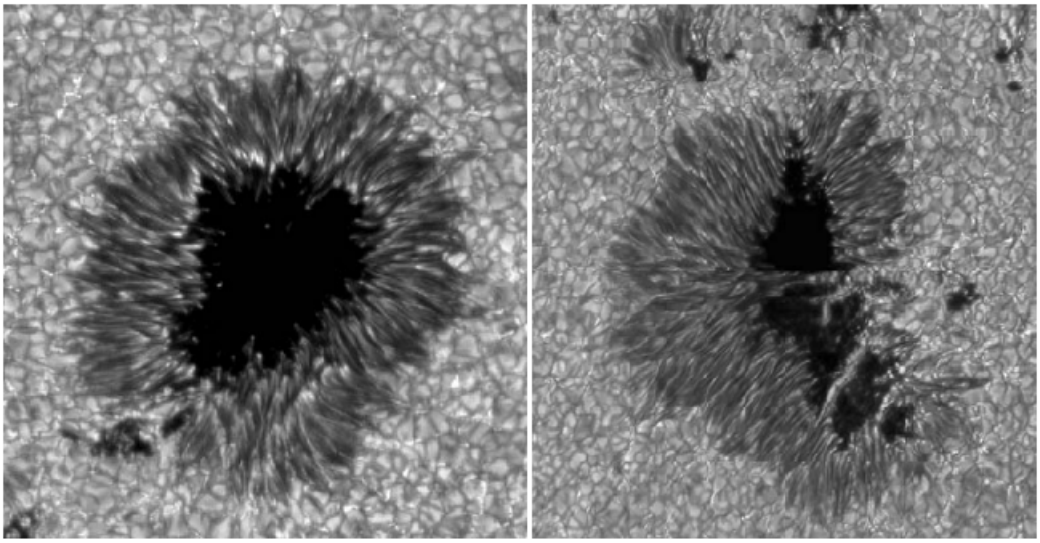

Figure 2.10: Examples of sunspots, showing the dark umbra and surrounding preumbra. Figure 1.1 from Solanki (2003).

change caused by sunspots between solar minimum and solar maximum is ≈ 0.1 percent (e.g. Kopp et al., 2016).

Of these findings, which are applicable to cold spots on young stars? Young stars have extremely strong magnetic fields to the order of a few kG (Johns-Krull, 2007), three orders of magnitude above the solar magnetic field (Babcock, 1961). It is therefore unsurprising that the CTTS host large spots that cover much larger surface fractions. Star spot coverage is expected to decrease with age (Morris et al., 2020). A significant proportion of cool spot measurements are on WTTS, which having ceased accretion and dissipated disc have few forms of variability. This allows for very 'clean' light curves where rotational modulation due to spots can be observed. While the spot distribution of the Sun follows the 11-year cycle, similar cycles have not been observed in YSOs thus far.

Multi filter photometry has been used to study the properties of spots for decades. The COYOTES campaign (Bouvier et al., 1993, 1995) used ground based observatories to monitor TTS in the Taurus-Auriga cloud in the U, B, V, R, I filters. Implementing a flux replacement model with black body spectra, the campaign identified cool spots on the surface of WTTS, alongside cool and hot spots on the surface of CTTS. Near infrared variability in J, H, and K was shown to caused by

spots in 55 – 77 percent of ONC objects in Carpenter et al. (2001). More recently light curves taken in U, B, V, R from WTTS in Taurus have been used to identify cool spots that are 500 – 1400 K below the stellar surface, covering 30 – 90 percent of the visible hemisphere (Grankin et al., 2008).

A limitation of broad band photometry is that when spots cover more than half the stellar surface, distinguishing between the stellar surface and the spots becomes challenging. Therefore, rotational modulation in emission lines is often used in conjunction with photometry and other methods. In Gully-Santiago et al. (2017) demonstrated that networks of cool spots covered 80 percent of the visible surface of WTTS LkCa4, using broad band photometry and low-resolution spectra. The corresponding V-band peak-to-peak amplitude was 0.6 mag, with the spot coverage filling factor varying between 67 percent at peak brightness, and 83 percent at minimum brightness. In the R-band the modulation was only 0.15 – 0.2 mag.

Direct imaging of surface spots is possible with Doppler imaging (Strassmeier, 2002; Strassmeier et al., 2003) and ZDI (Donati & Landstreet, 2009). Figure 2.11 presents surface brightness reconstructions from Doppler imaging and ZDI, the objects are orientated 'pole-on' and the equator is marked as a bold line. Figure 2.11 (left) shows the results from Doppler imaging of the WTTS V410 Tau from Hatzes (1995). These results were generated without photometry, but an unrelated concurrent study (Rice & Strassmeier, 1996) produced very similar results using both Doppler imaging and photometry. The middle panel of TW Hya shows a large polar dark spot (Donati et al., 2011b). This map is generated from the same observations used to reconstruct the accretion field lines in Fig. 2.6 (middle), however the spot was also observed two years prior. There are asymmetries which produce rotational modulation, although the photometric variability is dominated by other forms of variability as TW Hya is an active accretor. The final example in Fig. 2.11 is the WTTS LkCa4 (Donati et al., 2014). The ZDI map presented here was used in the analysis of the object in Gully-Santiago et al. (2017), which concluded 80 percent spot coverage. However, in Donati et al. (2014) the surface features were found to have 25 percent coverage, split between a cool polar spot and bright region. We will examine these bright regions in more detail in Section 2.6.2. It is worth noting that while ZDI is precise and very useful for detecting polar

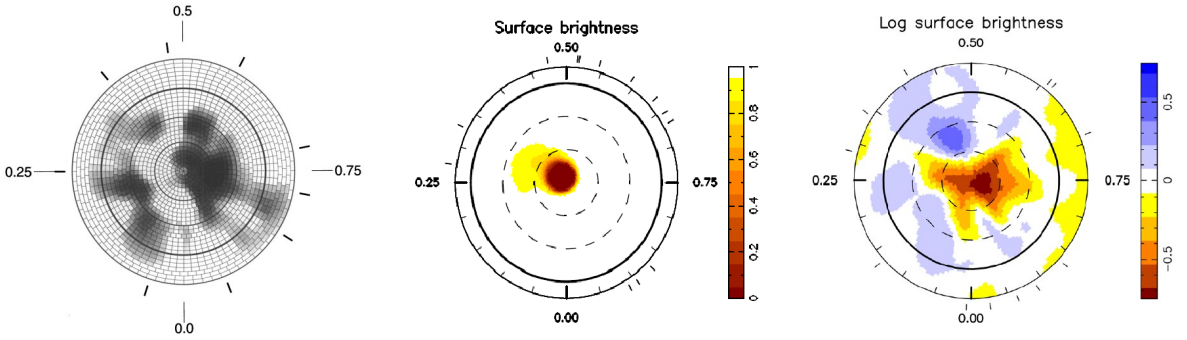

Figure 2.11: Surface brightness maps of three objects, orientated 'pole-on' the equator is marked as a bold line. **Left:** Doppler imaging brightness reconstruction of V410 Tau taken from Hatzes (1995). **Middle:** ZDI brightness reconstruction of TW Hya, taken from Donati et al. (2011b) **Right:** ZDI brightness reconstruction of LkCa4, taken from Donati et al. (2014).

features, it is only sensitive to large brightness features, so conclusions are generally considered the lower limit for coverage.

2.6.2 Hot spots

Accretion based hot spots

As discussed in Section 2.3.1 the shock of incident accretion columns heats the photosphere to 8000 – 10000 K, with coverage fraction of 0.001 – 0.01. This hot spot causes a significant contribution to the photometry as well as the addition of emission lines.

In more recent works, the assumption that accretion based hot spots have high temperatures and very small surface coverage have been demonstrated to be an incomplete picture. In Scholz et al. (2009, 2012); Bozhinova et al. (2016) hot spots were measured to be only a few hundred degrees above the stellar surface, and shows coverage values over 40 percent. In Ingleby et al. (2013), surface filling factors of accretion columns were identified for 13 nearby TTS, most had surface coverage less than one percent. However, one object was an outlier with 37 percent coverage, attributed to less dense accretion columns. In Espaillat et al. (2021), the extended low density portion of the accretion column on TTS GM Aur was found to dominate the photometry in the optical.

Key to the study of accretion columns is the study of emission lines. Emission lines such as H_α, H_β, Ca II and He I are used as indicators of accretion, alongside many metallic neutral and ionised lines (Muzerolle et al., 2003). Emission lines require specific temperatures and hence conclusions can be made about the accretion flow and the accretion shock. The emission lines of EX Lupi in quiescence and in outburst are compared in Sicilia-Aguilar et al. (2012). The observed He II line require temperatures around 15 000 K, while the Fe I: Fe II line ratio places an upper limit of the temperature at around 7000 K. It was therefore concluded that these lines are produced in different parts of the accretion column, with He II originating in the hottest part of the flow and the metallic lines arising from the cooler, less dense parts of the post-shock region. Dupree et al. (2012) tracks an accretion event on TW Hya with continuous spectroscopic and photometric observations. The observations highlight hourly changes between the accretion shock and photospheric and coronal heating, which contribute to the variation in the line emission profile.

The rotation of the star also affects the emission line profiles, being blue-shifted then red-shifted as the star rotates towards and away from the observer. The strength of the modulation depends on the height of the line-producing region from the surface, reinforcing the 3D structure of the accretion column. This method called emission line tomography (Sicilia-Aguilar et al., 2015; Campbell-White et al., 2021) establishes good constraints for the properties (position, temperature) of the line-emission region.

In order to produce rotational modulation over multiple cycles, the accretion column must be stable over this timescale. The accretion flow has the potential to be highly variable on the timescale of hours to days, which leads to stochastic variability rather than periodic variability. Manara et al. (2021) found changes in the accretion rates on the timescale of a few days. Figure 2.12 from Romanova et al. (2008) presents MHD simulations of a stable and an unstable accretion regime and the resulting light curves from the inner portion of the system. The instability in this case is not due to higher order fields but Rayleigh-Taylor instabilities in the disc.

High-cadence photometry from CoRoT and Spitzer was used to characterise the variability of 162 disc-bearing members of NGC 2264 (Cody et al., 2014). True periodicity (rotational modula-

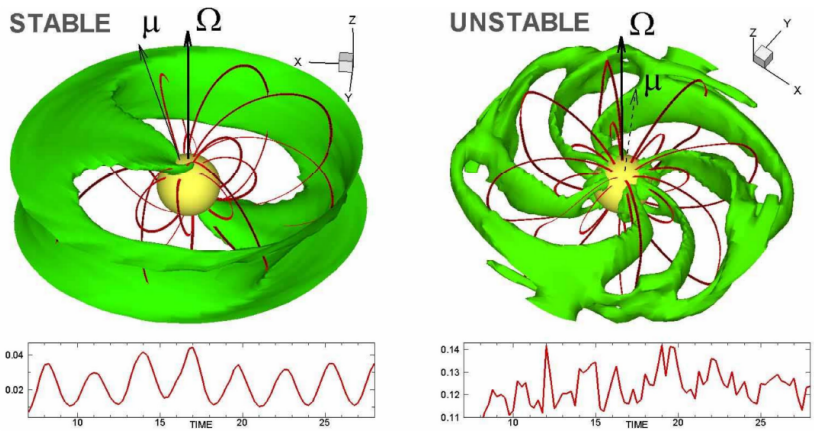

Figure 2.12: Simulation of stable and unstable accretion and the resulting light curves. Taken from Romanova et al. (2008)

tion over ∼40 d) was rare in the sample with four accretors presenting rotational modulation, with far more objects showing quasi-periodicity (Stauffer et al., 2014). Cody et al. (2014) also observed aperiodic bursting variability, which aligned with expectations for an unstable accretion regime established by Romanova et al. (2008).

The stable accretion columns of EX Lup and TW Hya were traced with emission line tomography, and compared with their photometric variability in Sicilia-Aguilar et al. (2023). In both cases, physical separation was observed between the hot regions dominating the photometric variability and the line emitting regions at the accretion columns. The hot regions were generally less than 1500 K above the stellar temperature, and had surface coverage values between 10 – 80 percent of the visible surface. The hot regions varied position relative to the accretion flows, and it was concluded that they were separate structures.

Plages as bright regions

Hot spots have also been observed on young stars that show no evidence of accretion, but are relatively less studied. Chromospheric warm regions known as plages have been extensively studied on active late-type stars such as LQ Hya (Strassmeier et al., 1993; Zhang et al., 2014) and RS CVn binaries (Frasca et al., 2008). These stars also show significant star spot activity, with spots and

plages spatially associated. Ingleby et al. (2013) showed that WTTS had increased chromospheric activity by a factor of three when compared to dwarf stars of the same spectral type. Therefore, it is possible that TTS show similar chromospheric plages.

Distinct from chromospheric plages are photospheric plages[1]. Photospheric plages are bright regions, as observed with ZDI brightness reconstruction. These are typically less than ten percent (Donati et al., 2014, 2017), although ZDI brightness reconstruction does only provide a lower limit for the coverage. In Fig. 2.11 (right) shows the bright regions observed on LkCa Donati et al. (2014). The reconstructed brightness maps from ZDI agree with photometric observations taken 1 – 4 months prior, implying that plages can last at minimum for this timescale.

Warm regions were identified through multi filter photometry on the WTTS V1598 Cyg (Froebrich et al., 2020). Plages add more flux than cool spots, and therefore should be well measured by analysing the rotational modulation with multi filter photometry. This is particularly true for WTTS which do not have photometry dominated by accretion.

2.7 Hunting Outbursting Young Stars

2.7.1 Project overview

This thesis is based on photometry taken as part of the HOYS citizen science project (Froebrich et al., 2018). In this project, a combination of amateur, university, and professional telescopes are used to monitor the brightness of stars in 25 nearby, young clusters and star forming regions (see Section 2.7.2). The project was designed to observe outbursting behaviour of young stars, such as FU Ori or EX Lupi type outbursts. To increase the science potential with high cadence observations, the aim is to measure the brightness of all stars in optical broad band filters every 12 to 24 hours.

The project now has over 100 telescopes in the network, the majority of which are amateur astronomers. The project has collected over 115 000 images, which corresponds to over 390 mil-

[1]Solar physics uses the term ‘plage’ for chromospheric bright regions, while others use plage to refer to a photospheric bright region.

lion magnitude measurements. This is equivalent to around 2000 hours of exposure time on a 1 m^2 telescope, demonstrating the effectiveness of utilising smaller telescopes. The sampling of each region is inhomogeneous due to several overlapping reasons. Firstly, all ground based data is subject to the inclement weather. HOYS does not require perfect weather conditions, accepting observations through thin cloud. Secondly, HOYS participants are not obligated to follow an observing schedule, rather they observe at-will, and then the data is collected for inclusion in the project. Finally, within each region the sampling is different due to equipment differences. Brighter objects are better sampled because the majority of observers will be able to image them, whereas fainter objects are limited to those with larger set ups or ideal conditions. The same is true for objects further from the centre of the field, some set ups are optimised for faint object with a narrow field of view (FOV) whereas some are designed for breadth rather than depth.

2.7.2 HOYS targets

HOYS monitors 25 nearby ($d < 1$ kpc) young (< 10 Myr) clusters and star forming regions. Nearby clusters were chosen so the majority of objects are observable with small telescopes, and they were selected as less than 10 Myr to increase the chances of observing outbursting behaviour alongside other forms of variability on TTS.

The HOYS target list of regularly observed clusters and star forming regions is: NGC 1333, IC 348, λ Ori cluster, M42, L 1641 N, σ Ori cluster, NGC 2068, NGC 2244, NGC 2264, MWSC 3274, P Cyg, Berkeley 86, IC 5070, IC 1396 A, IC 1396 B, NGC 7129, IC 5146, and FSR 408. Additionally, fields surrounding seven currently variable objects from the Gaia alert list[2] are also HOYS targets. These are fields surrounding: V898 Ori, YY Ori, ASASSN-13db, V555 Ori, Gaia 17 bpi, Gaia 19 fct, and Gaia 19 eyy.

The methodology and many of the results in this thesis will focus on the star forming region of IC 5070, also known as the Pelican Nebula. Together with NGC 7000 (North America Nebula) it is part of the large HII region W 80. The distance to the main cluster of YSOs in the region has been measured as 795 pc by Kuhn et al. (2020). The same authors identified a population of 395

[2]http://gsaweb.ast.cam.ac.uk/alerts/alertsindex

young stars in the region belonging to six different dynamic groups. Most of the YSOs are about 1 Myr old, and almost all of them have an age of less than 3 Myr.

2.7.3 Calibration of HOYS Data

The photometry pipeline is laid out in Froebrich et al. (2018), and the methodology used for colour correction is published in Evitts et al. (2020), both are summarised here.

HOYS participants upload dark, bias and flat-field corrected FITS images of target regions to the project website alongside the measurement equipment information. The FITS header contains the exposure information. The `astrometry.net` (Hogg et al., 2008) software is used to plate solve the astrometry of each image.

Aperture photometry is conducted in `Source-Extractor` (Bertin & Arnouts, 1996). The photometry in all images is calibrated against a deep reference frame in the u, B, V, R_C, and I_C filters. For targets visible in the northern hemisphere, the u-band reference frames was taken from the Thüringer Landessterwarte observatory[3], and the B, V, R_C, and I_C frames were taken at the Beacon Observatory at the University of Kent. The reference images for southern targets in all filters were obtained by the ROAD (Remote Observatory Atacama Desert) telescope (Hambsch, 2012). Calibration off-sets from instrumental to apparent magnitudes for the reference frames have been determined from the Cambridge Photometric Calibration Server[4].

$$f(m^i) = A \cdot \log(10^{B\cdot(m^i - C)} + 1) + P_4(m^i) \tag{2.3}$$

The calibration off-sets from a HOYS image to the reference frame are dependent on magnitude, and are determined by first calculating the difference between the instrumental and reference frame magnitudes. Then, a least-squares optimisation is conducted, comparing this difference to instrumental magnitudes in order to fit the eight parameters for Equation 2.3, which combined a photocurve function developed by Bacher et al. (2005) from Moffat (1969) with a fourth-order polynomial $P_4(m^i)$ in order to minimise the difference between the fitted magnitudes $f(m^i)$ and

[3] http://www.tls-tautenburg.de/TLS/index.php?id=25&L=1

[4] `http://gsaweb.ast.cam.ac.uk/followup`

the reference magnitudes. The results of Equation 2.3 is then taken as the calibrated magnitudes. The calibration is visually confirmed for all images. The resulting accuracy is within a few percent for brighter stars, and around 0.2 mag for stars below 15th magnitude.

Many of the HOYS images are taken in slightly different filters, such as the once used in DSLR cameras by some amateurs. Using these filters introduces colour terms in the photometry. Evitts et al. (2020) developed a procedure to correct these, which we detail here.

The non-variable stars in each field are identified, and the known colours and magnitudes are used to determine the colour terms for each image. These are then used to colour-correct the photometry.

To identify non-variable stars in each region, first the images with the maximum number of accurately measured and calibrated magnitudes in each of V, R and I filters are matched between the three filters to create a list of stars for the region. For stars with at least 100 data points in V, R and I the photometry in U, B, V, R, I, and H_α is extracted. To measure the variability of stars in the source list, we determine the Stetson index ($\mathcal{I}$) as definined in Welch & Stetson (1993). A star is classed as non-variable and therefore useful for calibration if $\mathcal{I} < 0.1$ in V, R and I. The median magnitudes and colours in all filters for the non-variable stars are then used as reference magnitudes.

In order to correct for systematic offsets due to colour, we define a function $\mathcal{W}_N(m, c)$ using a second-order polynomial $\mathcal{P}^2$ for each image, N,

$$\mathcal{W}_N(m, c) = p_0 + \mathcal{P}^2(m) + \mathcal{P}^2(c) \tag{2.4}$$

where p_0 is the offset, m is the calibrated magnitude in a chosen filter λ, and c is any $\lambda_1 - \lambda_2$ colour of the star. The colour term filters do not have to be the magnitude that is being calibrated $V - I$ is used as default. From the non-variable stars, any object is removed which has over 0.5 mag difference between the measurement in the image and the reference magnitude and has an uncertainty above 0.2 mag.

The calibration continues if the image contains at least ten stars identified as non-variable. The

five parameters of Equation 2.4 are then fitted using least squares optimisation. The fit is weighted against the fainter stars, which always outnumber the bright non-variable stars in the image.

The colour-corrected magnitude of a star is then calculated using the determined parameters, and the colour $\lambda_1 - \lambda_2$. The median magnitudes in λ_1 and λ_2 for the star over ± 5 d of the image are used to calculate the colour. The uncertainty is then defined as the RMS scatter of the magnitude offsets. When applied to a light curve of V1490 Cyg in Evitts et al. (2020) the result is that around 80 percent of magnitudes had less than 0.04 mag uncertainties, with median magnitudes in B, V, R and I of 0.02 mag.

3

Methodology

This chapter explains the methodology developed for identifying rotational modulation of YSOs in HOYS data. The majority of this work was published by the thesis author Herbert et al. (2023). The method for period identification was developed and published in Froebrich et al. (2021), which lists the thesis author as a contributor.

3.1 Periodic YSO identification

3.1.1 Period identification study

The core of this thesis is identifying brightness changes caused by surface spots. A cool spot 'in-front' will dim the star, whereas a hot spot will cause brightening. The star rotates causing modulation of the brightness. If the modulation approximates to a sinusoidal wave, then the change is the difference between the top of the peak and bottom of the trough, and therefore twice the amplitude of the sine wave. However, since only the peak and trough of the amplitude is considered, the shape of the light curve between these points is irrelevant. Spot distribution from light curve shape analysis is outside the scope of this thesis. The absolute difference in brightness is referred to as the peak-to-peak amplitude. In order to determine how the brightness changes with the rotation of the star, we start by determining the period of rotation.

HOYS data is inhomogeneously sampled and like all ground based data will produce a peak at $\sim$1 d due to the observational cadence. Identifying periodic variables in this style of data presents some challenges. Froebrich et al. (2021) conducted a double blind study to determine the optimum methods to identify periods in HOYS data. The data used for this study from high cadence photometry of IC 5070 taken over 80 day in the summer of 2018 (JD = 2458330 – 2458410), where the region was the focus of a campaign with HOYS observers. In the region 8548 stars were identified and HOYS data in U, B, V, R and I filters were extracted. Of these 6063 stars had at least 50 data points in at least one filter in this time period. The majority of these stars were not IC 5070 cluster members as no selections were made prior to searching for periodicity. The contaminants were either foreground stars or background giants.

Nine different period finding algorithms were evaluated to identify periodic variables. Two were commonly used methods, the Lombe-Scargle periodogram (LS) (Scargle, 1982) and the generalised Lombe-Scargle periodogram (GLS) (Zechmeister & Kürster, 2009), four were regression based from sine/cosine models which used either least squares regression or absolute deviation to determine the coefficients of the models (e.g. Liang et al., 2009), two utilised regression from fitting

B-splines with four knots (e.g. Akerlof et al., 1994), and the final method used both B-splines and sine/cosine least squares regression. The details and discussion can be found in Derezea (2023).

Candidate periods were identified for an object if the period was identified in two filters within two percent, and both periods had periodogram powers over 0.2. This corresponds to a typical False Alarm Probability (FAP) below 0.1 percent. Phase folded diagrams in all available filters covering one period were then presented blind to experienced co-authors, who decided whether a periodic signal was present. The features of the light curves between filters were compared to confirm the legitimacy of the period. In this way, 59 periodic variables were identified.

The proportion of 59 periodic variable sources identified by each method were used to evaluate the completeness and contamination for each method. The completeness is the fraction of the final list identified by each method, and the contamination is the fraction of periodic candidates that did not meet the standard for the final list. It was determined that a combination of four methods would provide optimal completeness. These were the GLS and three regression models named L1Boot, L1Beta, and L2Beta. The L1 models use absolute deviation optimisation, where L2 uses least squares. The 'Boot' and 'Beta' refer to the method used to obtain the critical value, above which a period is considered valid. This value is either obtained through bootstrapping the periodogram or by a hypothesis test based on a Beta distribution (Thieler et al., 2013).

The purpose of this study was primarily to evaluate period finding algorithms. Hence, all sources in the region were searched for periodicity. The sample of 59 objects also contained foreground and background objects that are not members of IC 5070. Using data from GaiaEDR3 40 YSOs were selected based on parallax $0.9 < p < 1.5$ mas, and proper motion selections in right ascension and declination of $-5 < \mu_\alpha < 0$ mas/yr and $-5 < \mu_\delta < -1$ mas/yr. Identifying YSOs based solely on kinematics does not allow for potential biases caused by sample selections based on IR colours, where cluster members that are either earlier or further in their evolution can be excluded.

3.1.2 Sample definition

The sample of periodic YSOs in IC 5070 defined in Froebrich et al. (2021) is used as the YSO sample to develop the methodology in this work. As we will see in Section 3.3 spot fitting analysis requires peak-to-peak measured amplitudes in at least three different filters, V, R and I. This leaves 31 objects for investigation, which will be referred to throughout as the F21 sample. Of those, 24 also include B and 5 have all amplitudes from U to I. Nine sources of the original sample have measurements only in R and I. As an example, the phase folded light curve for object 8038 is displayed in Fig. 3.1. The stellar properties of the sample will be examined in Section 4.1.

3.2 Peak-to-peak amplitudes

3.2.1 Amplitude determination

With the periods established for 31 YSOs, we now are able to measure the peak-to-peak amplitudes. The periods determined in Froebrich et al. (2021) were used to phase fold the photometry in each filter. A running median in phase space was determined, smoothed over 0.1 in phase, overplotted in Fig. 3.1. This smoothing includes on average 27 photometric data points from the typically 270 brightness measurements that are available in each filter per source. The peak-to-peak amplitude was determined as the difference between the minimum and maximum magnitude of the smoothed running median. These are denoted as $\hat{A}^o_\lambda$, where 'o' indicates these refer to the observed values and λ indicates the filter used.

The associated uncertainties $\sigma\left(\hat{A}^o_\lambda\right)$ are determined from the standard uncertainty of the mean of all photometric data points included in the determination of the minimum and maximum position of the running median. The investigated objects (ID numbers taken from Froebrich et al. 2021), their right ascension and declination, periods, amplitudes, and uncertainties are listed in Table 3.1.

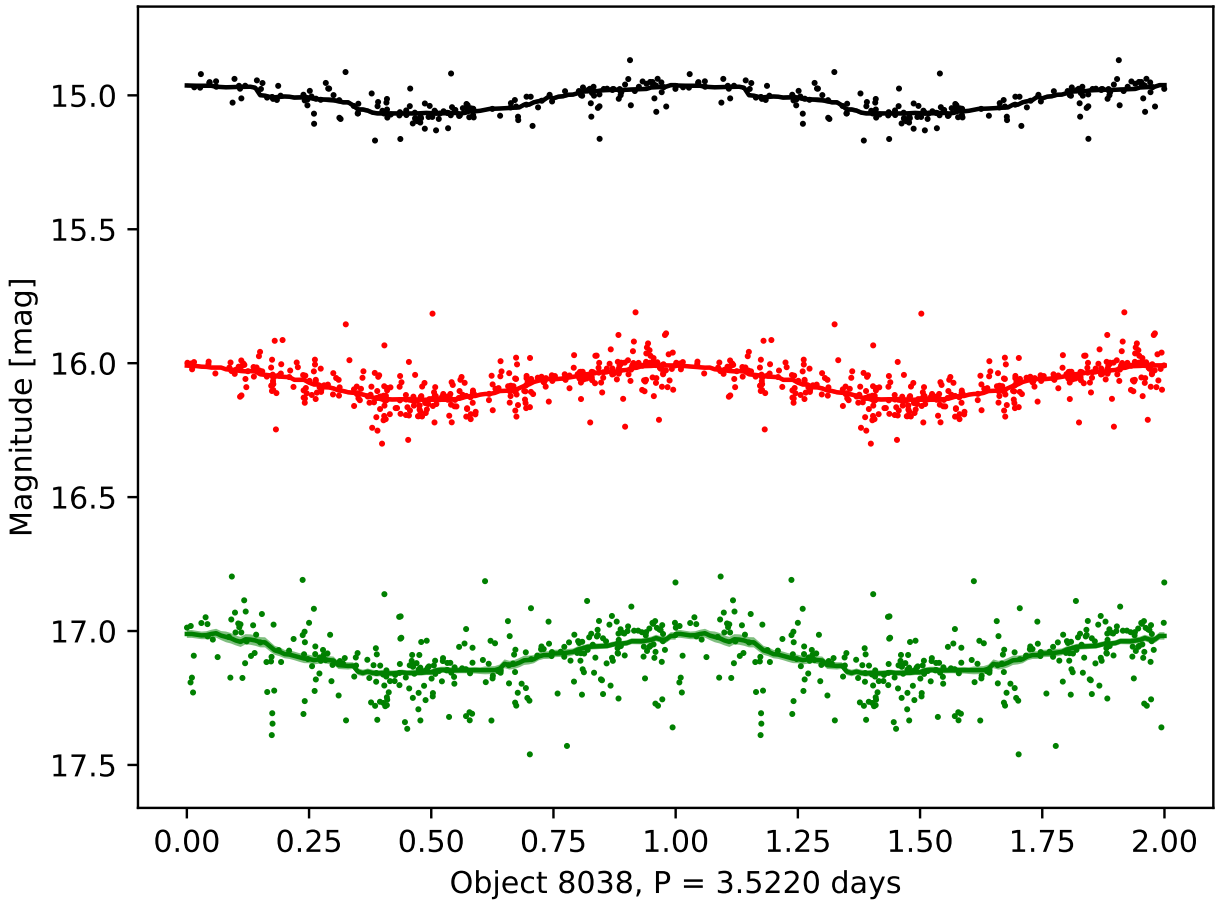

Figure 3.1: The phase folded light curve of object 8038 in V (green), R (red), and I (black) filters covering two periods. Over-plotted is the running median and uncertainty.

Table 3.1: Target list of all YSOs investigate in the F21 sample of YSOs in IC 5070. Listed for each object are the ID number, the J2000 coordinates, the period, as well as the peak-to-peak amplitudes and uncertainties measured in the phase folded light curves. [(1)] from Froebrich et al. (2021).

ID[(1)]	RA	DEC	Period[(1)]	$\hat{A}_I^o$	$\sigma\left(\hat{A}_I^o\right)$	$\hat{A}_R^o$	$\sigma\left(\hat{A}_R^o\right)$	$\hat{A}_V^o$	$\sigma\left(\hat{A}_V^o\right)$	$\hat{A}_B^o$	$\sigma\left(\hat{A}_B^o\right)$	$\hat{A}_U^o$	$\sigma\left(\hat{A}_U^o\right)$
	[deg]	[deg]	[d]	[mag]	[mag]	[mag]	[mag]	[mag]	[mag]	[mag]	[mag]	[mag]	[mag]
3220	313.37768	44.69840	0.866	0.052	0.012	0.057	0.017	0.089	0.022	-	-	-	-
3988	312.72581	44.63562	9.438	0.277	0.036	0.283	0.030	0.381	0.051	0.338	0.068	-	-
4097	313.25278	44.61654	1.683	0.061	0.012	0.077	0.019	0.075	0.037	-	-	-	-
4446	313.10924	44.57396	1.433	0.081	0.018	0.094	0.017	0.080	0.024	0.113	0.050	-	-
4766	312.75374	44.53048	6.602	0.667	0.046	0.606	0.032	0.817	0.041	1.066	0.080	-	-
5535	312.83745	44.43877	3.862	0.233	0.020	0.230	0.016	0.258	0.016	0.282	0.029	0.536	0.221
5548	312.99661	44.42881	4.157	0.047	0.012	0.063	0.012	0.071	0.016	0.075	0.026	-	-
5559	312.93711	44.43862	3.759	0.157	0.030	0.201	0.026	0.213	0.034	0.282	0.060	-	-
5575	313.41700	44.43060	1.390	0.053	0.015	0.086	0.028	0.104	0.047	-	-	-	-
5886	312.12005	44.40321	9.041	0.080	0.025	0.137	0.047	0.159	0.082	-	-	-	-
6060	312.81885	44.38279	2.427	0.075	0.018	0.104	0.012	0.116	0.012	0.130	0.016	0.181	0.073
6149	312.94395	44.37257	2.176	0.179	0.023	0.222	0.022	0.257	0.029	0.306	0.098	-	-
6259	312.77765	44.36132	1.398	0.095	0.020	0.107	0.014	0.112	0.014	0.119	0.021	-	-
6315	313.07439	44.35443	3.223	0.114	0.038	0.141	0.030	0.178	0.079	-	-	-	-
6337	312.84446	44.35212	3.911	0.313	0.028	0.290	0.024	0.296	0.025	0.308	0.054	-	-
6393	313.35269	44.34279	2.773	0.158	0.029	0.194	0.047	0.277	0.074	-	-	-	-
6813	312.81307	44.30490	4.167	0.091	0.022	0.143	0.021	0.165	0.022	0.250	0.054	-	-
6861	313.04822	44.29854	3.522	0.111	0.024	0.132	0.019	0.139	0.025	0.144	0.044	-	-
6929	312.74460	44.29190	7.276	0.122	0.017	0.144	0.016	0.166	0.017	0.177	0.040	-	-
7181	312.75654	44.26168	7.338	0.158	0.018	0.175	0.015	0.196	0.016	0.174	0.027	-	-
7422	312.74312	44.24232	4.901	0.058	0.017	0.059	0.010	0.066	0.011	0.082	0.015	0.144	0.079
7465	313.14529	44.23348	10.573	0.126	0.024	0.162	0.019	0.226	0.026	0.231	0.054	-	-
7472	313.09386	44.23339	3.049	0.120	0.026	0.147	0.019	0.181	0.026	0.199	0.043	-	-
7632	312.82600	44.21895	7.853	0.229	0.019	0.281	0.014	0.312	0.016	0.331	0.027	-	-
7954	313.35736	44.17926	1.449	0.103	0.030	0.128	0.047	0.194	0.067	-	-	-	-
8025	312.45491	44.17952	3.313	0.342	0.022	0.444	0.019	0.484	0.024	0.575	0.047	-	-
8038	312.78141	44.17628	3.522	0.095	0.020	0.118	0.017	0.140	0.024	0.157	0.047	-	-
8249	312.76358	44.15360	7.880	0.067	0.019	0.092	0.017	0.103	0.023	0.076	0.036	-	-
9267	312.87064	44.07309	4.830	0.133	0.010	0.137	0.009	0.141	0.006	0.157	0.006	0.132	0.018
9321	312.87737	44.06251	3.166	0.174	0.017	0.214	0.014	0.248	0.016	0.304	0.021	0.266	0.083
9961	313.09561	44.01582	3.625	0.053	0.019	0.062	0.017	0.050	0.023	0.073	0.046	-	-

3.2.2 A note on notation

Our data of the YSOs, i.e. the measured peak-to-peak amplitudes, have been obtained in multiple filters. In the analysis these measurements are compared with the model calculations for different sub-samples (sets) of amplitudes. These amplitude sets hence refer to the same model or observation in different filters. Although any combination of filters can be used, the filters here are used strictly sequentially from short to long wavelengths. The minimum data requirement for inclusion in the dataset are peak-to-peak amplitudes $\hat{A}_V$, $\hat{A}_R$, and $\hat{A}_I$. The notation used hereafter for such a set is $\hat{A}_{\{V\}}$, where V denotes the shortest wavelength filter included in a dataset. In this way $\hat{A}_{\{U\}} = \{\hat{A}_U, \hat{A}_B, \hat{A}_V, \hat{A}_R, \hat{A}_I\}$. A superscript when present refers to the origin of the amplitude, such as observed $\hat{A}^o_{\{\lambda\}}$ in Section 3.2.1.

3.3 Fundamentals of flux replacement

In the previous section, we have established the observed changes in brightness created as a spotted star rotates. We now consider how that is modelled.

It is assumed that the young stars investigated here have one dominant spot that is rotating completely in and out of line-of-sight. Therefore, the peak-to-peak brightness change is the difference between the spotted surface and the un-spotted surface. Flux replacement modelling has been used extensively to determine spot properties (e.g. Bouvier et al., 1993, 1995; Carpenter et al., 2001). However, here it is applied simultaneously to a multi-filter data set, atmospheric models are used as opposed to black body emission, and a full error treatment allows for accurate determination of reliability and accuracy.

This is a very simplified model, as we have seen in Section 2.6 these objects show complicat ed features. We assume a smooth stellar surface with a single effective temperature and a single uniform spot with a fixed temperature which covers a fraction of the visible stellar surface. By considering a single uniform spot, we model the dominant properties of the asymmetric component of the spot distribution. Additionally this approach considers the stellar surface to be otherwise uniform, and does not consider limb darkening. Limb darkening causes a systematic reduction in

the stellar flux, that would lead to an underestimation in spot size in the order of a few percent. This is significantly smaller than our statistical uncertainties. It is beyond the purpose of this work to model the shape of the phase-folded light curves to infer the spot latitude on the star and inclination of the stellar rotation axis. This would be influenced by limb darkening.

The ratio of the flux from the un-spotted surface in a filter λ, and the flux from the spotted surface corresponds to the peak-to-peak amplitude of the variation. The geometry of the system is simplified as either considering the spot to be visible when 'in front' or not visible when 'behind'. The model peak-to-peak amplitude $\hat{A}^m_\lambda$ in each filter is therefore determined by Equation 3.1, where $T_\star$ is the temperature of the star, T_S is the temperature of the spot, and f is the fraction of the visible hemisphere.

$$\hat{A}^m_\lambda = \left| 2.5 \cdot \log \left(\frac{F^\lambda \left(T_\star \right)}{(1-f) \cdot F^\lambda \left(T_\star \right) + f \cdot F^\lambda (T_S)} \right) \right| \tag{3.1}$$

Two sets of synthetic stellar atmosphere spectra (PHOENIX (Husser et al., 2013) and ATLAS9 (Castelli & Kurucz, 2003)) have been used to determine the fluxes $F^\lambda(T)$. They have been accessed through the astropy `PySynphot` distribution (Lim et al., 2015). To obtain the fluxes for each filter, the `speclite.filters`[1] package has been used to convolve the atmospheric model spectra with transmission curves for U, B, V, R, and I.

The PHOENIX models (Husser et al., 2013) are a library of synthetic spectra for effective temperatures from 2000 K to 70000 K, metallicities [M/H] from -4.0 to $+5.0$ and surface gravities $\log(g)$ from 0.0 to 6.0. The `PySynphot` distribution uses models obtained in 2011, although in 2021 the grid was updated to models from Husser et al. (2013) for [M/H] = 0.0, with updates for the other metallicities planned. This update has an improved resolution, which makes it more suited for spectroscopic work. In this work they are convolved with broad band filters.

The ATLAS9 grid (Castelli & Kurucz, 2003) is an update to previous models published in Kurucz (1991). The grid covers effective temperatures from 3500 K to 50000 K, metallicities [M/H] from -2.5 to $+0.5$, and $\log(g)$ from 0.0 to 5.0. The lower temperature limit is above that

[1] `https://github.com/desihub/speclite/blob/master/speclite/filters.py`

of the PHOENIX models, and limits the application to cold spots on our YSOs as there is less parameter space below the stellar temperature.

The PHOENIX models and the ATLAS9 grid are compared in Husser et al. (2013). The relevant points of interest for this work are that the PHOENIX models were generated using solar abundances from Asplund et al. (2009), whereas the ATLAS9 grid used solar abundances from Grevesse & Sauval (1998). The two models take different approaches to convection, which affects the line profiles. PHOENIX uses a mixing length parameter (α) for macroturbulence varied according to temperature, following Böhm-Vitense (1958). The low temperatures used in this work have a mixing length parameter of α between 1.5 and 3. The ATLAS9 models use a constant value of α = 1.5, and adjust for non-convective overshooting below 7000 K. Pre-main sequence stars are fully convective until they reach sufficient mass to generate a radiative core.

The ATLAS9 grid is less well suited for our purpose than the PHOENIX models due to the 3500 K lower effective temperature limit. This does not enable the accurate determination of cold spot properties on low effective temperature objects. In developing the methodology the analysis was performed using both sets of models. The results for both model sets agree for the high effective temperature objects, showing the results do not depend on the stellar atmosphere model used. An example object is shown in the Appendix A.1. Unless stated otherwise, all analysis, discussion, and results presented in this work are obtained using the PHOENIX model stellar atmospheres.

3.4 Identification of the single best spot model

To match observed amplitudes to modelled spot properties, peak-to-peak amplitude sets were modelled following Equation 3.1. The initially investigated parameter space for the spot temperature is $2000\ \mathrm{K} \leq \mathrm{T_S} \leq 10000\ \mathrm{K}$ (PHOENIX) and $3500\ \mathrm{K} \leq \mathrm{T_S} \leq 10000\ \mathrm{K}$ (ATLAS9). The upper limit for temperature was later increased to 12000 K and 14000 K dependent on stellar temperature, this will be detailed in Section 7.3. For the spot coverage up to half the visible surface ($0 \leq f \leq 0.5$) is investigated.

Equation 3.1 requires a fixed stellar temperature to create a set of model amplitudes. Instead of creating model amplitudes sets $\hat{A}^m_{\{\lambda\}}$ using precise stellar temperatures, a range (initially 3800 K – 5500 K to align with the temperatures of the F21 sample examined in Section 4.1, and later increased to allow for higher stellar temperatures) was sampled every 50 K. This saves significant computing time as the same amplitude sets can be used for several objects. For each object the model set closest in effective temperature was used. In Section 3.6 we will see that this has no significant influence on the results.

For each stellar temperature, $\sim 10^6$ modelled amplitude sets were generated by homogeneously, randomly sampling the spot temperature and coverage ranges times for each stellar temperature. This corresponds to an average spacing in spot temperature of 10 K and 0.0005 in spot coverage.

Solar metallicity and $\log(g)$ = 4.0 were assumed throughout, which are reasonable values for YSOs in HOYS regions. The systematic uncertainties when altering these parameters are less than the statistical uncertainties of our procedure, described in more detail in Section 3.6.

Equation 3.2 is used to determine the separation between the observed amplitude $\hat{A}^o_{\{\lambda\}}$ and the modelled amplitude set $\hat{A}^m_{\{\lambda\}}$. There, N is the length of the filter set $\{\lambda\}$, i.e. $N = 3$ for $\{V\}$. The observed amplitudes $\hat{A}^o_{\{\lambda\}}$ are compared to each of the 10^6 modelled amplitude sets $\hat{A}^m_{\{\lambda\}}$. The model with the minimum $RMS_{\{\lambda\}}$ is the best fitting spot model for the observations.

$$RMS_{\{\lambda\}} = \sqrt{\frac{1}{N}\sum_{\{\lambda\}}\left(\hat{A}^o_\lambda - \hat{A}^m_\lambda\right)^2} \tag{3.2}$$

Presented in the top panel of Fig. 3.2 is a contour map of $RMS_{\{V\}}$ for the example object 8038 using $\hat{A}^m_{\{V\}}$ from the PHOENIX models. The model with the absolute minimum in $RMS_{\{V\}}$ is marked by a red triangle. The contour map shows two local minima in the regions above and below the stellar temperature. The lowest contours on both, the cold and warm spot regimes, roughly follow reciprocal lines between spot temperature and spot coverage, i.e. $(T_S - T_\star) \propto \pm 1/f$. The minimum in the cold spot region has a value around $RMS_{\{V\}} \approx 0.01$ mag, whereas the minimum value in the hot spot region is $RMS_{\{V\}} \approx 0.02$ mag. For the majority of objects, one minimum (hot or cold spot) is significantly deeper than the other.

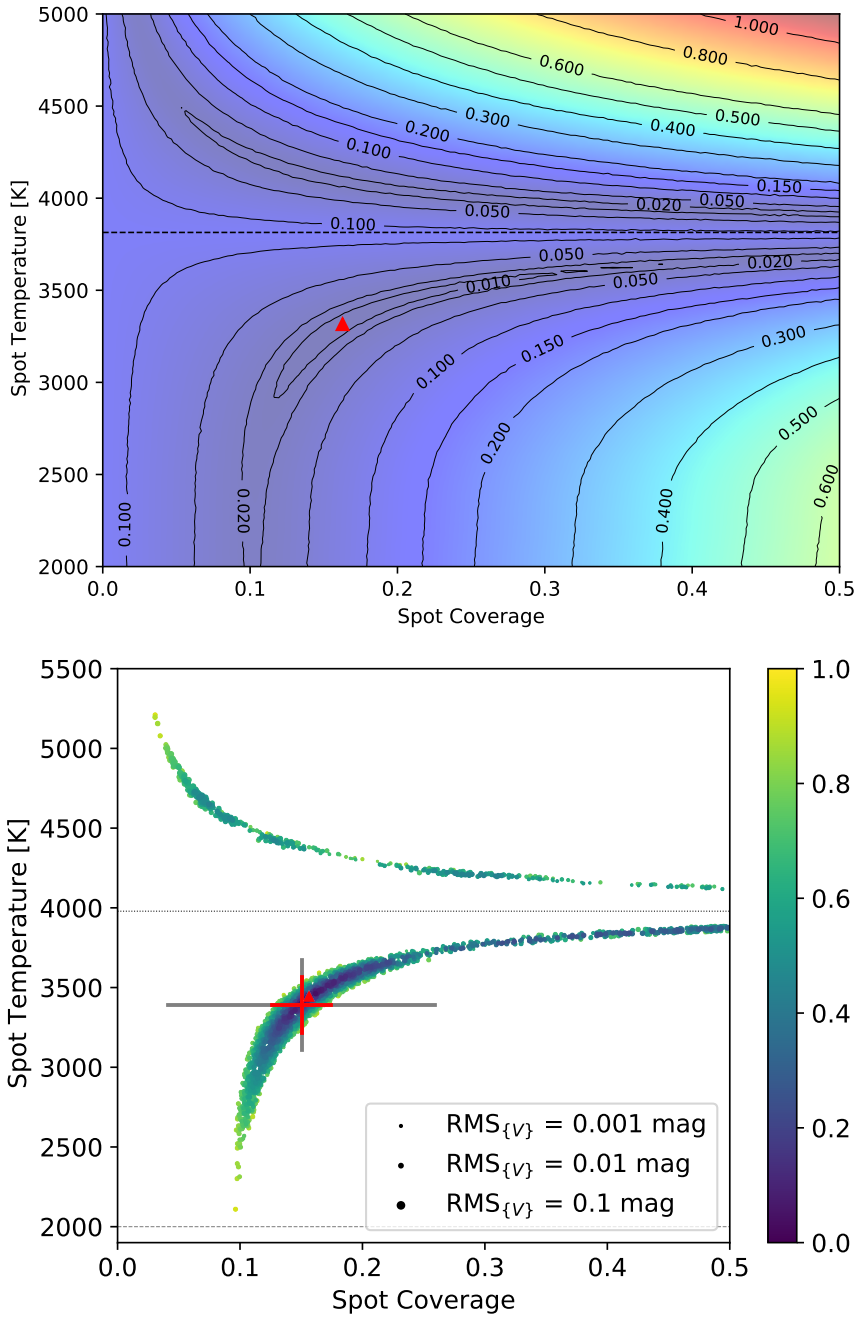

Figure 3.2: **Top:** Contour plot showing $RMS_{\{V\}}$ between the observed amplitudes $\hat{A}^{o}_{\{V\}}$ and the modelled amplitudes $\hat{A}^{m}_{\{V\}}$ for object 8038. A red triangle indicates the model with the absolute minimum $RMS_{\{V\}}$, i.e. the best fitting model. **Bottom:** The best fitting models for 10000 sets of varied amplitudes $\hat{A}^{v}_{\{V\}}$, for object 8038 varied within their associated uncertainties. The colour bar is the measure of the variation $RMS^{\sigma}_{\{\lambda\}}$ and the symbol size is inversely proportional to the minimum RMS. In this case $87.78\,\%$ of the resultant models are cold spots. Positioned on the median temperature and spot values, the grey cross is the standard deviation of cold spot solutions, and the red cross is the median absolute deviation for the cold spots. The red triangle is the best fitting model from the observed amplitudes. The dotted line indicates the stellar temperature, and the dashed line marks the minimum temperature available in the atmospheric models.

Values near the minimum $RMS_{\{\lambda\}}$ can cover a large area of the parameter space. In the case of object 8083 in Fig. 3.2, the $RMS_{\{V\}} \approx 0.01$ mag contour covers a range of about 500 K in spot temperature and 0.2 in coverage along the reciprocal. This equivocates to less than 0.5 percent of the investigated parameter space having $RMS_{\{V\}}$ below 0.1 mag. To estimate the uncertainties of the solution for the spot properties as well as to establish if the hot or cold spot solution dominates, the statistical uncertainties of the measured amplitudes need to be taken into account.

3.5 Spot property identification

3.5.1 Statistical uncertainty determination

The position of the absolute minimum of $RMS_{\{V\}}$ can be sensitive to small perturbations in the measured amplitudes, and is affected directly by the resolution of the model amplitude set. To consider the statistical uncertainties in the methodology the best model fitting was determined for amplitudes that are varied within their measurement uncertainties $\sigma\left(\hat{A}^o_\lambda\right)$, established in Section 3.2.1.

The observed amplitudes $\hat{A}^o_\lambda$ for each object were varied with a Gaussian distribution according to their associated uncertainties. This generates sets of varied amplitudes $\hat{A}^v_{\{\lambda\}}$. These variations are limited to those that are within 1σ of the measured amplitude in each filter. Our tests (outlined in Section 3.5.2) have shown that the values of the spot properties and their uncertainties stabilise after 3000 iterations or more. To create a robust measure 10000 iterations of $\hat{A}^v_{\{\lambda\}}$ within their 1σ uncertainties has been generated for all cases.

As the amplitude in each filter was varied independently, to determine the extent of the perturbation upon $\hat{A}^o_{\{\lambda\}}$, a measure $RMS^\sigma_{\{\lambda\}}$ is defined in Equation 3.3. A low value for $RMS^\sigma_{\{\lambda\}}$ indicates little variation. In cases where $RMS^\sigma_{\{\lambda\}}$ is close to one, each of the amplitudes in the set has been varied close to 1σ.

$$RMS^\sigma_{\{\lambda\}} = \sqrt{\frac{1}{N}\sum_\lambda \frac{\left(\hat{A}^o_\lambda - \hat{A}^v_\lambda\right)^2}{\sigma^2\left(\hat{A}^o_\lambda\right)}} \tag{3.3}$$

The best fitting spot properties for each $\hat{A}^v_{\{\lambda\}}$ were determined by identifying the minimum $RMS_{\{\lambda\}}$ between $\hat{A}^v_{\{\lambda\}}$ and $\hat{A}^m_{\{\lambda\}}$. The distribution of best fit spot properties from the 10000 sets of $\hat{A}^v_{\{\lambda\}}$ shows a clear trend towards cold or hot spots for the majority of targets. In a small number of cases, the best fit spots do not show a clear preference to hot or cold. To indicate cases where the solution is ambiguous, the ratio of hot to cold spot solutions HS:CS$_{\{\lambda\}}$ is determined. If the value is close to zero or one, the object is clearly a cold or hot spot, respectively. In cases where the ratio is close to 0.5, the solution is ambiguous. The ratio depends on the filter set used and the signal to noise ratio of the measured amplitudes.

Ideally, there would be a point in HS:CS$_{\{\lambda\}}$ at which the solution is defined and clearly unambiguous. However, as we will see in Section 4 the resultant values of HS:CS$_{\{\lambda\}}$ form a near-continuum. To remove results that are close to 50 percent HS:CS$_{\{\lambda\}}$, and hence cannot be definitively decided as either a hot or cold spot the ten percent on either side of 50 percent is classified as the ambiguous region, i.e. $0.4 <$ HS:CS$_{\{\lambda\}} < 0.6$. Spot properties in this region are removed from statistical analysis. The HS:CS$_{\{\lambda\}}$ is therefore generally presented alongside spot properties as an indicator of reliability. We will examine parameters that affect the HS:CS$_{\{\lambda\}}$ in Section 4.3.2.

The best fitting spot properties and their uncertainties are determined using only the results in the regime (hot or cold spot) which contains the minimum of 60 percent majority of best fitting spots. The median and median absolute deviation (MAD) of those were determined for the spot temperature and spot coverage, and their respective uncertainties. Figure 3.2 (bottom) shows the distribution of best models results for the 10000 iterations of $\hat{A}^v_{\{V\}}$ for object 8038. The object has HS:CS$_{\{V\}} = 0.1222$ (see Table 4.1). The model with the lowest $RMS_{\{V\}}$ from $\hat{A}^o_{\{V\}}$ is marked again as a red triangle. Figure 3.2 (right) also shows the standard deviation as a grey cross for comparison and the MAD as a red cross. The MAD is taken as the uncertainty measurement instead of the standard deviation because the spot temperature and spot coverage are correlated. Therefore, the standard deviation is not a good representation of the uncertainty. The MAD is always significantly smaller than the standard deviation, especially in spot coverage. The measure of dispersion $RMS^{\sigma}_{\{\lambda\}}$, indicated by the colour bar in the figure, shows that the $\hat{A}^v_{\{V\}}$ values that

have been varied less are grouped around the median. In this example, the hot spot solutions are produced by $\hat{A}^{v}_{\{V\}}$ with high $RMS^{\sigma}_{\{V\}}$.

3.5.2 Iteration reliability

In determining the statistical uncertainties of spot properties, the number of $\hat{A}^{v}_{\{\lambda\}}$ must be sufficient that the spot properties are stable within their associated uncertainties and that the value of HS:CS$_{\{\lambda\}}$ is stable. Figure 3.3 in the top two panels displays the median spot temperature and median spot coverage sampled every 20 iterations, alongside ten percent of their MAD uncertainties as a shaded area. The bottom panel of Fig. 3.3 shows the HS:CS$_{\{V\}}$ for object 8038, also sampled every 20 iterations. Again, the median and MAD uncertainties are calculated from the regime (hot or cold) that contains the majority of sampled iterations.

In this case, after $\sim$2000 iterations the spot properties are within ten percent of their MAD uncertainties. There is as upward trend in the median spot temperature and coverage value towards 3000 iterations. However, it is important to note that in Fig. 3.3 the iterations are not sorted according to any measure and therefore have random $RMS^{\sigma}_{\{\lambda\}}$. Iterations with higher $RMS^{\sigma}_{\{\lambda\}}$ are more likely result in spot properties further from the median spot property result, as seen in the bottom panel of Fig. 3.2. Therefore, if sorted or reordered, the shape of the black lines in Fig. 3.3 are altered. After $\sim$ 5000 iterations the spot properties are established and resistant to small changes.

Spots are classified as cold, hot, or ambiguous from their HS:CS$_{\{V\}}$ ratios therefore this ratio must be as robust as possible. The given HS:CS$_{\{V\}}$ ratio for this object is 0.1222 after 10000 iterations, the standard error on this value is ± 0.0033. Further iterations decrease the standard error by progressively smaller gains. To demonstrate this, 50000 iterations were generated for this object which provides HS:CS$_{\{V\}} = 0.1234 \pm 0.0015$. Using 50000 iterations is a minimal improvement in the reliability HS:CS$_{\{V\}}$ and no change in the spot property results. Hence, 10000 iterations are generated for all objects.

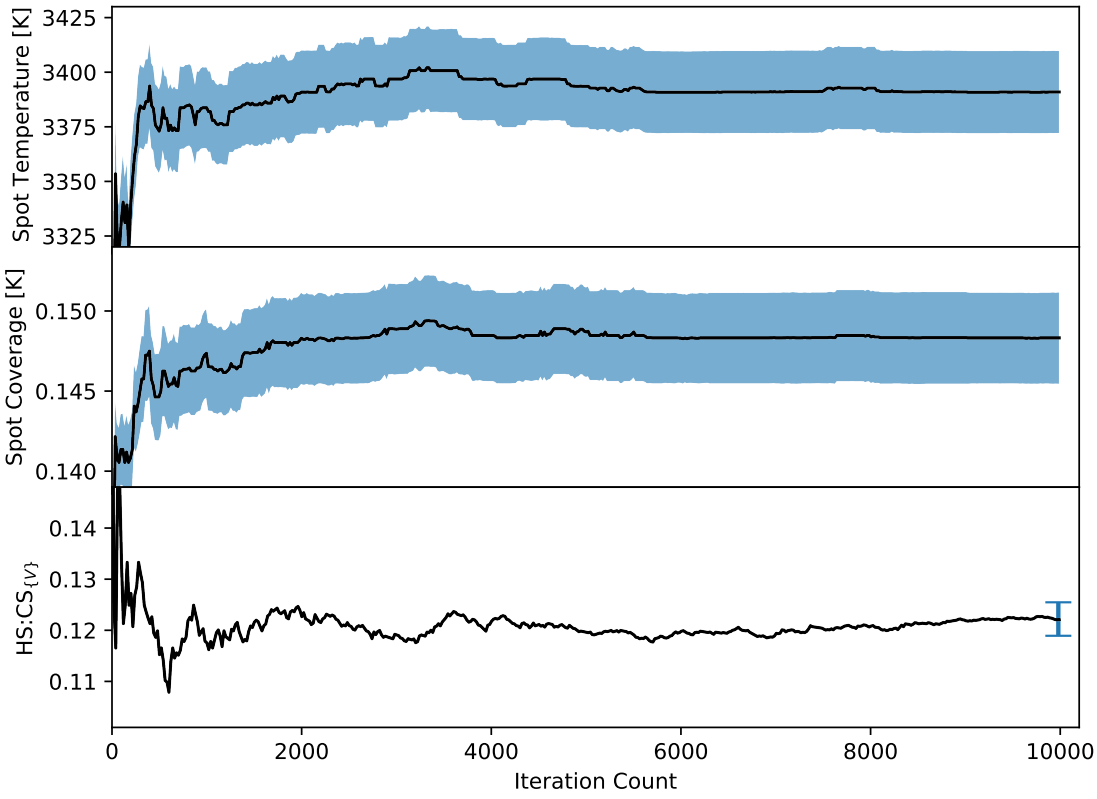

Figure 3.3: The spot temperature (top), coverage (middle) and HS:CS$_{\{V\}}$ (bottom) calculated from the majority of iterations of $\hat{A}^{v}_{\{V\}}$, sampled every 20 iterations. In the top two panels the shaded area shows ten percent of the MAD uncertainties. The standard error on HS:CS$_{\{V\}}$ after 10000 iterations is marked on the lower panel.

3.6 Systematic uncertainties of spot properties

In the previous sections we have established the methodology to infer spot properties and their statistical uncertainties from a set of peak-to-peak amplitudes. In this section we will investigate potential systematic uncertainties.

3.6.1 Changing the stellar properties

The modelled amplitudes $\hat{A}^m_{\{\lambda\}}$ are all calculated from one stellar atmosphere model, with a fixed stellar temperature, metallicity, and surface gravity. The assumption of solar metallicity and $\log(g) = 4.0$ is reasonable but not measured for all YSOs. As discussed in Section 3.3 $\hat{A}^m_{\{\lambda\}}$ is not modelled using the exact stellar temperature when the stellar temperature is known, and as we will see in Section 4.1 a stellar temperature reference is not always available. Therefore, the effects of altering these stellar parameters in the models was investigated individually to quantify their influence on the results.

A *simulated* spot is created which generates a set of $\hat{A}^s_{\{\lambda\}}$ amplitudes. They were generated for a star with $T_\star = 4000$ K, $\log(g) = 4$, [M/H] = 0.0 and for spot properties $T_S = 3200$ K and $f = 0.1$. These correspond to typical values for the F21 sample of YSOs, as shown in Section 4.2.1.

Alternative sets of $\hat{A}^m_{\{\lambda\}}$ were generated with one of the parameters ($T_\star, \log(g)$, [M/H]) adjusted and the rest kept at the original value. The $\log(g)$ was varied between $3.5 \leq \log(g) \leq 4.5$, and the metallicity between $-0.5 \leq$ [M/H] ≤ 0.5, both in steps of 0.5. The stellar temperature was varied from 3800 K to 4200 K in 100 K steps.

In the top panel of Fig. 3.4 we show the inferred spot parameters when we use the $\hat{A}^m_{\{V\}}$ set created with the different stellar parameters. The background contour in the figure is $RMS_{\{V\}}$ between $\hat{A}^s_{\{V\}}$ and $\hat{A}^m_{\{V\}}$ with the original stellar parameters. Following the procedure laid out in Section 3.5.1, we determine the best fitting spot parameters and the MAD uncertainties. For the latter we use the mean uncertainties of the amplitudes of the F21 YSO sample for the $\hat{A}^s_{\{\lambda\}}$ values.

Examining the changes in $\hat{A}^m_{\{\lambda\}}$ when altering metallicity and temperature, the changes are more significant as the wavelength decreased and hence $\hat{A}^m_U$ is the most changed. However, the

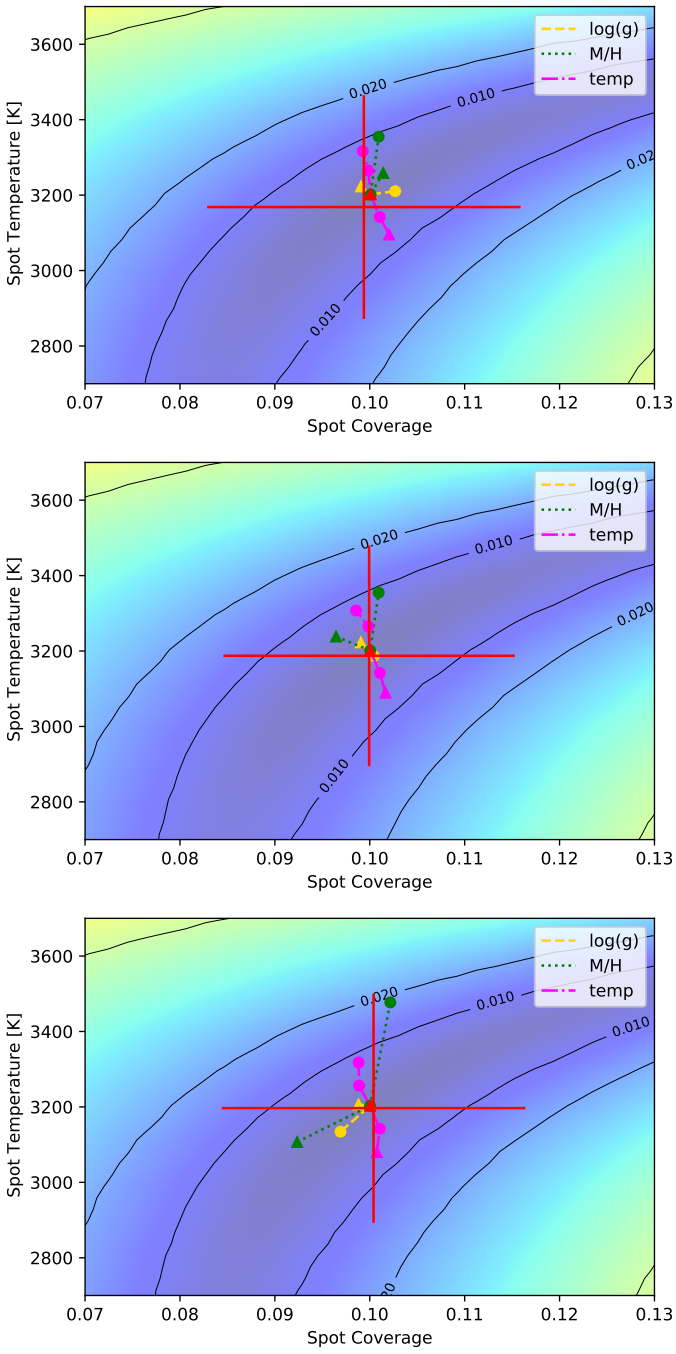

Figure 3.4: **Top:** Contour plot showing $RMS_{\{V\}}$ between $\hat{A}^s_{\{V\}}$ and $\hat{A}^m_{\{V\}}$ for a simulated spot with parameters $T_\star = 4000$K, $T_S = 3200$K and $f = 0.1$. The red triangle indicates the best fitting model with stellar parameters $T_\star = 4000$ K, $\log(\mathrm{g}) = 4.0$, and [M/H] = 0.0. The pink dash-dot track indicates the best models when 3800 K $\leq \mathrm{T}_\star \leq$ 4200 K, in 100 K steps. The green dotted track shows the best models when $-0.5 \leq$[M/H]≤ 0.5, in 0.5 steps. The yellow dashed track shows the best models when $3.5 \leq \log(g) \leq 4.5$, in 0.5 steps. The start of each track is marked by a triangle. The red cross indicates the MAD uncertainty - see text for details. **Middle:** As top panel but for $\hat{A}^s_{\{B\}}$. **Bottom:** As top panel but for $\hat{A}^s_{\{U\}}$.

amplitudes in all bands underwent some change. Altering $\log(g)$ affected all $\hat{A}^m_{\{V\}}$ equally, though to a lesser extent than $\hat{A}^m_B$ and $\hat{A}^m_U$. This was the case for both the ATLAS9 and PHOENIX atmosphere models.

For all available filter sets, altering the stellar parameters caused the best fitting model to change by less than the statistical uncertainties.

3.6.2 Effect of non-variable extinction

There are two kinds of extinction to consider with regards to YSOs. Firstly, there is potential extinction caused by the circumstellar disc which can vary with time producing 'dipper' light curves as introduced in Section 2.5.2. We will examine how these are identified in our data in Section 3.7. Secondly, there is non-variable extinction caused by the abundance of dust in SFRs, interstellar reddening, or a non-variable portion of the disc. We will discuss the possible effect of non-variable extinction here.

This methodology is based on Equation 3.1, which is dependent on peak-to-peak amplitudes that are unaffected by non-variable extinction. Interstellar dust causes objects to appear dimmer and redder. This affects the relative magnitude of an object, and is filter dependent, however extinction that is non-variable over time leaves the peak-to-peak amplitudes unaffected. The star and spot undergo the same interstellar reddening. Hence, the difference between the spotted surface and unspotted surface remains the same whether or not both surfaces have been reddened.

In the case of significant extinction, or dim objects, the signal to noise is not be sufficient to establish periodicity or generate an amplitude across all three filters required for spot fitting. Therefore, it is likely that many objects that have undergone heavy extinction are not identified in this work.

Interstellar reddening can significantly challenge the determination of the stellar temperature, which is a fixed parameter in Equation 3.1. In Section 3.6.1, we have demonstrated that the spot properties remain within their statistical uncertainties when the stellar temperature is adjusted by 400 K.

Section 4.1 details the stellar properties of the F21 sample of objects in IC 5070, which have been determined spectroscopically in Fang et al. (2020). Therefore, these temperatures can be considered reliable and non-variable extinction does not influence the results from this sample.

In Chapter 7, we apply this methodology to objects across all HOYS fields, for which we do not have effective temperature references available. For these objects, we define a function which uses survey colours to approximate stellar temperatures. This is explained and discussed in Section 7.3.

Non-variable extinction does not affect the peak-to-peak amplitudes used to determine spot properties. However, it has the potential to affect the stellar temperature which is a fixed parameter in Equation 3.1. By using spectroscopically identified reference temperatures where possible, this risk is mitigated. Due to this methodology's resilience to changing stellar properties, in order for the spot properties to be affected, the extinction would have to influence the stellar temperature determination by over 400 K.

3.6.3 Resultant simulated spot properties

We have seen in Section 3.6.1 that the statistical uncertainties are always larger than the potential systematic uncertainties from unknown exact stellar parameters. However, we have seen that there are small systematic shifts, even if they are smaller than the statistical uncertainties. We examine those systematic shifts here.

Stellar parameters $T_{\rm eff}$ = 4000 K as well as $\log(g) = 4.0$ and [M/H] = 0.0 are used again as a 'typical' object. Amplitude sets $\hat{A}^s_{\{\lambda\}}$ are created for simulated spots of different properties. Seven spot coverage values are used, $f = 0.05, 0.1, 0.15, 0.2, 0.3, 0.4, 0.5$ and for each of those, two sets of hot and cold spots are generated. One has a temperature difference of 400 K and one of 800 K compared to the stellar temperature, this is a 10% and 20% temperature contrast. For each of these 28 cases, the spot properties and MAD uncertainties are determined following the procedure laid out in Section 3.5.1. The average $\sigma\left(\hat{A}^o_\lambda\right)$ of the F21 sample is used to generate $\hat{A}^v_\lambda$ for the spot property uncertainty calculation.

In the top panel of Fig. 3.5 the resultant spot properties from $\hat{A}^s_{\{V\}}$ are compared with the spot

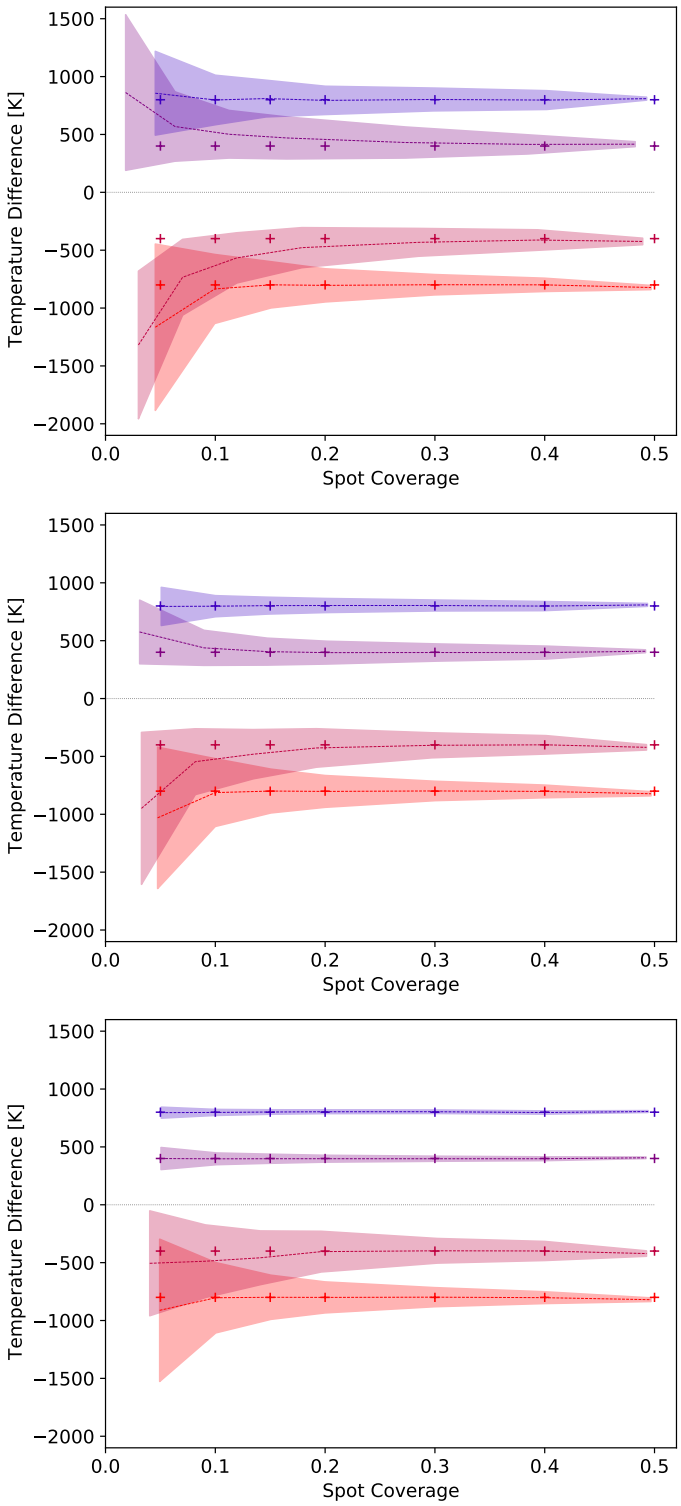

Figure 3.5: **Top:** The resultant spot properties and uncertainty in temperature (shaded area) for a series of amplitudes $\hat{A}^s_{\{V\}}$ for simulated spots. Crosses mark input spot values and circles the resultant properties using the PHOENIX models. The dashed lines connect the resultant spot properties for the same spot-star temperature difference. Crosses, lines, and shaded areas of the same colour have the same spot-star temperature difference. **Middle:** As top panel but for $\hat{A}^s_{\{B\}}$. **Bottom:** As top panel but for $\hat{A}^s_{\{U\}}$.

properties of the simulated spots. The crosses mark the input properties and circles the resultant values. The dashed lines connect the resultant spot temperatures for each of the four values of input temperature contrast between spot and star. The shaded areas indicate the MAD uncertainty in spot temperature. The uncertainties in coverage are not shown but are typically of the order of 0.035.

As one can see, the trend is to recover the spot as slightly smaller and further away from the stellar temperature compared to the input values. The spot temperature uncertainties increase systematically for smaller spot coverage values and also with decreasing temperature difference of spot and star. This is caused by the fact that the amplitudes for the smallest spots have very low signal-to-noise ratios (SNRs). The exception is the case for $f = 0.05, T_S = 3600$ K, where the temperature values cluster around the 2000 K limit of the PHOENIX models and thus artificially create small uncertainties.

3.6.4 Choice of filters

Early flux replacement works such as Bouvier et al. (1993, 1995) which utilised black body spectra concluded that the detection of hot spots required all broad band filters. The peak of the SED for an 8000 K spot is well past V-, R-, and I-bands. However, here we examine whether this remains the case with synthetic spectra and full uncertainty treatment.

The recovery of simulated spots has been repeated using $\hat{A}^s_{\{B\}}$ and $\hat{A}^s_{\{U\}}$ to test the effect of including shorter wavelength filters. The middle and bottom panel of Fig. 3.5 show the spot property measurements for amplitudes generated for the same simulated spots as in the top panel, but using $\hat{A}^s_{\{B\}}$ and $\hat{A}^s_{\{U\}}$.

The SNR of the amplitudes is a function of size and temperature contrast. The SNR in each filter for each input spot property value is shown in Table 3.2. Cool spots have a lower absolute flux, and warm spots contribute more in the shorter wavelengths. Consequently, a pair of cool and warm spots with the same size and absolute temperature contrast can produce dramatically different SNRs in the same filter.

Table 3.2: The signal-to-noise ratio of simulated spots in broad band filters. Generated using $T_\star = 4000$ K, $\log(g) = 4.0$, [M/H] = 0.0 and average uncertainties from the F21 sample of YSOs.

T_s [K]	f	SNR$_I$	SNR$_R$	SNR$_V$	SNR$_B$	SNR$_U$
3200	0.05	1.88	2.13	2.06	1.69	1.82
3200	0.10	3.82	4.36	4.21	3.46	3.71
3200	0.15	5.84	6.69	6.47	5.32	5.70
3200	0.20	7.93	9.13	8.84	7.27	7.78
3200	0.30	12.38	14.40	14.00	11.52	12.29
3200	0.40	17.23	20.29	19.80	16.30	17.33
3200	0.50	22.55	26.95	26.45	21.79	23.06
3600	0.05	1.07	1.43	1.42	1.20	1.21
3600	0.10	2.17	2.89	2.88	2.42	2.45
3600	0.15	3.29	4.40	4.39	3.70	3.73
3600	0.20	4.43	5.96	5.96	5.01	5.05
3600	0.30	6.79	9.23	9.25	7.79	7.83
3600	0.40	9.25	12.72	12.80	10.80	10.79
3600	0.50	11.83	16.48	16.65	14.07	13.99
4400	0.05	1.34	2.15	2.41	2.49	3.64
4400	0.10	2.64	4.22	4.70	4.82	6.98
4400	0.15	3.92	6.20	6.88	7.01	10.09
4400	0.2	5.16	8.11	8.96	9.09	12.98
4400	0.3	7.57	11.72	12.86	12.92	18.22
4400	0.4	9.88	15.09	16.45	16.40	22.89
4400	0.5	12.09	18.25	19.78	19.58	27.09
4800	0.05	3.11	4.87	6.07	7.08	14.31
4800	0.10	6.04	9.31	11.44	13.03	24.98
4800	0.15	8.83	13.38	16.24	18.17	33.49
4800	0.20	11.48	17.16	20.58	22.68	40.57
4800	0.30	16.43	23.95	28.21	30.35	51.93
4800	0.40	20.96	29.94	34.75	36.72	60.88
4800	0.50	25.14	35.29	40.48	42.16	68.25

Table 3.2 lists the SNRs for the simulated spots in all of the broad band filters, the noise is the mean uncertainty of amplitudes in each filter for the F21 sample. Spots with $T_S = 3600$ K do not produce a SNR above three in any filter for $f < 0.15$. Whereas for $T_S = 4400$ K which is the same absolute temperature difference, the SNR$_U$ is above three even in the smallest case ($f = 0.05$). The SED of 4400 K has a far larger contribution in the U-band than 3600 K. Spots with $T_S = 3200$ K have a SNR in all filters above three for $f > 0.1$.

Comparing the resultant spot properties from the simulated spot amplitude SNRs shown in Fig. 3.5, it can clearly be seen that SNR values above three produces results that are closer to the input properties.

The inclusion of the shorter wavelength data reduces the uncertainties in temperature and coverage significantly for hot spots. The accuracy and systematic off-sets for the recovery of the cold spots is almost not changed. The most significant differences caused by the inclusion of shorter wavelength filters comes in the $f = 0.05$ cases. The median result is much closer to the simulated spot properties, although there is an apparent increase in the temperature uncertainty for the smallest cool spots, but this is due to the models not clustering at the edge of the parameter space. This lack of improvement for the cold spots is understandable due to the temperatures of our 'typical' 4000 K YSO and simulated cold spots, whose spectral energy distribution peaks in the V, R, and I filter range.

3.7 Identification of non-spot contaminants

Periodic variability with light curves of similar appearance to spot modulation, can also be caused by other sources. The nature and selection of the F21 sample excludes non-YSO causes such as pulsations in giant stars. However, there remains the possibility of AA Tau type occulations (Section 2.5.2). AA Tau undergoes quasi-periodic dimming of ≈ 1.4 mag in B, V, R, and I due to a warp in the inner disc. To identify variability caused by such occultations in the YSO sample, the spot recovery method used to determine the systematic uncertainties with simulated spots in Section 3.6 is applied to amplitudes generated artificially according to various extinction laws.

Three models of extinction have been tested: $R_V = 3.1$ and $R_V = 5.0$ modelled from Mathis (1990), and grey extinction. The latter indicates equal extinction in all filters caused by large ($> 1\mu m$) dust grains or opaque material. Amplitudes in the different filters have been generated according to the three extinction models and the spot properties and uncertainties were calculated using the same method as laid out in Section 3.5.1 using $A^m_{\{V\}}$, the PHOENIX models, a stellar temperature of 4000 K, and the average associated uncertainties for the F21 YSO sample (0.02 – 0.03 mag, depending on the filter). The resultant spot properties for these extinction models are shown in Fig. 3.6. In Fig. 3.6 $\hat{A}_{\{V\}}$ is shown and the amplitudes in the visual filter are A_V = 0.05, 0.1, 0.2, 0.5, 0.8, 1.2, and 1.8 mag. For clarity in Fig. 3.6, only the data points that correspond to the solution (hot/cold spot) where the majority of the 10000 iterations fall are presented. For the gray extinction model, the HS:CS$_{\{V\}}$ is basically zero or one in all cases. The HS:CS$_{\{V\}}$ for the $R_V = 5.0$ simulation is close to 0.6 for V-band amplitudes below 0.2 mag and one for the others. None of these amplitudes recover spots which have an ambiguous solution with $0.4 <$ HS:CS$_{\{V\}} < 0.6$.

From Fig. 3.6 it is clear that for grey extinction the inferred spot temperatures cluster near the minimum temperature available, as long as the amplitudes are small (less than half a magnitude). For larger amplitudes, the properties cluster near the upper limit of the spot coverage investigated. The former is understandable as the grey extinction essentially blocks the same small fraction of light in all filters. This is equivalent to a small, completely black (T = 0 K) object transiting the star.

When the resulting spot fits cluster at the edge of the coverage/spot temperature parameter space the uncertainties (marked by red crosses in Fig. 3.6) are artificially reduced. The calculated uncertainties are the median absolute distribution of the spot fit properties from the majority of the varied amplitudes. When these resulting spot fits are clustered at the edge of the parameter space the spread is limited by the parameter space. Therefore, results at the edges of the parameter space are not trusted regardless of the size of their associated uncertainties.

The $R_V = 5.0$ and 3.1 reddening leads to solutions that are mimicking hot spots. The coverage

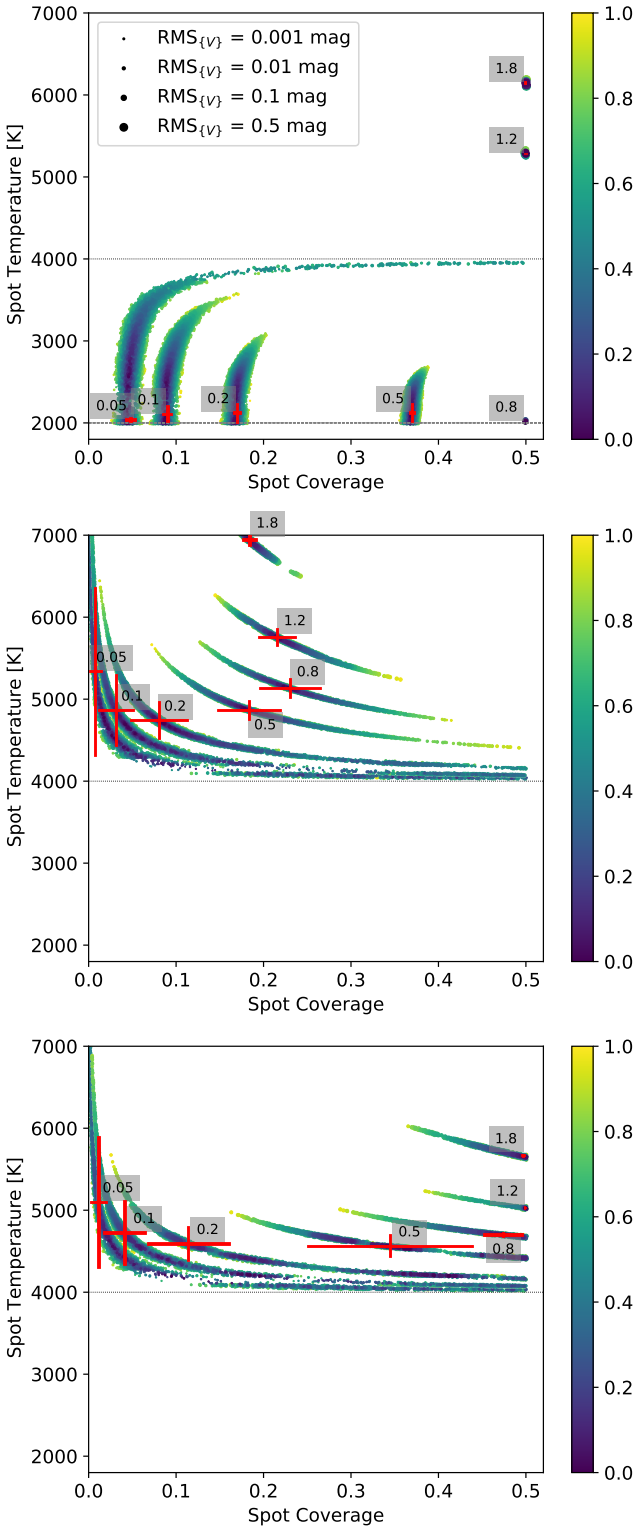

Figure 3.6: Spot properties estimated for simulated grey (top), $R_V = 3.1$ (middle) and $R_V = 5.0$ (bottom) extinction caused by AA Tau like sources. The red crosses mark the position and uncertainties of the spot properties for $\hat{A}^v_{\{V\}}$. The values in the grey boxes indicate the $\hat{A}_V$ amplitudes. The coloured symbols follow the same scheme as in the right panel of Fig. 3.2.

and spot temperature increases with $\hat{A}_V$, with the $R_V = 3.1$ creating large ($f \sim 0.25$) hot spots with increasing temperature, and $R_V = 5.0$ coverage reaching the limit of the investigated parameter space. With the exception of low amplitudes, the inferred spot coverage is significantly larger than expected for spots with the inferred temperatures. The low amplitude $R_V = 5.0$ and 3.1 solutions have the most potential to contaminate based on their coverage and temperature. With the exception of object 4766, all the $\hat{A}_V$ measurements in the F21 sample are below 0.5 mag, and the majority are below 0.3 mag. The colour modulation in $\{V\}$ is examined for potential contaminant results, to ensure the validity of the results.

Occulations by interstellar dust therefore have the potential to contaminate the spot properties by causing resulting low temperature contrast hot spots. However, as we have seen in Section 2.5.2 it is likely that the dust grain size for the transiting material is in the order of a few μm. Less likely are sizes on the order of 0.1 μm typical in the ISM which lead to $R_V = 5.0$ and 3.1 (Weingartner & Draine, 2001). Hence, it is more likely that transiting material produced grey extinction as in AA Tau. Nonetheless, we identify the amplitudes caused by reddening and their resultant spot properties.

Altering the stellar properties or using the ATLAS9 models leads to the same results. Thus, our method is able to identify non-spot contaminants. They are selected as either showing up as very cold spots (at the minimum temperature investigated), unrealistically large spots (coverage near 0.5), or hot spots with very large coverage and/or amplitudes too small to be associated with a hot spot. Based on this, two objects have been identified and removed from the F21 sample as likely AA Tau objects. The properties of these are consistent with having grey extinction. They are indicated in Table 4.1 and discussed in Section 4.2.1.

4

High cadence IC 5070 sample

This chapter examines the results of the spot fitting methodology applied to a sample of high cadence light curves from 31 YSOs in IC 5070. The majority of the results and discussion are published by the thesis author in (Herbert et al., 2023).

4.1 Sample properties

Many of the YSOs in IC 5070 have spectroscopic estimates of their effective temperatures ($T_{\rm eff}$) and spectral types in Fang et al. (2020). Of the 31 YSOs in the F21 sample, 25 have a counterpart in that work.

The $V - I$ vs. I colour magnitude diagram for all sources with V, R, and I data available is displayed in Fig. 4.1. In this figure the colour code of the symbols represents known $T_{\rm eff}$ from Fang et al. (2020) and the symbol size represents the optical extinction from the same work. One can see that the majority of low effective temperature (4000 K) objects are spread out over a wide range of colours (1.6 mag $\leq V - I \leq$ 2.5 mag), due to varying extinction. Slightly higher temperatures (4400 K) can be found for bluer colours. Interestingly, the three hottest stars are found at the reddest colours. These highly reddened sources are likely embedded YSOs or stars with their disc seen edge on. The A_V values are presented here to provide a complete picture of these objects. It is worth noting that since these effective temperatures have been determined considering extinction, the extinction does not affect the spot property results.

For the six objects without $T_{\rm eff}$ measurements in Fang et al. (2020), estimations are made using the $V - I$ vs I colour magnitude diagram shown in Fig. 4.1. Four of the six objects in question are at colours redder than 1.8 mag, and for these the sample median $T_{\rm eff}$ value of 3979 K of the other sources in this colour range is used. For the two brighter and bluer objects at about $I = 11.5$ mag a higher value of 5000 K is adopted as effective temperature to account for the brightness.

Theses estimations are sufficient for our purpose as we have seen in Section 3.6.1 the influence of erroneous stellar temperatures by 500 K alters the spot properties by less than the statistical errors.

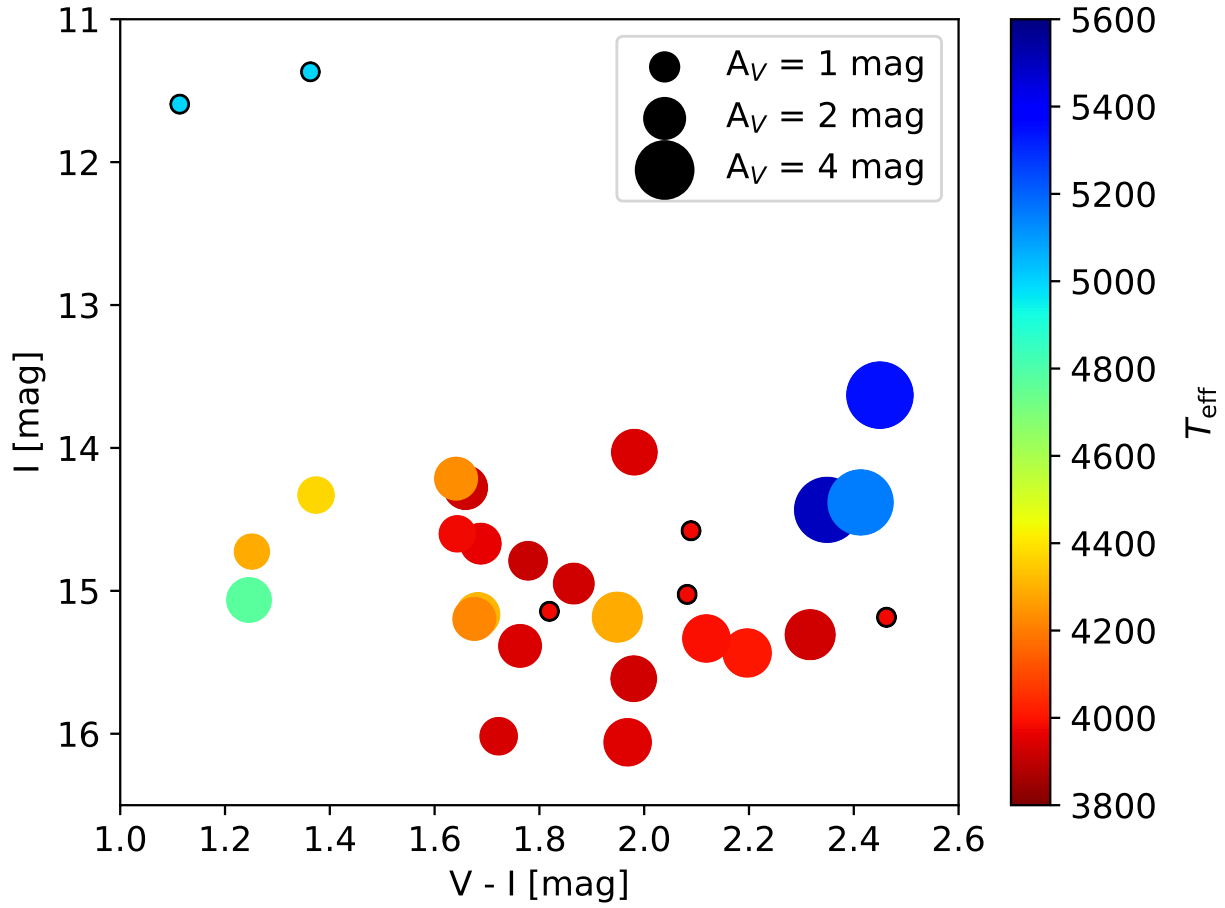

Figure 4.1: $V - I$ vs I colour magnitude diagram of the F21 YSO sample with data available in V, R, and I. The colour code displays the effective temperature and the symbol size represents the optical extinction A_V (Fang et al., 2020), as shown in the legend. For the objects without literature $T_{\rm eff}$ values we use our adopted values and indicated them by black rings around the symbols. No A_V values are available for these.

4.2 First spot property results

4.2.1 Spot properties

Based on the methodology outlined in the Chapter 3 spot properties are fit using the $\{V\}$ amplitudes for all objects. The spot temperatures and their MAD uncertainties are listed in Table 4.1. In the table the objects are sorted into four categories: hot spots, cold spots, ambiguous sources (according to the HS:CS$_{\{V\}}$ ratio), and potential AA Tau contaminants. There are six stars with hot spots, 21 with cold spots, two ambiguous objects, and two potential AA Tau contaminants. In Fig. 4.2 the spot coverage vs. the temperature difference of spot and star (with the MAD uncertainties) for the 27 stars with hot or cold spots is displayed. If the data is available, the spot property calculations have been repeated for $\{B\}$ (24 sources) and $\{U\}$ (5 sources). The values for the spot properties are not listed in Table 4.1, but the HS:CS ratios and minimum SNRs are presented. We will examine the effect of shorter wavelengths in Section 4.3.

The detected hot spots have temperatures from about 700 K to 2800 K above the stellar surface temperature. The coverage ranges from 0.02 to 0.12. There is a general trend that larger temperature differences are associated with smaller coverage. The trend largely follows the detection limit of the objects, as smaller spots with less temperature difference create lower amplitude variations, which are more likely not to be included in the sample. However, it is clear that there are no large hot spots covering more than 10 percent of a hemisphere with a temperature difference larger than 1000 K. Generally, the spot temperatures are consistent with low temperature contrasts on low mass stars and brown dwarfs observed by e.g. Bouvier et al. (1993, 1995); Scholz et al. (2009, 2012); Bozhinova et al. (2016) and predicted by Muzerolle et al. (1998); Kurosawa et al. (2006). The simplified model expects a uniform spot temperature and determines the spot temperature averaged over the spot coverage, therefore, the maximum spot temperatures on the surface could be significantly higher.

The general trends of the detected cold spots mirror the hot spots. Higher temperature differences are typically associated with smaller spots. In this sample there are no stars with large spots

Table 4.1: The resultant spot properties and uncertainties for the F21 YSO sample from Table 3.1. The objects are listed based on our adopted classification as hot/cold spot, ambiguous source, or potential AA Tau contaminant. Listed is the ID number, the used effective temperature of the star during the modelling, the spot properties (temperature and coverage), and their MAD uncertainties obtained from the $\{V\}$ data. In the last six columns listed are the HS:CS ratios and the minimum signal to noise ratio of the associated amplitudes (see text for details). Objects marked with a (*) have no effective temperature reference in Fang et al. (2020), and have adopted temperatures of the sample mean (rounded to 4000 K) or 5000 K for the two bright objects. [(1)] from Froebrich et al. (2021); [(2)] from Fang et al. (2020).

ID[(1)]	$T_{\rm eff}$ [(2)] [K]	T_S [K]	T_S MAD [K]	f	f MAD	HS:CS$_{\{V\}}$	Min SNR$_{\{V\}}$	HS:CS$_{\{B\}}$	SNR$_B$	HS:CS$_{\{U\}}$	SNR$_U$
Hot spot in HS:CS$_{\{V\}}$											
3220*	5000	6643	753	0.026	0.014	0.8168	3.43	-	-	-	-
5575	5150	7798	972	0.021	0.010	0.6829	2.21	-	-	-	-
5886*	4000	4910	609	0.054	0.042	0.6024	1.95	-	-	-	-
6393	4000	5182	384	0.066	0.029	0.6029	3.71	-	-	-	-
7465	4200	4882	184	0.125	0.049	0.8879	5.29	0.4081	4.28	-	-
7954	4000	5372	579	0.032	0.018	0.6787	2.72	-	-	-	-
Cold spot in HS:CS$_{\{V\}}$											
3988	3950	3139	112	0.311	0.025	0.0557	7.49	0.0011	4.97	-	-
4097	5350	3477	631	0.067	0.010	0.2769	2.04	-	-	-	-
4446	5500	2880	851	0.078	0.006	0.0216	3.26	0.3240	2.29	-	-
5535	3900	2654	147	0.207	0.006	0.0000	11.53	0.0000	9.77	0.8491	2.42
5548	3950	3424	211	0.086	0.021	0.1714	3.97	0.2901	2.86	-	-
5559	3950	3261	191	0.216	0.030	0.0221	5.20	0.6198	4.69	-	-
6060	4300	3791	272	0.155	0.045	0.1696	4.10	0.0642	7.92	0.4130	2.48
6149	3950	3327	120	0.259	0.028	0.0231	7.86	0.4926	3.13	-	-
6259	4750	3337	431	0.104	0.009	0.0029	4.82	0.0000	5.59	-	-
6315	3950	3186	295	0.154	0.032	0.3825	2.27	-	-	-	-
6861	4300	3255	290	0.132	0.015	0.0535	4.66	0.0301	3.30	-	-
6929	3900	3205	130	0.164	0.016	0.0005	7.27	0.1600	4.38	-	-
7181	4000	3072	143	0.175	0.010	0.0000	8.94	0.0000	6.55	-	-
7422	4350	2848	680	0.059	0.004	0.0763	3.32	0.2219	5.42	0.6330	1.84
7632	3950	3218	77	0.290	0.013	0.0000	11.92	0.0000	12.13	-	-
8025*	4000	3296	61	0.430	0.017	0.0000	15.61	0.2482	12.12	-	-
8038*	4000	3391	187	0.150	0.025	0.1222	4.86	0.3512	3.33	-	-
8249	3950	3414	210	0.121	0.027	0.2193	3.47	0.0066	2.10	-	-
9267*	5000	2896	253	0.122	0.003	0.0000	13.36	0.0000	28.30	0.0000	7.34
9321	4250	3482	107	0.241	0.018	0.0521	10.48	0.3371	14.61	0.0000	3.22
9961*	4000	2409	396	0.053	0.006	0.0166	2.13	0.2968	1.59	-	-
Ambiguous source in HS:CS$_{\{V\}}$											
6813	3950	3604	114	0.248	0.060	0.4987	4.06	0.9985	4.64	-	-
7472	4300	3457	218	0.170	0.021	0.4229	4.67	0.2488	4.59	-	-
Potential AA Tau contaminant											
4766	4100	2774	59	0.4996	0.0003	0.0002	14.54	1.0000	13.35	-	-
6337	3950	2007	4	0.2412	0.0040	0.0001	11.15	0.0000	5.73	-	-

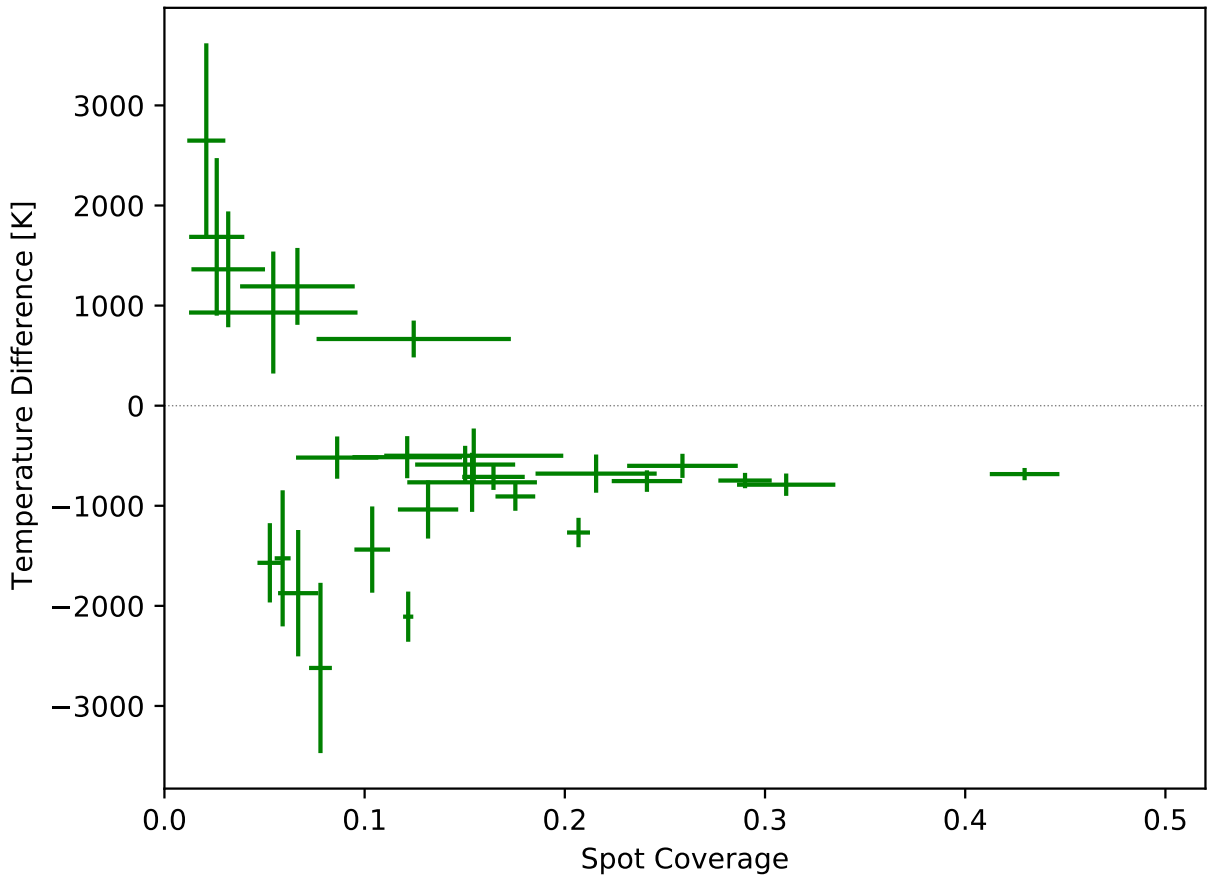

Figure 4.2: The determined spot properties of the F21 YSO sample listed in Table 4.1 using $\hat{A}^o_{\{V\}}$. We plot the coverage of the visible surface and the temperature difference $T_S - T_\star$. The horizontal dotted line separates hot spots (top) from cold spots (bottom). The error bars represent the MAD uncertainty (see text for details).

that also have a large temperature contrast. The sample contains objects with star-spot temperature difference between 500 K and 2500 K, with most being between 500 and 1000 K. Smaller temperature differences than 500 K do not create amplitudes with sufficient SNR and therefore are not included in the sample. The two stars with highest star-spot temperature difference (4097, 4467) are also the two with the highest effective temperatures, around 5500 K. The absolute spot temperatures for these two objects are in line with the other stars that have effective temperatures of the order of 4000 K.

The cold spot coverage ranges from 0.05 to 0.43, with typical values between 0.1 and 0.3. The maximum coverage is well constrained, while the lower bound is due to an observing bias. With the typical stellar surface temperatures and the wavelength range of our observations, cold spots with smaller coverage do not cause large enough variability. Compared to the hot spots, the coverage for cold spots can be much larger, and reach up to half the visible surface. This has also been seen in previous works (e.g. Strassmeier, 1992; Bouvier et al., 1995). Similar to the hot spots, it is important to note that the temperatures are averages over the spot area.

There are two stars in the sample that are potential AA Tau contaminants. Objects 4766 and 6337 have spot solutions at the edges of the parameter space. In the case of 6337 the solutions are in exactly the place that is predicted by our simulations of variability due to grey extinction with an amplitude of approximately 0.3 mag. This source is categorised as an AA Tau type object, with large dust grains in the inner disc warp. Object 4766 has much higher amplitudes which are similar but not the same in all the filters. The spot solution places it at a coverage of 0.5. Therefore, it cannot be fully excluded that this is a star with very large spots but most likely is an AA Tau source due to its extremely high amplitudes. There are two stars with ambiguous solution based on the $\{V\}$ data, which are classified as ambiguous. We will discuss the ambiguity of these objects, as well as the inclusion of shorter wavelength filters in Section 4.3.

4.2.2 Spots and stellar properties

Spots and stellar stage

In this section we examine if and how the evolutionary stage or stellar properties of the YSOs in this sample influence the spot properties. The F21 sample of young stars used has been obtained solely by the presence of periodic variability and their astrometric properties (Froebrich et al., 2021). All objects have parallax and proper motion values that indicate they are members of the IC 5070 star forming region. The typical age of members of this region is 1 Myr (Kuhn et al., 2020).

The presence of discs is first determined, using indicators for the infrared excess. Traditionally the slope (α_{SED}) of the infrared spectral energy distribution (SED) has been used to distinguish between stars with (Class 2) and without discs (Class 3) (Lada, 1987; Myers & Ladd, 1993). Majaess (2013) has used Equation 4.1 to determine the SED slope from WISE photometry:

$$\alpha_{SED} = 0.36(W1 - W2) + 0.58(W2 - W3) + 0.41(W3 - W4) - 2.90 \tag{4.1}$$

A value for α_{SED} between -0.3 and -1.6 indicates Class 2, between 0.3 and -0.3 indicates flat spectrum sources, and $\alpha_{SED} < -1.6$ indicates Class 3 (see Table 2.1). Based on the α_{SED} values the majority of the sample is Class 2 – 24/31 or 77%. However, this metric is only deemed reliable if the star has SNR > 5 in all four WISE bands (Majaess, 2013). Nine of our stars do not meet this standard in $W4$. Five of these nine also fail the SNR requirement in $W3$. Most of the ones failing the SNR criterion (5/9) are nominally Class 3, the remaining 4 Class 2. Thus, using α_{SED} we can reliably classify 20/31 or 65% as Class 2. Two of these Class 2 objects are the AA Tau contaminants identified in this sample, confirming that they host a circumstellar disc. There is one flat spectrum source in the sample.

An alternative and simpler disc indicator is the $K - W2$ colour, which traces again the slope of the SED, but without using the two longest wavelengths in WISE. In $K - W2$, values above ~ 0.5 mag generally indicate an infrared excess due to dust in the inner disc (Teixeira et al., 2012).

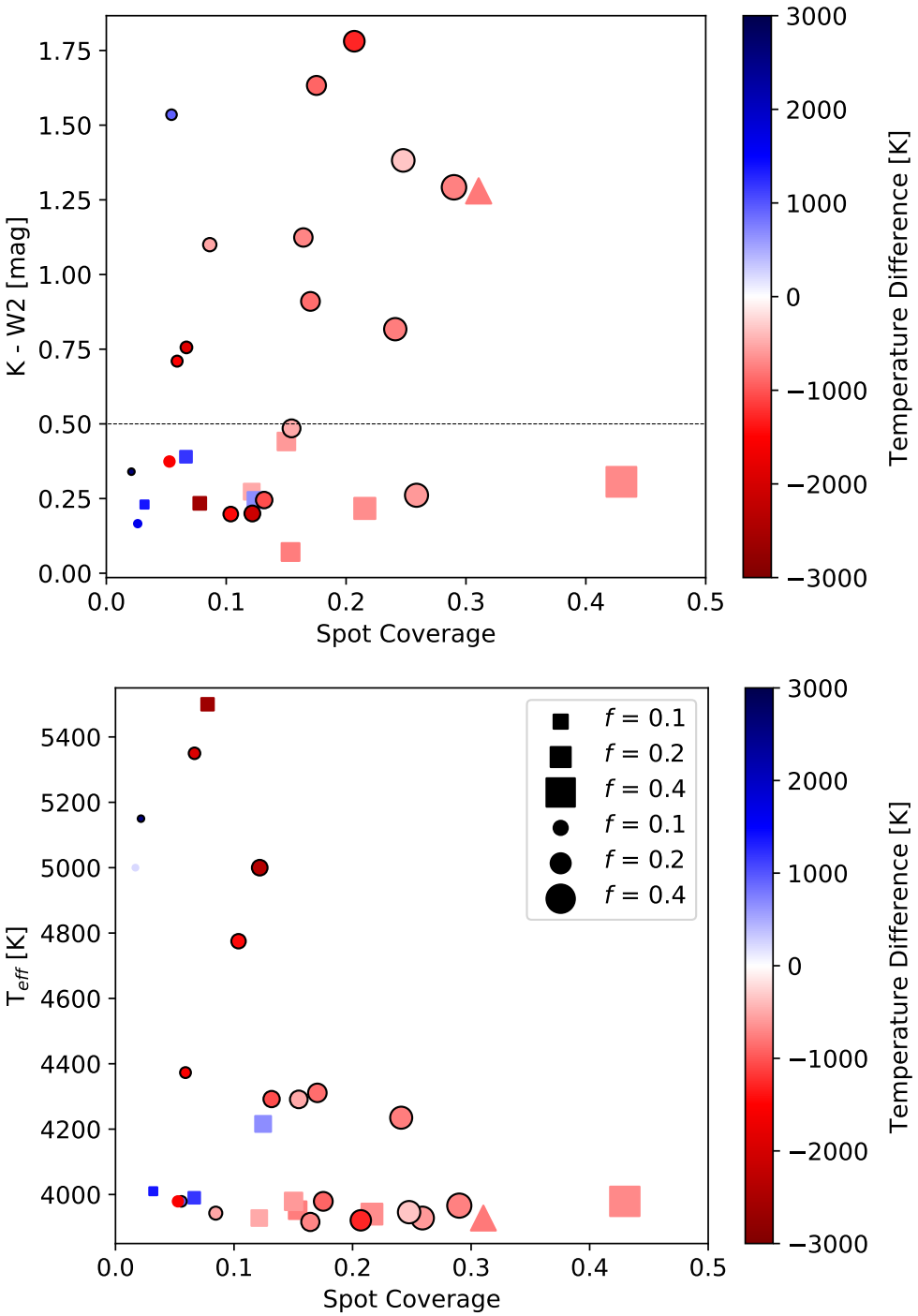

Figure 4.3: **Top:** Spot coverage against $K-W2$ colour for our objects. The marker size represents the spot coverage (as shown in the legend) and the colour the temperature difference $T_S - T_\star$. Hot spots are blue and cold spots are red. The horizontal dashed line separates sources with and without disc excess emission. Objects classified as Class 2 according to α_{SED} are highlighted with a black circle. The triangle marks the only flat spectrum source in the sample. Square symbols indicated sources with SNR < 5 in $W3$ or $W4$. **Bottom:** Spot coverage vs. stellar effective temperature. The colour coding and symbol size is the same as in the top panel.

It is possible however that the $K-W2$ excess is influenced by long term variability of the star due to the time delay of several years between 2MASS and WISE. According to this criterion 12/31 stars have infrared excess due to a disc, fewer than when using the slope of the SED. However, $K-W2$ only traces warm material in the inner disc, within 1 AU. Therefore, it will not identify more evolved discs either transitional discs or pre-transitional discs with depleted inner region. Considering both criteria together, it is reasonable to conclude that about two thirds of the sample are objects hosting a circumstellar disc (Class 2), and about half of those are likely to be evolved.

In the top panel of Fig. 4.3 the spot coverage is plotted against the $K-W2$ disc excess indicator. The horizontal dotted line separates the objects with and without disc excess. Class 2 objects according to α_{SED} are marked with an extra black circle; squares denote stars where the SNR is too low to distinguish between Class 2 and Class 3. The triangle marks the flat spectrum source. The symbol size is proportional to the spot coverage and the symbol colour shows the temperature difference between star and spot based on the legend.

There is no statistically significant correlation of the spot properties with the indicators for the presence of the disc. For the stars with cold spots, the coverage and temperature contrast are homogeneously distributed amongst the objects with and without excess emission. Furthermore, the small number of hot spot sources also does not show any preference to occur on sources with infrared excess. All but one of the stars with hot spots do not show infrared excess in $K-W2$. These include the two reliably classified Class 3 sources from α_{SED}. The lack of $K-W2$ excess does not necessarily exclude the presence of a disc, or the presence of accretion. We have seen in Section 2.3.2 that accretion is common on transition disc objects, which likely accounts for many of these objects. Most of the stars with hot spots without $K-W2$ excess also do not have sufficient SNR to identify the disc from α_{SED}. Globally evolved discs may demonstrate accretion, albeit at a reduced rate, for a limited time (Thanathibodee et al., 2022).

Distinct from a disc with an inner cavity, an alternative explanation for hot spots on stars without apparent infrared excess is emission from chromospheric plage, as for the star V1598 Cyg found in Froebrich et al. (2020). This could be akin to plages or faculae on the Sun, but for much

more active stars. Due to the larger SNRs produced by hot spots, in this methodology, if stars have dark spots and a plage, the plage is likely to dominate and be detected. Shapiro et al. (2016) investigated if a broad band light curve for the Sun would be dominated by cool or hot regions, and the answer is it depends on viewing angle and timescale. This illustrates that even for the Sun hot spots can show up in light curves.

The F21 sample is split into fast and slow rotators, with a clear gap of periods around five days. Similar to the evolutionary stage indicators, there is no significant correlation of the spot properties with the stellar rotation period. For this limited sample, there is a link between spot coverage and effective temperature. These two quantities are plotted in the lower panel of Fig. 4.3. It is clear that the maximum coverage decreases with increasing $T_{\rm eff}$. This indicates that cooler, lower mass stars can have larger cold spots. However, this may be an observing bias as this sample contains only a small number of stars with high $T_{\rm eff}$. If most spots are small, then randomly drawing coverage values for a few high temperature objects and a large number of low temperature sources, will create a similar trend. However, the median and maximum spot coverage clearly decreases with effective temperature.

Hot spot rarity

Two thirds of the YSOs in this sample have discs in varying states of evolution. It may therefore seem surprising to find only six objects with hot spots induced by accretion from a disc, corresponding to around 19 percent of the total sample. There are two potential reasons for the scarcity of hot spots in our sample, one is spot instability, the other the properties of the underlying magnetic field.

Only stable accretion columns on stars are able to create periodic variability. Class 2 sources with unstable accretion do not produce regular periodic light curves that can be identified in the photometry (Kurosawa & Romanova, 2014). This sample was created from a dataset that was taken over a duration of 80 d. Therefore, the accretion column is required to be somewhat stable for this period in order to have been included in our analysis. This study demonstrates that potentially only a small number of accreting stars is found in the stable regime of accretion, in the context of those

models.

The second explanation for finding only few stars with hot spots is the magnetic field configuration. As YSOs evolve, they develop a radiative core with the timescale depending on the mass ranging from 0.5 Myr (for 2 $M_\odot$) to 9.3 Myr (for 0.5 $M_\odot$) (Tognelli et al., 2015). As examined in Chapter 2 the radiative core develops the dipole component of the magnetic field weakens. Based on the Hertzsprung-Russel diagram for the IC 5070 region discussed in Froebrich et al. (2021) and $T_{\rm eff}$ values, the masses of these objects should be in the range of 0.5 to 2 $M_\odot$. In combination with the typical age of 1 Myr, this sample therefore represents a mix of simple and complex magnetic fields. Complex fields result in hot spots at a range of latitudes while simple fields give preferably spots at high latitudes which are less likely to create rotational modulation.

4.3 Reflections on methodology

In this thesis, the aim is to apply the developed methodology to large samples of YSOs over time. This section evaluates some of the rationale in the methodology and its reflection in the results for this sample, to guide next steps.

4.3.1 Evaluation of HS:CS

The classification of hot, cold, or ambiguous objects is defined by the ratio HS:CS$_{\{V\}}$. In the spot fitting process (detailed in Section 3.5.1) values for the ratio HS:CS$_{\{V\}}$ that are close to 0.5 show no clear preference for hot or cold spot solutions. To remove objects that are close to 0.5, a ten percent cut on either side was implemented, i.e. a 60 percent majority. We can now analyse how the threshold affected the results in the F21 sample.

Presented in Fig. 4.4 in grey are the HS:CS$_{\{V\}}$ results for the objects in the F21 sample. The classification of sources into hot/cold spot objects has been based on the $\{V\}$ data, because it is available for all objects. The values are listed in Table 4.1. Also listed in Table 4.1 are the HS:CS ratios for all filter sets investigated and we will also discuss the inclusion of shorter wavelength filters in Section 4.3.3.

The majority (17/32) of our objects have cold spots with HS:CS$_{\{V\}}$ below 0.1. There are

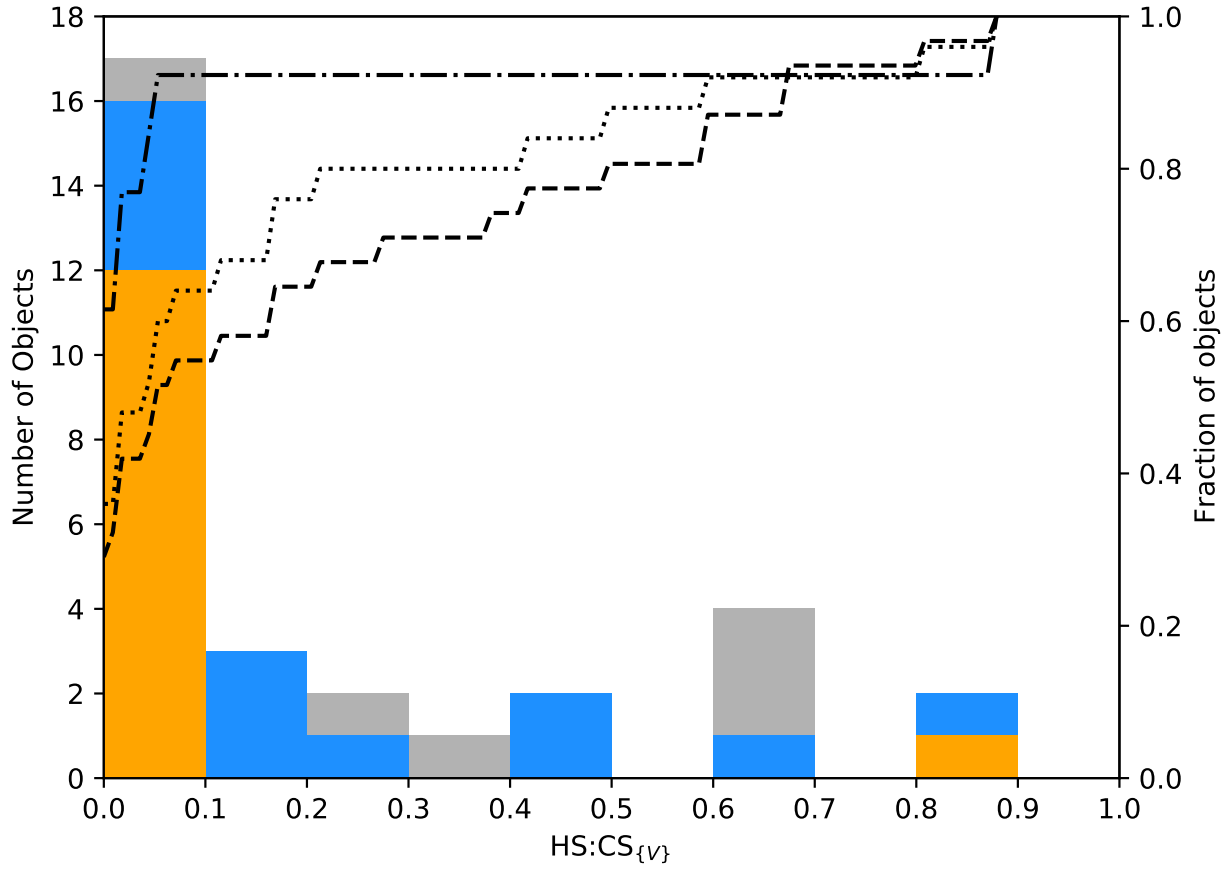

Figure 4.4: A histogram and cumulative distribution function (CDF) of the HS:CS$_{\{V\}}$ for YSOs with varying SNR cuts. The full F21 sample is shown in grey with a dashed CDF. The sample with amplitudes of SNR above 3 is in blue with dotted CDF. The sample with amplitudes of SNR above 5 is in orange and dot-dashed CDF.

decreasing numbers of cold spots towards the ambiguity threshold. One source (6315) has a HS:CS$_{\{V\}}$ ratio of 0.38, close to our adopted borderline. Two objects (6813, 7472) are classified as ambiguous with $\mathrm{HS:CS_{\{V\}}}$ values of 0.49 and 0.42 respectively. Two of the stars with hot spots (5886, 6393) have HS:CS$_{\{V\}}$ ratios above the threshold by less than 0.03. This is below the standard error of the hot spot ratios which are both around ± 0.04. They are marginally above the threshold, and could be considered unreliable. However, the aim of implementing a 60 percent majority is to remove objects that are close to 50/50, and while the two objects are barely above the 60 percent threshold they are definitively above 50 percent.

If the threshold were increased to classify $0.35 < \mathrm{HS:CS_{\{V\}}} < 0.65$ as ambiguous, these two objects would be removed as would a cold spot on object 6315. However, there is no apparent reason why these spots should be distrusted. The temperature and coverage values align with theory and other studies, and therefore increasing the 60 percent threshold would remove their results.

Conversely, if the threshold were decreased to five percent of 50 percent (i.e. $0.45 < \mathrm{HS:CS_{\{V\}}} < 0.55$), one of the spots (7472) classified as ambiguous would enter the sample as a cold spot. With available B-band data, the spot is confirmed as a cold spot that is somewhat larger and warmer than the $\{V\}$ results. However, in future YSO samples shorter wavelength filters are likely not available. Including one more spot which can be considered a feasible result out of 29 spots will not greatly increase the statistics and the reduction in the threshold in the future may include more questionable spot fits. In this methodology, distinguishing between hot and cold spots reliably is crucial for the accuracy of the sample statistics. Hence, setting a higher threshold is preferable.

The boundary of $0.4 < \mathrm{HS:CS_{\{V\}}} < 0.6$ establishes a high standard for whether spot fits follow with the hot spot or cold spot regime. Additionally, $\mathrm{HS:CS_{\{V\}}}$ can be considered alongside the spot property results as an indicator of reliability.

4.3.2 The impact of SNR on HS:CS

Listed in Table 4.1 are the minimum signal-to-noise ratio (SNR) of any of the amplitudes in $\{V\}$, as well as the SNRs of the B-band and U-Band amplitudes, if available. The distribution of HS:CS$_{\{V\}}$ for the F21 sample with different SNR restrictions is presented in Fig. 4.4.

The two sources classified as ambiguous have in HS:CS$_{\{V\}}$ SNRs less than five, and when including shorter wavelength filters there are two objects with ambiguous HS:CS$_{\{B\}}$, and one with ambiguous HS:CS$_{\{U\}}$ which all have SNRs below five. Therefore, first instinct may be to assume SNRs below five cause ambiguous results. In Fig. 4.4, the HS:CS$_{\{V\}}$ for objects that have SNR above five in all filters is presented in orange. The sample is reduced to 13 objects; 12 cold spots with HS:CS$_{\{V\}} < 0.1$ and one hot spots HS:CS$_{\{V\}} > 0.8$. This is definitive, but very restricted. As these amplitude sets were gathered during an observing campaign all objects in the sample have a high density of data points in their light curves and relatively low errors. The objects with SNR > 5 in all filters have above average amplitudes for the sample. Therefore, these objects show a very clear preferences to hot or cold spots displaying larger spots with greater temperature contrast. There are many results that are removed with a requirement for SNR > 5 which otherwise appear to be reliable spot fits.

In Section 3.6 we demonstrated that a SNR above three led to accurate recovery of simulated spots. Figure 4.4 shows the sample with SNR > 3 in all filters in blue. This removes six objects from the sample, five of which are close to the ambiguity threshold. Three hot spots (5575, 6393, 7954) are removed, object 6393 being one of the two objects that is just above the ambiguity boundary. The two objects with ambiguous results remain in the sample with SNR above three.

This highlights that the distinction between hot and cold spots is only reliable when sufficient SNR amplitudes in multiple filters are available. A limitation of SNR above three in all filters reduces the number of objects close to, but not crossing the ambiguity boundary without dramatically reducing the sample. Employing a SNR above three threshold for the amplitudes prior to spot fitting will ensure the fitting is of an acceptable quality. Further limitations can be applied post fitting, to examine this relationship in more detail.

4.3.3 Inclusion of B- and U-band data

This sample, due to being the subject of an observing campaign has more available data in shorter wavelength filters than is typical for HOYS targets. Here, 24/31 objects have sufficient data to generate a B-band amplitude. This allows us to examine the effects of including shorter wavelength data.

Figure 4.5 presents the measured spot properties for objects with B- and U-band amplitudes. A dashed line connects the measured properties, with the colour indicating the shortest wavelength the set of amplitudes. Including shorter wavelengths may help classify objects that are ambiguous in HS:CS$_{\{V\}}$, therefore ambiguous solutions are presented but marked with a black square. In the top panel, all objects (except the two potential AA-Tau type contaminants) which have B- and U-band amplitudes are presented. In the lower panel, only objects that change classification between cold, hot, or ambiguous are included.

Two objects (7465, 6149) change from their initial spot classification to ambiguous when B-band amplitudes are included in the analysis. Additionally, one object (5559) changes from cold to hot with B-band inclusion. All of these objects have values for SNR$_B$ between three and five.

The two sources (6813, 7472) classified as ambiguous from their HS:CS$_{\{V\}}$ have B-band data. Object 6813 has a HS:CS$_{\{B\}} = 0.9985$, clearly classifying it as a hot spot, while object 7472 results in HS:CS$_{\{B\}} = 0.2488$ classifying it as a cold spot. The inclusion of shorter wavelength filters is hence useful to classify ambiguous results.

Two objects (5535, 4722) change from cold to hot when U-band data is included, and one (6060) changes from cold to an ambiguous solution with HS:CS$_{\{U\}} = 0.413$. These are three of the 5 objects with available U-band data, which implies that inclusion of U-band data can drastically changes results. However, the SNR of the U-band data for all three objects is below 2.5. The remaining two objects with U-band data in the F21 sample have SNR above three and do not change regime from their $\{V\}$ classification. The U-band has potential to dramatically alter the results of the spot fitting, especially distinguishing between hot and cold spots but in this sample with a sufficient SNR$_U$, the $\{U\}$ results support the $\{V\}$ results.

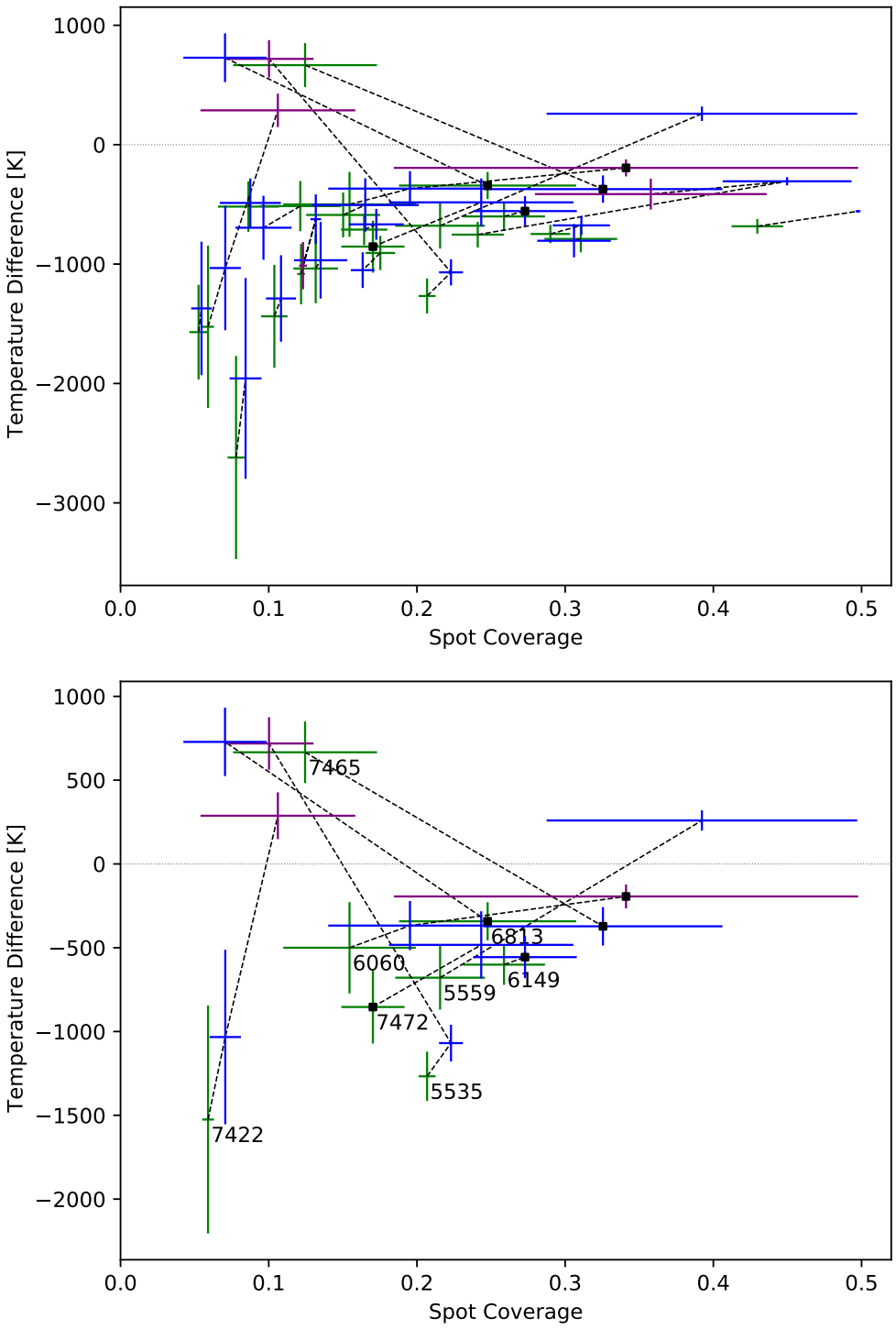

Figure 4.5: **Top:** Resultant spot properties for YSOs using $\hat{A}^o_{\{V\}}$ (green) and $\hat{A}^o_{\{B\}}$ (blue) for objects with B amplitudes. If U-band data is available the $\hat{A}^o_{\{U\}}$ is also presented (purple). The spot properties of the same YSO are connected by a dashed black line. Spot properties that have an ambiguous HS:CS$_{\{V\}}$ are presented marked by a black dot. **Bottom:** The above plot but only the objects that change regime with the addition of shorter wavelength filters. These are labelled.

For the majority of objects $\{V\}$ data is suitable to determine spot properties. Figure 4.5 (top) demonstrates the similarity of results for $\{V\}$ and $\{B\}$ data. If we disregard the two objects which change classification due to U-band data with SNR_U below three, only one object changes regime without being classified as ambiguous in $\mathrm{HS{:}CS}_{\{\lambda\}}$. While high quality B- and U-band data would be ideal, for the vast majority (83 percent) of classifications the $\{V\}$ results are reliable.

5

Long duration IC 5070 sample

This chapter details the data analysis used to examine spot property evolution, and identify a sample of YSOs in IC 5070 with data over time. This chapter highlights changes made to the methodology established in Chapter 3 to identify periodic YSOs in IC 5070, identify peak-to-peak amplitudes, and fit spots. This chapter then identifies a sample of periodic variables, and establishes the sample properties. The majority of this work is published by the thesis author in (Herbert et al., 2024).

5.1 IC 5070 cluster membership

The previous chapters have developed a methodology and examined the results for the F21 YSO sample. The F21 YSOs were identified as a selection of periodic objects, and then confirmed to be IC 5070 cluster members. Here, cluster members are first identified kinematically and then searched for periodicity. This selection order has the same end result of identifying periodic YSOs in the region but is less computationally intensive, as we are only concerned with YSOs it would not be productive to identify periodicity in non-members.

Potential IC 5070 cluster members were identified using using Gaia DR3 (Gaia Collaboration et al., 2016, 2023) astrometry. This was part of a larger work characterising the YSO populations in all HOYS fields (Froebrich et al., 2024). All Gaia sources within 0.6 degrees of the cluster centre were selected. Sources were removed that had parallax values of less than 0.3 mas, a SNR of the parallax of less than five, and that were fainter than 18 mag in the Gaia G-band. Objects with colours indicative of white dwarfs and cataclysmic variables were also removed. Therefore, sources with $BP - G < -0.2$ mag, and $G - RP < 0.0$ mag were excluded. Cluster members were initially manually identified through a histogram of the distances, using a bin width of 20 pc. Stars in a distance range of 750 pc to 900 pc were selected. Within that selection, two groups of stars denoted a and b with coherent proper motions were identified. For each group the median distance and proper motions and their RMS scatter were determined. Candidate cluster members were then selected as all stars that are within three standard deviations around these median values. The potential cluster members were assigned to the group they were closest to in proper motion space. A summary of the astrometric properties of the two groups can be found in Table 5.1.

There are a total of 366 potential cluster members based on the Gaia DR3 astrometry in the two groups of IC 5070. Of those 252 are in group a, the other 114 are in group b. Of these 366 cluster members, there are corresponding HOYS light curves for 131 (84, and 47 in groups a and b, respectively) with at least 100 photometry data points in each of the V, R, and I filters. The majority of the YSOs with HOYS light curves identified in Froebrich et al. (2021) using

Table 5.1: Properties of the two astrometric groups of young stars in the IC 5070 region, as determined in Froebrich et al. (2024). The columns contain the following information: Group: The group name; d, d^e, d^s: median distance, standard error of the median, RMS scatter from the median of the cluster members; $\mu_{\alpha/\delta}$, $\mu^e_{\alpha/\delta}$, $\mu^s_{\alpha/\delta}$: median proper motion in RA/DEC, standard error of the median, RMS scatter from the median of the cluster members; N: Number of Gaia DR3 selected potential members;

Group	d	d^e	d^s	μ_α	μ^e_α	μ^s_α	μ_δ	μ^e_δ	μ^s_δ	N
	[pc]			[mas/yr]			[mas/yr]			
a	832.4	2.7	33.6	-1.328	0.028	0.347	-3.076	0.026	0.320	252
b	824.7	4.43	36.0	-0.977	0.036	0.294	-4.148	0.041	0.335	114

Gaia EDR3, were again identified as cluster members. Seven of the objects previously analysed are not included in this list. This is due to a parallax or proper motion value in Gaia DR3 that is beyond the selection range applied. Two objects that were not previously investigated are now included in this sample.

65 of the 366 potential cluster members have recently been identified as H_α emission line stars in Panwar et al. (2023). The overlap between the samples will be examined in more detail in Section 6.1.4.

5.2 Additions to methodology

This section establishes the methodology identifying periodic objects in IC 5070 from light curves spanning several years. This is largely based on the methodology in Chapter 3. The differences are highlighted in this section.

5.2.1 Sliced light curves

The aim of this thesis is to analyse the properties of surface spots over time. HOYS observations in the IC 5070 field begin in 2014, and the light curves were extracted from the HOYS database on October 21st, 2022. The V, R, and I light curves are dissected (*sliced*) into blocks of six months in length, every three months. Therefore, consecutive slices of light curve data overlap by three months. The starting date for the first slice was chosen as Feb 14, 2014, 12 noon UT. The following slices are numbered consecutively by integers. The start date for the first slice (indexed as zero) is

in the first year of HOYS data available for this field, and this period of the year corresponds to the time of worst observability for the IC 5070 field, given its Right Ascension (i.e. it is at its lowest altitude at midnight). Therefore, slices with numbers 3, 7, 11, etc. [1] are centered on February, and usually contain the least amount of data. On the other hand, slices numbered 1, 5, 9, etc [2]. are centred on mid August each year and generally have the most photometry data points.

For our analyses we require a minimum of photometry data points in each slice. We need at least 50 data points in at least two filters from V, R, and I to determine the possible period (see Section 5.2.2), and at least 50 data points in each of those filters to measure the peak-to-peak amplitudes (see Section 5.2.3). Therefore, the first slice with sufficient data for the majority of objects is centred on mid May 2018 (MJD = 58162.5), i.e. slice number 16. The final slice with sufficient data in all filters is slice 33, and so at most there are 17 slices with sufficient data for spot fitting. Hence, the light curves for the region are typically $\sim$5 yr in length. The observational cadence of an object, and therefore the number of photometry data points available, is affected by its brightness and distance from the centre of the HOYS field. The majority of images in the HOYS database come from amateur telescopes with varying fields of view and limiting magnitude. In general, fainter objects, further from the central part of the field have less data points available for analysis. In all figures where properties are shown as function of time, the data points are plotted at the start date of their respective slice.

5.2.2 Period identification

The study identifying periodic objects in IC 5070 from HOYS data in Froebrich et al. (2021) has been outlined in Section 3.1.1. The double-blind study of period-finding algorithms was conducted on data from an high-cadence 80 day section of light curves in the summer of 2018 (MJD ranging from 58329.5 to 58409.5). Photometry data from this period appears in slices 17 and 18. The campaign was repeated every August in subsequent years, but for the majority of stars this time remains the part of the light curve data with the highest cadence.

[1] This is $3N - 1$. This numbering system arises from the programming, the slices are counted from the start date and are zero indexed.

[2] Similarly, this is $3N + 1$

As discussed in Section 3.1.1, the Froebrich et al. (2021) study identified a combination of four period finding algorithms optimal for completeness in identifying periodic objects in HOYS data. The four methods that were identified are: L1Boot, L1Beta, L2Beta, and the generalised Lomb-Scargle (GLS) periodogram. The L1Boot, L1Beta, and L2Beta methods are run using the R module `RobPer` (Thieler et al., 2016). The GLS periodogram is based on Scargle (1982); Zechmeister & Kürster (2009) and its implementation in `astropy` is utilised[3].

For the purpose of investigating spot evolution, some small changes are made to the period identification methodology as laid out in Section 3.1.1. First of all, previously periodic light curves were identified for all stars in the IC 5070 field. Here, the search is limited to the light curves of stars identified as potential cluster members based on Gaia DR3 astrometry (see Section 5.1). Furthermore, each of the light curve slices is searched for significant periods independently. This ensures that for objects which show periodic light curve modulation only at certain times, e.g. due to varying surface spot properties, a period can be identified. Therefore, a more complete sample of rotational variables of the region is obtained.

Further minor adjustments are made to the selection of the best period, compared to Froebrich et al. (2021), which are detailed below. The four period finding algorithms (L1Boot, L1Beta, L2Beta, and GLS) were applied to the photometry in each slice and filter (V, R, and I), separately. Only slices which had at least 50 data points in two of these filters were considered. For all four period finding methods periodograms with 1000 test periods were obtained. These test periods were sampled homogeneously in frequency space between 0.5 d and 20 d. This range was chosen as most appropriate based on the typical cadence of HOYS data and the periods identified in Froebrich et al. (2021).

In each periodogram the highest peak was chosen as the candidate period. To ensure periods were real, only candidate periods with a peak periodogram power above 0.15 were considered (for L1Boot, L1Beta and L2Beta). This differs from Froebrich et al. (2021), where a slightly higher threshold of 0.2 was used. The reduction in the detection threshold is justified by the larger

[3]As in Froebrich et al. (2021), the period identification analysis using the GLS method was conducted by Herbert et al. (2024) co-author Siegfried Vanaverbeke.

amount of data available in the current analysis. As such, there is more opportunity to identify and remove questionable periods as opposed to the Froebrich et al. (2021) study which only had one 80 d section of light curve for each object. The GLS equivalent to this peak periodogram power is the False Alarm Probability (FAP). A threshold of FAP below 0.1 was used, and the peak with the lowest FAP per periodogram was accepted as the candidate period. Despite the geographically distributed nature of the HOYS observations, the typical cadence in the data is approximately one day. Therefore, candidate periods identified within one percent of one day were removed. Additionally any candidate periods that were within one percent of 0.5 d and 20 d were also removed, as these are near the edges of the investigated period parameter space.

If in a given slice a period was detected matching the above criteria and in at least two filters with a separation of less than 0.05 d, then it was retained as a candidate period for this slice. This generated a list of such candidate periods for each object. In some objects these lists contained periods that were not all identical within the uncertainties. In which case, the following methodology was applied to select the most likely correct period in all cases. A histogram of all candidate periods for each object was created with a bin-width of 0.1 d for the entire range of investigated periods (0.5 to 20 d). This resulted in groups of candidate periods in individual or immediately adjacent bins, and distinct groups being separated by one or more bins with no candidate periods within them. Typically these groups span less than two adjacent bins (i.e. 0.2 d) and the maximum range was 0.4 d. In all cases, the scatter of the periods within each group was below ten percent of the median. In Fig. 5.1, the histograms for two periodic objects (1, 2) are presented. In both cases, one group contains the majority of the candidate periods.

For most objects one of these groups contained the vast majority of candidate periods. The phase folded light curves with the median period for each group were visually inspected. Phase plots from groups with a small number of periods presented no clear systematic periodic variability that could be visually identified. Therefore, only groups with more than five candidate periods were kept. For most objects this left only one single group of candidate periods. In all other cases the dominant group was selected if it had more than 2/3rd of the candidate periods for this

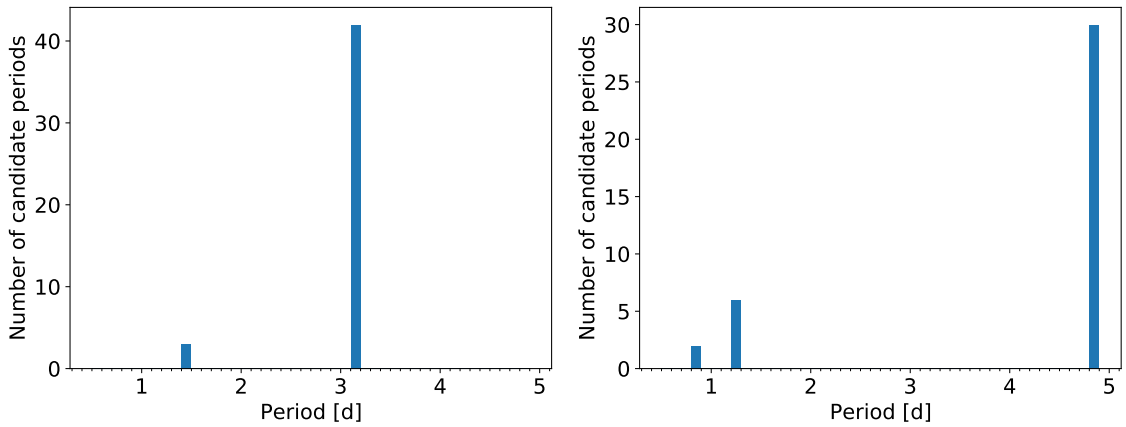

Figure 5.1: Example histograms showing the groups of candidate periods for two periodic objects (later numbered objects 1 and 2).

object. There were only two objects (18, 26) where this was not possible and two almost equal sized groups with different periods remained. In those cases the group with the most likely correct median period was manually selected by inspecting the phase folded light curves. The manual selection involved inspecting all available slices to evaluate the scatter of the data points, and the fit of the running median to the shape of the points. In both cases the group with the shorter candidate periods was chosen.

Finally, again following established procedure in Sect. 3.1.1, the final period was determined for each object in the following way. For each filter, a simple Lomb-Scargle periodogram with 1000 homogeneously distributed test periods was determined for the entire light curve within ten percent of the median of the candidate periods in the dominant group. This resulted in a much higher period resolution. The peak in this periodogram was used as the most likely period of this object in each filter. The median of these periods from the V, R, and I data have been adopted as the final period of the object. Similarly, the standard deviation of these three values is used as the final period uncertainty for the object throughout the analysis. These values are listed in Table 5.2 for all objects.

5.2.3 Peak to peak amplitude identification

In order to analyse the spot property evolution we require peak to peak amplitudes in V, R, and I over time. This essentially follows the procedure established in Section 3.2.1. For each periodic object the photometry data slices that were created in Section 5.2.1 were phase folded with the period determined in Section 5.2.2. A minimum of 50 data points per slice and filter were required for this. The running median in the phase plot was calculated, using a smoothing over 0.1 in phase. The $\hat{A}^o_\lambda$ is determined as the difference between the maximum and minimum of the smoothed running median brightness in the phase plot. The associated uncertainties $\sigma\left(\hat{A}^o_\lambda\right)$ are determined as the standard error of the mean of the data used to calculate the maximum and minimum median.

The threshold of 50 data points is equivalent to a data point every 3.6 days in the slice. This is fewer points per day than the F21 sample, which required 50 data points per filter for the time period of 80 days, equivalent to one data point per 1.6 d. Therefore, to ensure a high SNR in the measured peak to peak amplitudes and good quality fitting additional selection criteria are applied.

All peak to peak amplitudes in slices for which one or more filters has an SNR below three were discarded. As discussed in Section 4.3 the reliability of the spot property fit is strongly linked to the SNR of the light curve amplitudes. Invoking a SNR threshold of five as examined in Section 4.3 for all amplitudes was deemed to be too restrictive as a threshold, although we will examine how the statistics change if the threshold is increased to five.

Furthermore, an additional selection criterion is introduced considering the phase of the folded light curve. The peak to peak amplitudes in a particular slice were discarded when the phase position of the maximum or minimum in the folded light curve scattered by more than 45 degrees between the three filters. This removed any slices where there was no consistent periodicity between filters. This mostly occurred where the SNR of the peak to peak amplitudes were just above the threshold of three. The phase of each slice shown later on, is calculated relative to a phase zero point. This has been calculated as the median phase value of the maxima in the phase folded light curves across all slices and filters.

5.2.4 Spot property fitting

In Chapters 3 and 4 we have established and tested a method for determining spot properties from $\hat{A}^o_\lambda$ values. This method is applied to every slice with $\hat{A}^o_{\{V\}}$ that fulfilled the criteria in Section 5.2.3.

The spot fitting requires a known stellar temperature for each star. These were taken again, if available, from Fang et al. (2020). As for previous analysis, the stellar temperatures are rounded to the nearest 50K for the spot fitting. Where there is no stellar temperature reference available the median temperature of the astrometric group (a or b) the star belongs to (as discussed in Section 5.1) was used. This is functionally 4100 K for group a, and 3950 K for group b. In Table 5.2 the astrometric group each star belongs to is listed. Adopted temperatures were used for five stars that did not have a temperature reference. As seen in Section 3.6, when the stellar temperature were altered by ± 200 K, the resultant spot properties varied within the statistical uncertainties. The exception to the astrometric group temperature median is object 2, which is significantly brighter at 12 mag in the Gaia G-band. This was identified previously in Section 4.1 where an effective temperature of 5000 K was used to account for its brightness.

5.3 Rotation periods

The previous section establishes the procedure to identify periodic variables and measure peak-to-peak amplitudes with spots. This section examines the resultant periods of the sample of YSOs in IC 5070.

5.3.1 Rotation period distribution

The data set contains light curves in V, R, and I for 131 objects. When divided into the six-month slices, 126 objects had sufficient data in one or more slices to search for a period. For 68 objects a period is detected in at least one slice. Of those, 31 objects meet the criteria laid out in Section 5.2.2 to determine a final period. An additional object is included in the sample (19, separate in Table 5.2) that was removed due to the vicinity of the object to a naked eye star (about three arcminutes away) and the unreliability of the photometry for such objects (see Froebrich

Table 5.2: The target list of all YSOs investigated in this sample. Listed for each object is the assigned ID number, the J2000 coordinates, proper motions, and parallax from Gaia DR3, the astrometric group it belong to, the effective temperature used for spot fitting, the determined period and its uncertainty as determined in Section 5.2.2, its $K - W2$ colour (discussed in Section 6.1.4), the Gaia DR3 ID number, and the F21 ID number of the object in Froebrich et al. (2021). Objects marked with (*) have no effective temperature reference in Fang et al. (2020) and the median of all astrometric group members were used or 5000 K for the bright object (see details in text).

Object ID	RA [deg]	Dec	μ_α [mas/yr]	μ_δ	Parallax [mas]	Group	$T_{\rm eff}$ [K]	Period [d]	Period error	$K - W2$ [mag]	Gaia DR3 ID	F21 ID
1	312.87736	44.06249	-2.125	-3.563	1.270	a	4250	3.165756	0.000050	0.817	2066866222797779072	9321
2	312.87063	44.07308	-1.824	-2.883	1.212	a	5000*	4.82799	0.00026	0.200	2066866287224242432	9267
3	312.78140	44.17626	-1.870	-3.665	1.162	a	4100*	3.53001	0.00013	0.441	2066870689567848192	8038
4	312.74312	44.24230	-1.198	-4.790	1.308	b	4350	4.87960	0.00028	0.710	2067058740416252416	7422
5	312.74341	44.24562	-1.643	-3.794	1.090	a	3700	3.42336	0.00028	0.789	2067058740416252544	-
6	312.45490	44.17951	-1.991	-3.440	1.209	a	4100*	3.30975	0.00019	0.306	2067061042518587264	8025
7	313.09560	44.01580	-1.460	-3.895	1.181	b	3950*	3.63383	0.00055	0.374	2162929419847388544	9961
8	313.35736	44.17924	-0.815	-2.950	1.217	a	4000	1.4533437	0.0000056	0.230	2162934986124720896	7954
9	313.35268	44.34278	-1.226	-3.110	1.291	a	4000	2.779205	0.000058	0.390	2162941273956895872	6393
10	313.09386	44.23338	-1.234	-3.571	1.219	a	4300	3.00608	0.00023	0.910	2162944916089431168	7472
11	312.82599	44.21893	-1.046	-3.998	1.211	b	3950	7.87849	0.00090	1.292	2162947596149035648	7632
12	312.92257	44.25196	-1.278	-3.644	1.339	b	3800	6.7210	0.0018	1.527	2162949382855434496	-
13	312.94394	44.37256	-1.743	-3.242	1.164	a	3950	2.175035	0.000017	0.261	2162950413647417728	6149
14	313.14528	44.23346	-1.826	-3.406	1.209	a	4200	10.63240	0.00042	0.245	2162950546789495552	7465
15	313.14322	44.29450	-1.116	-3.690	1.216	b	3900	7.27588	0.00066	1.508	2162951753677142784	-
16	313.07438	44.35441	-1.463	-3.256	1.239	a	3950	3.211	0.069	0.071	2162955086571795712	6315
17	313.46770	44.28486	-1.437	-3.392	1.234	a	4950	7.3783	0.0076	0.274	2162960481050791936	-
18	313.42432	44.36014	-0.934	-3.183	1.226	a	4900	1.44775	0.00013	0.174	2162964088823157632	-
20	312.75611	44.25956	-1.208	-3.744	1.171	b	3900	5.523	0.051	1.093	2163135573981345280	-
21	312.75654	44.26166	-1.232	-3.811	1.239	b	4000	7.35691	0.00057	1.633	2163135578281583744	7181
22	312.81307	44.30488	-1.019	-4.277	1.197	b	3950	4.22837	0.00032	1.382	2163136059317926016	6813
23	312.71903	44.27889	-1.215	-4.409	1.267	b	4300	8.311	0.089	1.451	2163136368555566848	-
24	312.74460	44.29188	-0.746	-4.149	1.270	b	3900	7.2272	0.0029	1.124	2163136402915307136	6929
25	312.77764	44.36131	-1.538	-2.702	1.285	a	4750	1.39729	0.00013	0.198	2163137261908777472	6259
26	312.84446	44.35210	-1.062	-4.050	1.198	b	3950	3.882	0.021	1.176	2163137742945115136	6337
27	312.81884	44.38277	-1.213	-2.641	1.176	a	4300	2.4243735	0.0000087	0.485	2163138601938577024	6060
28	312.69199	44.31941	-1.146	-4.597	1.379	b	3500	13.690	0.262	1.200	2163139594070911360	-
29	312.93710	44.43861	-1.235	-3.185	1.172	a	3950	3.77296	0.00011	0.217	2163144271295324544	5559
30	313.10923	44.57394	-1.501	-2.871	1.244	a	5500	1.43272	0.00013	0.234	2163146779556221952	4446
31	312.84503	44.56183	-2.157	-3.099	1.273	a	3950*	4.96447	0.00090	1.023	2163148772421081728	-
32	312.72580	44.63561	-2.087	-2.686	1.241	a	3950	9.5466	0.0030	1.280	2163156056685634944	3988
19	313.36180	44.42429	-1.326	-2.740	1.248	a	4100*	0.6261	0.0034	0.259	2162965252757133056	-

et al. (2024)). In the case of object 19, the photometry in the V-band is affected, but a good quality period was determined prior to removal from R- and I-band data, and so is included as part of our period discussion but is not followed up on in spot properties.

From the 32 objects, 22 overlap with the F21 high cadence sample. The objects where a final period could not be determined were also not included in the high cadence sample, with the exception of V1701 Cyg. This source will be discussed in more detail in Section 6.2.1. The high cadence sample identified in Froebrich et al. (2021) contained 40 YSOs. Objects in that work may not be included in this sample because of the change to Gaia DR3 astrometry, or because there was not sufficient available V-band data for the object. The requirement for period searching was the availability of over 50 data points in at least two filters. Therefore, objects that had little to no V-band coverage were not investigated as they would not be suitable for spot fitting analysis.

The final periods for this sample and their uncertainties are listed in Table 5.2 together with other source properties. Listed in this table are the adopted source ID number (based on the sorted order of their Gaia DR3 ID), the J2000 positions, proper motions, and parallax, the astrometric group they are a member of, the effective temperature used for the spot fitting (from Fang et al. (2020) and discussed in Section 5.2.4), the final periods and their uncertainties, their $K - W2$ colour (discussed in Section 6.1.4), their Gaia DR3 ID, and the F21 ID numbers from Froebrich et al. (2021) for overlapping sources from the F21 sample.

The period distribution of the sample in presented in Fig. 5.2. In blue a histogram of the periods, with 1 d bins, is displayed. A CDF is over plotted as a solid black line. The vertical dashed line at $P = 5.5$ d separates fast and slow rotators. The F21 sample was identified as bimodal with the separation of fast and slow rotators at $P = 5.5$ d, the same value is adopted here as this distribution follows the same bimodality.

This bimodality has been identified in many other samples of YSOs, such as e.g. in ONC, NGC 2264, and the Perseus molecular cloud (Rodríguez-Ledesma et al., 2010; Herbst et al., 2007; Wang et al., 2023). The cause of this bimodality is attributed to star-disc interactions via magnetic fields. Long rotation periods are hence indicating a disc slowing the rotation rate. Conversely,

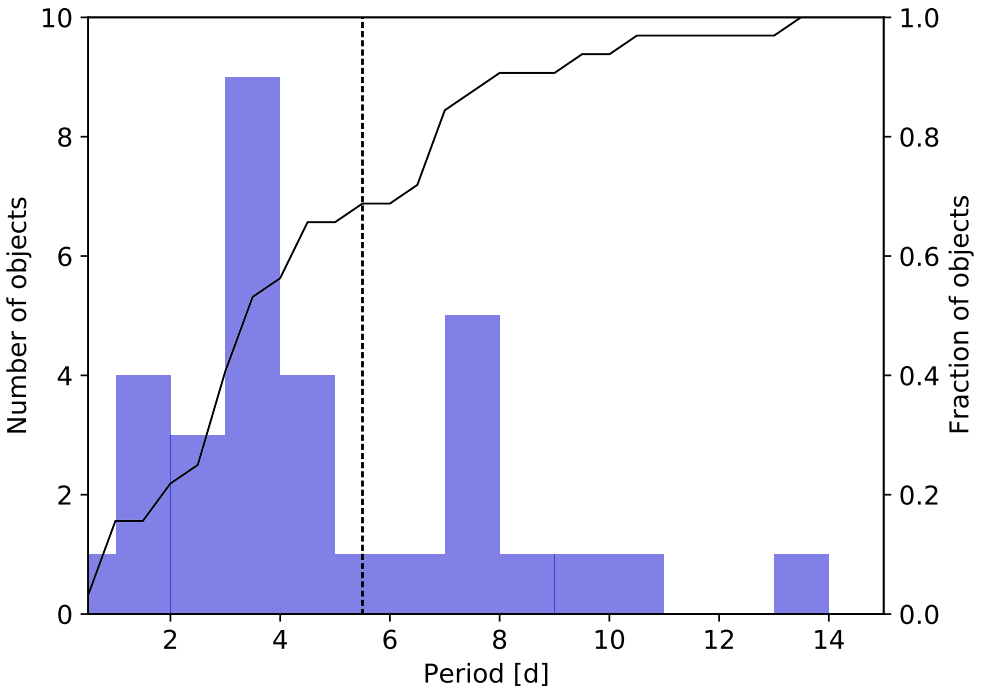

Figure 5.2: Distribution of measured periods of YSOs in the IC 5070 sample. The solid black line represents the cumulative distribution function. The dashed vertical line placed at a period of 5.5 d separates slow from fast rotators.

once the disc is dissipated or looses the magnetic connection to the star, the star begins to 'spin up', leading to fast rotators.

Of these objects, 23 are found to have $P < 5.5$ d and 9 have $P > 5.5$ d. The distribution roughly peaks at $\sim$3 d and $\sim$7 d, with a gap in-between. This is, within the statistical noise, comparable to the F21 sample, which found 25 fast and 15 slow rotators. Therefore, roughly two thirds of the YSOs in IC 5070 are fast rotators. In the F21 sample, there is a gap in the period distribution between five and six days was identified. Here, object 20 is the first source that populates this gap with a period of $P = 5.52$ d. This object is in the transition between the slow and fast rotators in its evolution.

5.3.2 Comparison with literature periods

Listed in Table 5.2 are the ID numbers from the F21 sample for the objects that were previously identified as periodic. The ten objects that do not have such an ID are hence newly identified

rotational variables. They were investigated in Froebrich et al. (2021) but no period was found. That work focused only on an 80 d duration, high cadence part of the HOYS IC 5070 light curves in 2018. These data are roughly in the middle of slice 17, but that slice contains all the data for the 6-month period from MJD = 58162.5 − 58345.5. For five of the new periodic sources (object 5, 15, 17, 23, 28) no periodicity is observed in slice 17. But they have been identified as periodic in other slices. Therefore, it is most likely that their amplitudes of variability were too low during that time for the periodic signal to be detectable. For the remaining five sources (object 12, 18, 19, 20, 31) a period is detected in the slice 17 data. This can have two reasons: i) The object has shown slightly stronger (higher amplitude) periodic variability outside the 80-day window investigated in Froebrich et al. (2021), which is included in the slice 17 data. ii) The slight lowering of the detection threshold in the periodograms (see Section 5.2.2) and the ability to confirm these periods in many other slices.

The periods identified here do not all lie within the previously identified uncertainties (see Table 3.1). However, the median separation between these periods and the previously identified periods is 0.27 percent, with a maximum of 1.45 percent. Therefore, there are no significant changes in the determined periods between the two works. Here, the entire light curve is used, and are therefore the periods are verified with multiple slices. Therefore, the periods identified here are more accurate/reliable.

Bhardwaj et al. (2019) also investigated variability of YSOs in IC 5070. Six objects from their work overlap with objects previously identified in Froebrich et al. (2021), where all but one agree on the period. Now identified are three additional overlapping objects, namely objects 20, 23, and 28. Object 20 was identified in Bhardwaj et al. (2019) as variable but not periodic. Object 23 was identified in Bhardwaj et al. (2019) with a period of 8.446 d, as opposed to 8.3115 ± 0.089 d identified here. The earlier value is slightly outside our uncertainty range. Given this work's longer data set and the identification of this period in seven slices, the period identified here is more reliable. Most noteworthy is object 28 which was identified in Bhardwaj et al. (2019) with a period of 0.518 d. This object, as shown in Table 5.2, has the longest period in the sample at

$P = 13.690 \pm 0.262$ d. It also has the highest absolute period uncertainty in the sample (object 16 has the highest relative period uncertainty). This is due to the best period measurement from the I-band periodogram being quite far from the results using the R- and V-Band periodograms (see Section 5.2.2). The amplitudes in V and R for this source are much higher than for the I-band, which can explain this difference. Furthermore, in the period search periods within 1% of 0.5 d are excluded, as these are on the edge of the investigated parameter space. In order to confirm a period close to 0.5 d as in Bhardwaj et al. (2019) was not excluded, the original identified candidate periods, prior to these exclusions were investigated. Object 28 had no other significant candidate periods outside of the primary group of 15 detections. That group had a median period of 13.620 d, and a standard deviation of 0.098 d. This implies that our period for this source is reliable and the nominal uncertainty is lower than the quoted ± 0.2618 d.

5.3.3 Gaia colour magnitude diagram

Presented in Fig. 5.3 is the Gaia $BP-RP$ versus G colour magnitude diagram (based on Gaia DR3) for all 336 potential IC 5070 cluster members (groups a and b). The periodic objects in the sample are overlaid as coloured circles. The symbol size is proportional to the period and the colour indicates the $T_{\rm eff}$ used in the spot property determination (as in Table 5.2). The periodic variables show the same distribution as the other potential cluster members. There is no significant trend between period and colour. They cover a colour range of 1.8 mag $< BP - RP < 2.8$ mag, and have a lower brightness limit of $G \sim 17$ mag. This is due to fainter sources having more noisy HOYS photometry, not allowing the detection of low amplitude periodicity. The brightest source is object 2 at $G \sim 12$ mag. As discussed in Section 4.1 a temperature of 5000 K is used for the surface temperature of this source.

Object 30 is the hottest object with a temperature of 5500 K. However, it is also the reddest with $BP-RP \sim 2.8$ mag. Fang et al. (2020) provide an extinction of $A_V = 5.0$ mag for this source. In the F21 sample contained three objects similar to this. However, in the updated Gaia DR3 cluster members list, object 30 is the only object that is identified and crosses over with the previous

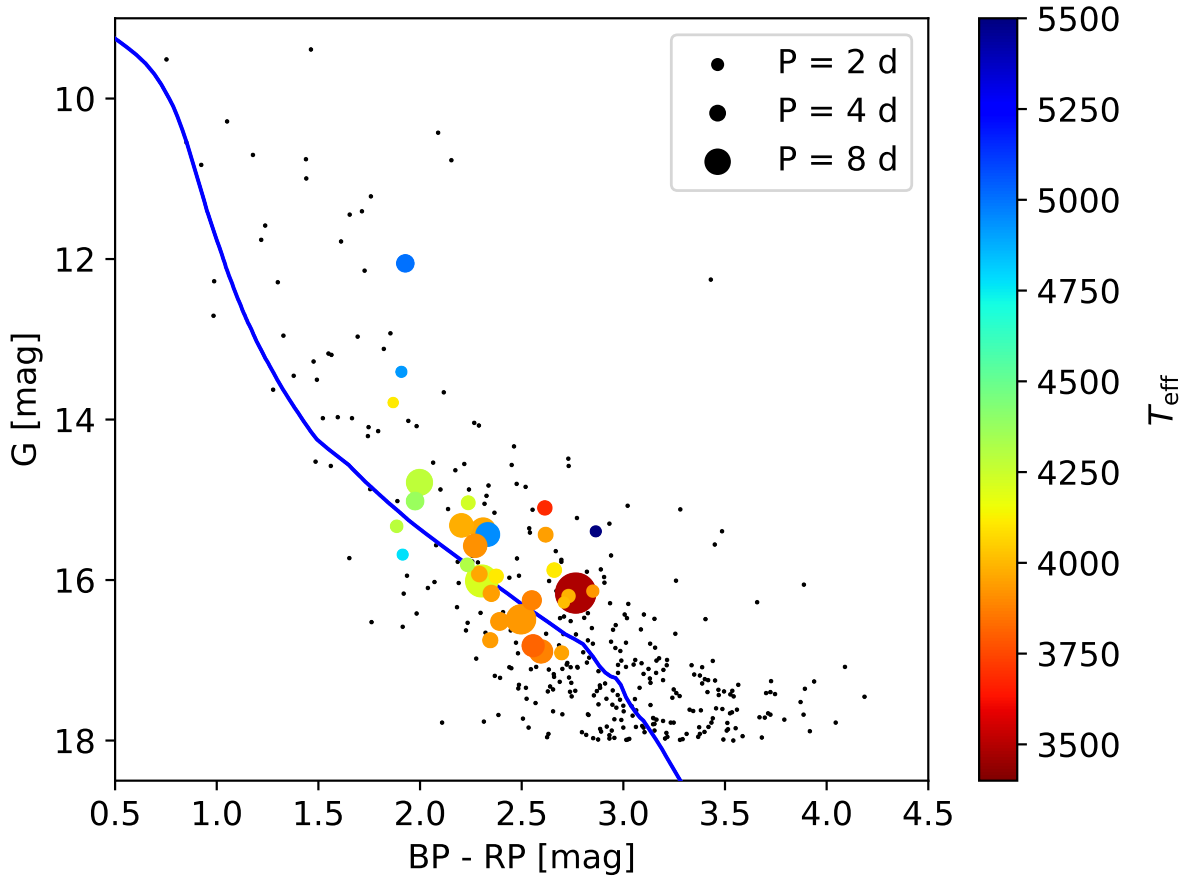

Figure 5.3: $BP - RP$ vs. G colour magnitude diagram. All selected IC 5070 cluster members are shown as black points and periodic objects are in colour mapped to their effective temperature from Fang et al. (2020), or the sample median. The marker size is scaled to the period, as shown in the legend. Overlaid in blue is a 1 Myr PARSEC isochrone, translated to apparent magnitude with the sample median distance (Bressan et al., 2012).

sample. The potential that the object is a contaminant is considered, but it has $d = 803.5\,\mathrm{pc}$, $\mu_\alpha = -1.501$ mas/yr, $\mu_\delta = -2.871$ mas/yr which places it within group a of the cluster. It has a short period with $P = 1.4327 \pm 0.0001\,\mathrm{d}$, which indicates it has lost its connection with its disc. The $K - W2$ colour of 0.23 mag indicates a lack of inner disc material. No $W3 - W4$ colour is available for the object due to a poor signal to noise.

A digitized sky survey (DSS) image of the region is shown in Fig. 5.4. The positions of all identified periodic objects are over plotted. Object 30 is the only object positioned among one of the dark clouds in the North of the region. It is likely then that this object is strongly reddened by non-variable extinction.

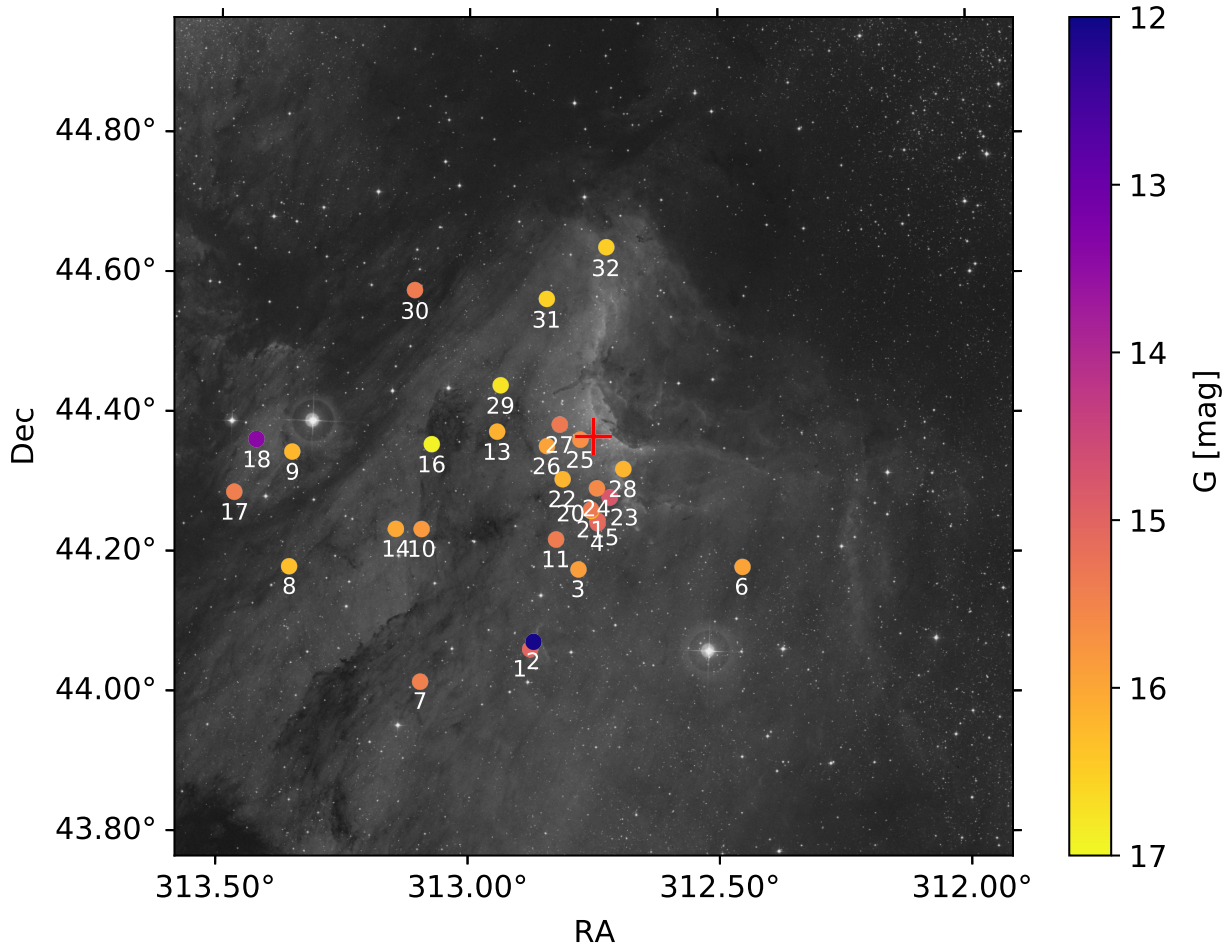

Figure 5.4: DSS Red image of IC 5070, 1.2 degree square measured from the centre point. Centre point marked with red cross. Objects in our sample are labelled and color scaled to the Gmag brightness.

6

Spot property evolution

This chapter examines the results of the spot fitting methodology applied to 32 YSOs in IC 5070 over $\sim$5 yr of available light curves. The majority of the results and discussion are published by the thesis author in Herbert et al. (2024).

6.1 Results and discussion of spot properties

This section will discuss the results from the peak to peak amplitude measurements and the spot property determination. Three of the 32 objects with periods determined from R- and I-band data have no fitted $\hat{A}^o_{\{V\}}$. Object 19 is removed to due to unreliable V-band photometry, as mentioned in Section 5.3. The other two (12 and 15) are due to an insufficient number (less than 50) of data points in V.

6.1.1 Object result summary plots

All measured and determined properties for objects in this sample are summarised in result summary plots, the first of which, for object 1, is shown in the left panel in Fig. 6.1. The plots for all other objects can either be found in the main body of the paper (1,2,3, and 4) if they are discussed in detail, or in the Appendix B.2. In this section we describe the details of these plots.

The data points in each panel of these figures are plotted at the Modified Julian Date (MJD) of the start of each slice (bottom x-axis), and the slice number is shown at the top x-axis. Above that axis the period for the object is noted. The vertical gray dashed lines indicate one year intervals every start of February. Therefore, the slices just left of the gray lines are centred on the times of worst observability of the field and hence usually contain the least amount of data (as discussed in Section 5.2.1).

The first (top) panel in these result summary plots (as e.g. Fig. 6.1) shows the peak to peak amplitude $\hat{A}^o_V$ (green), $\hat{A}^o_R$ (red), and $\hat{A}^o_I$ (black) values as coloured dots and their uncertainties $\sigma\left(\hat{A}^o_\lambda\right)$. The second panel shows the phase position (in degrees) of the maximum brightness in the phase folded light curve in each filter with the same colour coding as in the top panel. The zero point for these phase values has been set as the median of all determined values for each object. The blue line indicates the running median of the phase positions over all filters in the slice and the light blue shaded area indicates the RMS scatter of the points from that running median.

As laid out in Section 5.2.3, there are requirements for SNR above three for all amplitude measurements and an RMS scatter below 45 degrees for the minimum/maximum brightness phase

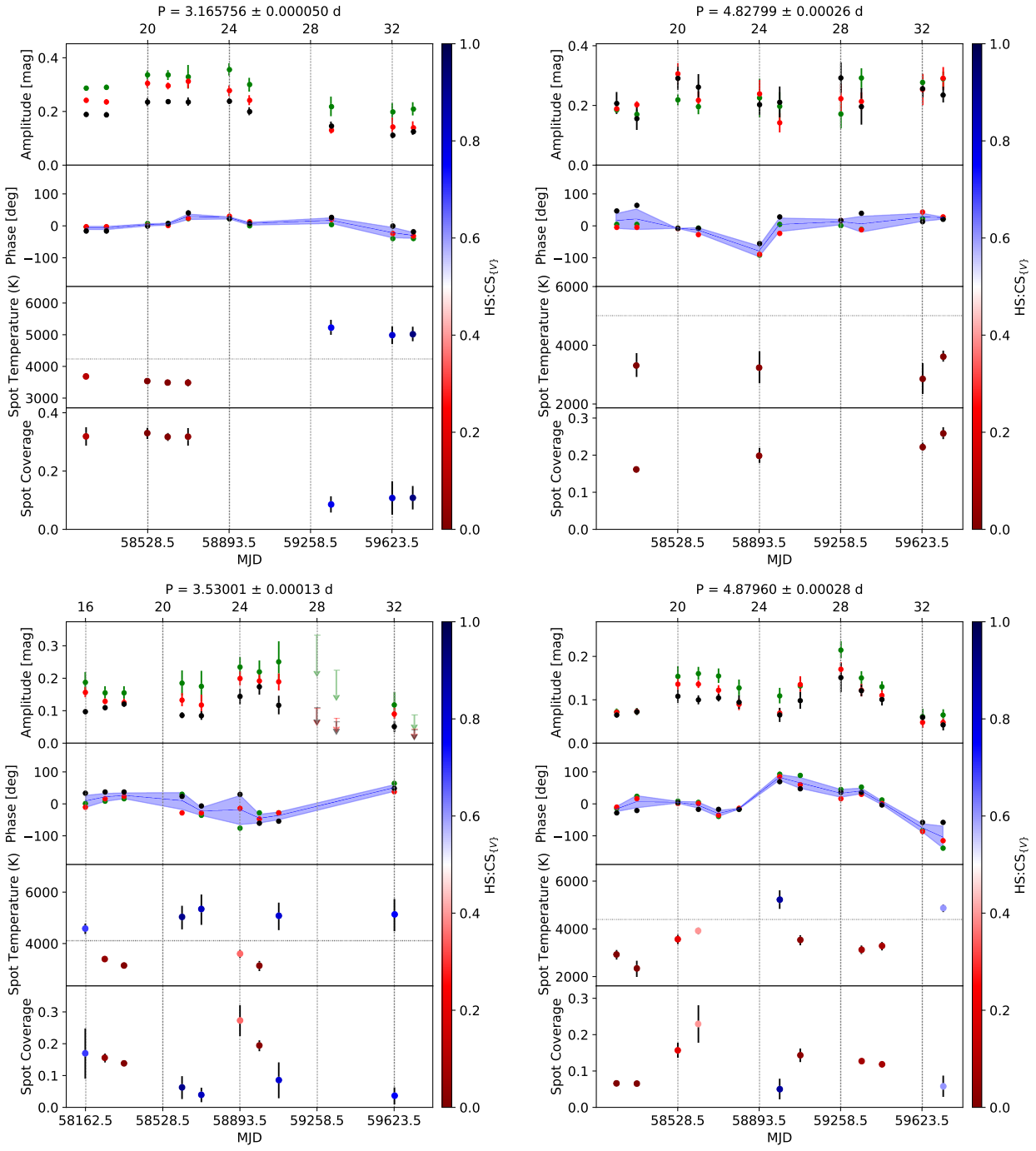

Figure 6.1: Result summary plots for the first four objects in our sample. The data for object 1 are shown in the top left panel, object 2 in the top right panel, object 3 in the bottom left panel, and object 4 in the bottom right panel. In each of the summary plots we show from top to bottom the peak to peak amplitudes, the maximum brightness phase positions, the determined spot temperatures, and the spot coverage against time. For more details see the description in Section 6.1.1.

positions. Therefore, only data in slices where these criteria are satisfied are shown as coloured points in the top two panels. In slices where one or more of the filters do not have a SNR above three for the peak to peak amplitudes, the 3σ uncertainties are shown as light-coloured arrows instead and no phase positions are shown. The first example of this is object 3 (see bottom left panel in Fig. 6.1). In cases where the amplitudes have the required SNR but the phase position varies more than 45 degrees between filters, the three sigma noise is displayed as light coloured crosses and again no phase positions are shown. This happens e.g. for object 7 (see Fig. B.2 in the Appendix). In all slices without any data shown, there are less than 50 data points in at least one of the filters.

The third and fourth (bottom) panels in the result summary plots show the determined spot properties and uncertainties for each slice, if the $\hat{A}_{\{V\}}$ amplitudes and phase positions have the required accuracy. The spot temperatures (in degrees Kelvin) are shown in the third panel. The dashed horizontal line indicates the surface temperature of the star (as listed in Table 5.2). The bottom panel shows the spot coverage. The displayed error bars represent the MAD uncertainties. The colour coding of the symbols in the bottom two panels follows the scale shown at the right hand side of the figure. It represents the ratio of the hot spot to cold spot solutions (HS:CS$_{\{V\}}$) during the spot property fitting. Therefore, spots that are mostly fitted as cold spots are shown in red, and spots that are mostly classified as hot spots are displayed in blue.

6.1.2 Amplitude and phase evolution

A quarter of the objects have $\hat{A}^o_{\{V\}}$ values near continuously from the start to the end of their light curve, only missing individual or pairs of $\hat{A}^o_{\{V\}}$ due to insufficient data or low signal to noise. Two objects only contain a single slice with $\hat{A}^o_{\{V\}}$ measurements. The median number of $\hat{A}^o_{\{V\}}$ values is nine, and the maximum is 15. The primary reason for slices missing $\hat{A}^o_{\{V\}}$ values is insufficient data. As mentioned in Section 5.2.1, slices centred on February contain the fewest data points, and as such these slices are often missing. A number of objects show longer breaks in $\hat{A}^o_{\{V\}}$ values due to low signal to noise values and have hence the 3 σ noise shown in their result summary plots.

These sources are thus showing longer periods of no or undetectable spots on their surface. We are unable to observe any activity cycles in the sample as this requires longer light curves.

The periodic variability detected here is due to rotational modulation over the ~ 180 d length of a light curve slice. Not showing $\hat{A}^{o}_{\{V\}}$ values with the required signal to noise during a slice does not mean that the object has become quiescent. Rotational modulation is caused by asymmetry in the spot distribution. Therefore, two similar surface features separated by 180° in longitude, i.e. on opposite 'faces' of the star, will not produce a detectable rotational brightness modulation. Additionally, a significant change of the spot properties (temperature, coverage) or position (phase) during the 180 d in a slice, will not allow for detection of the periodic brightness changes. Such slices will hence usually only have the noise shown in the result summary plots.

Examining the phase position over the length of the light curves provides a further check of the quality of the period determination. In case there is a systematic, linear trend in the phase position over time, then this can be considered as an indicator of a small systematic error in the period of the object. None of the objects shows such a behaviour over the typically 4 – 5 yr length of the light curves. Furthermore, the phase position tracks the longitudinal position of the surface feature on the star. The average uncertainty in the phase is 15° . Therefore, changes in phase can track the relative longitudinal position of the spot on the surface relative to the start of the light curve. These changes can either be caused by actual movement of the spots on the surface, or the appearance/disappearance of spots at different longitudes. The majority of objects show no significant phase shifts over the length of their light curve. There are some exceptions to this, and two examples are discussed in Sects. 6.2.3 and 6.2.4. An in depth study of the spot lifetimes and their appearance at different longitudes requires much longer datasets.

6.1.3 Spot property distribution

In the F21 sample, the cold spot objects outnumbered the hot spot objects by a factor of 3.5, the proportion of hot spots this therefore 0.22 ± 0.08. About 13 percent (4 stars) of the periodic YSOs did not result a valuable spot solution (2 stars) or they are potential AA Tau-like contaminants (2

stars).

We now consider the determined spot properties from the observed $\hat{A}^o_{\{V\}}$ values for all slices in the periodic objects. Each of the 234 slices with high signal to noise peak to peak amplitudes is considered in the statistical analysis. However it is important to note, that neighbouring slices do overlap by 3 months. In those 234 amplitude sets 180 are reliably fit as spots. Of these 125 are identified as cold spot solutions and 55 solutions as warm or hot spots. Therefore, cold spot solutions outnumber the warm/hot spot solutions by a factor of about 2.3, slightly less than the F21 sample. The proportion of warm/hot spots is therefore 0.31 ± 0.03, which is within the error of the F21 sample results. In the remaining 54 slices no reliable spot solution can be found (21) or the best solution is at the edge of the investigated parameter space (33). This fraction of about 23 percent is about twice as high as the first sample.

In Section 4.3.2, it was demonstrated that a limitation of SNR > 3 effectively removed many objects that had HS:CS$_{\{V\}}$ ratio close to the ambiguity threshold. Meanwhile, SNR above five removed all but the extremes in HS:CS$_{\{V\}}$. These statistics for $\hat{A}^o_{\{V\}}$ of this sample are repeated, with a lower limit of five for the SNR of the amplitudes. There are 138 $\hat{A}^o_{\{V\}}$ with SNR over five, 109 are reliably fit as spots. There are 15 spots classified as ambiguous due to their HS:CS$_{\{V\}}$ ratio, and 14 at the edge of the temperature/coverage parameter space . The removal fraction when using a threshold of five is therefore 21 percent. In the SNR over five sample 23 are warm/hot, and 86 are cold. This is a somewhat larger fraction of cool spots, but with a smaller sample the number statistics are limited. The distribution of the spots are included in the Appendix (Section B.1), the population of low coverage cold spots is significantly reduced. This reinforces the decision to use SNR threshold of three. The sample size is greatly increased, as 40 percent of the slices have amplitudes with SNR 3 – 5. Additionally, using SNR above five does not provide greater retention or reliability when fit with spots.

The difference between the spot temperature and stellar surface temperature $T_S - T_\star$ for all spot solutions is plotted against the spot coverage in the left hand panel of Fig. 6.2. The colour coding of the symbols refers to the HS:CS$_{\{V\}}$ ratio. We see that there is a 'gap' in the temperature difference

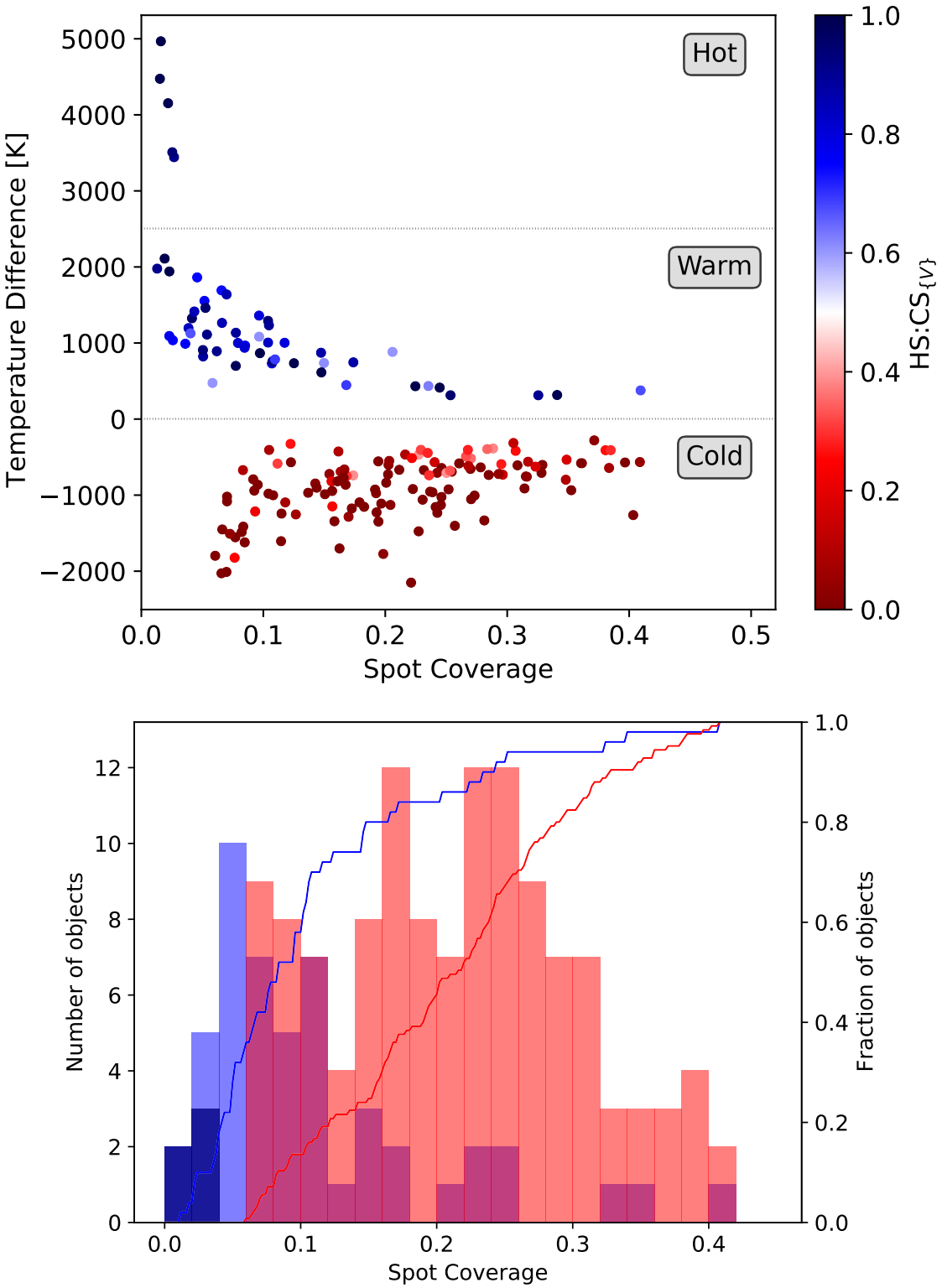

Figure 6.2: **Top:** Spot temperature difference $T_S - T_\star$ versus spot coverage. Horizontal dotted lines mark $T_S - T_\star = 0$ K and $T_S - T_\star = 2500$ K, which separate the cold, warm and hot spot solutions. The markers are colour coded according to the HS:CS$_{\{V\}}$ ratio. **Bottom:** Distribution of spot coverage of hot (dark blue), warm (blue), and cold spots (red). The solid lines are the CDFs of the warm (blue) and the cold spots (red).

distribution between about two and three thousand Kelvin. Thus far we have considered all spots above the stellar temperature as 'hot' spots. Now, we refine this as spots with a temperature difference above 0 K and below 2500 K are denoted as warm spots, and all spots that have more than 2500 K temperature difference are denoted as hot spots. The differences between these groups will be discussed in Section 6.1.3. Presented in the right hand panel of Fig. 6.2 is the distribution of the spot coverage for hot, warm, and cold spots as histograms, as well as cumulative distribution functions (CDFs) for the latter two.

Cold spots

In Section 3.7 we simulated periodic variability due to extinction from large dust grains as found in the inner disc, and found that when this variability is fit as spots, the resultant spots clustered at the lower temperature boundary of the PHOENIX models (2000 K), or at the $f = 0.5$ boundary for the coverage. Therefore, spots are removed if they are fitted as implausibly large or cold, i.e. within 10 percent of $f = 0.5$ and $T_S = 2000$ K. 27 spots were removed because of their temperature, all but two were within 2.5 percent of the lower temperature limit. Six further spots were removed for being too close to $f = 0.5$. Although a ten percent margin was adopted near this value, all spots that were removed were within three percent of it. The largest spot remaining in the sample has a coverage of $f = 0.408$. The clustering around the parameter space boundaries indicates that the peak to peak amplitudes for these objects cannot be fit with our simple spot model. The remaining objects which are considered valid solutions for the spot properties are significantly away from the parameter space borders.

Among the cold spots 90 percent are between 0 K and 1500 K below the stellar surface temperature. The coldest spots with temperatures more than 1500 K below the surface temperature, have a spot coverage of less than $f = 0.25$. There are no observed cold spots with a coverage above $f = 0.25$ and more than 1500 K below the surface temperature, which has several contributing factors. These objects likely have a complex network of surface features, and the model simplifies it to one uniform spot temperature and a fixed surface coverage. The coverage calculated is the asymmetrical part of the spot distribution, and so it represents a lower limit. The distribution of

the cold spot coverage values appears homogeneous from the lower limit of $f = 0.06$ to $f \sim 0.3$, where it tails off. A two sided KS-test indicates a probability of 34.4 percent that the observed coverage distribution in this range is homogeneous. This is well above the 5 percent threshold for rejection of the null hypothesis, the null hypothesis that the two distributions are dissimilar is rejected.

Spots are modelled up to 0 K temperature difference compared to the star and zero spot coverage. However, there is a clear observational bias just above and below $T_S - T_\star$ = 0 K and for very small coverage values. There the temperature difference and/or spot coverage are not sufficient to produce a SNR above three for the peak to peak amplitudes. This is demonstrated in the left panel of Fig. 6.2, where for the cold spots the minimum coverage is $f = 0.061$ and the smallest temperature difference is 283 K below the stellar temperature. Thus, we are unable to detect objects above the upper envelope of points in the $T_S - T_\star$ vs. f plot (Fig. 6.2, left). The lack of objects at larger temperature differences and large coverage values is however real. This is reminiscent of the simulations discussed in Section 3.6, which demonstrated the systematic effects in the methodology. These cause the spot properties near the upper envelope to be determined as slightly smaller and at a slightly larger temperature difference. However, these systematic shifts are always smaller than the MAD uncertainties for the spot temperature and coverage.

Warm and hot spots

For spot solutions with temperatures above the surface temperature, the spot parameters cover a wide range of temperatures and sizes. 90 percent of these spot solutions have temperatures that are less than ∼2000 K above the stellar temperature. There is also a dearth of spots found between 2000 K and 3000 K above the stellar temperature. Due to this large apparent gap in the distribution, we use a spot temperature of 2500 K above the stellar temperature to separate warm and hot spots, and discuss these separately. The number of warm/hot spots in the F21 sample was very small. Only six warm/hot spot solutions were found, 19 percent of all spot solutions in that sample. Five of these were warm spots and one object had a spot temperature difference of 2650 ± 970 K, i.e was situated in the apparent gap of temperature differences. With many more YSOs in all HOYS

fields to be investigated in Chapter 7, we will have a much better statistical picture if this apparent gap is indeed real.

Five hot spot solutions are identified that have a temperature difference of more than 3000 K above the stellar temperature. The upper limit for the temperature in the spot models is 10000 K. Three of the hot spots are within ten percent of this upper limit. All of the hot spots are very small, with a maximum coverage of $f = 0.027$. This is expected for accretion column footprints (e.g. Hartmann et al., 2016; Muzerolle et al., 1998). Four of the five hot spot solutions occur on a single object (30, see Fig. 6.5). We will discuss this star in more detail in Section 6.2.7. There are currently very limited statistics about the hot spot solutions.

Similar to the cold spots, there is a bias against the detection of small warm spots with low temperature differences compared to the stellar temperature. The smallest temperature difference measured in the warm spot regime is 310 K above the stellar temperature. However, due to the temperatures and filters involved, the regions of undetectable warm spots (defined by the lower envelope in the $T_S - T_\star$ vs. f plot in the left panel of Fig. 6.2) are much smaller. Similarly it again appears that higher temperature differences between spot and stellar surface usually correspond to low coverage values. However, small coverage values do not necessarily correspond to a high temperature difference, as a number of warm spots also occupy the low temperature difference and coverage range. Furthermore, there is a much better defined upper envelope in the $T_S - T_\star$ vs. f plot, above which either spots do not exist or are rare enough that they do not appear in this sample.

Compared to the hot spot solutions, the warm spot solutions cover a wide range of sizes. The largest warm spot is as large as the largest cold spot. However, unlike the cold spots the distribution in coverage is not homogeneous. The histogram in the right hand panel in Fig. 6.2 shows a clear peak at lower coverage values. A two-sided KS-test was performed comparing the coverage values for the warm spots with coverage values between zero and 0.2. We find a probability of 43.3 percent that the distribution can be drawn from a normal distribution in this range. However, there is a clear tail of much larger coverage values and that the low coverage values are influenced by bias in the detections. There are eight warm spots (16 percent of total warm spots) that have a

coverage above $f = 0.2$, as opposed to a 60 percent of the cold spots. The largest warm spot from the F21 sample was $f = 0.125$.

Although, we observe the distribution as an approximate normal distribution, this may be heavily influenced by observing bias. As discussed in Section 3.6, a warm spot that is 400 K above the stellar temperature requires a coverage of at 0.1 – 0.15 to generate SNR above three in all amplitudes. Therefore, the true distribution may approximate to a power-law with an observing bias against low temperature contrast, low coverage warm spots.

Rapidly changing spot properties

If one looks through the result summary plots for all objects (e.g. Fig. 6.1 or in Appendix B.2), there are several examples where a spot solution changes from a warm to a cold spot (or the other way) in neighbouring slices. Usually these cases create single-slice warm spots on otherwise cold spot dominated objects. Note that there is not a single case of three consecutive slices where the middle one has a different classification (warm/cold) from the two others. Here we briefly examine these changes in the classification from one slice to the next, and how they relate to changes in the HS:CS$_{\{V\}}$ ratio.

In the spot fitting methodology (see Section 3.5.1) the measured $\hat{A}^o_{\{V\}}$ values are varied within their uncertainties 10000 times, to estimate the MAD errors for the spot properties, and to determine the HS:CS$_{\{V\}}$ ratio. This ratio indicates the fraction of all solutions that are hot/warm spots compared cold spots. The cut-off for HS:CS$_{\{V\}}$ values for spot fitting solutions to be considered ambiguous is somewhat arbitrarily decided as between 0.4 and 0.6. Examining the relationship of the spot parameters (in particular the temperature) and HS:CS$_{\{V\}}$ over time, shows that in many occasions towards a switch from a cold to a warm spot or visa versa, the HS:CS$_{\{V\}}$ value does approach the boundary for ambiguous solutions.

A small hot spot can make a significant contribution to the peak to peak amplitudes. In the 180 d long slices used here, the asymmetric part of the spot distribution on the stars can evolve. In particular contributions from accretion hot spots, caused by material flowing along magnetospheric structures which might be short lived compared to the duration of a slice (e.g. Donati et al.,

2012), need to be stable throughout the slice to create regular periodic light curves (Kurosawa & Romanova, 2014), and hence allowing us to reliably determine their resulting spot properties. Therefore, evolving spots will most likely lead to HS:CS$_{\{V\}}$ values changing or moving into the range where no clear solution can be found. Given the very small fraction (5/234, i.e. 2.1 percent) of hot spot solutions, we can conclude that it is highly unlikely that the spot footprints of the accretion columns are stable over timescales of half a year. Object 30 which seems to be the exception to this is discussed in Section 6.2.7. On the other hand, the much larger fractions of reliable warm and cold spot solutions found indicate that the physical causes (see Section 6.1.4) for these are typically stable for longer than half a year.

In Fig. 6.3 two examples are presented (object 13 left panel, and object 18 right panel) of these changes for the classification from a warm to a cold spot solution within the duration of one slice. Object 13 shows predominately cold spots, with exceptions in slices 21 and 24. The slices next to them, which contain overlapping data show cold spot solutions. The peak to peak amplitudes surrounding this pattern do not show any corresponding significant change. For slice 21, the HS:CS$_{\{V\}}$ ratio is 0.608, very close to the adopted cut-off. The spot properties for slice 23 are ambiguous since the HS:CS$_{\{V\}}$ ratio is 0.423, and in slice 24 the ratio is 0.795. Therefore, during this entire period the surface features on this objects probably evolve on timescales shorter than half a year and hence no clear, indisputable spot solution with our simple model can be found. Similarly, slice 20 in object 18 shows a brief change in classification (warm spot compared to cold spots throughout), accompanied by a HS:CS$_{\{V\}}$ ratio of 0.848. In this slice the peak to peak amplitudes are clearly different, especially in the V-band, and that there is no data in the preceding slice 19. Therefore, the statistical interpretation of the distribution of the warm and cold spot solutions, needs to take the respective HS:CS$_{\{V\}}$ ratio into consideration. In other words, the more lightly coloured spot solutions in the bottom panel of Fig. 6.2 should be considered slightly less reliable than the darker coloured ones.

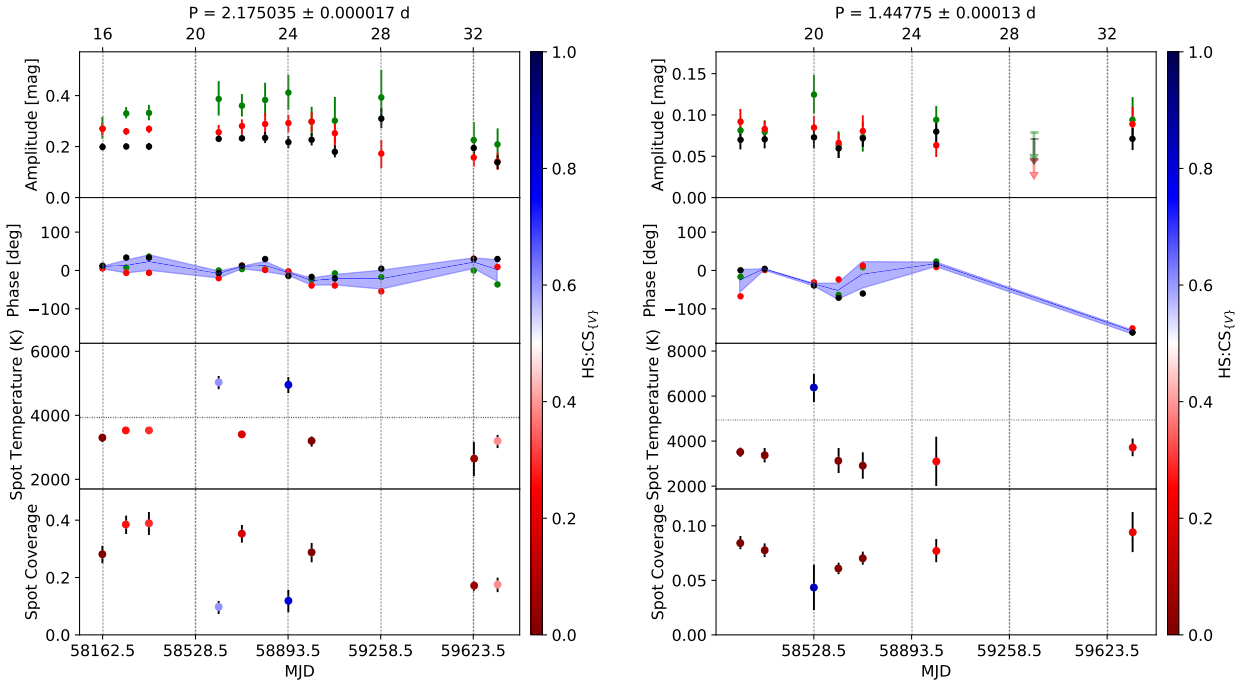

Figure 6.3: As Fig. 6.1, but for the objects 13 (left) and 18 (right).

6.1.4 Relation of spot and stellar properties

In this section we briefly examine how the determined spot properties relate to the stellar properties. These objects are likely to exhibit multiple, potentially evolving, surface features at once. As discussed in Section 6.1.2, rotational modulation is caused by the asymmetric part of the spot distribution. In order to represent the spot properties of individual objects, we will consider *dominant spot properties* throughout this section. These are defined as the proportion of reliable spot property solutions for an object, as plotted on Fig. 6.1 and subsequent figures, that are above (warm/hot) or below (cold) the stellar temperature.

Stellar rotation periods and disc excess emission

In Fig. 6.4 the dominant spot properties are related to the period and $K - W2$ colours for the objects. The marker colour in the figure indicates the proportion of the spot properties that are warm/hot spots. One (dark blue symbols) indicates that all reliable spot solutions are warm/hot and zero (dark red) means they are all cold. This is not to be confused with the ratio HS:CS$_{\{V\}}$,

which is part of the result of the spot fitting process for an individual slice. There are three objects that show equal numbers of warm/hot and cold spots. The marker size in the plot is scaled to the number of spot measurements, i.e. larger circles represent sources with more reliable spot solutions. Note that this is not equal to the number of $\hat{A}^{o}_{\{V\}}$ values, as some of them result in ambiguous spot solutions for which no spot temperature and coverage can be reliably determined.

In Fig. 6.4 a horizontal dashed line marks $K - W2 = 0.5$ mag (Teixeira et al., 2012) which separates sources with a detectable warm inner disc (above) and without (below). The $W2$ data is obtained in all cases from the WISE All-sky catalogue (Cutri & et al., 2013). For the K-band magnitude we generally use 2MASS (Skrutskie et al., 2006), with the exception of object 17 for which this is not available. We utilise the UKIDSS GPS data (Lucas et al., 2008) for this source. The absence of excess $K - W2$ emission typically indicates a lack of warm dust in the inner ($\sim$1 AU) disc. The vertical dashed line at 5.5 d in Fig. 6.4 separates fast (left) from slow (right) rotators.

In this sample 15 objects do not show a disc excess emission and 14 objects do. This disc fraction of about 50 percent is consistent with the value for this cluster determined in Froebrich et al. (2024), and also with the typical age of about 1 Myr of the objects in the region (Kuhn et al., 2020). Based on this age it is unlikely that the non-disc objects have fully evolved discs. It is more likely that they have cleared their inner discs as transition disc objects or pre-transition disc objects.

Observations at longer wavelengths can be used to probe the presence of disc material further from the star. Unfortunately almost half of our objects do not have a detection with a sufficient SNR in the $W3$ and $W4$ bands to characterise the cooler material of the outer disc. There are 17 objects, however, that have a better than 5σ detection in all four WISE filters. We determine the slope of the spectral energy distribution (α_{SED}) following Equation 4.1 for all of these. We find that amongst the 17 objects, one is classified as a Class 1 protostar (28), 15 are Class 2 objects, and one (7) is a Class 3 source. Therefore, if these objects are representative of the entire sample, we find that 88 percent of our objects are Class 2 sources, in good agreement with the typical age of

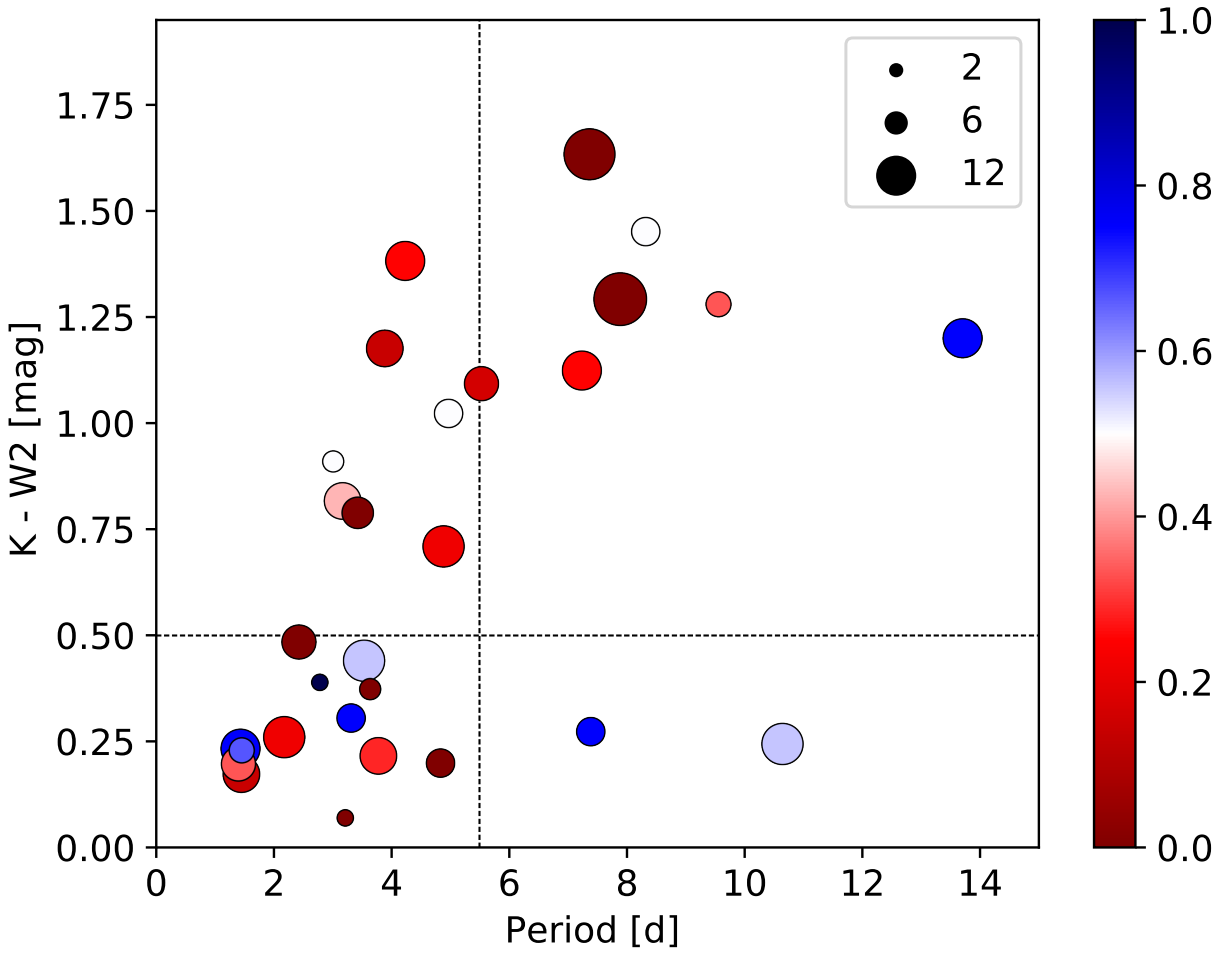

Figure 6.4: Period against $K - W2$ for periodic YSOs. The horizontal dashed line separates objects with a detectable inner disc (above) from sources without (below). The vertical dashed line separates fast and slow rotators. Markers are coloured based on the proportion of warm/hot spot measurements on them, according to the colour scale on the right. Values of zero (dark red) indicate that all spot solutions are cold, values of one (dark blue) mean all spot solutions are warm/hot. The marker size is scaled to number of spot property measurements, as shown in the legend.

the stars in the region.

The bimodal period distribution in our sample has been discussed in Section 5.3. A longer period may indicate that the central star still has magnetic ties to the inner disc, slowing rotation. Faster rotators have been spinning up due to a lack of this disc-breaking mechanism (Herbst et al., 2007). The majority (20/29, i.e. 70 percent) of our objects are fast rotators. Of those, a majority of 13/20 (65 percent) show no detectable inner disc. There is a loose positive correlation of the rotation period and disc excess emission, with the exception of a few select objects (14 and 17), which have a longer period without inner disc emission. The very fast rotators ($P < 3\,\mathrm{d}$) do not show evidence of an inner disc.

Causes of the surface spots

In Fig. 6.4 it is clear that the majority of the objects in this sample are dominated by cold spots. This is expected as 70 percent of our reliable spot solutions are cold. The presence of these cold spots on young stars is well understood as being caused by magnetic activity on the stellar surfaces, driven by the rotation of the stars (see reviews by Herbst et al. (2007) and Bouvier et al. (2014)). These spots are known to have a range of temperatures and can reach up to half the visible surface (Strassmeier, 1992; Bouvier et al., 1995).

The sample also includes eight warm/hot spot dominated objects. One of these consists of only a single warm spot measurement. It is also demonstrated that objects with a higher number of reliable spot solutions (larger circles) are more likely to be dominated by cold spots. Investigating the result summary plots for all sources in the sample shows that cold spot dominated objects are more 'consistent' in their behaviour. In other words they are more likely to show cold spot solutions throughout, or for longer continuous periods. On the other hand, warm/hot spot solutions on objects tend to be shorter lived. Only four individual objects in the sample contain four or more warm/hot spot solutions. Therefore, a more reliable statistical analysis of these warm/hot spot dominated sources will require a larger sample.

All but one of the warm/hot spot dominated objects have $K - W2$ colour below 0.5 mag, indicating a lack of an inner disc. Can these mostly warm/hot spot sources be caused by accretion,

despite the lack of a detectable inner disc? Accretion on such transitional disc objects has been the source of multiple studies. As we have seen in Section 2.3.2, transition discs are frequently observed to be actively accreting. The young age of IC 5070, combined the high disc percentage implies that these objects are at the start of disc evolution. In these stages the inner disc may be cleared of dust but remain gas-rich and hence able to sustain accretion. Furthermore, eleven of our objects are identified in Panwar et al. (2023) as Hα emission sources. Not all our sources are in the surveyed region. The slit-less spectroscopy data for that study was obtained in December 2012 and January 2013, and so unfortunately are not concurrent and the accretion rate may have varied since 2012/2013. An object that is an Hα emission source in Panwar et al. (2023) is likely to remain an emission source, without a quantified emission rate it is only an indicator.

The above reinforces that many of our hot/warm spot dominated objects are still accreting despite their lack of detectable inner discs. Can the determined hot/warm spot properties be explained by accretion? Hot spots as the footprints of accretion are predicted to have temperatures of 8000-10000 K and a small surface coverage of less than a few percent (Hartmann et al., 2016; Muzerolle et al., 1998). Recent works have identified a wider range of lower temperatures and higher coverage values (Scholz et al., 2009, 2012; Bozhinova et al., 2016). These lower limits of temperature do, however, not explain the lines identified with spectroscopy which require higher energies (Muzerolle et al., 2003, 2005). In Espaillat et al. (2021) the dense line producing region has a coverage of 0.1 percent, but the cooler, extended region has a coverage in the range of 10-20 percent of the stellar surface. When the high density region disappears, the UV emission dramatically decreases but the optical peaks remain. Therefore, a large fraction of our warm spot solutions could be explained by low density accretion columns.

Furthermore, Sicilia-Aguilar et al. (2023) identified stable accretion hot spots on EX Lup and TW Hya with emission line spectroscopy. The photometry of the objects was dominated by spots that are 500 – 2000 K above the stellar surface temperatures. These spots were found to vary in longitudinal position distinctly from the line emission region. In the case of EX Lup, which has a cleaner sinusoidal rotational modulation than TW Hya, the warm spot was sometimes ahead and

sometimes behind of the line emission hot spot. Over the course of 55 days the spot reduced in size from 88 percent to 10 percent coverage while simultaneously increasing in temperature from 4700 K to 5200 K. This behaviour is consistent with the rapidly changing spot properties discussed in Section 6.1.3.

Accretion is not the only possibility for warm spots on young stars. Froebrich et al. (2020) identified warm spots on the active young star V1598 Cyg, an object which shows no evidence of accretion or mass transfer. Chromospheric active regions known as plages or faculae have been identified on stars of varying ages and types, from active main-sequence stars (Strassmeier et al., 1993), to late type stars (Zhang et al., 2014) and commonly on close binaries (Frasca et al., 2008). However, there is limited data or studies of these on young stars. The young solar type star HD 171488, aged 30 – 50 Myr, has been observed to have chromospheric plages and spots with a 20° difference in phase (Frasca et al., 2010).

Several studies have also identified photospheric warm spots on WTTSs (Xiang et al., 2023; Gully-Santiago et al., 2017; Donati et al., 2014). These are also referred to as plages but are distinct from chromospheric plages. Strassmeier et al. (2019) observed warm spots alongside cool spots with opposing polarities, each with a coverage of a few percent, spatially distinct with longitudinal separations of 10° to 50°. These are presumed to be caused by mass flow between the regions of opposing polarities. The warm regions in this case would always be accompanied by cool regions. In our methodology, a smaller warm region will dominate the photometric variability in the light curves. This scenario hence may provide an explanation of the behaviour seen in many of our objects (see Section 6.1.3), where spot temperatures change (from warm to cold and vice versa) without detectable phase changes.

Photospheric plages have been observed to have coverage values on the smaller side of our warm spot distribution. Donati et al. (2017) observes a coverage of six percent for warm spots but also clarifies that Zeeman Doppler Imaging constrains the lower boundary for coverage. A number of our low coverage warm spots may hence also be explained by photospheric plages. Low density accretion columns as in Espaillat et al. (2021) have an upper limit of 20 percent coverage. However,

the very large warm features observed on EX Lup in Sicilia-Aguilar et al. (2023) reveal a possible explanation for the small number of larger ($f > 0.2$) warm spots in our distribution. Object 28, which accounts for five of these eight large warm spots, is discussed in Section 6.2.6.

6.2 Discussion of Individual Objects

In the previous section we have examined the distribution of spot properties on the YSOs in IC 5070, and discussed potential causes of spots. In this section we will discuss individual objects that displayed interesting behaviour.

6.2.1 The variable star V1701 Cyg

The variable star V1701 Cyg was identified in Froebrich et al. (2021) (F21 ID: 4766) with a period of 6.602 d. Slice 17, which contains the majority of the 2018 high cadence data used in Froebrich et al. (2021), resulted in a candidate period of 6.55 d. Five distinct candidate periods were identified for this object in different slices. The most common being 6.55 d, which was identified in two different slices. The additional four candidate photometric periods were 7.67 d, 9.69 d, 12.61 d, and 14.58 d.

The spot fitting in Chapter 4 identified V1701 Cyg as a likely AA-Tau type contaminant. A $K - W2$ colour of 1.6 mag showed the presence of an inner disc, and the slope of the spectral energy distribution ($\alpha_{sed} = -0.62$) from WISE classified it as a Class 2 object. It is therefore possible that the lack of consistent periods indicates dust occultations at varying distances from the central star over time. Therefore, while not suited to the analysis here, this object is interesting and should be followed up in detail.

6.2.2 Very cold spots or dust extinction on object 2

Object 2 (see result summary in top right panel of Fig. 6.1) contains ten $\hat{A}^{o}_{\{V\}}$ measurements. Yet only four reliable spot solutions are found. The remaining six slices were removed as solutions were less than 10 K above the lower limit 2000 K. Four of these slices are 'pairs' with overlapping data. The causes of these very cold spots are therefore either dust extinction from the disc, or cold

spots below the 2000 K lower limit.

This object was discussed in Section 5.3.3, as the brightest object in the sample at G $\approx$ 12 mag. The stellar temperature of 5000 K was chosen to account for this, and yet the majority of the spot solutions are at a temperature difference of 3000 K below stellar surface. We have considered whether an underestimation of the stellar temperature would lead to the spot solutions changing. In Section 3.6 we have examined the effects of altering stellar temperature by $\pm$200 K, this altered the spot temperatures by less than the statistical uncertainties. The hottest object in the sample is object 30 (see Section 6.2.7) which has a temperature of 5500 K. It cannot be directly compared with object 2 as it undergoes extreme reddening due to non local extinction. While near a bright rimmed globule (see Fig. 5.4) object 2 is not located within an obvious dark cloud. Even if the true temperature is 5500 K, then this would still not effect the spot temperatures by more than the typical statistical uncertainties. Object 2 would therefore require a significantly higher stellar temperature to affect the temperature of the resultant spot properties.

The object has $K - W2 = 0.20$ mag and $\alpha_{SED} = -1.39$. This classifies it as a Class 2 object with a transitional disc. For dust to produce AA-Tau like variability it has to be close to the co-rotation radius, and the $K-W2$ value implies that this is not the case. Furthermore, as discussed in Section 3.7 that dust extinction causing spot solutions to approach the lower temperature limit are caused by achromatic extinction. The $\hat{A}^o_{\{V\}}$ values in object 2, however, are not achromatic. The filter with the highest amplitude varies throughout the light curve. In general, $\hat{A}^o_V$ is expected to be the highest and $\hat{A}^o_I$ the lowest. The light curve modulation is strong, with an amplitude (0.2 mag) that is higher than the median of our sample, but the modulation in colour is erratic.

The alternative solution to dust is that the spots can indeed be colder than 2000 K at times. In either case, the source warrants more detailed further investigation.

6.2.3 Phase shifts on object 3

Object 3, shown in the bottom left panel in Fig. 6.1, has $\sim$2.5 yr of detectable rotational variability at the start of the light curve. During that time the phase position remains constant within the

measurement uncertainties. Note that the dominant spot temperature changes between warm and cold during that period. This is discussed in Section 6.1.3. After slice 26 there is break in detectable $\hat{A}^o_{\{V\}}$ values for about 18 months. Two slices in the break have sufficient data but the $\hat{A}^o_{\{V\}}$ values have a SNR below three (due to high noise in the V-band). When the $\hat{A}^o_{\{V\}}$ values resume, the amplitudes are reduced and there is a 90° shift in phase. The higher noise in the gap may be due to more complex spot activity. When the sinusoidal modulation resumes after the gap, a surface spot at a different part of the surface compared to the earlier dominating spot might have formed.

6.2.4 Potential spot motion on object 4

The evolution of object 4 is shown in the bottom right panel in Fig. 6.1. This source only has four gaps in the $\hat{A}^o_{\{V\}}$ values, mostly in the slices centred on the worst observability of the source. Between slices 17 to 23 the amplitudes increase and decrease slowly, while showing a near constant phase position. This changes from slice 25 onward. A warm spot is found with a phase shift of 90° compared to the earlier cold spots. Together with the lack of successful spot property fitting for slices 22 and 23, this indicates a more complex situation of no clear single dominating spot for the duration of a slice (half a year). Between slices 25 and 34 the $\hat{A}^o_{\{V\}}$ values increase and then decreases (similar to the first two years). During this time the phase position changes gradually. Again, in some slices no spot properties can be fitted, indicating a constant change in the nature of the dominating spot. However, the longitudinal position of the most asymmetric part of the spot distribution on the surface of the star is systematically moving at a rate of about 90° per year.

6.2.5 Very cold spots on object 5

Similar to object 2 (Section 6.2.2) object 5 (Fig. 6.5, top left) has eight spot temperature solutions too close to the lower 2000 K limit. Indeed these two objects account for nearly half of these cases. Object 5 has an effective temperature of 3686 K (Fang et al., 2020), $K - W2 = 0.79$ mag, and $\alpha_{sed} = -1.02$. Therefore, it is a Class 2 object with an inner disc. The spot temperatures (albeit low) and coverage values for the reliable solutions do not stand out compared to the values found in the rest of the sample. Thus, similar to object 2, this source might have some of the lowest

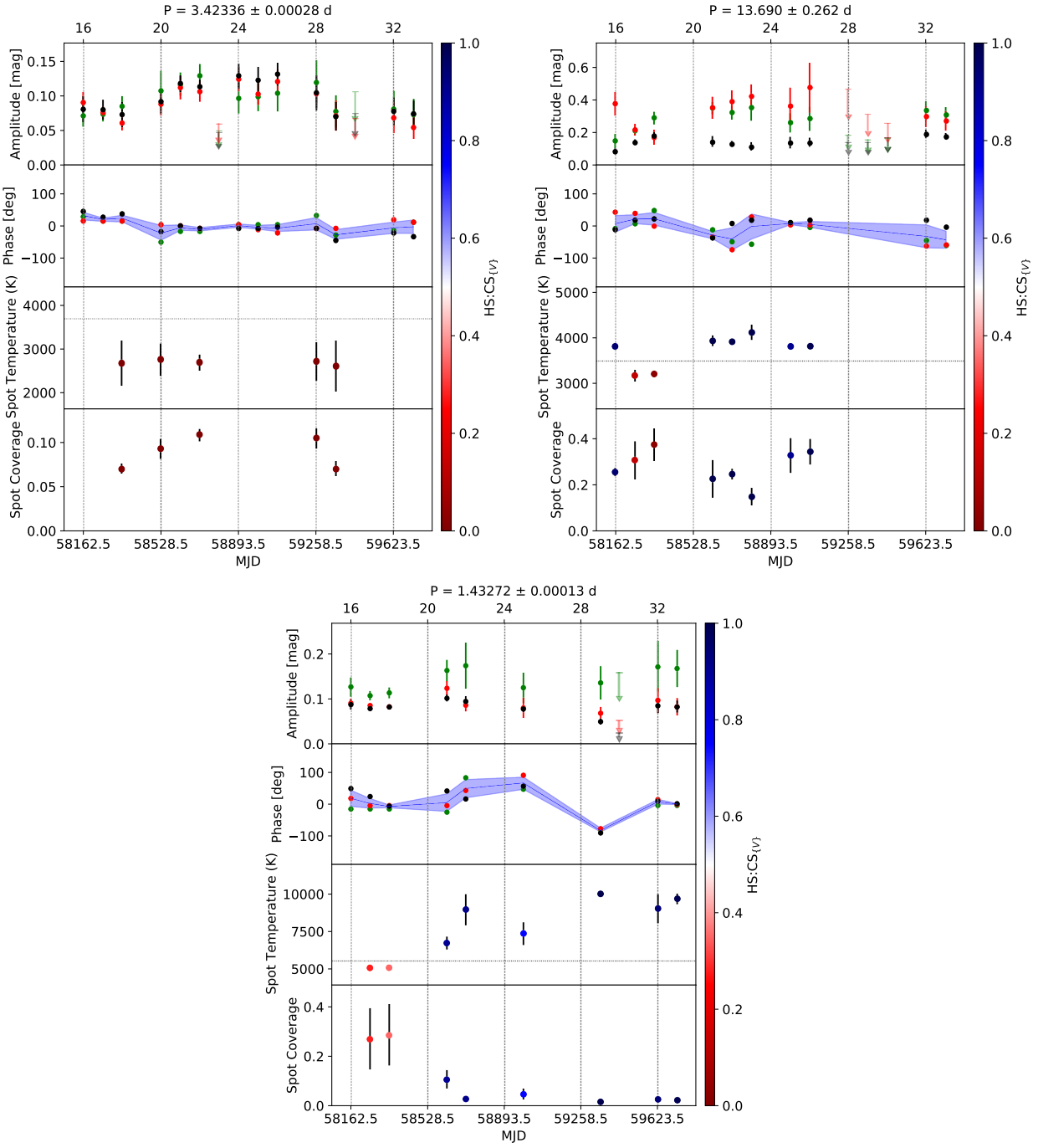

Figure 6.5: As Fig. 6.1 for the objects 5 (top left), 28 (top right), and 30 (bottom centre).

temperature spots and should be investigated in more detail.

6.2.6 Large warm spots on object 28

Object 28 (Fig. 6.5, top right) displays five of the eight warm spot measurements with coverage values over $f = 0.2$. It has the longest period of the sample at $P = 13.69$ d and $K - W2 = 1.20$ mag. Hence, it has an inner disc, and it is therefore extremely likely that this object is accreting. It is not identified as an emission line star in Panwar et al. (2023), but this does not exclude accretion as the data is not contemporary to our observations. It also has $\alpha_{sed} = 0.32$ mag, making it the one Class 1 protostar in our sample.

In Section 3.7 we tested the outcome of simulated variability induced by small particle dust with $R_V = 5$ and $R_V = 3.1$. This could in principle result in large warm spots. However, this can be excluded for this source as the colour modulation is not in agreement with such extinction. Object 28 has above average peak to peak amplitudes in our sample, with the largest amplitudes in the R-band. Coverage values above $f = 0.2$ are not expected from low density accretion columns (Espaillat et al., 2021). Large warm regions on EX Lup (Sicilia-Aguilar et al., 2023) show that on a stably accreting object it is possible for the photometry to be dominated by large features with low temperature contrast.

Object 28 is one of the two objects in our sample with three consecutive warm spot solutions in slices 21 – 23. Slice 24 has insufficient data, and then slices 25 and 26 have two further large warm spot solutions. This period of extreme stability implies large warm features as observed on EX Lup.

The stability seen on object 28 could partly be due to its early evolutionary stage. As pre-main sequence stars develop a radiative core their magnetic fields become increasingly complex, and their dipole field becomes weaker (Gregory et al., 2012; Donati et al., 2011b). This object is unlikely to have had sufficient time to develop a radiative core, therefore it is likely to host a strong, simple magnetic field. This supports the stability of the spot observed here.

6.2.7 Stable hot spots on object 30

Object 30 (Fig. 6.5, bottom centre) is discussed in Section 5.3, as the hottest star in our sample and with high reddening due to non-local extinction. Both, the period and $K - W2$ indicate that this object has no inner disc. Object 30 accounts for four of the five hot spot solutions in our sample. These spot solutions have a temperature of more than 3000 K above the stellar temperature. The object has a very short period of 1.433 d and $K - W2 = 0.234$ mag. It is not included in the emission line star catalogue of Panwar et al. (2023) as it is outside of their search area.

The spot solutions for the object start with two cool spots in slices 17 and 18. This correspond to the high cadence period of the light curve in 2018. The HS:CS$_{\{V\}}$ values are 0.27 and 0.34 indicating these solutions are credible but not definitive on the side of cold spots. From slice 21 to the end of the light curve, every $\hat{A}^{o}_{\{V\}}$ identified leads to a strong warm/hot spot classification, with the lowest HS:CS$_{\{V\}}$ being 0.75. Four of these spot solutions have temperatures above 8900 K and very small coverage values. These align with the expectations for accretion based hot spots.

There are two 'pairs' of hot spots in slices 21/22 and 32/33, with overlapping data. There are two spots on this object which are not 2500 K hotter than the stellar surface and are hence classified as warm spots. These have temperatures of 6700 K and 7300 K, which is not out of the range of accretion based activity. Hence, we can reasonably consider this object to be accreting, and all of the warm/hot spot solutions can be considered accretion based hot spots.

7

Application to all YSOs in HOYS fields

This chapter details the data analysis used to identify periodic YSOs across all HOYS fields, establish peak-to-peak amplitudes, and details a new methodology to establish approximate stellar temperatures for these YSOs. Spot properties are then fit to the sample to reinforce the conclusions from Chapter 6. The findings in this chapter are in preparation for publication.

7.1 YSOs in all HOYS fields

The HOYS project monitors 25 nearby, young star forming regions. In Froebrich et al. (2024) 45 groups/clusters were identified from Gaia DR3 astrometry (Gaia Collaboration et al., 2016, 2023). From ~ 17000 Gaia members, the HOYS project has ~ 3000 corresponding light curves. Here, we extracted light curves for all objects in identified in young clusters.

Light curves of 2047 young cluster members with over 100 data points in V, R, and I were extracted on October 21st, 2022. The data was sliced into six month sections, every three months as in Section 5.2.1. The start of the boundary dates were calculated to coincide with the worst observability for each region, in order for the resulting slices to contain the minimum or maximum number of data points available. The date for the least favourable observing for each field was calculated given its Right Ascension (i.e. it is at its lowest altitude at midnight). The M42 field has the longest available light curves, with the earliest data points in 2013. Hence, 2013 is chosen as the starting year for all objects. The starting date for each field is the date with the worst observability in 2013. The slice numbers follow the sequence established in Section 5.2.1 that slices numbered $3N - 1$ contain the least data whereas slices $3N + 1$ contain the most. In this way, the boundary dates of slices do not match up between regions, but retain some indication of similarity, e.g. slice 32 for all regions contains data obtained in 2021.

Slices were retained if they contained 50 data points in V, R, and I. The majority of light curves did not have the necessary observational cadence to meet this threshold. From 2047 light curves, 918 objects had slices with the required number of data points corresponding to 3752 individual slices. Table 7.1 lists the young clusters with light curves, the number of light curves and slices with sufficient data, and the number of periodic light curves and slices. Periodicity will be examined in Section 7.2.

The majority of the available slices arise from regions that have been the subject of HOYS observing campaigns. IC 5070 clearly has the most available data, with 970 slices available for investigation. Note, in Section 5.2.1 the boundary date was chosen as 14th February as the middle

Table 7.1: HOYS target regions investigated for periodic YSOs. Listed are the region name, the three digit region ID, the number of light curves and slices investigated, and the number of light curves and slices found to show a periodic signal.

Region		Investigated		Periodic	
Name	ID	N LC	N slices	N LC	N slices
NGC 1333	001	20	-	-	-
IC 348	002	79	-	-	-
M42	003	74	155	9	34
NGC 2264	004	285	1	-	-
σ Ori cluster	005	69	324	17	90
λ Ori cluster	006	18	-	-	-
L 1641 N cluster	007	108	130	11	22
NGC 2264	008	58	-	-	-
V898 Ori cluster	202	13	30	3	8
YY Ori cluster	203	52	160	9	32
V555 Ori cluster	210	80	226	10	48
Gaia 19 fct	213	145	409	2	3
Gaia 19 eyy	214	58	229	-	-
Berkeley 86	110	229	25	-	-
P Cyg cluster	111	196	15	-	-
IC 1396 N	114	150	405	17	71
IC 1396 A	115	187	528	25	78
NGC 7129	116	25	24	1	4
IC 5070	118	136	970	31	211
IC 5146	119	65	121	9	19

of the least favourable month. When the exact least favourable date is calculated for slicing the data, the boundary has moved to the 1st February. Any changes in the sample that arise due to this change will be noted.

The Orion star forming complex has been the focus of observing campaigns since the winter 2020/2021. The σ Ori cluster was the focus of a campaign in the preparation for Froebrich et al. (2022). The majority of the light curves in the Orion fields have $\sim$ 7 yr light curves in the V- and I-bands, but only have R-band coverage from 2020. Therefore, only two years of data are available for spot fitting.

Four regions have objects with over 100 data points per filter in the light curve, but the cadence is not sufficient to generate slices with 50 data points per filter when divided. NGC 2264 has 285 such objects with light curves, however nearly all light curves have just over 100 data points in all filters, and hence only one slice is generated. Outside of long-running observing campaigns, the majority of objects have very few slices with sufficient data. From 918 objects, 138 produce only one slice and 206 contain two.

7.2 Period and amplitude identification

Here, we summarise the periodic variable search of the YSOs across all HOYS fields and the peak-to-peak amplitude identification, detailing any changes made to the previously established methodologies.

Slices with 50 data points in all $\{V\}$ filters were considered. In Section 5.2.2 light curve slices were searched for a period with two of the three filters. This change was made because objects in many regions have long light curves in two filters only, and these are not suitable for spot fitting analysis. The period finding algorithms were applied to the sliced data as in Section 5.2.2, in the same 0.5 – 20 d range. The candidate periods were accepted with the same threshold values for the periodogram power for the L1Boot, L1Beta, and L2Beta methods or FAP for the GLS. Each candidate period, before acceptance, must be detected within 0.05 d simultaneously in two filters by the same method. Any candidate periods within one percent of 0.5 d, 1 d, or 20 d were removed

as previously.

For the objects in Section 5.2.2, five candidate periods were required in a single group to establish a final period, with that group containing two thirds of the total candidate periods. Due to the excellent sampling and long light curves in IC 5070, this was an appropriate threshold. However, for many of the objects in the wider HOYS fields this was not possible. In this sample, five candidate periods (with a two thirds majority) in a group was used as a threshold for acceptance. However, the remaining slices were inspected and additional objects were found with good quality periods. The minimum number of candidate periods accepted was two, which were detected by two methods in a single slice.

Due to the limited number of long duration high cadence light curves, every available slice was included to increase the statistics. The final period was established in the same method as Section 5.2.2. A LS periodogram is applied over the light curve in each filter, centred on the median of the candidate periods in the primary group with 1000 homogeneously distributed test periods surrounding the median. The median of these periodograms is taken as the final period and the error is the standard deviation between them.

All slices of the periodic variables with sufficient data were phase folded with their established periods. The peak-to-peak amplitudes were calculated following the procedure established in Section 5.2.3. The same threshold of SNR above three for the amplitudes was required, and the minima and maxima in phase were also required to align within 45° between filters. This removed the majority of slices which did not have good quality fitting. All light curves were inspected for goodness of fit, and five additional slices were removed manually due to the running median not well representing the data. This is generally due to gaps in the data in phase space which commonly occurs with integer number periods. In total 630 $\hat{A}^{o}_{\{V\}}$ across 144 YSOs were identified.

Table 7.1 lists the HOYS regions with identified periodic YSOs, alongside the number of light curves tested for periodicity, the number of periodic light curves and the number of good quality slices available for spot fitting. Figure 7.1 presents the distribution of identified periods for YSOs across all regions. The object ID, region, coordinates, period, period error, fitted temperature

(to be discussed in Section 7.3), alongside the number of slices and the Gaia DR3 ID with the F21 ID number and/or ID number from Chapter 5 for overlapping sources is presented in full in Table C.1 in the Appendix. There is an approximate bimodal distribution with approximately half the rotation periods are less than 4 d. We consider $P < 5.5$ d to be a short period for consistency with previous results however, to properly understand the rotation period distribution one would consider the regions independently. Unfortunately, the majority of regions do not have sufficient statistics to support this.

In Froebrich et al. (2024) objects were assigned to the cluster that best fit the parallax and proper motion, but it was noted that many regions spatially overlap. Hence, two groups were created by merging fields. The fields surrounding M42 are combined to form one group, these are M42, L 1641 N, V 898 Ori, and YY Ori. This group contains 42 periodic objects. Similarly, IC 1396 A and IC 1396 N are combined, the resulting group also contains 42 objects. The period distributions of these two groups are presented in Fig. 7.2.

The M42 group contains a majority of objects with rotation periods less than 3 d. The centre of the ONC is estimated to be < 1 Myr, and the surrounding fields are slightly older (Rebull et al., 2006; Ramírez et al., 2004). M42 shows a peak in the period distribution in 1 – 2 d. As discussed in Section 5.2.2, to avoid aliasing associated with the one day cadence of ground based observations periods within one percent of 1 d are automatically removed, additionally any periods within ten percent of one day were investigated. The final periods are presented in Table C.1. All of the periods in the 1 – 2 d peak are longer than 1.3 d. The IC 1396 group is older at around 4 Myr (Pelayo-Baldárrago et al., 2023). The period distribution is separated at $P \sim 5.5$ d, but also demonstrates greater diversity than the M42 group. The median period in IC 1396 is longer than the median period in the M42 group, which is unexpected given its older age. This is likely due to the high density of massive stars in the M42 region causing external photoevaporation of the discs, accelerating the disc evolution. This demonstrates some of the diversity in rotation across HOYS fields.

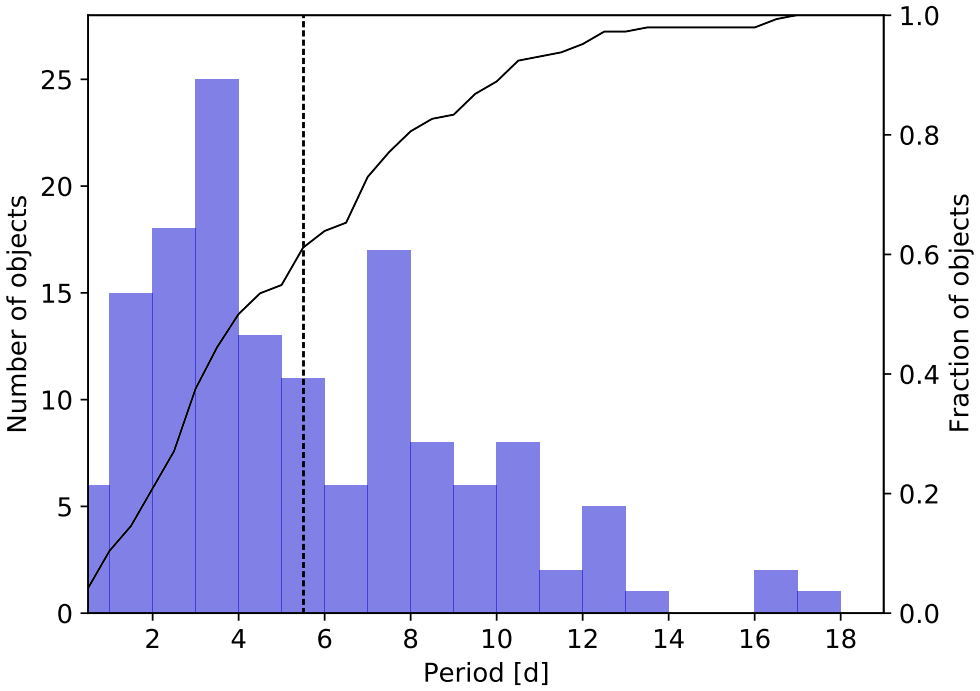

Figure 7.1: The distribution of measured periods of YSOs in all HOYS regions. The solid black line represents the cumulative distribution function and the dashed vertical line at $P = 5.5$ d separates slow from fast rotators.

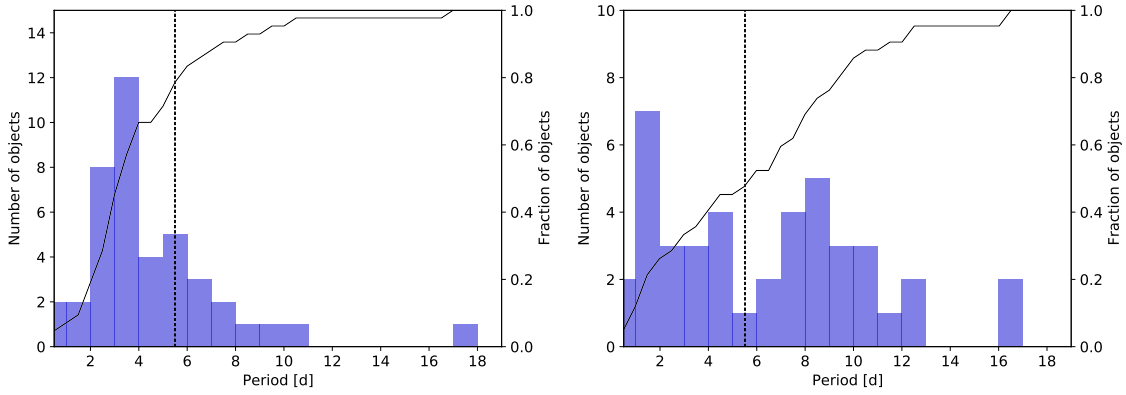

Figure 7.2: Distribution of measured periods of YSOs in the M42 group (left) and IC 1396 group (right). The solid black line represents the cumulative distribution function and the dashed vertical line at $P = 5.5$ d separates slow from fast rotators.

7.3 Approximation of stellar temperatures

The majority of the analysis in this thesis has been conducted on YSOs in IC 5070. This region is well studied, and the majority of YSOs have available effective temperature measurements from Fang et al. (2020). Unfortunately, YSOs in other HOYS regions do not often have a temperature reference available. As we have seen in Section 3.6, the stellar temperature of YSOs can be altered by 400 K without affecting the spot property results beyond their statistical uncertainties. In this section, a method is outlined to obtain an approximate temperature from survey colours to facilitate spot fitting.

7.3.1 Temperature fitting

Firstly, all Gaia members in the North American and IC 5070 (IC 5070 is the Pelican Nebula, an therefore combined the regions are referred to NAP) are matched with the reference effective temperatures in Fang et al. (2020) to generate a list of $\sim$200 NAP cluster members with known effective temperatures. The upper limit of temperatures considered is $T_{eff} = 8000$ K, as this temperature is the upper limit expected for CTTS.

$$T = x_0 + a \cdot G_G + b \cdot (G_{BP} - G_{RP}) + c \cdot G_G \cdot (G_{BP} - G_{RP}) + d \cdot col_1 + e \cdot col_2 \qquad (7.1)$$

A function is then defined to calculate temperature based on survey colours. As the objects are defined by their Gaia astrometry, the absolute Gaia G-band magnitude (G_G) and ($G_{BP} - G_{RP}$) colour are used as the basis. Two additional colours col_1 and col_2 are used to refine the function. The parameter col_1 is $\lambda_1 - \lambda_2$, and col_2 is $\lambda_3 - \lambda_4$. All objects have Gaia colours already included in the fitting. 2MASS (Skrutskie et al., 2006) magnitudes in J, H and K are also available for almost all objects, and when not available (as for object 17 in Section 6.1.4) are identified in UKIDSS GPS data (Lucas et al., 2008). From the WISE All-sky catalogue (Cutri & et al., 2013) $W1$ and $W2$ were considered, $W3$ and $W4$ were not due to poor SNR for the majority of objects.

The fitting was conducted in `SciPy` (Virtanen et al., 2020) to fit parameters to Equation7.1 using the reference temperatures. The parameters can then be used to calculate temperatures following Equation 7.1 using the given colours.

The additional colours col_1 and col_2 are used to refine the function in the place of an extinction measurement, which is not available for objects outside of the NAP reference sample. To determine the optimal combination of the filters to create these colours, the parameters were fit for Equation 7.1 for every combination of filters above. New temperatures were then calculated for the reference sample. The RMS between the reference and calculated temperatures was measured, and the combination of filters which produced the minimum RMS was selected. The lowest RMS came from $col_1 = G_{BP} - J$ and $col_2 = W1 - W2$, and the resulting calculated temperatures were adopted as the fitted temperatures. These colours were available for all objects in the sample.

Figure 7.3 presents the effective temperature distribution of YSOs in NAP with temperatures in Fang et al. (2020) in green. There is a significant peak in the distribution where 30 percent of the objects have temperatures between 3900 – 4000 K. To avoid bias for the parameter fitting, objects in this range are excluded from the fitting process. However, since the majority of the objects are low temperature, the fitting is also weighted against higher temperatures by a factor of 1/T. Presented in blue in Fig. 7.3 is the temperature distribution for the same YSOs with fitted temperatures following Equation 7.1. The reference temperatures have a significant peak at T$\sim$ 3900 K, and very few objects have temperatures between 4000 – 5000 K.

The fitted temperatures are generally above the reference temperatures by a median of 400 K, but present a smoother distribution of temperatures across the sample. It has been demonstrated that the systematic effect of altering the stellar temperature by 400 K is less than the statistical uncertainties.

7.3.2 Application to IC 5070 YSOs

To establish whether the adopted stellar temperatures have a significant effect on the distribution of spot properties, the spot fitting for the YSOs in Chapter 6 is repeated using the fitted stellar

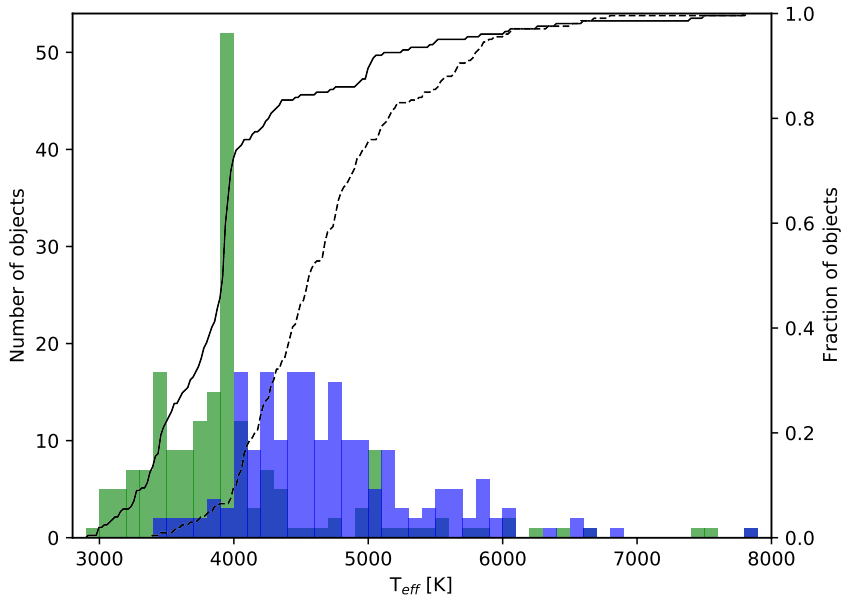

Figure 7.3: Histogram of stellar temperatures for YSOs in NAP region. In green with a solid line CDF are the measured effective temperatures in Fang et al. (2020), and in blue with a dashed CDF are the temperatures calculated using Equation 7.1.

temperatures.

The fitted temperatures for the IC 5070 sample of YSOs is presented in Fig. 7.4. The majority of the fitted temperatures are between 4000 – 5100 K. Across the entire NAP region the fitted temperatures are typically 400 K above the reference temperatures. Among the IC 5070 sample, there are a few notable outliers. Object 2 which is the brightest object in the sample had a previously estimated temperature of 5000 K, is fit with a value of 7350 K. Object 18 in Fang et al. (2020) was identified with a temperature of 4900 K, while the fitted value is 6300 K, likely due to being 1 mag brighter than the rest of the sample. Object 30 was the hottest object in the sample with a temperature of 5500 K, but also it is heavily reddened by non-local extinction. Object 30 has a fitted temperature of 5050 K which places it in the upper half of the sample, but the temperature fit does not identify the extreme reddening as in Fang et al. (2020).

The spot fitting methodology was applied exactly as in Section 5.2.4, with the exception of using the fitted temperature values, and changes to the upper limit. The upper limit for the modelled spot temperatures was increased to 12000 K for stellar temperatures below 5500 K and 14000 K for

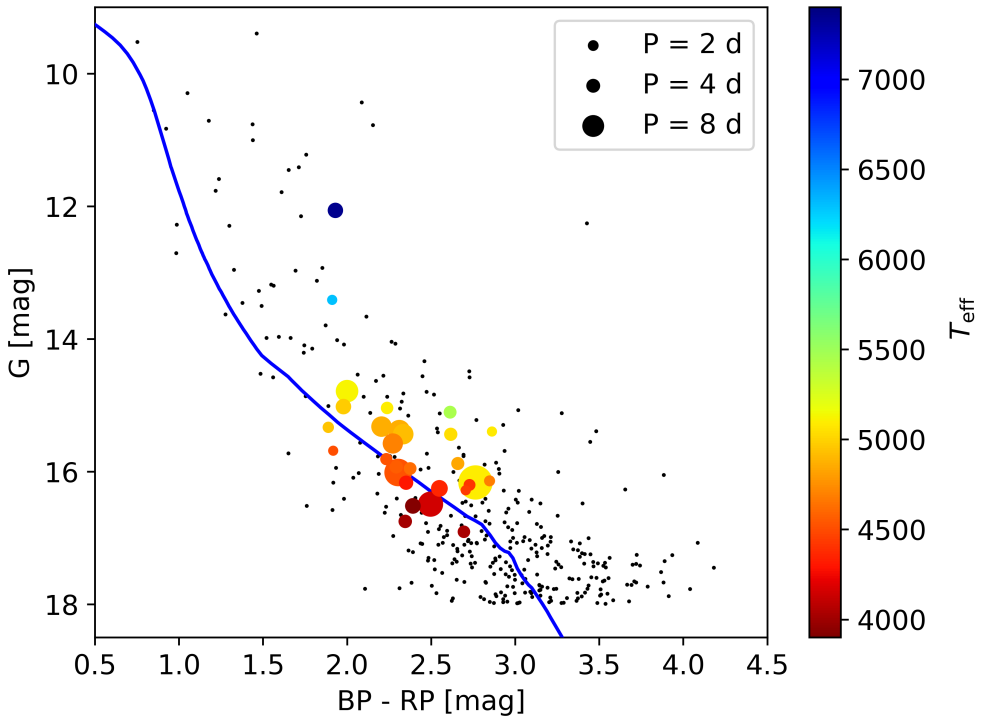

Figure 7.4: $G_{BP} - G_{RP}$ vs. G_G colour magnitude diagram. All selected IC 5070 cluster members are shown as black points and periodic objects are in colour mapped to their adopted stellar temperature from Equation 7.1. The marker size is scaled to the period, as shown in the legend. Overlaid in blue is a 1 Myr PARSEC isochrone, translated to apparent magnitude with the sample median distance (Bressan et al., 2012).

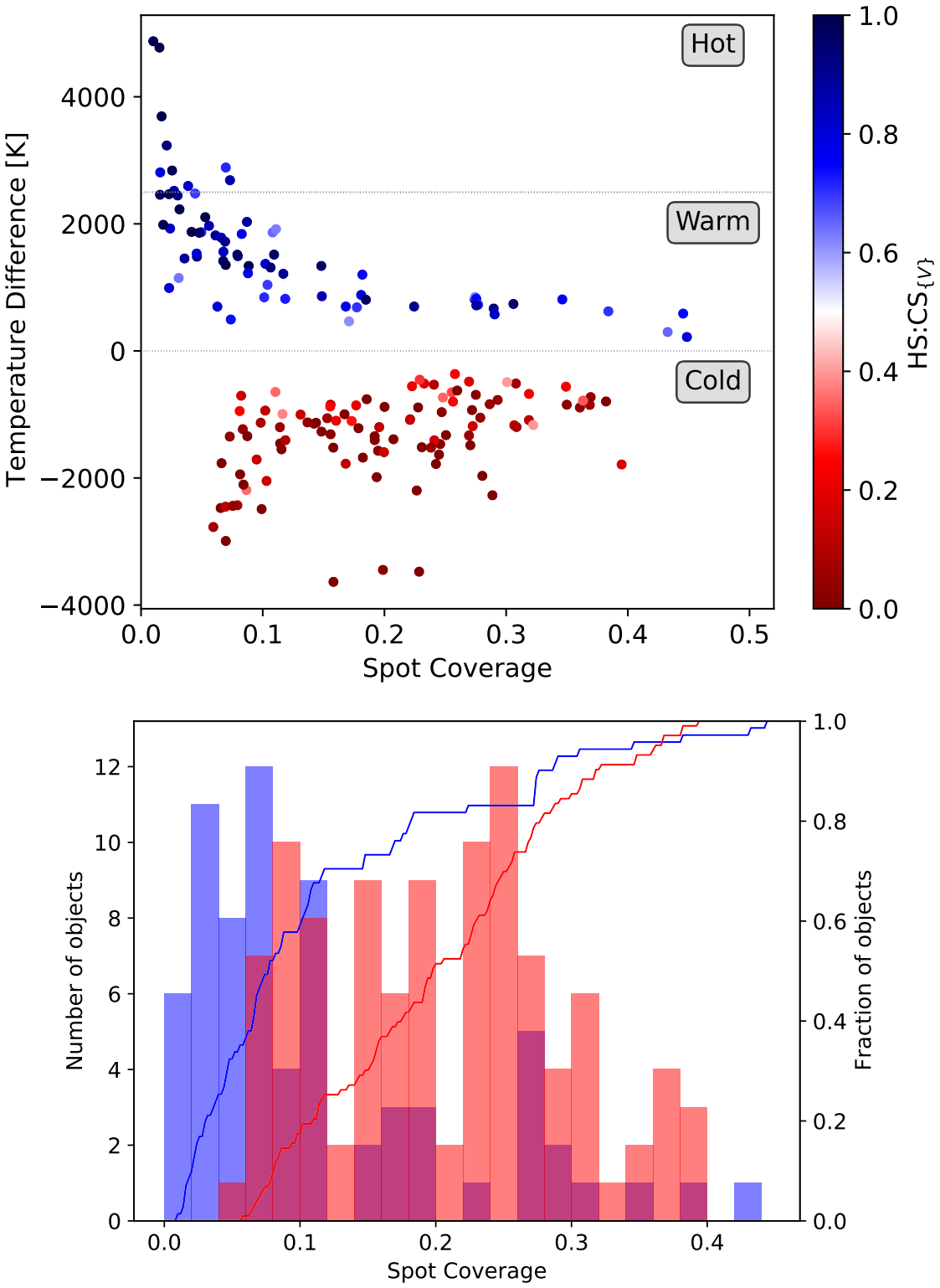

Figure 7.5: **Top:** Spot temperature difference $T_S - T_\star$ versus spot coverage, for spot fits with fitted stellar temperatures according to Equation 7.1. Horizontal dotted lines mark $T_S - T_\star = 0$ K and $T_S - T_\star = 2500$ K, which separate the cold, warm, and hot spot solutions. The markers are colour coded according to the HS:CS$_{\{V\}}$ ratio. **Bottom:** Distribution of spot coverage of warm/hot (blue), and cold spots (red). The solid lines are the CDFs of the warm (blue) and the cold spots (red).

stellar temperatures above 5500 K. Figure 7.5 presents the results of the spot property fits. This is equivalent to Fig. 6.2 in Section 6.1.1.

From the 234 slices, 176 are fit here with spots, 104 are fit with cold spots, and 72 are fit with warm/hot spots. The cold spots outnumber the warm/hot spots by a factor of 1.5, as opposed to 2.3 in Section 6.1.3. The proportion of warm spots in this sample is 0.43 ± 0.04, this is above the error on the proportion of 0.31 ± 0.03 identified in Section 6.1.3. The slices that could not be fit with spots are either due to interacting with the lower temperature limit (25), reaching the upper limit on coverage (11), or classified as ambiguous from HS:CS$_{\{V\}}$ (23). The proportion of slices removed due to ambiguous HS:CS$_{\{V\}}$ or interacting with the edge of the parameter space is 2 percent higher here. The spot fits that are removed for interacting with the lower limit for temperature occur in 24 of the same slices, implying that stellar temperature does not significantly affect whether these slices can be fit with spots. The spots that interact with the upper coverage limit overlap for six slices, and ten slices with spots that are classified as ambiguous due to HS:CS$_{\{V\}}$ in Section 6.1.3 are also classified as ambiguous here.

The majority of spot temperatures do not change dramatically, with around half the spot fits changing spot temperature by less than 500 K. It is unsurprising that the most changed spot properties occur on objects with significantly altered stellar temperatures. Object 28 for example, has one of the largest changes to stellar temperature, increasing by 1600 K, which previously had ambiguous spot fits in later slices, now show additional large warm spots in slices 32 and 33.

A consequence of raising the stellar temperature without a significant change in the resulting spot temperature is that some spots appear very cold. Object 2 previously presented a number of spots that were removed for interacting with the 2000 K lower limit, and some spots at ~ 3200 K. The spot fits that are removed are still removed, and the apparently valid spot results now have results at ~ 3800 K. This is a typical spot temperature when compared to the spot fits for the sample, however with the very high stellar temperature these three spots appear approaching -4000 K.

For the warm spots, the apparent gap at 2500 K above the stellar temperature does not appear.

There are now ten spots that appear over 2500 K above the stellar temperature. The $\hat{A}^{o}_{\{V\}}$ that are identified as the five hot spots in Section 6.1.3 are included in the ten spots identified here.

The spot size distributions for the warm/hot distribution is presented in the bottom panel of Fig. 7.5. Due to no clear distinction between the warm and hot distributions all warm/hot spots are considered together. A two sided KS-test between the coverage distribution of the cold spots obtained in Section 6.1.3 reveals that the two distributions are statistically similar. A p-value threshold 5% is generally used to prove the distributions dissimilar. The p-value between the cold spots is 81%. Similarly, a two sided KS-test between all the warm/hot spots provides a p-value of 64%. Therefore, while using adopted stellar temperatures one should be cautious about drawing conclusions about specific objects the distributions have not been found to be dissimilar and therefore the temperature fitting methodology can be reasonably applied to the wider YSO sample.

7.4 Spot fitting results

In this section, having established in the previous section that the use of adopted temperatures does not meaningfully impact the statistical distribution of the results, the spot fitting methodology is applied to the YSOs in the wider HOYS fields. The modelled spot temperatures are increased to 12000 K for all stellar temperatures, and 14000 K for stellar temperatures above 5500 K. The stellar temperatures are adopted from Section 7.3. The spot property results here are to reinforce the conclusions made in Chapter 6.

7.4.1 Spot fitting distribution

Across all YSOs in HOYS fields 630 $\hat{A}^{o}_{\{V\}}$ are identified. From these, 463 spots are fit, 305 are cool, and 158 are warm/hot. The proportion of warm/hot spots is therefore 0.36 ± 0.02, which is inside the uncertainty of the proportion (0.31 ± 0.03) identified in Section 6.1.3. The spot fitting success rate is 73 percent, while the IC 5070 sample had a 77 percent success rate. 64 spots interact with the lower temperature limit, 50 spots are removed for interacting with the upper limit for coverage, and 41 were classified as ambiguous from their HS:CS$_{\{V\}}$. Spots are removed from

the sample in the order listed here, but it is notable that many spot fits overlap between these categories.

Objects in IC 5070 make a significant contribution to the sample with 211/630 slices. The IC 5070 objects are re-examined here with fitted stellar temperatures, and with marginally adjusted light curve slices as noted in Section 7.1. The change in the date leads to one object (16) not being identified again, previously only a single slice was identified, with the altered boundary dates this slice was divided and did not meet the 50 data point threshold. Three additional objects are also included due to either the change in dates altering the number of data points per slice, the signal-to-noise of the amplitude in the slice, or were identified as periodic manually. These additional objects combined introduce seven $\hat{A}^{o}_{\{V\}}$.

For the IC 5070 sample when spots are fit using the adopted temperatures as demonstrated in Section 7.3.2 the warm/hot spot proportion is increased above the results in Section 6.1.3. The warm/hot spot proportion of the YSOs in non-IC 5070 HOYS fields is 0.32 ± 0.03. This is within the uncertainty of the proportion identified in Section 6.1.3.

Cold spot distribution

The distribution of spot properties is presented in Fig. 7.6. There is a greater diversity of cold spot temperatures in this wider sample than identified in Section 6.1.3. Around 70 percent of cold spots are below stellar temperature by less than 1500 K, while in IC 5070 this value was 90 percent. Here, 80 percent are below the stellar temperature by less than 2000 K.

It is worth noting however, that this sample has a wider range of stellar temperatures which likely influences this statistic. Three of the coldest spots occur on object 2, which has the adopted temperature of 7350 K and is the hottest adopted temperature in the sample. Due to the use of adopted temperatures we refrain from drawing specific conclusions about individual objects, instead focusing on the statistical understanding.

The observational bias against low temperature contrast and very small coverage values is clearly reinforced in this sample. The minimum spot coverage among the cold spots is $f \approx 0.05$. Many spots are recovered at this lower limit, with varying $T_S - T_\star$ values. The clear demarcation

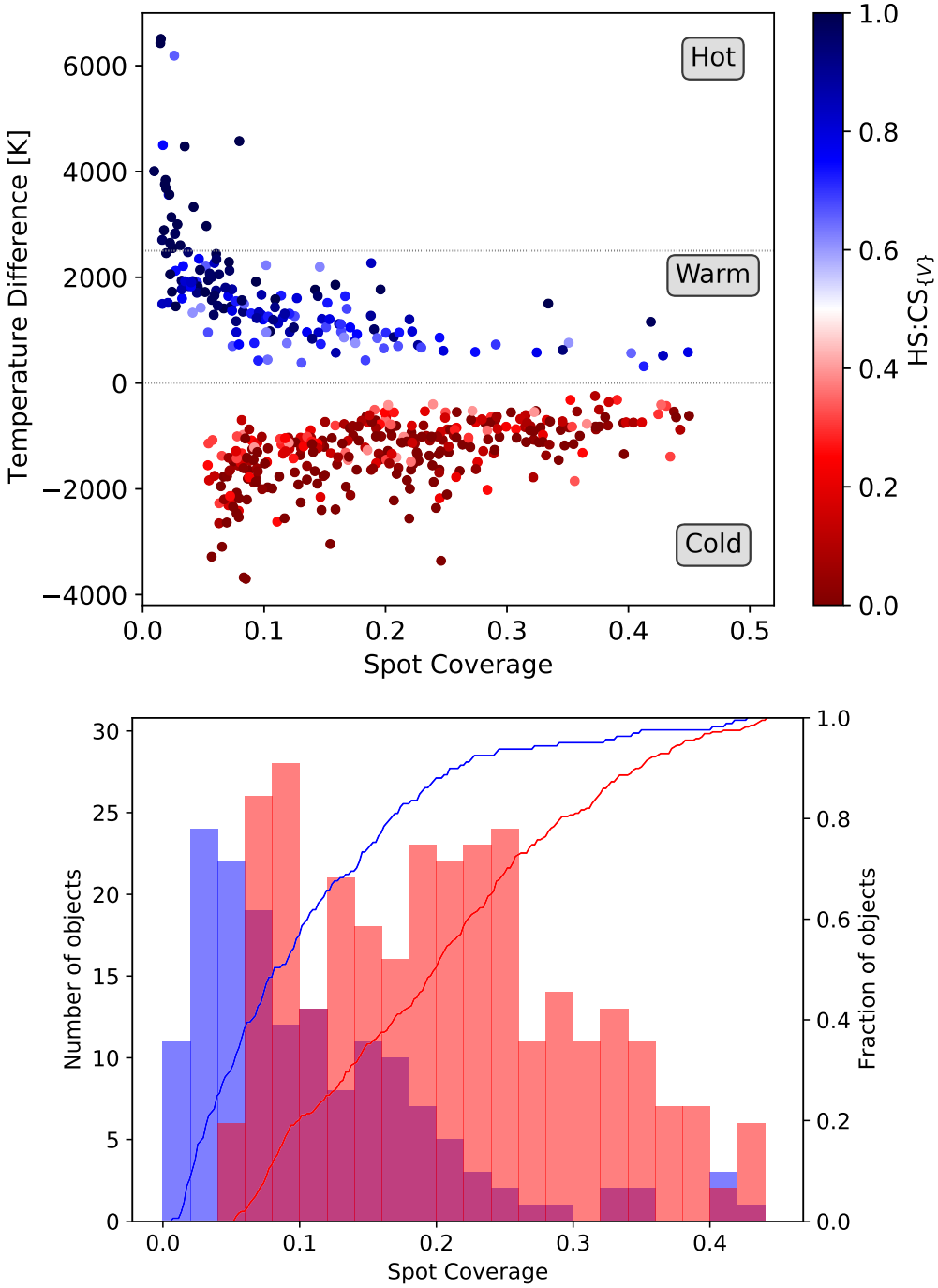

Figure 7.6: **Top:** Spot temperature difference $T_S - T_\star$ versus spot coverage for objects across all HOYS fields. Horizontal dotted lines mark $T_S - T_\star = 0$ K and $T_S - T_\star = 2500$ K, which separate the cold, warm and hot spot solutions. The markers are colour coded according to the HS:CS$_{\{V\}}$ ratio. **Bottom:** Distribution of spot coverage of warm/hot spots (blue) and cold spots (red) for objects across all HOYS fields. The solid lines are the CDFs of the warm (blue) and the cold spots (red).

of this limit is likely influenced by the SNR requirements for $\hat{A}^{o}_{\{V\}}$, and the systematic shift discussed in Section 3.6 and Section 6.1.3 in which simulated small, low temperature contrast cold spots are identified as somewhat smaller and colder than the simulated spot properties. This is also demonstrated as very low temperature contrast spots do not appear in this sample until the coverage values are above $f \sim 0.2$. As the spot coverage increases, the required temperature contrast also is reduced.

The spot coverage distribution for cold spots in this sample is presented in the bottom panel of Fig. 7.6. There are fewer spots with coverage above $f \sim 0.26$, between the lower limit and this value the distribution very closely follows a homogeneous distribution with a p-value of 64 percent on a two sided KS-test. This was also the conclusion for the IC 5070 distribution of cold spots which was homogeneous between $f = 0.06 - 0.3$. Comparing the two samples directly provides a p-value that the two are similar of 23 percent. Therefore, the results for cold spots reinforce the conclusions for IC 5070.

Warm and hot spots

The greater number statistics of warm/hot spots in this sample provide a clearer understanding of the distribution of warm and hot spots. In the top panel of Fig. 7.6 a dashed line marks $T_S - T_\star = 2500$ K, the previously identified division between what we denote warm and hot spots. In Section 6.1.3, it was theorised that the clear break dividing warm and hot was due to the limited statistics and the true distribution was more similar to a continuum. This appears to be the case here.

In this sample there are 23 hot spots that are above the stellar temperature by more than 2500 K, this is 15 ± 3 percent of all warm/hot spots which is statistically indistinguishable from 9 ± 4 percent in Section 6.1.3. These spots all have temperatures above 8000 K, and therefore can reasonably be considered to be accretion based hot spots. However, this does not mean that warm spots below 8000 K are not related to accretion. As discussed in Section 6.1.4, warm spots can be caused by the low density portion of the accretion column dominating the optical photometry.

The warm spot regime makes up 85 percent of the total warm/hot spots. Here, there is also a

greater diversity of warm/hot spot coverage values below $f \sim 0.2$. In IC 5070 the upper envelope of $T_S - T_\star$ was clearly defined. In the top panel of Fig. 7.6 there are a small number of spots with higher temperatures than their coverage would imply following the upper envelope identified in Section 6.1.3. Notable, is one $f \sim 0.08$ spot appearing at ~ 4200 K above the stellar temperature although individual spot fits may be affected by the use of adopted temperatures. The colour modulation for these spots was examined and it was confirmed the amplitudes were not similar to the reddening extinction as simulated in Section 3.7. It is therefore likely that this greater diversity is representative of the actual distribution, and the distribution in Section 6.1.3 was restricted by the limited statistics.

Our understanding of the warm spot regime in Section 6.1.3 is limited by the statistics available. Here, the coverage values warm spots form a near continuous distribution. Like the cool spots, there is clearly an observing bias against small, low temperature contrast warm spots. However, unlike the cool spots the lower coverage limit is overtaken by greater temperature contrast. The smallest warm/hot spot has a coverage value of $f \sim 0.01$. In the lower panel of Fig. 7.7 the coverage distribution of all warm and hot spots are presented together. The distribution of warm and hot spots here follows a proportion where $y \propto -x$, with an observing bias against small spots, until $f \sim 0.3$. This follows a similar distribution to the IC 5070 distribution. The two distributions compared below coverage 0.3 are found to be statistically similar, with a p-value of 20 percent.

The abundant population of the warm spot regime is a key conclusion of Chapter 6, and it is reinforced here.

7.4.2 Spot and stellar properties

This section relates the spot property fits to the spot properties for YSOs in all HOYS regions. Figure 7.7 presents the period against $K - W2$ inner disc excess for periodic YSOs in HOYS regions. The markers are coloured according to dominant spot properties, calculated as the proportion of hot spots to all spots for each object. In this way, dark blue (1.0) is all warm/hot spots and dark red (0) is no warm/hot spots. The boundary for $K - W2$ is marked, as a value below 0.5 mag indi-

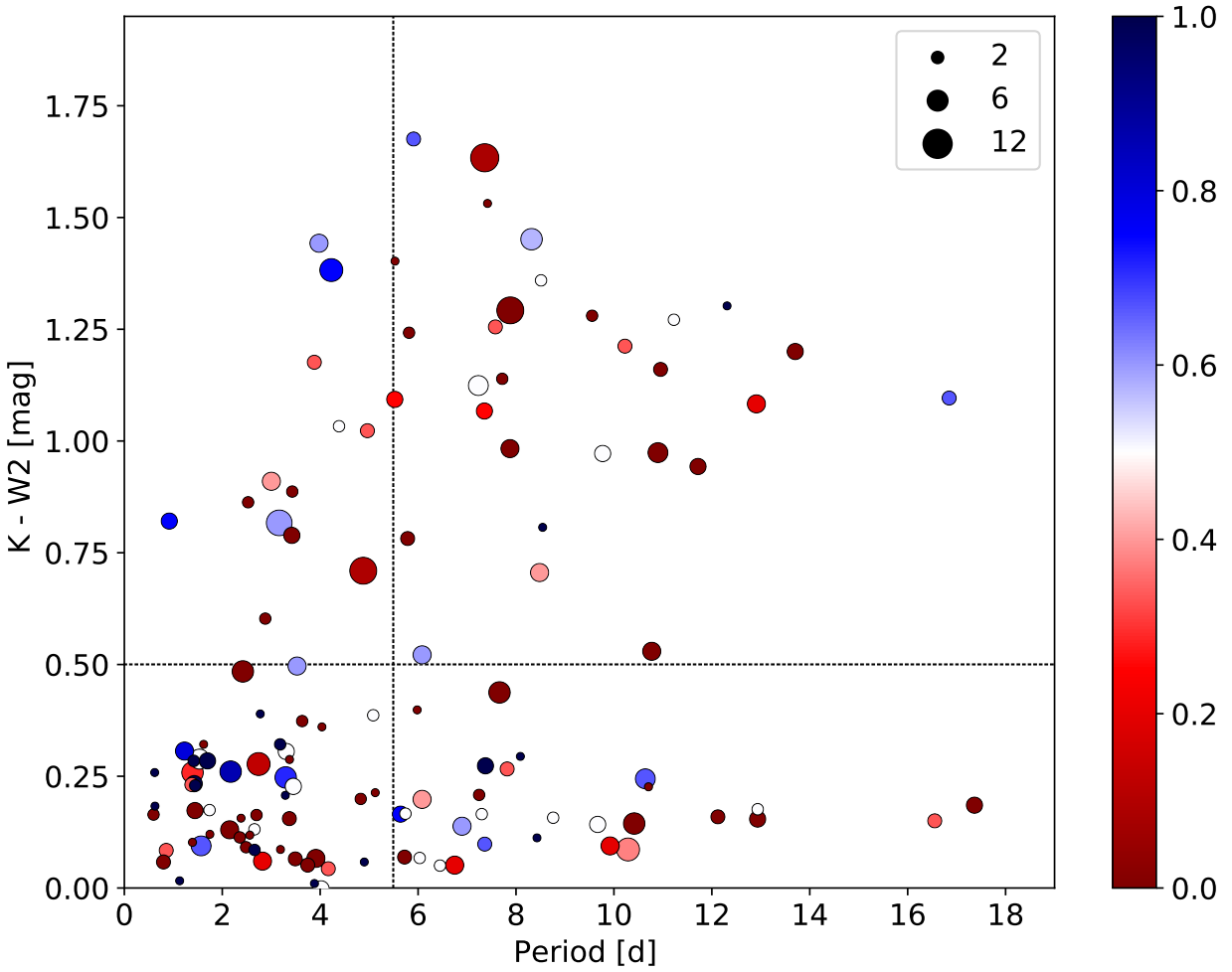

Figure 7.7: Period against $K - W2$ for periodic YSOs across HOYS fields. The horizontal dashed line separates objects with a detectable inner disc (above) from sources without (below). The vertical dashed line separates fast and slow rotators at $P = 5.5$ d. Markers are coloured based on the proportion of warm/hot spot measurements on them, according to the colour scale on the right. Values of zero (dark red) indicate that all spot solutions are cold, values of one (dark blue) mean all spot solutions are warm/hot. The marker size is scaled to number of spot property measurements, as shown in the legend.

cates no inner disc excess. The boundary for $P = 5.5$ d is also marked, represented the adopted separation for fast rotators in this sample. This is the equivalent plot to Fig. 6.4 in Section 6.1.4.

The majority of the periodic YSOs across HOYS fields do not have a detectable inner disc with $K - W2 < 0.5$ mag. From 144 sources, 94 have $K - W2 < 0.5$ mag. This fraction remains true, even when only spot bearing sources (of which there are 132) are included. The proportion of objects showing an inner disc excess here is the same as in IC 5070 alone, as in Section 6.1.4. Although here there are fewer objects that show an inner disc with a short period, and more objects that do not show an inner disc with a long period.

While objects with periods shorter than 5.5 d are denoted fast rotators here, it is not strictly necessary to denote objects with periods above 5.5 d as 'slow'. Depending on the region the division between fast and slow rotators (that have or have not lost their connections with the disc) is at a different position. Among objects that do not show an inner disc excess, 72 have periods longer than 5.5 d. This sample contains more long period objects than IC 5070 without $K - W2$ excess. Similar long period objects have been observed in a range of clusters (e.g. Moraux et al., 2013). These distributions are usually mass dependent, which is not characterised here.

The objects in this sample are likely in a variety of stages of disc evolution. Although $K - W2$ indicates the presence of an the inner disc, 75 of the 144 periodic sources have wise colours with SNR above five in all filters, allowing for classification according to α_{SED}. In the sample, 7 are Class 1 protostars, 10 are flat spectrum sources, 52 are Class 2, and 6 are Class 3. Therefore, it is reasonable to approximate two thirds of the YSOs examined here are Class 2 CTTS, with two thirds of these showing disc evolution.

In the sample, 35 objects are dominated by warm/hot spots, this is $26 \pm 4\%$ of the spot identified sources. In IC 5070, this percentage was 27 percent, and in the first sample was $20 \pm 8\%$, and hence the proportion identified here is consistent with previous findings. Among the sources that do not show an inner disc excess, 25 are dominated by warm/hot spots, with 13 of these containing only one or two slices.

The proportion of warm spot dominated objects that have $K - W2 < 0.5$ mag is 25/35 (71 ± 8

percent). The proportion of all spot baring objects with $K - W2 < 0.5$ mag objects is 86/132 (65 ± 4 percent). Therefore, warm spot dominated objects are not preferential to the presence or absence of an inner disc. This is the only statistically significant difference between the distribution identified here and the distribution identified in Section 6.1.4. Previously, the proportion of warm spot dominated objects with $K - W2 < 0.5$ mag was 88 ± 12 percent. The presence of an inner disc excess indicates that the object is still likely undergoing accretion, and therefore any warm/hot spots are related to this. However, a lack of $K - W2$ excess does not exclude emission related to accretion. According to the distribution of α_{SED}, the majority of these are likely to be transitional or pre-transitional discs which may still be actively accreting. Alternatively, these could be plages that as they appear on WTTS. Section 6.1.4 discusses causes of warm/hot spots in detail.

20 objects show equal cool and warm/hot spots, most of these are objects that do not show an inner disc excess. However, the distribution is approximately proportionate to the distribution of all objects across inner disc excess and period.

77 objects are cool spot dominated, with 50 showing entirely cool spots. It is worth noting that because of the very short well-sampled light curves, most of these only contain one or two slices. The percentage of cold spot dominated objects across all samples is $58 \pm 4\%$, which is the same (within the uncertainty) as the results of Section 6.1.4. The proportion of cold spot dominated objects that have $K - W2 < 0.5$ mag is 47/77 (61 ± 6 percent), showing that cold spot dominated objects are just as likely to appear with or without an inner disc excess. This is the same as in IC 5070 in Section 6.1.4.

The majority of objects here have available $\hat{A}^{o}_{\{V\}}$ in one or two slices, and therefore it is not possible to analyse spot evolution as it was in IC 5070. However, the range of YSOs analysed here provide a 'snapshot' into the spot properties of YSOs across all HOYS regions. The spot property distributions here closely reflect those observed in IC 5070 in Section 6.1.4, and reinforce the discussion and conclusions there.

8

Summary and conclusions

This chapter provides a detailed summary of the analysis and results presented in this thesis. The overall conclusion are provided, and potential future work is outlined.

8.1 Summary

Introduction

This chapter provided an one-page overview of the context for this thesis. The aim for this thesis alongside the outline of this thesis was given.

Young stellar objects: theory and data (Chapter 2)

This chapter provided relevant theory surrounding YSOs. This chapter started with the classification of YSOs from their spectral energy distributions. Details surrounding discs and disc evolution were provided. Next, accretion on YSOs and the relation between accretion and disc evolution was examined. The rotation of YSOs was discussed, with specific reference to star-disc interactions.

Following this, an overview of photometric variability of YSOs was provided, focusing on rotational modulation due to surface spots. Cool spots are often treated as analogous to sunspots, so the comparisons between sunspots and cold spots observed on YSOs are discussed. The causes of hot spots were introduced, as the footprints of accretion or photospheric/chromospheric bright regions known as plages.

Finally, an overview of the HOYS citizen science project that provided the data for this project was given. The target regions are identified, and information about IC 5070 (a key region in this thesis) was provided. A summary of the HOYS data calibration procedure was also presented.

Methodology (Chapter 3)

This chapter detailed the spot fitting methodology developed here and used throughout this thesis. A simple spot model has been utilised. It assumes a single temperature dominating spot, situated on a homogeneous stellar surface without limb darkening. Using stellar atmosphere template spectra peak-to-peak amplitudes are modelled for a range of spot temperatures and surface coverages. These are compared to the measurements for periodic YSOs in at least three optical filters to evaluate the best fitting spot properties. Measurement uncertainties are used to conduct a full error propagation. The typical uncertainties in spot temperatures are of the order of 200 K. The spot

coverage can be evaluated within a few percent of the stellar surface area. Also demonstrated are the systematic uncertainties caused either by uncertain stellar properties (e.g. $T_{\rm eff}$, $\log(g)$, [M/H]) or the choice of filter set. These are smaller than the statistical errors of the method. Furthermore, the methodology here allows us to identify AA Tau type contaminants in the sample of periodic YSO variables.

High cadence IC 5070 sample (Chapter 4)

The developed spot fitting methodology has been applied to a sample of 31 YSOs (denoted the F21 sample) that were selected based on their periodic light curves and astrometric properties as members of IC 5070 by Froebrich et al. (2021). The results are presented and analysed in this chapter.

In the F21 sample, two thirds (21/31) of the stars showed variability caused by cold spots, 19 % (6) show evidence for hot spots and two are AA Tau-type contaminants. A further two objects are considered ambiguous and cannot be classified. The identified hot spots have a coverage of less than 0.15 and a temperature up to 3000 K above the surface of the star. The cold spots have a temperature of up to 2500 K colder than the stellar surface, and the spots can cover up to 0.4 of the visible surface.

The spot properties do not show any significant correlation with the stellar rotation period or the presence of a disc. In particular, hot spots are present on objects without any significant infrared excess emission. This is examined with increased statistics in later chapters.

Additionally in this chapter, the influence of methodology on the results is discussed to inform the analysis conducted on long duration light curves.

Long duration IC 5070 sample (Chapter 5)

This chapter established a sample of YSOs in IC 5070 with long duration light curves suitable for spot fitting analysis. Froebrich et al. (2024) identified 366 YSOs in IC 5070 from Gaia DR3 data. Of these, 131 have light curves with at least 100 data points in V, R, and I from the HOYS citizen science project. These light curves have been sliced into six month long sections, every three

months. In this way, half of each slice overlaps with the previous. Using previously established best methods for identifying periodic variables in HOYS data from Froebrich et al. (2021), each individual slice that contained at least 50 data points in two of three filters was searched for a period. Slices that contained 50 data points in V, R, and I are suitable for spot fitting analysis. Any changes made to the established spot fitting methodology as a result of the discussion in Chapter 4 were detailed.

In this way, 32 periodic YSOs were identified, many of which overlapped with the sample identified in Froebrich et al. (2021). The period distribution and properties of the sample were established and suitable slices were fit for spots.

Spot property evolution (Chapter 6)

The sample identified in Chapter 5 provided 234 amplitude sets, the results are examined in this chapter. From 234 amplitude sets, 180 find reliable spot solutions. The amplitude sets that are not fit as spots are either near the edge of our parameter space, or create ambiguous solutions between cold and warm spots. The latter is most likely caused by complex spot structures, such as multiple spots with different temperature contrasts, which cannot be fit by our simple model.

A wide range of spot properties were measured. Roughly two thirds of all reliable spot solutions are cold. The coverage values of cold spots are homogeneously distributed between our lower detection limit of 6 percent and 30 percent, with maximum coverage values of around 40 percent. 90 percent of the cold spot solutions are between 0 K and 1500 K below the surface temperature. The minimum temperature difference is $\sim$ 280 K and the maximum temperature difference is $\sim$ 2150 K. We do not consider spot solutions that are within ten percent of our lower temperature limit (2000 K), as these measurements are potentially non-spot contamination. Alternatively, the spot temperatures are indeed below the lower temperature limit of our models. We discuss two objects (2, 5) that display the majority of these spot solutions and conclude that in these cases it is likely that the spot temperatures are indeed lower than we are able to fit.

A significant proportion (almost one third) of the spot solutions have temperatures above the stellar temperature, but by less than $\sim$2000 K. We find no spot temperatures between $\sim$2000 K

and 3000 K above the stellar temperature. Thus, a limit is proposed at 2500 K above the stellar temperature, separating warm and hot spots. Warm spots have a temperature contrast between 0 K and 2500 K and hot spots are more than 2500 K above the stellar temperature. Warm spots have a wide range of surface coverage values. The maximum coverage is around 40 percent, although 84 percent of warm spots have a coverage of less than 20 percent. The coolest warm spots have a temperature contrast of $\sim$ 310 K above the stellar temperature.

Five hot spot solutions are $\sim$3000 K above the stellar temperature, with coverage values of less than three percent. These align with expectations for accretion column footprints. Four of these five hot spot solutions are on the same object (30), which is a YSO without a detectable inner disc (in $K - W2$). This object can be considered to be actively accreting over the gap in the inner disc. The rarity (5/180, $\sim$3 percent) of such hot spot solutions shows that such accretion column photometric footprints are i) usually not stable on the timescale (6 months) at which we are able to investigate the spot properties, and/or ii) the photometry is not dominated by the accretion shock region.

The long-duration YSO sample in IC 5070 has an inner disc fraction of about 50 percent, based on the $K - W2$ infrared excess. The objects in this sample are dominated by cold spot variability, which is expected considering that approximately two thirds of the spot solutions here are cold. We find that objects with more reliable spot solutions overall tend to have a higher proportion of cold spot solutions. Warm/hot spot dominated objects tend to have fewer reliable spot solutions. This implies that cold spots are longer lived, or more likely to produce simple rotational variability over longer timescales.

We find eight warm/hot spot dominated objects. Only one of these has a detectable inner disc (28). Accretion is common over an inner disc gap, although whether the rate is equivalent with full disc objects is subject to debate, and so these warm/hot spots may be accretion related features. Alternatively, warm photospheric plages have been observed on WTTSs with coverage values of around six percent (Donati et al., 2017). The low coverage warm spots may be accretion related warm regions or plages, whereas the larger regions are more likely accretion related. The single

warm/hot spot dominated object with a detectable inner disc is the only Class 1 protostar in our sample. It displays large warm spots in consecutive slices indicating extreme stability in the spot behaviour and therefore accretion.

Application to all YSOs in HOYS fields (Chapter 7)

In this chapter the spot fitting methodology is applied to a large sample of YSOs across all HOYS regions. All YSOs in HOYS young clusters with light curves containing over 100 data points in V, R, and I have been examined. Across all fields, 2047 objects are examined. Light curves were sliced into six month slices, searched for periodicity, and peak-to-peak amplitudes were determined following the previously established methodology. Across all fields, 144 objects were identified as periodically variable YSOs. Hence, seven percent of the sample was observed to display periodic variability for at least six months. This is the lower limit for the proportion of variable objects in the sample, as many objects are likely quasi-periodic, aperiodic, or were not displaying periodic variability during the observed period.

In IC 5070, the effective stellar temperatures have been obtained from Fang et al. (2020). There is not an available temperature reference for the majority of HOYS field YSOs. Therefore, a methodology to approximate stellar temperatures was developed here, in order to facilitate spot fitting. To validate the use of these adopted stellar temperatures, the YSOs in IC 5070 were re-examined. It was determined that while quantitive results for individual objects may be altered, the distributions were statistically similar and therefore the adopted temperatures could be used to fit spots on the YSOs across all HOYS fields.

Across all HOYS fields, 144 periodic YSOs produced 630 sets of peak-to-peak amplitudes, and from this 463 spots are fit. The ratio of warm/hot to cold spot fits is the same as identified in the previous chapter. The distribution of spot coverage values between the cold spots and the warm/hot spots are identical between the larger sample and the IC 5070 sample in Chapter 6.

There is a greater diversity of cold spot temperatures, although this may be a consequence of the wider range of stellar temperatures in the sample. The observing limits the coverage of cold spots detectable to $f \sim 0.05$. The majority of cold spots are below $f = 0.3$, although it appears

that as coverage increases, the temperature contrast decreases. This implies that very large spots are less likely to be very cold.

In Chapter 6 there was a dearth of spot fits around 2500 K above the stellar temperature, which created the threshold between warm and hot spots. With increased statistics, this gap does not appear and instead the distribution appears to follow a continuum. The boundary between warm and hot spots is kept at 2500 K for consistency, and the same proportion of spot fits appear above this boundary. The coverage distribution of these warm/hot spots was statistically identical to the distribution observed in Chapter 6.

The larger sample here has allowed for a wider picture of spot and stellar properties. The dominant spot properties of the objects have been considered alongside their periods and inner disc excess. Two thirds of the YSOs lack an inner disc excess, with more long period objects appearing without a $K - W2$ excess. The sample contains YSOs from many different regions, therefore while $P = 5.5$ d is used to separate the fast and slow rotators, the period distribution is more nuanced than in IC 5070.

Both the warm/hot and cool spot dominated objects show no preference with regards to inner disc excess. This is the only statistically significant change from the distributions in from Chapter 6, where warm spot objects were preferential to not showing a $K - W2$ excess. Objects with an inner disc are likely accreting, and therefore warm/hot spot variability is expected. Although, as discussed in Chapter 6, accretion is not the only cause of warm spot variability.

This chapter has summarised the spot property distribution and the relationship with stellar properties across all periodic, spot bearing YSOs in all HOYS fields and has demonstrated that the conclusions from Chapter 6 are reinforced with greater number statistics.

8.2 Overall conclusions

This thesis has established a methodology to effectively characterise the spot properties of YSOs from V-, R-, and I-band photometry with full uncertainty analysis. The spot fitting process utilises a flux replacement method with PHEONIX synthetic spectra to compare modelled peak-to-peak

amplitudes to the observed amplitudes of rotational modulation in the V-, R-, and I-bands.

The spot fitting methodology has been applied to two sample of YSOs in IC 5070, firstly to short-term high cadence data and secondly to long duration data. Following this, every YSO across all HOYS target regions was searched for periodicity, and spot properties were identified for all suitable sections of light curve.

The results of the spot fitting has demonstrated that approximately two thirds of the periodic rotational modulation observed is caused by cold spots, and one third is caused by warm/hot spots. The distribution of spot property results are statistically similar across all observed YSO samples. The majority of surface spots have been identified with coverage values less than $f \sim 0.3$. Rotational modulation is sensitive to the asymmetry in the spot distribution, and therefore this coverage is a lower limit of the total spot coverage area. A wide temperature range of cold and warm/hot spots has been identified, with a sensitivity to around 300 K above and below the stellar surface, dependent on spot coverage.

A significant population of large, low temperature contrast warm spots has been identified. These have previously been identified (Scholz et al., 2009, 2012; Bozhinova et al., 2016), but here it is demonstrated that this regime causes around 30 percent of all spot-related rotational variability. The photometry used here in V-, R-, and I-band data does not cover the peak of the spectral energy distribution for high temperature accretion shocks, and therefore this methodology is more sensitive to low temperature contrast warm spots.

Spot properties have also been related to stellar properties of YSOs, notably rotation period and inner disc excess. It has been demonstrated that cold spot variability dominates for the majority of objects, and this is not related to the presence of an inner disc. Warm/hot spots are also common on objects that do not present with an inner disc. However, the majority of YSOs in all these samples are Class 2 objects, and a significant proportion of objects with $K - W2 < 0.5$ mag are likely to be pre-transition or transition disc objects which are still undergoing accretion. Hence, these warm/hot spots are either related to ongoing accretion, such as the low density accretion columns or photospheric/chromospheric plages as observed on WTTS which dominate the photometry.

8.3 Future work

The light curves analysed in this thesis contain observations up to October 2022. Since, then the HOYS project has continued to collect data at a growing rate. As the project continues, the number of objects for which long-duration light curves are available will increase. The results of the long-duration light curves in IC 5070 imply that cold spots are longer lived, or more likely to produce rotational variability over longer timescales. Increasing our sample size will allow us to investigate this relationship in depth. A wider sample of long-duration light curves will also allow for investigations of cyclical spot behaviour, which thus far has not been observed on YSOs.

In this work, the majority of periodic objects identified across HOYS fields are located in regions that have been the focus of observing campaigns. Other regions can become the target of such campaigns in future years, although individual regions have been observed with high cadence observations since 2022. A short, high cadence period of observations allows for the accurate identification of rotation periods. Once rotation periods have been obtained, peak-to-peak amplitudes can be identified and fit with spot properties in regions which are not currently well characterised. A distribution of objects across regions with well characterised spot behaviour will inform the expectations of astronomers with regards to spot induced variability.

Additionally, with increased cadence, amplitudes may be generated from shorter slices of light curves, or generated without oversampling. Shorter slices would allow for greater understanding of rapidly changing spot properties. This has particular relevance to warm and hot spots related to accretion, which are expected to vary on shorter timescales.

It has been demonstrated that warm and hot spots contribute significantly to rotational variability in YSOs. Our understanding of warm and hot spots would be greatly informed by concurrent spectroscopic observations. As yet it is not clear what proportion of warm/hot spot behaviour is accretion driven. It appears that often accretion, even when present, does not dominate the photometry of these objects. Concurrent spectroscopic and photometric studies will allow us to probe the relationship between accretion and photometric variability.

A

Additional plots from Chapter 3

A.1 Comparison between PHOENIX and ATLAS9 results

Figure A.1 presents the spot property results of 10000 iterations for the F21 sample object 6393, the top panel uses the PHEONIX spectra models and the bottom panel uses ATLAS9. Warm spot objects such as 6393 have good agreement. Cool spot objects are greatly affected by the 3500 K lower temperature limit. Therefore, PHOENIX models are used throughout this thesis.

A.2 Dusty extinction results with shorter wavelength filters

Figures A.2 and A.3 presents the spot property results for grey extinction (top), $R_V = 3.1$ (middle), and $R_V = 5.0$ (bottom) for $\hat{A}^v_{\{B\}}$ and $\hat{A}^v_{\{U\}}$. These have good agreement with the $\hat{A}^v_{\{V\}}$ results discussed in Section 3.7.

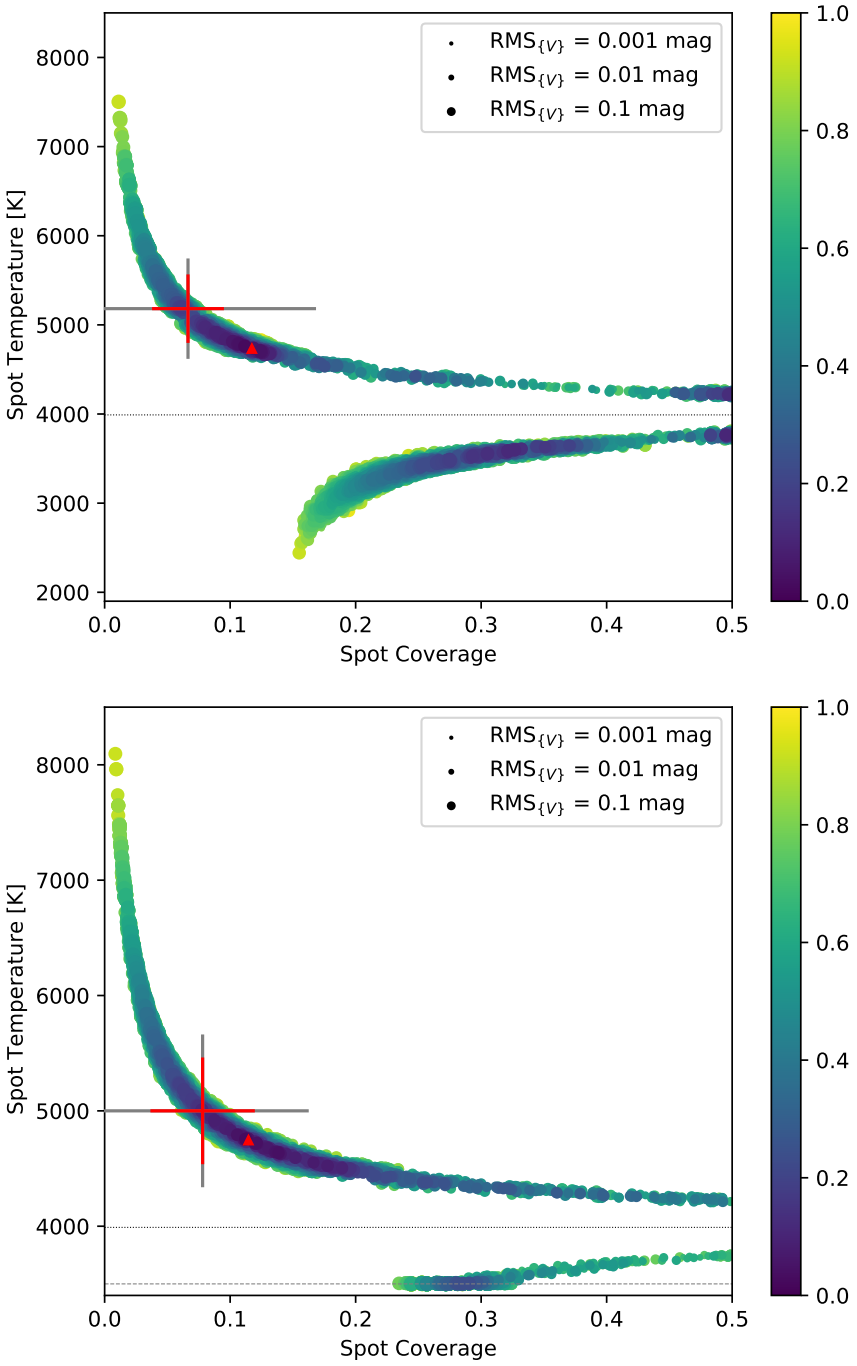

Figure A.1: As the bottom panel of Fig. 3.2 for F21 object 6393 using PHOENIX models (top) and ATLAS9 models (bottom). The horizontal dotted line at 4000 K marks the stellar temperature, and the horizontal dashed line in the bottom panel marks the lower limit of the ATLAS9 models. HS:CS$_{\{V\}}$ when using PHEONIX is 0.6029, and when using ATLAS9 is 0.7433. The object is classified as a hot spot regardless of models used.

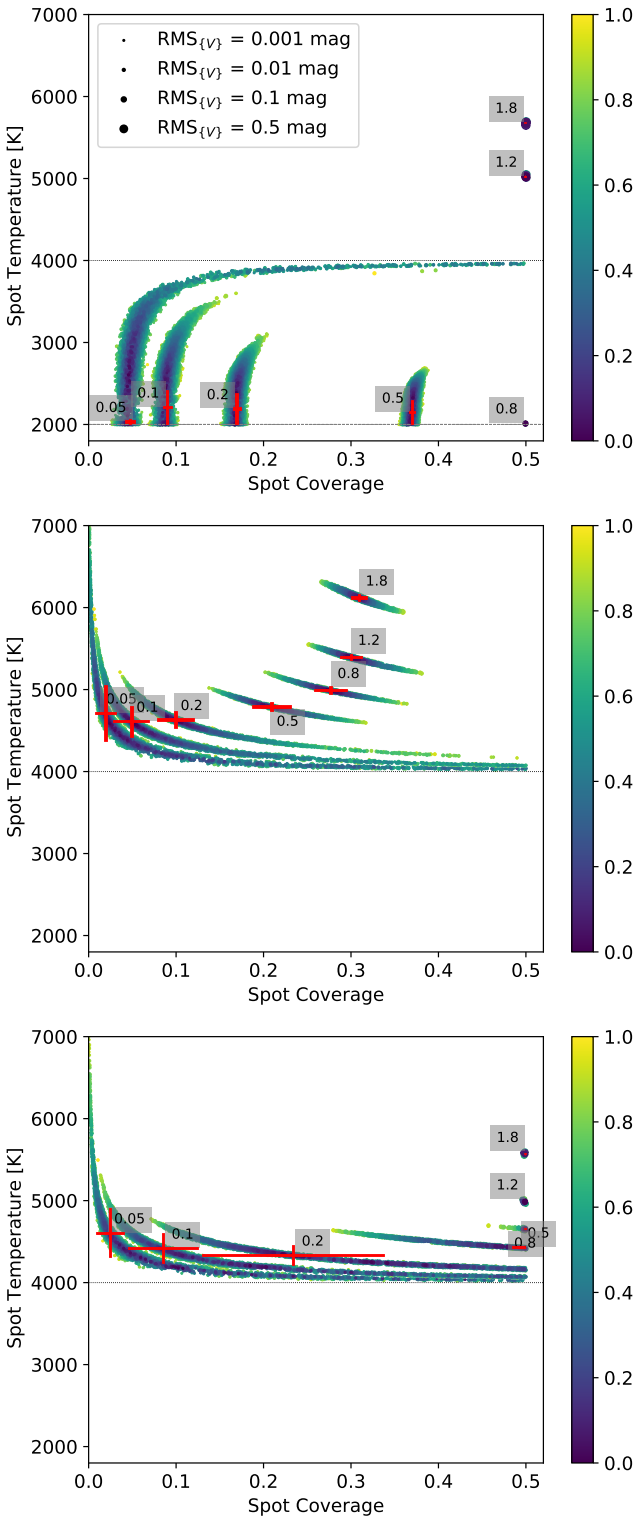

Figure A.2: As Fig. 3.6 for $\hat{A}^{v}_{\{B\}}$. The values in the grey boxes indicate the $\hat{A}_V$ amplitudes.

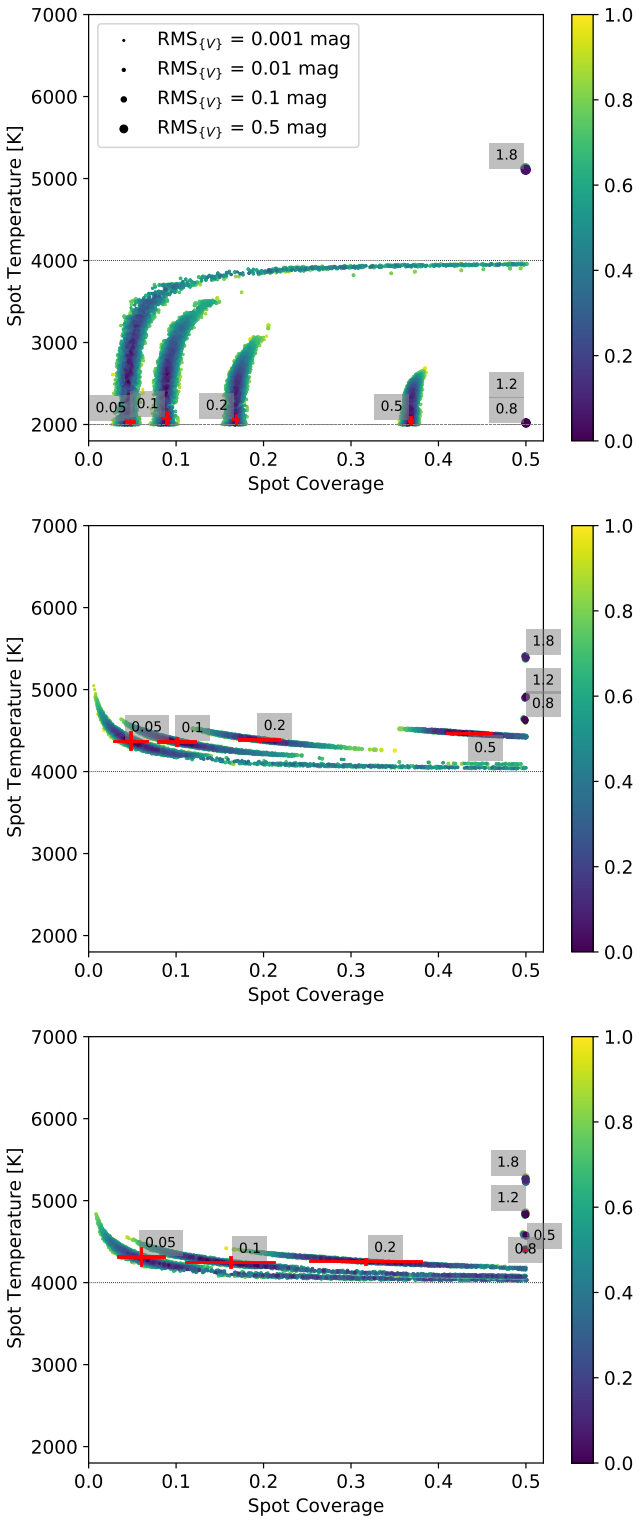

Figure A.3: Spot properties estimated for simulated grey (top), $R_V = 3.1$ (middle) and $R_V = 5.0$ (bottom) extinction caused by AA Tau like sources.The red crosses mark the position and uncertainties of the spot properties for $\hat{A}^v_{\{U\}}$. The values in the grey boxes indicate the $\hat{A}_V$ amplitudes. The coloured symbols follow the same scheme as in the right panel of Fig. 3.2.

B

Additional plots from Chapter 6

B.1 Spot property distribution with increased SNR requirement

Figure B.1 presents the spot property results and spot coverage distribution for the IC 5070 long duration sample with an SNR > 5 requirement for $\hat{A}^{o}_{\{V\}}$.

B.2 Object property plots

Presented here are the individual object property plots for the long duration YSO sample for all objects not in the main body of this thesis.

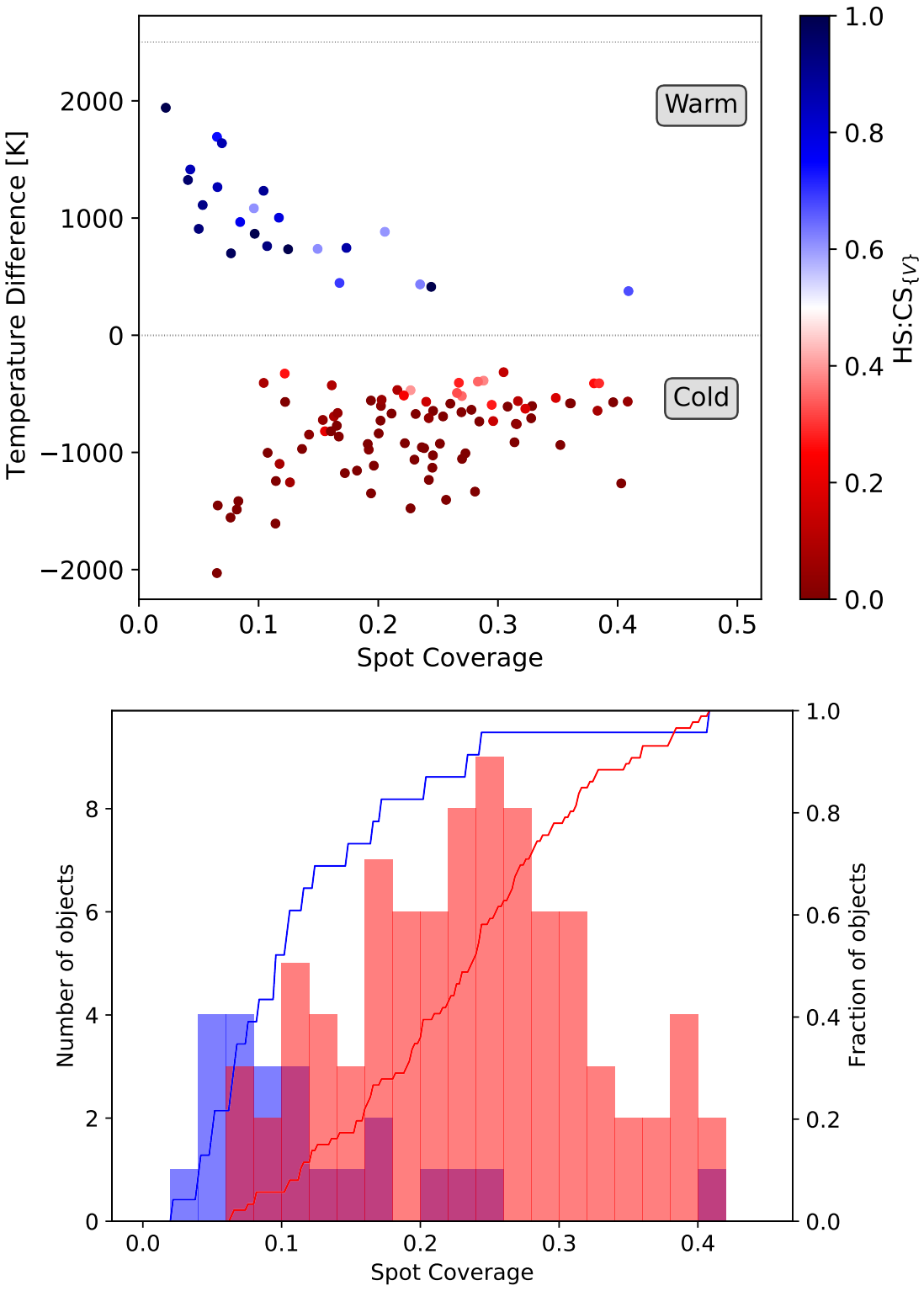

Figure B.1: As Fig. 6.2 for $\hat{A}^{o}_{\{V\}}$ with SNR above five in amplitude in all filters.

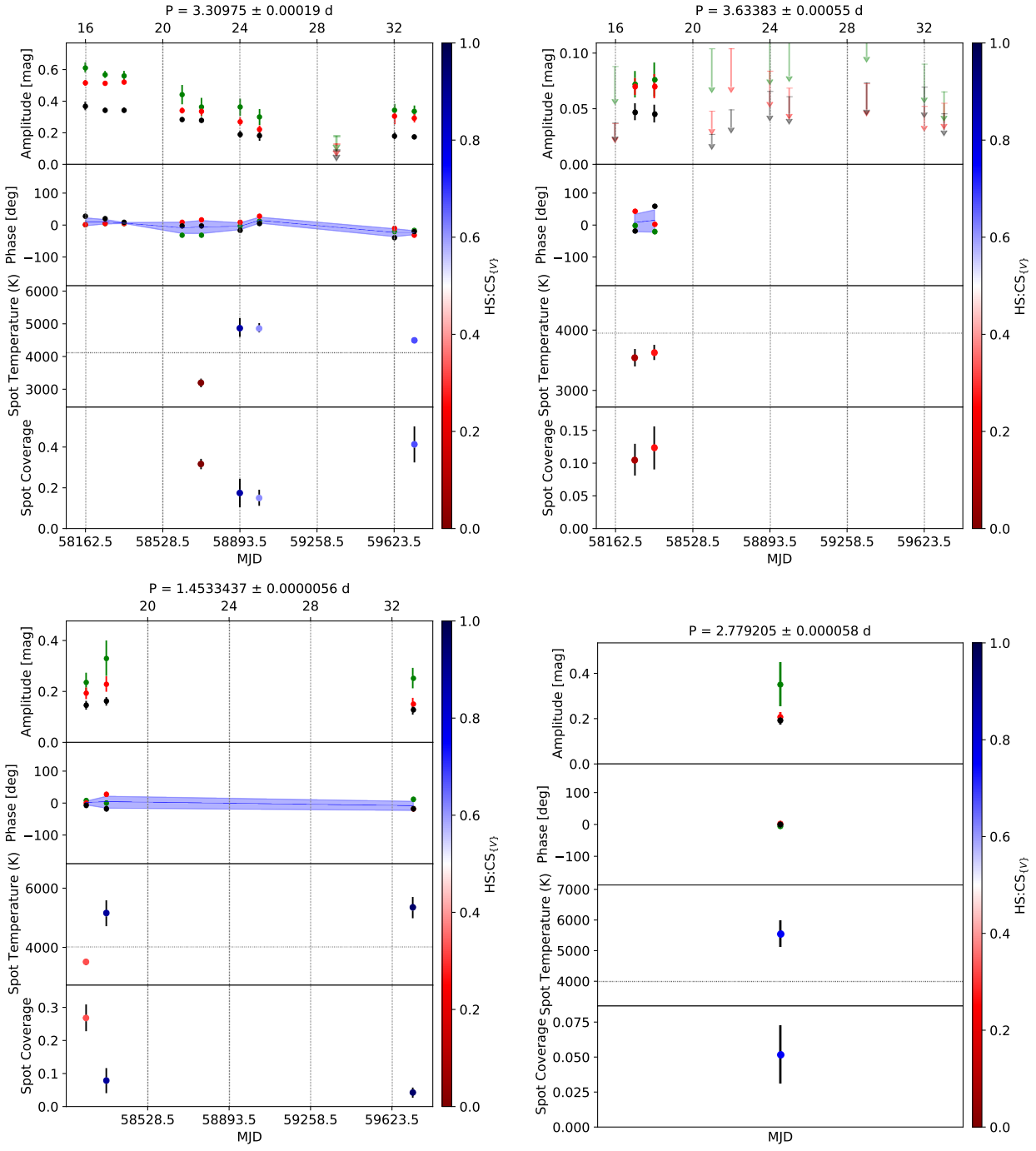

Figure B.2: As Fig. 6.1 for objects 6, 7, 8, and 9.

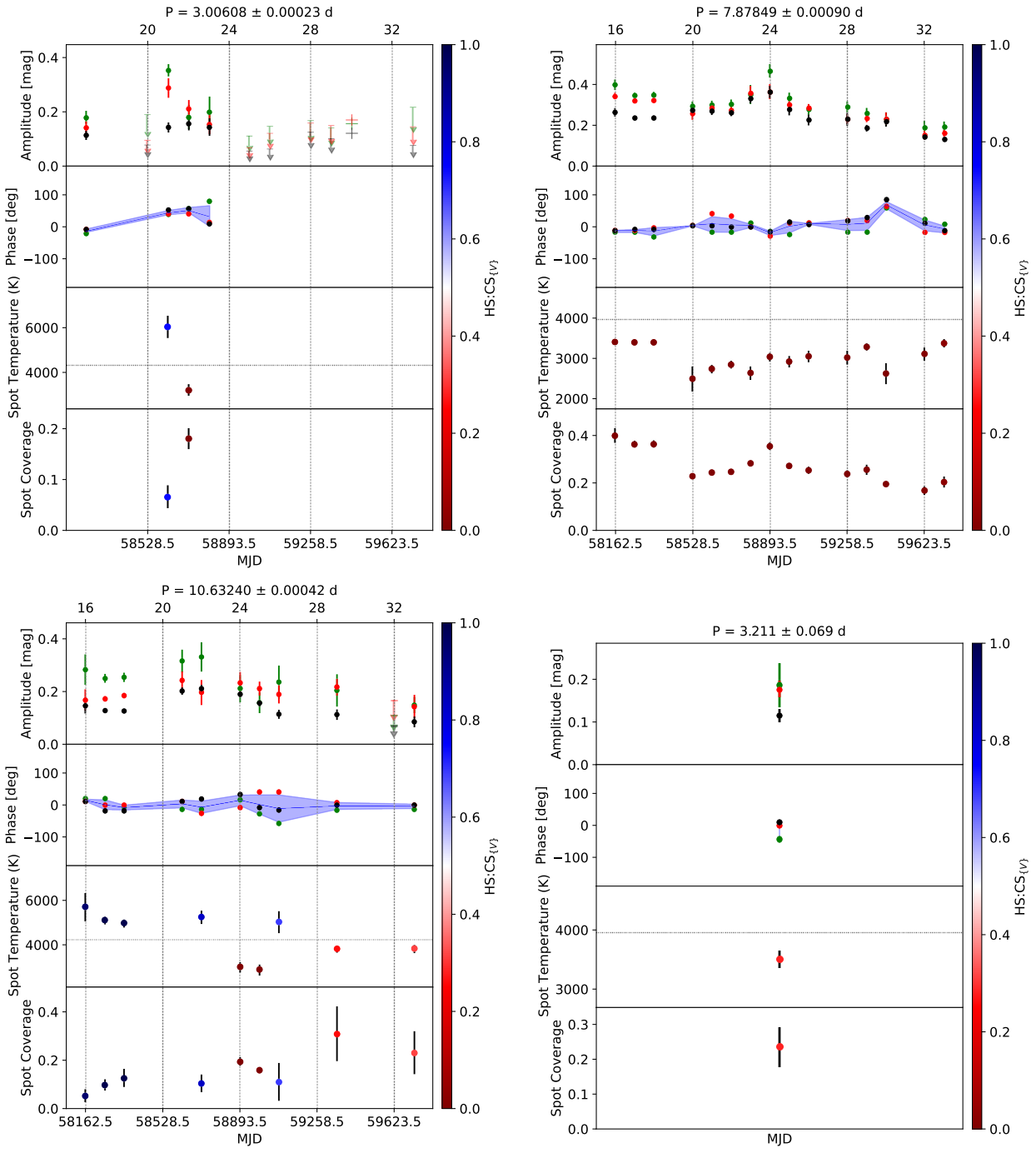

Figure B.3: As Fig. 6.1 for objects 10, 11, 14, and 16.

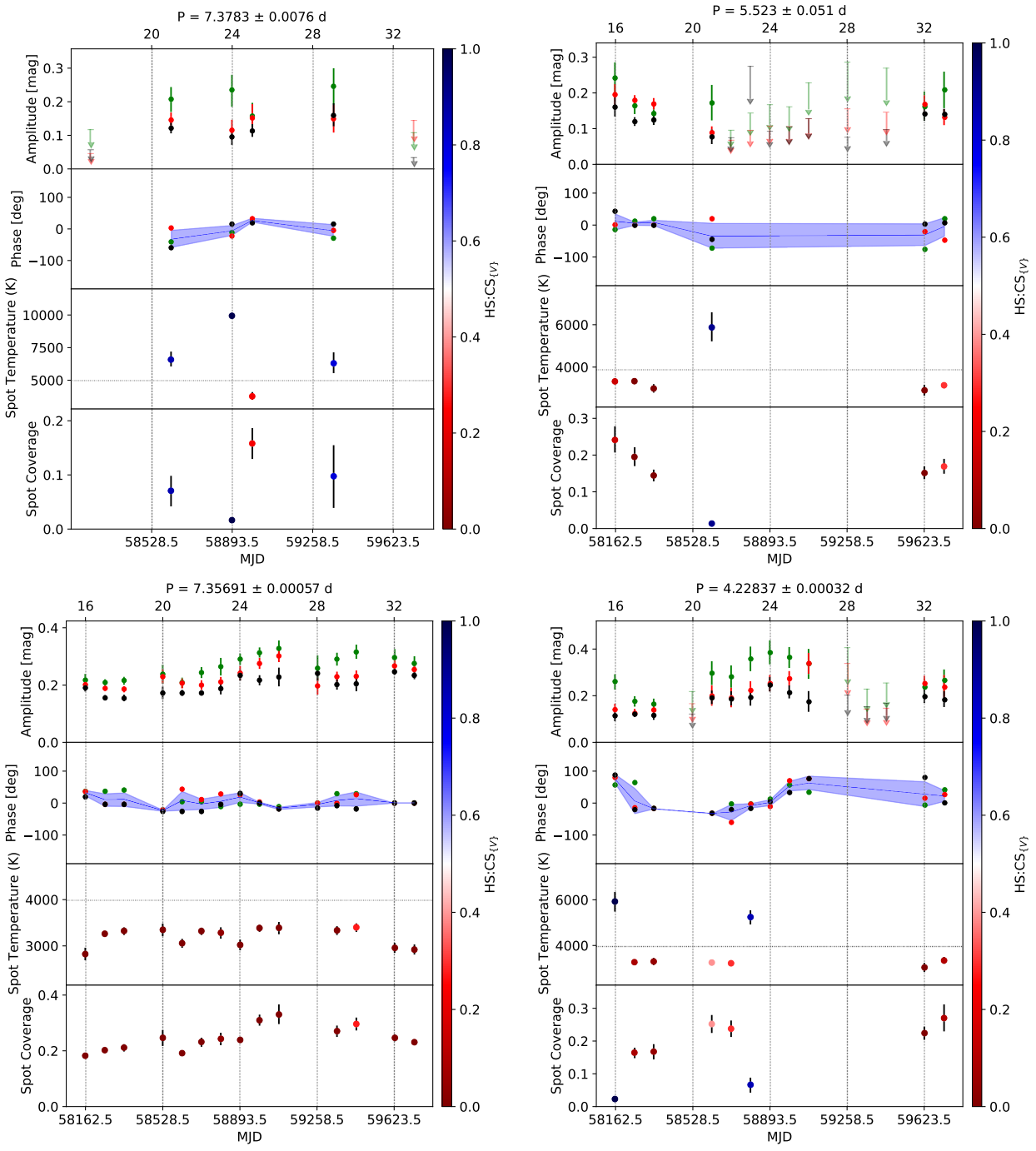

Figure B.4: As Fig. 6.1 for objects 17, 20, 21, and 22.

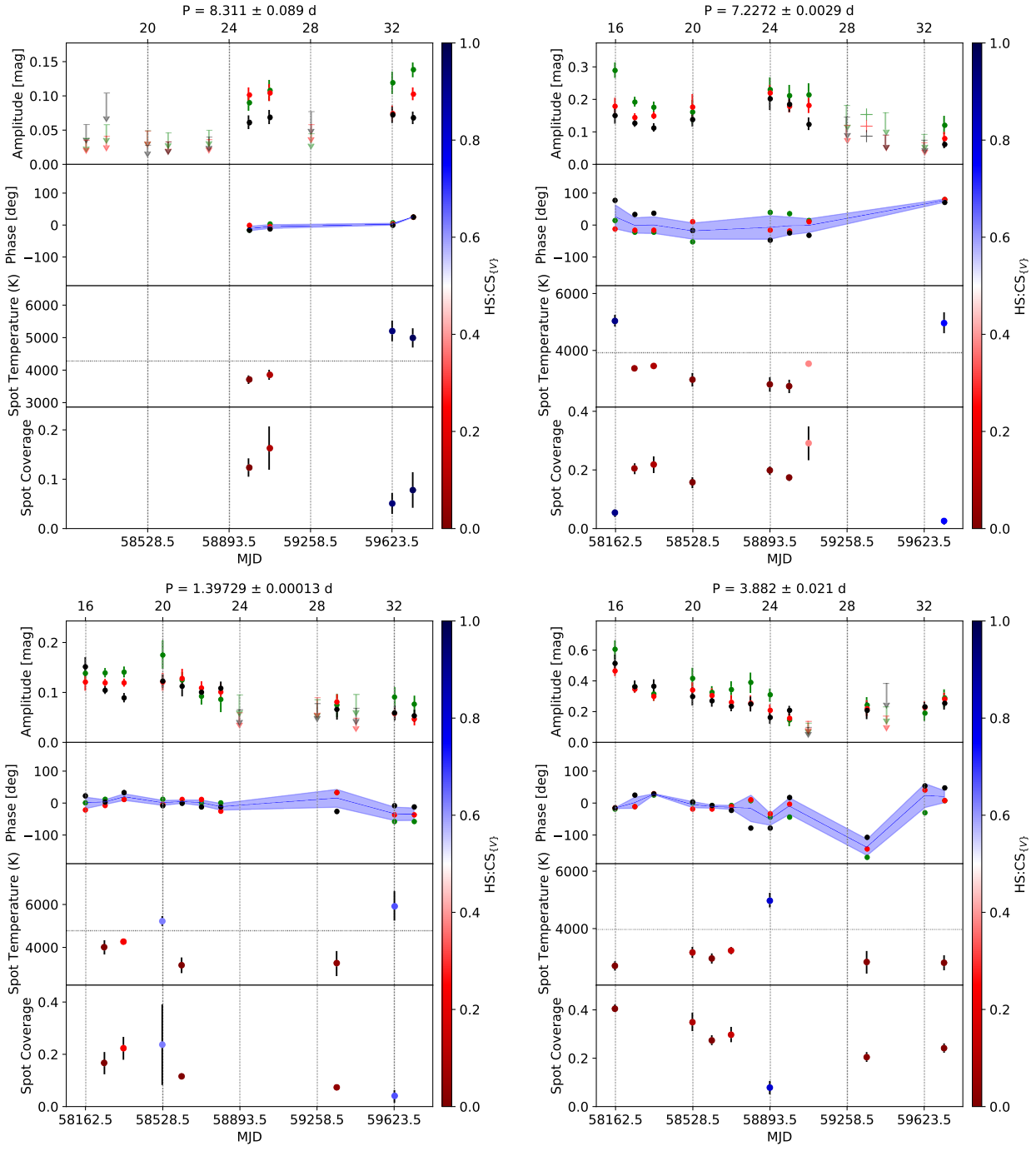

Figure B.5: As Fig. 6.1 for objects 23, 24, 25, and 26.

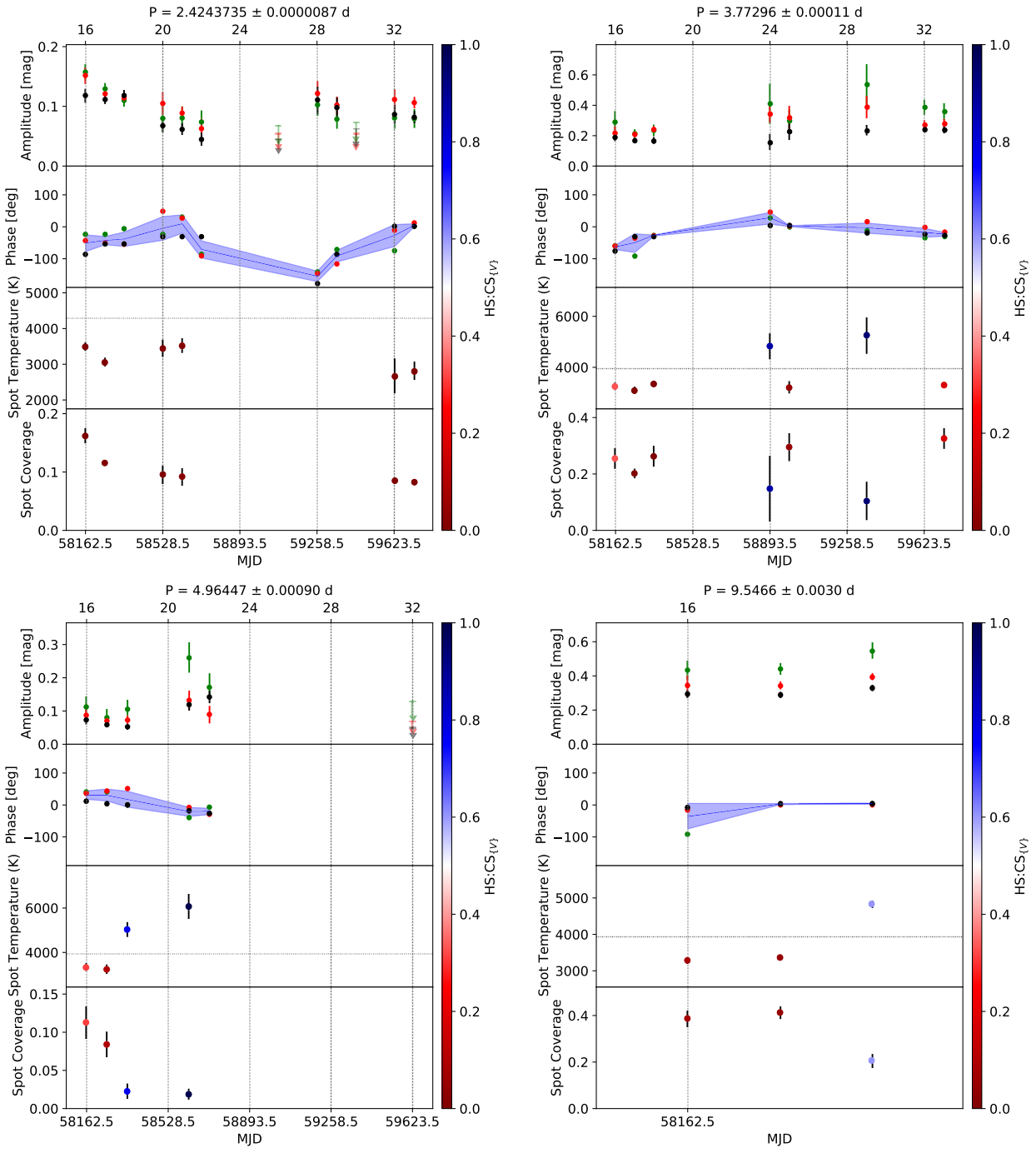

Figure B.6: As Fig. 6.1 for objects 27, 29, 31, and 32.

C

Additional data from Chapter 7

C.1 Target list of all periodic YSOs in HOYS regions

Provided in Table C.1 is the full target list of YSOs that have been identified as periodic with six month slices containing over 50 data points.

Table C.1: Target list for all periodic YSOs with sufficient data for spot fitting across all HOYS regions. Objects are listed in the order of their sorted Gaia DR3 ID numbers. Listed are the Gaia DR3 ID number, the associated HOYS region ID number, the J2000 coordinates, the determined period and its uncertainty, the adopted temperature used for spot fitting (discussed in Section 7.3), the number of six month slices available for spot fitting, and for overlapping sources in IC 5070, the F21 ID number and/or the ID number assigned in Chapter 5.

Gaia DR3 ID	Region ID	μ_α [mas/yr]	μ_δ [mas/yr]	Period [d]	Period error [d]	T_{fit} [K]	N slices	F21, Object ID
1974542739683523584	119	328.2868	47.1183	2.56542	0.00022	4900	2	- , -
1974545282304297856	119	328.3771	47.2455	5.81396	0.00031	3900	2	- , -
1974545625901682816	119	328.4204	47.2617	12.299	0.043	3850	2	- , -
1974545694621155584	119	328.4209	47.2810	3.42041	0.00064	4200	2	- , -
1974546072578275584	119	328.3576	47.2643	11.215	0.034	4550	2	- , -
1974546450535495680	119	328.4107	47.2860	2.88	0.11	5200	3	- , -
1974731890034857600	119	328.1940	47.2139	3.43143	0.00012	4750	2	- , -
1974731993119999616	119	328.1718	47.2145	7.7144	0.0016	4000	2	- , -
1974738418391182592	119	328.2666	47.3919	4.385	0.023	4800	2	- , -

2066866222797779072	118	312.8774	44.0625	3.16567	0.000034	5050	10	9321 , 1
2066866287224242432	118	312.8706	44.0731	4.82797	0.00020	7350	6	9267 , 2
2066870689567848192	118	312.7814	44.1763	3.52986	0.000096	4850	6	8038 , 3
2067058740416252416	118	312.7431	44.2423	4.87958	0.00029	4950	12	7422 , 4
2067058740416252544	118	312.7434	44.2456	3.4234	0.0003	5400	9	- , 5
2067061042518587264	118	312.4549	44.1795	3.30949	0.00014	4600	7	8025 , 6
2162929419847388544	118	313.0956	44.0158	3.63388	0.00057	5000	2	9961 , 7
2162934986124720896	118	313.3574	44.1792	1.45322	0.00013	4450	3	7954 , 8
2162941273956895872	118	313.3527	44.3428	2.77937	0.00014	4400	1	6393 , -
2162944916089431168	118	313.0939	44.2334	3.00580	0.00027	4500	5	7472 , 10
2162947596149035648	118	312.8260	44.2189	7.87857	0.00078	4900	13	7632 , 11
2162950413647417728	118	312.9439	44.3726	2.17499	0.00013	4700	11	6149 , 13
2162950546789495552	118	313.1453	44.2335	10.63256	0.00027	4500	7	7465 , 14
2162952475231874688	118	313.1180	44.3541	5.7851	0.0019	4050	3	- , -
2162960481050791936	118	313.4677	44.2849	7.3719	0.0071	4900	5	- , 17
2162964088823157632	118	313.4243	44.3601	1.4476257	0.0000039	6250	7	- , 18
2162965252757133056	118	313.3618	44.4243	0.626	0.018	5950	1	- , -
2163135573981345280	118	312.7561	44.2596	5.523	0.048	4400	5	- , 20
2163135578281583744	118	312.7565	44.2617	7.35702	0.00055	4900	13	7181 , 21
2163136059317926016	118	312.8131	44.3049	4.2280	0.0004	4350	12	6813 , 22
2163136368555566848	118	312.7190	44.2789	8.312	0.089	5150	7	- , 23
2163136402915307136	118	312.7446	44.2919	7.2271	0.0027	4700	9	6929 , 24
2163137261908777472	118	312.7776	44.3613	1.3974285	0.0000019	4500	9	6259 , 25
2163137742945115136	118	312.8445	44.3521	3.882	0.021	4600	9	6337 , 26
2163138601938577024	118	312.8188	44.3828	2.42438	0.00014	4950	10	6060 , 27
2163139594070911360	118	312.6920	44.3194	13.69	0.26	4250	8	- , 28
2163140319925497088	118	312.7639	44.4043	5.906	0.011	4150	3	- , -
2163144271295324544	118	312.9371	44.4386	3.77296	0.00017	4000	8	5559 , 29
2163146779556221952	118	313.1092	44.5739	1.4325902	0.0000039	5050	5	4446 , 30
2163148772421081728	118	312.8450	44.5618	4.96431	0.00093	3900	3	- , 31
2163156056685634944	118	312.7258	44.6356	9.5473	0.0031	4200	2	3988 , 32
2178374878170801792	115	324.5560	57.1863	4.9012	0.0062	4500	1	- , -
2178377901827757056	115	324.6805	57.3100	10.28020	0.00084	4750	8	- , -
2178383601237749632	115	324.8094	57.3703	4.03718	0.00041	4500	1	- , -
2178386045086501760	115	325.0386	57.4609	3.29054	0.00017	4500	1	- , -
2178386938439659392	115	324.9366	57.5111	0.924	0.035	6150	5	- , -
2178387556914944896	114	325.0083	57.5653	8.422	0.022	5150	2	- , -
2178391199046443648	115	324.4901	57.3799	7.57471	0.00039	4750	6	- , -
2178392740924572800	115	324.4370	57.4037	1.62422	0.00014	4500	1	- , -
2178392848313851392	115	324.3684	57.3902	16.53	0.36	4750	3	- , -
2178393982185180288	115	324.3181	57.4445	7.414	0.011	3800	1	- , -
2178394016544915328	115	324.2946	57.4362	1.3955	0.0039	7000	4	- , -
2178394291422867840	115	324.4593	57.4302	2.66041	0.00028	4650	2	- , -
2178394394502330496	115	324.5275	57.4560	1.70361	0.00013	5250	5	- , -
2178394497581292800	115	324.4461	57.4346	6.0797	0.0018	5500	5	- , -
2178394531941271936	115	324.4657	57.4479	2.362	0.087	7000	3	- , -
2178394699429915904	115	324.4628	57.4639	8.5386	0.0015	4300	2	- , -
2178395489703989504	115	324.4816	57.4922	7.2963	0.0017	4650	2	- , -
2178395631452868224	115	324.4119	57.4936	10.217	0.039	4450	4	- , -
2178395975050257024	114	324.4922	57.5222	1.3834637	0.00000031	4750	5	- , -
2178398895628585984	114	324.8588	57.5298	2.155	0.036	6750	5	- , -
2178399101787006464	114	324.8732	57.5616	0.861421746	0.0000000069	5200	5	- , -
2178400098219387904	114	324.8006	57.6045	16.8292	0.0057	5000	3	- , -
2178401575688130688	114	324.7310	57.5916	8.303	0.004	5100	1	- , -
2178402056712608896	114	324.6082	57.5692	9.30624	0.00048	4800	6	- , -
2178402400321563904	114	324.5666	57.6157	8.7529	0.0034	5100	2	- , -
2178402606480266112	115	324.6897	57.6333	3.8835	0.0093	4350	1	- , -
2178402675199735424	114	324.6682	57.6437	9.9132	0.0011	4550	6	- , -
2178417346809283456	115	324.0296	57.3786	1.745	0.034	5300	2	- , -
2178421195099930240	115	324.0530	57.4768	4.645	0.012	5450	1	- , -
2178434938995215232	114	323.8276	57.5692	11.7067	0.0018	4600	5	- , -
2178440814510995456	115	324.2248	57.4663	4.1669	0.0005	5950	6	- , -
2178440951949966848	115	324.2793	57.4502	12.8977	0.0019	4950	5	- , -
2178441261187598208	115	324.2892	57.4948	3.493	0.021	5200	3	- , -
2178441432986447744	114	324.2939	57.5201	10.943	0.002	4650	5	- , -
2178442188900684032	114	324.2753	57.5338	1.23416	0.00047	5350	5	- , -
2178443185333123584	114	324.4591	57.5612	12.924	0.061	4650	6	- , -
2178446793105656704	114	324.0795	57.6362	7.01448	0.00076	4200	3	- , -
2178449438799259520	114	324.5703	57.6573	8.0844	0.0019	5050	2	- , -
2178449919842118144	114	324.6450	57.6886	1.53967	0.0000031	5150	6	- , -
2178451019353727104	115	324.5940	57.7314	6.4447	0.0018	5300	2	- , -
2178452668621309568	114	324.6846	57.7908	9.66039	0.00097	5050	4	- , -
2178498882466387072	115	324.9171	57.7823	5.6398	0.0012	4900	4	- , -
2221015863228441856	116	325.6784	66.2078	0.63188428	0.00000050	6050	4	- , -
3016871585188001536	007	84.1696	-6.8679	0.602436831	0.000000015	3850	2	- , -
3016879556647282816	007	84.4641	-6.6643	0.80573197	0.000000044	5150	4	- , -
3016882374145831680	202	84.4283	-6.6711	3.74654	0.00097	5200	4	- , -
3016904192579682176	202	84.6331	-6.6069	1.42	0.06	3650	2	- , -
3016935563020738688	007	84.2457	-6.4847	10.70	0.02	3650	1	- , -
3016957278375450752	202	84.5426	-6.4241	3.3764	0.0006	4050	2	- , -
3017197830905390592	007	83.8739	-5.8125	1.75181	0.00000088	5200	2	- , -
3017199170935143680	007	84.1010	-5.7469	5.9794	0.0065	4700	1	- , -
3017237993141611776	203	83.6677	-5.8377	2.3913	0.0082	5800	3	- , -
3017244216552060672	007	83.6985	-5.7308	4.2183	0.0059	5450	6	- , -
3017245831459893760	007	83.7997	-5.7605	4.0381	0.0018	4550	1	- , -
3017246651795678720	007	83.8245	-5.7097	5.52737	0.00075	5600	1	- , -

3017250087773385344	007	83.8042	-5.6597	3.04868	0.0000059	6350	1	- , -
3017250126427057024	007	83.7124	-5.7060	3.1840	0.0065	5450	2	- , -
3017251947493281536	003	83.9301	-5.6076	2.6630	0.0025	5750	3	- , -
3017265377852811776	203	83.8067	-5.5160	8.505	0.013	5650	5	- , -
3017265760107995904	003	83.7353	-5.5267	5.74028	0.0000063	5550	5	- , -
3017266168126793984	210	83.7625	-5.5004	5.0828	0.0044	5400	2	- , -
3017266206784582144	203	83.7877	-5.4998	4.07794	0.00047	5500	2	- , -
3017267306296233216	203	83.6465	-5.5362	5.12	0.14	5800	1	- , -
3017267478094926720	003	83.6154	-5.5320	3.3726	0.0004	6400	4	- , -
3017270669252519680	210	83.6883	-5.4178	3.45359	0.00024	5950	5	- , -
3017291942240221056	007	84.2538	-5.6936	3.1916	0.0073	5350	1	- , -
3017346952181228416	203	83.8743	-5.5482	3.9141	0.0034	6200	7	- , -
3017347291470793216	003	83.8849	-5.5198	2.313	0.033	6650	3	- , -
3017355400367313024	203	84.1339	-5.3959	4.020	0.011	6700	5	- , -
3017359527845298048	203	83.8955	-5.4873	2.532	0.075	4550	2	- , -
3017364544367271936	210	83.7113	-5.4003	2.35	0.11	5300	2	- , -
3017364613086735360	203	83.7332	-5.3870	17.35	0.34	6850	4	- , -
3017367494996951424	210	83.8269	-5.2771	3.76	0.17	5500	4	- , -
3017368014699258240	003	84.0437	-5.3292	6.03019	0.00042	4900	4	- , -
3017371588112037248	003	84.0708	-5.1952	7.38	0.32	5550	1	- , -
3017373924574255488	003	83.9282	-5.1985	3.29813	0.00053	5050	7	- , -
3017374233811898880	210	83.9422	-5.1811	3.59665	0.00014	4150	3	- , -
3017375951801904256	003	83.9652	-5.1359	2.82524	0.00065	5750	5	- , -
3017382407121669504	203	84.2156	-5.2250	2.48995	0.00053	5300	3	- , -
3046357806990068096	213	107.0442	-10.7691	1.1351	0.0022	6100	2	- , -
3046581110929906560	213	107.1821	-10.4137	2.3871	0.0061	5250	1	- , -
3209521037582290304	210	83.7599	-5.2633	6.0803	0.0017	5850	5	- , -
3209522618130302720	210	83.7368	-5.1925	3.97728	0.00059	5400	7	- , -
3209527634652049408	210	83.8477	-5.1810	7.65863	0.00045	4850	7	- , -
3209528012609165440	210	83.9128	-5.1490	6.7452	0.0052	5350	5	- , -
3209528523708699392	003	83.8055	-5.1555	9.742	0.052	4150	2	- , -
3209528905962364544	210	83.8595	-5.1445	2.7453	0.0028	6300	8	- , -
3216061001461614976	005	84.7167	-2.7788	10.763	0.083	4700	5	- , -
3216062272771926144	005	84.7216	-2.7314	7.8142	0.0059	4000	4	- , -
3216107490187638784	005	84.6136	-2.7527	7.0805	0.0026	4200	6	- , -
3216109861009561728	005	84.6843	-2.6722	10.890	0.011	5000	6	- , -
3216432464593272960	005	84.8872	-2.7970	2.70295	0.00042	4600	6	- , -
3216439023007610624	005	84.8857	-2.6622	6.8943	0.0019	5400	5	- , -
3216439847641330816	005	84.8550	-2.6395	9.762	0.022	4700	4	- , -
3216446547790307584	005	84.9493	-2.5403	1.57340	0.00015	5150	6	- , -
3216446689524900480	005	84.9687	-2.5340	12.923	0.039	4850	4	- , -
3216447239280699008	005	85.0141	-2.4837	7.357	0.031	4600	3	- , -
3216485722187722752	005	84.7985	-2.6008	12.1119	0.0058	4600	6	- , -
3216487749412405376	005	84.8453	-2.5592	7.2427	0.0017	3650	6	- , -
3216488329232163328	005	84.7725	-2.5418	5.7223	0.0047	4800	5	- , -
3216490223313304576	005	84.6478	-2.5310	10.4049	0.0044	5050	7	- , -
3216491151026233472	005	84.6678	-2.5052	7.8721	0.0011	4600	6	- , -
3216492869013787264	005	84.7002	-2.4539	8.4758	0.0082	5500	5	- , -
3216502798977562112	005	84.5281	-2.5063	7.351	0.002	4200	6	- , -

Bibliography

ALMA Partnership et al., 2015, ApJ, 808, L3

Akerlof C., et al., 1994, ApJ, 436, 787

Andre P., Ward-Thompson D., Barsony M., 1993, ApJ, 406, 122

Andrews S. M., Wilner D. J., Espaillat C., Hughes A. M., Dullemond C. P., McClure M. K., Qi C., Brown J. M., 2011, ApJ, 732, 42

Asplund M., Grevesse N., Sauval A. J., Scott P., 2009, ARA&A, 47, 481

Audard M., et al., 2014, in Beuther H., Klessen R. S., Dullemond C. P., Henning T., eds, Protostars and Planets VI. pp 387–410 (arXiv:1401.3368), doi:10.2458/azu˙uapress˙9780816531240-ch017

Babcock H. W., 1961, ApJ, 133, 572

Bacher A., Kimeswenger S., Teutsch P., 2005, MNRAS, 362, 542

Barenfeld S. A., Carpenter J. M., Ricci L., Isella A., 2016, ApJ, 827, 142

Baumann I., Solanki S. K., 2005, A&A, 443, 1061

Bedding T. R., et al., 2020, Nature, 581, 147

Bertin E., Arnouts S., 1996, A&AS, 117, 393

Bhardwaj A., Panwar N., Herczeg G. J., Chen W. P., Singh H. P., 2019, A&A, 627, A135

Böhm-Vitense E., 1958, Z. Astrophys., 46, 108

Bouvier J., Bertout C., Benz W., Mayor M., 1986, A&A, 165, 110

Bouvier J., Cabrit S., Fernandez M., Martin E. L., Matthews J. M., 1993, A&A, 272, 176

Bouvier J., Covino E., Kovo O., Martin E. L., Matthews J. M., Terranegra L., Beck S. C., 1995, A&A, 299, 89

Bouvier J., et al., 1999, A&A, 349, 619

Bouvier J., Matt S. P., Mohanty S., Scholz A., Stassun K. G., Zanni C., 2014, in Beuther H., Klessen R. S., Dullemond C. P., Henning T., eds, Protostars and Planets VI. p. 433 (arXiv:1309.7851), doi:10.2458/azu_uapress_9780816531240-ch019

Bozhinova I., Scholz A., Eislöffel J., 2016, MNRAS, 458, 3118

Bressan A., Marigo P., Girardi L., Salasnich B., Dal Cero C., Rubele S., Nanni A., 2012, MNRAS, 427, 127

Calvet N., Gullbring E., 1998, ApJ, 509, 802

Calvet N., et al., 2005, ApJ, 630, L185

Campbell-White J., Sicilia-Aguilar A., Manara C. F., Matsumura S., Fang M., Frasca A., Roccatagliata V., 2021, MNRAS, 507, 3331

Cao L., Pinsonneault M. H., van Saders J. L., 2023, ApJ, 951, L49

Carpenter J. M., Hillenbrand L. A., Skrutskie M. F., 2001, AJ, 121, 3160

Carpenter J. M., Mamajek E. E., Hillenbrand L. A., Meyer M. R., 2006, ApJ, 651, L49

Castelli F., Kurucz R. L., 2003, in Piskunov N., Weiss W. W., Gray D. F., eds, IAU Symposium 210 Vol. 210, Modelling of Stellar Atmospheres. p. A20 (arXiv:astro-ph/0405087)

Cieza L. A., et al., 2010, ApJ, 712, 925

Cody A. M., et al., 2014, AJ, 147, 82

Cutri R. M., et al. 2013, VizieR Online Data Catalog, 2328

D'Alessio P., Calvet N., Hartmann L., Lizano S., Cantó J., 1999, ApJ, 527, 893

D'Alessio P., Calvet N., Hartmann L., Franco-Hernández R., Servín H., 2006, ApJ, 638, 314

Derezea E., 2023, PhD thesis, University of Kent,, https://kar.kent.ac.uk/100735/

Donati J. F., Landstreet J. D., 2009, ARA&A, 47, 333

Donati J. F., et al., 2011a, MNRAS, 412, 2454

Donati J. F., et al., 2011b, MNRAS, 417, 472

Donati J. F., et al., 2012, MNRAS, 425, 2948

Donati J. F., et al., 2014, MNRAS, 444, 3220

Donati J. F., et al., 2017, MNRAS, 465, 3343

Duchêne G., et al., 2024, AJ, 167, 77

Dupree A. K., et al., 2012, ApJ, 750, 73

Edwards S., et al., 1993, AJ, 106, 372

Espaillat C., Calvet N., D'Alessio P., Hernández J., Qi C., Hartmann L., Furlan E., Watson D. M., 2007, ApJ, 670, L135

Espaillat C., et al., 2010, ApJ, 717, 441

Espaillat C., et al., 2012, ApJ, 747, 103

Espaillat C., et al., 2014, in Beuther H., Klessen R. S., Dullemond C. P., Henning T., eds, Protostars and Planets VI. pp 497–520 (arXiv:1402.7103), doi:10.2458/azu˙uapress˙9780816531240-ch022

Espaillat C. C., Robinson C. E., Romanova M. M., Thanathibodee T., Wendeborn J., Calvet N., Reynolds M., Muzerolle J., 2021, Nature, 597, 41

Evans Neal J. I., et al., 2009, ApJS, 181, 321

Evitts J. J., et al., 2020, MNRAS, 493, 184

Fang M., Kim J. S., van Boekel R., Sicilia-Aguilar A., Henning T., Flaherty K., 2013, ApJS, 207, 5

Fang M., Hillenbrand L. A., Kim J. S., Findeisen K., Herczeg G. J., Carpenter J. M., Rebull L. M., Wang H., 2020, ApJ, 904, 146

Fischer W. J., Hillenbrand L. A., Herczeg G. J., Johnstone D., Kospal A., Dunham M. M., 2023, in Inutsuka S., Aikawa Y., Muto T., Tomida K., Tamura M., eds, Astronomical Society of the Pacific Conference Series Vol. 534, Protostars and Planets VII. p. 355 (arXiv:2203.11257), doi:10.48550/arXiv.2203.11257

Frasca A., Biazzo K., Taş G., Evren S., Lanzafame A. C., 2008, A&A, 479, 557

Frasca A., Biazzo K., Kővári Z., Marilli E., Çakırlı Ö., 2010, A&A, 518, A48

Froebrich D., et al., 2018, MNRAS, 478, 5091

Froebrich D., Scholz A., Eislöffel J., Stecklum B., 2020, MNRAS, 497, 4602

Froebrich D., et al., 2021, MNRAS, 506, 5989

Froebrich D., Eislöffel J., Stecklum B., Herbert C., Hambsch F.-J., 2022, MNRAS, 510, 2883

Froebrich D., et al., 2024, MNRAS, 529, 1283

Gaia Collaboration et al., 2016, A&A, 595, A1

Gaia Collaboration et al., 2023, A&A, 674, A1

Gallet F., Bouvier J., 2012, in Boissier S., de Laverny P., Nardetto N., Samadi R., Valls-Gabaud D., Wozniak H., eds, SF2A-2012: Proceedings of the Annual meeting of the French Society of Astronomy and Astrophysics. pp 35–38

Gallet F., Zanni C., Amard L., 2019, A&A, 632, A6

Grankin K. N., Bouvier J., Herbst W., Melnikov S. Y., 2008, A&A, 479, 827

Gravity Collaboration et al., 2023, A&A, 674, A203

Greene T. P., Wilking B. A., Andre P., Young E. T., Lada C. J., 1994, ApJ, 434, 614

Gregory S. G., Donati J. F., 2011, Astronomische Nachrichten, 332, 1027

Gregory S. G., Donati J. F., Morin J., Hussain G. A. J., Mayne N. J., Hillenbrand L. A., Jardine M., 2012, ApJ, 755, 97

Grevesse N., Sauval A. J., 1998, Space Sci. Rev., 85, 161

Gully-Santiago M. A., et al., 2017, ApJ, 836, 200

Haisch Karl E. J., Lada E. A., Lada C. J., 2001, ApJ, 553, L153

Hale G. E., Ellerman F., Nicholson S. B., Joy A. H., 1919, ApJ, 49, 153

Hambsch F.-J., 2012, Society for Astronomical Sciences Annual Symposium, 31, 75

Hartmann L., 1998, Accretion Processes in Star Formation. Cambridge University Press

Hartmann L., Kenyon S. J., 1996, ARA&A, 34, 207

Hartmann L., Herczeg G., Calvet N., 2016, ARA&A, 54, 135

Hathaway D. H., 2013, Sol. Phys., 286, 347

Hatzes A. P., 1995, ApJ, 451, 784

Herbert C., Froebrich D., Scholz A., 2023, MNRAS, 520, 5433

Herbert C., et al., 2024, MNRAS, 529, 4856

Herbig G. H., 1960, ApJ, 131, 632

Herbig G. H., 1977, ApJ, 217, 693

Herbst W., Herbst D. K., Grossman E. J., Weinstein D., 1994, AJ, 108, 1906

Herbst W., Bailer-Jones C. A. L., Mundt R., 2001, ApJ, 554, L197

Herbst W., Bailer-Jones C. A. L., Mundt R., Meisenheimer K., Wackermann R., 2002, A&A, 396, 513

Herbst W., Eislöffel J., Mundt R., Scholz A., 2007, in Reipurth B., Jewitt D., Keil K., eds, Protostars and Planets V. p. 297 (arXiv:astro-ph/0603673)

Hernández J., et al., 2007, ApJ, 662, 1067

Hogg D. W., Blanton M., Lang D., Mierle K., Roweis S., 2008, in Argyle R. W., Bunclark P. S., Lewis J. R., eds, Astronomical Society of the Pacific Conference Series Vol. 394, Astronomical Data Analysis Software and Systems XVII. p. 27

Hueso R., Guillot T., 2005, A&A, 442, 703

Hughes A. M., Duchêne G., Matthews B. C., 2018, ARA&A, 56, 541

Husser T. O., Wende-von Berg S., Dreizler S., Homeier D., Reiners A., Barman T., Hauschildt P. H., 2013, A&A, 553, A6

Ingleby L., et al., 2011, ApJ, 743, 105

Ingleby L., et al., 2013, ApJ, 767, 112

Ingleby L., Calvet N., Hernández J., Hartmann L., Briceno C., Miller J., Espaillat C., McClure M., 2014, ApJ, 790, 47

Johns-Krull C. M., 2007, ApJ, 664, 975

Johnstone C. P., Jardine M., Gregory S. G., Donati J. F., Hussain G., 2014, MNRAS, 437, 3202

Joy A. H., 1945, ApJ, 102, 168

Kenyon S. J., Hartmann L., 1987, ApJ, 323, 714

Kenyon S. J., Hartmann L. W., Strom K. M., Strom S. E., 1990, AJ, 99, 869

Kim K. H., et al., 2009, ApJ, 700, 1017

Kirmizitas O., Çavuş S., Aliccavucs F. K., 2022. https://api.semanticscholar.org/CorpusID:251800014

Koenigl A., 1991, ApJ, 370, L39

Kopp G., Krivova N., Wu C. J., Lean J., 2016, Sol. Phys., 291, 2951

Kuhn M. A., Hillenbrand L. A., Carpenter J. M., Avelar Menendez A. R., 2020, ApJ, 899, 128

Kurosawa R., Romanova M. M., 2014, in European Physical Journal Web of Conferences. p. 04004, doi:10.1051/epjconf/20136404004

Kurosawa R., Harries T. J., Symington N. H., 2006, MNRAS, 370, 580

Kurucz R. L., 1991, in Crivellari L., Hubeny I., Hummer D. G., eds, NATO Advanced Study Institute (ASI) Series C Vol. 341, Stellar Atmospheres - Beyond Classical Models. p. 441

Lada C. J., 1987, in Peimbert M., Jugaku J., eds, Star Forming Regions Vol. 115, Star Forming Regions. p. 1

Lamm M. H., Mundt R., Bailer-Jones C. A. L., Herbst W., 2005, A&A, 430, 1005

Li J., 2018, ApJ, 867, 89

Liang K.-c., Wang X., Li T.-H., 2009, BMC bioinformatics, 10, 15

Lim P. L., Diaz R. I., Laidler V., 2015, PySynphot User's Guider (ascl:1303.023)

Lorenzetti D., Larionov V. M., Giannini T., Arkharov A. A., Antoniucci S., Nisini B., Di Paola A., 2009, ApJ, 693, 1056

Lucas P. W., et al., 2008, MNRAS, 391, 136

Luger R., Foreman-Mackey D., Hedges C., Hogg D. W., 2021, AJ, 162, 123

Luhman K. L., Esplin T. L., 2020, AJ, 160, 44

Luhman K. L., Mamajek E. E., 2012, ApJ, 758, 31

Majaess D., 2013, Ap&SS, 344, 175

Manara C. F., Testi L., Natta A., Rosotti G., Benisty M., Ercolano B., Ricci L., 2014, A&A, 568, A18

Manara C. F., et al., 2021, A&A, 650, A196

Mathis J. S., 1990, ARA&A, 28, 37

Matt S., Pudritz R. E., 2008, ApJ, 681, 391

Matt S. P., MacGregor K. B., Pinsonneault M. H., Greene T. P., 2012, ApJ, 754, L26

Matthews B. C., Krivov A. V., Wyatt M. C., Bryden G., Eiroa C., 2014, in Beuther H., Klessen R. S., Dullemond C. P., Henning T., eds, Protostars and Planets VI. pp 521–544 (arXiv:1401.0743), doi:10.2458/azu˙uapress˙9780816531240-ch023

McGinnis P. T., et al., 2015, A&A, 577, A11

McLaughlin D. B., 1945, AJ, 51, 136

Merín B., et al., 2010, ApJ, 718, 1200

Moffat A. F. J., 1969, A&A, 3, 455

Mohanty S., Shu F. H., 2008, ApJ, 687, 1323

Monsch K., Drake J. J., Garraffo C., Picogna G., Ercolano B., 2023, ApJ, 959, 140

Moraux E., et al., 2013, A&A, 560, A13

Morris B. M., Hoeijmakers H. J., Kitzmann D., Demory B.-O., 2020, AJ, 160, 5

Muzerolle J., Calvet N., Hartmann L., 1998, ApJ, 492, 743

Muzerolle J., Calvet N., Hartmann L., 2001, ApJ, 550, 944

Muzerolle J., Hillenbrand L., Calvet N., Briceño C., Hartmann L., 2003, ApJ, 592, 266

Muzerolle J., Luhman K. L., Briceño C., Hartmann L., Calvet N., 2005, ApJ, 625, 906

Myers P. C., Ladd E. F., 1993, ApJ, 413, L47

Najita J. R., Carr J. S., Glassgold A. E., Valenti J. A., 2007a, in Reipurth B., Jewitt D., Keil K., eds, Protostars and Planets V. p. 507 (arXiv:0704.1841), doi:10.48550/arXiv.0704.1841

Najita J. R., Strom S. E., Muzerolle J., 2007b, MNRAS, 378, 369

Najita J. R., Andrews S. M., Muzerolle J., 2015, MNRAS, 450, 3559

Ostriker E. C., Shu F. H., 1995, ApJ, 447, 813

Panwar N., Jose J., Rishi C., 2023, Journal of Astrophysics and Astronomy, 44, 42

Pei Y. C., 1992, ApJ, 395, 130

Pelayo-Baldárrago M. E., Sicilia-Aguilar A., Fang M., Roccatagliata V., Kim J. S., García-Álvarez D., 2023, A&A, 669, A22

Penza V., Berrilli F., Bertello L., Cantoresi M., Criscuoli S., 2021, ApJ, 922, L12

Pinte C., Dent W. R. F., Ménard F., Hales A., Hill T., Cortes P., de Gregorio-Monsalvo I., 2016, ApJ, 816, 25

Pollack J. B., Hollenbach D., Beckwith S., Simonelli D. P., Roush T., Fong W., 1994, ApJ, 421, 615

Pudritz R. E., Matt S., 2014, in European Physical Journal Web of Conferences. p. 04001, doi:10.1051/epjconf/20136404001

Ramírez S. V., et al., 2004, AJ, 128, 787

Rebull L. M., Stauffer J. R., Megeath S. T., Hora J. L., Hartmann L., 2006, ApJ, 646, 297

Rice J. B., Strassmeier K. G., 1996, A&A, 316, 164

Rodríguez-Ledesma M. V., Mundt R., Eislöffel J., 2010, A&A, 515, A13

Rodriguez J. E., et al., 2015, AJ, 150, 32

Romanova M. M., Kulkarni A. K., Lovelace R. V. E., 2008, ApJ, 673, L171

Rydgren A. E., Vrba F. J., 1983, ApJ, 267, 191

Scargle J. D., 1982, ApJ, 263, 835

Scholz A., Eislöffel J., 2004, A&A, 419, 249

Scholz A., Xu X., Jayawardhana R., Wood K., Eislöffel J., Quinn C., 2009, MNRAS, 398, 873

Scholz A., Stelzer B., Costigan G., Barrado D., Eislöffel J., Lillo-Box J., Riviere-Marichalar P., Stoev H., 2012, MNRAS, 419, 1271

Shapiro A. I., Solanki S. K., Krivova N. A., Yeo K. L., Schmutz W. K., 2016, A&A, 589, A46

Shu F. H., Adams F. C., Lizano S., 1987, ARA&A, 25, 23

Sicilia-Aguilar A., Hartmann L. W., Fürész G., Henning T., Dullemond C., Brandner W., 2006, AJ, 132, 2135

Sicilia-Aguilar A., Henning T., Juhász A., Bouwman J., Garmire G., Garmire A., 2008, ApJ, 687, 1145

Sicilia-Aguilar A., Henning T., Hartmann L. W., 2010, ApJ, 710, 597

Sicilia-Aguilar A., Henning T., Kainulainen J., Roccatagliata V., 2011, ApJ, 736, 137

Sicilia-Aguilar A., et al., 2012, A&A, 544, A93

Sicilia-Aguilar A., Kim J. S., Sobolev A., Getman K., Henning T., Fang M., 2013, A&A, 559, A3

Sicilia-Aguilar A., Fang M., Roccatagliata V., Collier Cameron A., Kóspál Á., Henning T., Ábrahám P., Sipos N., 2015, A&A, 580, A82

Sicilia-Aguilar A., et al., 2023, MNRAS, 526, 4885

Skelly M. B., Unruh Y. C., Barnes J. R., Lawson W. A., Donati J. F., Collier Cameron A., 2009, MNRAS, 399, 1829

Skrutskie M. F., Cutri R. M., Stiening R., Weinberg M. D., Schneider S., Carpenter J. M., et al. 2006, AJ, 131, 1163

Solanki S. K., 2003, A&ARv, 11, 153

Sousa A. P., Alencar S. H. P., Rebull L. M., Espaillat C. C., Calvet N., Teixeira P. S., 2019, A&A, 629, A67

Stauffer J., et al., 2014, AJ, 147, 83

Strassmeier K. G., 1992, in Filippenko A. V., ed., Astronomical Society of the Pacific Conference Series Vol. 103, Robotic Telescopes in the 1990s. pp 39–52

Strassmeier K. G., 2002, Astronomische Nachrichten, 323, 309

Strassmeier K. G., 2009, A&ARv, 17, 251

Strassmeier K. G., Rice J. B., Wehlau W. H., Hill G. M., Matthews J. M., 1993, A&A, 268, 671

Strassmeier K. G., Kratzwald L., Weber M., 2003, A&A, 408, 1103

Strassmeier K. G., Carroll T. A., Ilyin I. V., 2019, A&A, 625, A27

Strom K. M., Strom S. E., Edwards S., Cabrit S., Skrutskie M. F., 1989, AJ, 97, 1451

Tan J. C., Beltrán M. T., Caselli P., Fontani F., Fuente A., Krumholz M. R., McKee C. F., Stolte A., 2014, in Beuther H., Klessen R. S., Dullemond C. P., Henning T., eds, Protostars and Planets VI. pp 149–172 (arXiv:1402.0919), doi:10.2458/azu˙uapress˙9780816531240-ch007

Teixeira P. S., Lada C. J., Marengo M., Lada E. A., 2012, A&A, 540, A83

Thanathibodee T., Calvet N., Hernández J., Maucó K., Briceño C., 2022, AJ, 163, 74

Thieler A. M., Backes M., Fried R., Rhode W., 2013, Statistical Analysis and Data Mining: The ASA Data Science Journal, 6, 73

Thieler A. M., Fried R., Rathjens J., et al., 2016, Journal of Statistical Software, 69, 1

Tognelli E., Prada Moroni P. G., Degl'Innocenti S., 2015, MNRAS, 454, 4037

Vargas-González J., Forbrich J., Rivilla V. M., Menten K. M., Güdel M., Hacar A., 2023, MNRAS, 522, 56

Venuti L., et al., 2014, A&A, 570, A82

Vicente S. M., Alves J., 2005, A&A, 441, 195

Virtanen P., et al., 2020, Nature Methods, 17, 261

Wang X.-L., Fang M., Herczeg G. J., Gao Y., Tian H.-J., Zhou X.-Y., Zhang H.-X., Chen X.-P., 2023, Research in Astronomy and Astrophysics, 23, 075015

Weingartner J. C., Draine B. T., 2001, ApJ, 548, 296

Welch D. L., Stetson P. B., 1993, AJ, 105, 1813

Wilking B. A., 1989, PASP, 101, 229

Williams J. P., Cieza L. A., 2011, ARA&A, 49, 67

Wyatt M. C., Panić O., Kennedy G. M., Matrà L., 2015, Ap&SS, 357, 103

Xiang Y., Gu S., Donati J. F., Hussain G. A. J., Collier Cameron A., MaTYSSE Collaboration 2023, MNRAS, 520, 3964

Zanni C., Ferreira J., 2013, A&A, 550, A99

Zechmeister M., Kürster M., 2009, A&A, 496, 577

Zhang L., Pi Q., Zhu Z., Zhang X., Li Z., 2014, New Astron., 32, 1

Publications

Lead author

Herbert, C., Froebrich, D., et al. (2024) A survey for variable young stars with small telescopes: IX – Evolution of Spot Properties on YSOs in IC 5070. *MNRAS 529 4856-4878.*

Herbert, C., Froebrich, D., Scholz, A., (2023) A survey for variable young stars with small telescopes: VII – Spot Properties on YSOs in IC 5070. *MNRAS 520, 5433-5445.*

Co-author

Sicilia-Augilar, A., Kahar, R. S., Pelayo-Barldárrago, M. E., **et al. including Herbert, C.**, (2024) North-PHASE: Studying Periodicity, Hot Spots, Accretion Stability and Early Evolution in young stars in the northern hemisphere *Accepted by MNRAS.*

Froebrich, D., Scholz, A., Campbell-White, J., Vanaverbeke, S., **Herbert, C.,** et al. (2024) A survey for variable young stars with small telescopes: VIII – Properties of 1687 Gaia selected members in 21 nearby clusters. *MNRAS 529 1283-1298*

Froebrich, D., Hillenbrand, L. A., **Herbert, C.,** et al., (2023) A survey for variable young stars with small telescopes: VI – Analysis of the outbursting Be stars NSW 284, Gaia 19eyy, and VES 263. *MNRAS 520 5413-5432.*

Froebrich, D., Eisloffel, J., Stecklum, B., **Herbert, C.**, Hambsch, F.-J., (2022) A survey for variable young stars with small telescopes: V – Analysis of TX Ori, V505 Ori, and V510 Ori, the HST ULLYSES targets in the σ Ori cluster. *MNRAS 510, 2883-2899.*

Froebrich, D., Derezea, E., **et al. including Herbert, C.**, (2021) A survey for variable young stars with small telescopes: IV – Rotation Periods of YSOs in IC 5070. *MNRAS 506, 5989-6000.*